SC5544.FR

Copy No. 4

# STUDIES OF PHASE-CONJUGATE OPTICAL DEVICE CONCEPTS



**FINAL REPORT FOR THE PERIOD**
**May 1, 1988 through September 30, 1990**

**CONTRACT NO. N00014-88-C-0230**

**Prepared for:**

**Dr. Herschel Pilloff**
**Office of Naval Research**
**Physics Division, Code 1112**
**800 N. Quincy Street**
**Arlington, VA 22217-5000**

**Prepared by:**
**William Christian, Ian McMichael and Pochi Yeh**

**APRIL 1991**

**Approved for public release; distribution unlimited**

Rockwell International
Science Center

UNCLASSIFIED

SECURITY CLASSIFICATION OF THIS PAGE

# REPORT DOCUMENTATION PAGE

*FORM APPROVED OMB No. 0704-0188*

**1a. REPORT SECURITY CLASSIFICATION**
UNCLASSIFIED

**1b. RESTRICTIVE MARKINGS**

**2a. SECURITY CLASSIFICATION AUTHORITY**

**3. DISTRIBUTION/AVAILABILITY OF REPORT**
Approved for public release, Distribution Unlimited

**2b. CLASSIFICATION/DOWNGRADING SCHEDULE**

**4. PERFORMING ORGANIZATION REPORT NUMBER(S)**
SC5544.FR

**5. MONITORING ORGANIZATION REPORT NUMBER(S)**

**6a. NAME OF PERFORMING ORGANIZATION**
ROCKWELL INTERNATIONAL
Science Center

**6b. OFFICE SYMBOL** *(If Applicable)*

**7a. NAME OF MONITORING ORGANIZATION**

**6c. ADDRESS** *(City, State and ZIP Code)*
1049 Camino Dos Rios
Thousand Oaks , CA 91360

**7b. ADDRESS** *(City, State and ZIP Code)*

**8a. NAME OF FUNDING/SPONSORING ORGANIZATION**
Physics Division, Code 1112
Office of Naval Research

**8b. OFFICE SYMBOL** *(If Applicable)*

**9. PROCUREMENT INSTRUMENT IDENTIFICATION NUMBER**
NOOO14-88-C-0230

**8c. ADDRESS** *(City, State and ZIP Code)*
800 North Quincy St.
Arlington, VA 22217-5000

**10. SOURCE OF FUNDING NOS.**

| PROGRAM ELEMENT NO. | PROJECT NO. | TASK NO. | WORK UNIT ACCESSION NO. |
|---|---|---|---|
| | | | |

**11. TITLE** *(Include Security Classification)*
STUDIES OF PHASE-CONJUGATE OPTICAL DEVICE CONCEPTS

**12. PERSONAL AUTHOR(S)**
Christian, W., McMichael, I. and Yeh, P.

| 13a. TYPE OF REPORT | 13b. TIME COVERED | 14. DATE OF REPORT *(Year, Month, Day)* | 15. PAGE COUNT |
|---|---|---|---|
| FINAL REPORT | FROM 05/01/88 TO 09/30/90 | 1991, APRIL | 127 |

**16. SUPPLEMENTARY NOTATION**

| 17. COSATI CODES | | | 18. SUBJECT TERMS *(Continue on reverse if necessary and identify by block number)* |
|---|---|---|---|
| FIELD | GROUP | SUB-GROUP | Phase Conjugation<br>Phase Conjugate Gyros<br>Phase Conjugate Optical Devices |
| | | | |
| | | | |

**19. ABSTRACT** *(Continue on reverse if necessary and identify by block number)*

We investigate various nonlinear optical phase conjugators and their application in optical devices. Several of the device concepts are demonstrated including phase conjugate fiber-optic gyros, optical pattern classifiers.

**20. DISTRIBUTION/AVAILABILITY OF ABSTRACT**
UNCLASSIFIED/UNLIMITED [X] SAME AS RPT. [ ] DTIC USERS [ ]

**21. ABSTRACT SECURITY CLASSIFICATION**
UNCLASSIFIED

**22a. NAME OF RESPONSIBLE INDIVIDUAL**
Dr. Herschel Pilloff

**22b. TELEPHONE NUMBER** *(INCLUDE AREA CODE)*

**22c. OFFICE SYMBOL**

DD FORM 1473 Previous editions are obsolete.

UNCLASSIFIED

SECURITY CLASSIFICATION OF THIS PAGE

# TABLE OF CONTENTS

## LIST OF FIGURES

# 1.0 SUMMARY

## 1.1 Contract Description

This contract focused on the physics of novel phase-conjugators. Progress was made towards the development of a fiber version of our phase-conjugate gyro. This involved both theoretical and experimental studies of photorefractive phenomena and novel phase conjugators, especially mutually pumped phase conjugators (MPPC's). With a coupled-mode theory of the hologram sharing model we have been able to accurately describe the formation process of gratings in the MPPC and have provided a quantitative explanation as to why phase conjugation occurs in an MPPC. A study of the effects of seeding a mutually pumped phase conjugator was performed to further our understanding of the grating formation mechanism in this important class of phase conjugators. Also considered under this contract were issues related to long-term optical storage in photorefractive media. In particular, the diffraction properties of fixed gratings in photorefractive media were examined in the context of their possible use in both optical memory systems and optical pattern classifiers.

## 1.2 Scientific Problem

Optical phase conjugation has been investigated extensively for the purpose of wavefront aberration correction. Under contract No. N00014-85-C-0219 we demonstrated the first phase-conjugate fiber-optic gyro (PCFOG) and its ability to use low cost multimode fiber components. Key to the success of this effort was the use of a new class of phase conjugators (mutually pumped conjugators) that have the ability to operate with mutually incoherent beams at milliwatt power levels. Performance of the gyro was found to be limited by an unacceptable amount of noise in the PCFOG beat signal. Measurements indicated that this noise was associated with the use of bulk-optic components in the setup. To reduce the amount of noise present in the gyro we have constructed, under this contract, an all-fiber PCFOG using a low-cost single mode diode laser (operating at 830 nm) as the optical source. Difficulties in obtaining operation of the conjugator at 830 nm with only 200 μW of optical power from the fiber precluded measurements of the noise characteristics on this gyro.

Also investigated under this contract have been issues related to the grating formation mechanism in MPPC's, including the effects of seeding the grating formation process. As a result of our work we now have a clearer understanding of this important class of phase conjugators. The diffraction properties of both fixed and photoinduced gratings in photorefractive media have been examined in the context of their use in optical memory systems and optical pattern classifiers. Both of these devices have come under increased scrutiny in recent years as a result of growing interest in optical computing.

## 1.3 Progress Summary

There have been many areas of significant progress achieved under this contract. They include:

- Construction of an all-fiber PCFOG.
- Experimental and theoretical investigation of the effects of seeding on the phase of the grating in an MPPC.
- Development of a model to provide a quantitative basis for the hologram sharing model of MPPC formation.
- Formation of an analytical model to solve the interaction of N mutually incoherent pairs of beams in a photorefractive medium.
- Modeling the diffraction properties of photorefractive media with fixed gratings.
- Experimental and theoretical studies of the diffraction efficiency of strong volume holograms written in photorefractive media.
- Implementation of a novel optical learning machine using the Perceptron algorithm for pattern recognition.

Details of this progress are presented in Section 2.0, and in the publications included in this report as Appendices.

## 1.4 Publications and Presentations

### Publications

"Seeding and Grating Phase in Mutually Pumped Phase Conjugators," W.R. Christian, R. Saxena, and I. McMichael, submitted to J. Opt. Soc. Am. B (1991).

* "Diffraction Properties of Fixed Gratings in Photorefractive Media," Claire Gu and Pochi Yeh, J. Opt. Soc. Am. B **7**, 2339 (1990).

* "Diffraction Properties of Multiple-Beam Photorefractive Gratings," R. Saxena, F. Vachss, I. McMichael, and Pochi Yeh, J. Opt. Soc. Am. B **7**, 1210 (1990).

* "Optical Pattern Classifier with Perceptron Learning," J. H. Hong, S. Campbell, and Pochi Yeh, Appl. Opt. **29**, 3019 (1990).

* "Diffraction Efficiency of Strong Volume Holograms," J. H. Hong, Pochi Yeh, D. Psaltis and D. Brady, Opt. Lett. **15**, 344 (1990).

* "Coupled-Mode Theory of Hologram Sharing in Mutually Pumped Phase Conjugators," Pochi Yeh, Appl. Opt. **28**, 1961 (1989).

* "Two-Wave Mixing in Nonlinear Media," Pochi Yeh, IEEE J. Quantum Electron. **25**, 484 (1989).

### Presentations

"Grating Phase in Mutually Pumped Phase Conjugators," W. Christian, R. Saxena, and I. McMichael, presented at the Annual Meeting of the Optical Society of America, Orlando, Florida, October 15-20, 1990.

"Phase-Conjugate Interferometry," I. McMichael, presented at the Conference on Nonlinear Optics, Kauai, Hawaii, July 16-20, 1990.

"Seeded Mutually Pumped Phase Conjugators," W. Christian, R. Saxena, and I. McMichael, presented at the Conference on Lasers and Electro-Optics, Anaheim, CA, May 21-25, 1990.

"Phase Conjugate Fiber-Optic Gyros," I. McMichael, W. Christian, P. Beckwith, M. Khoshnevisan and Pochi Yeh, presented at Photorefractive Materials, Effects and Devices II, Ausois, France, January 17-19, 1990.

"Polarization-Preserving Phase Conjugators," I. McMichael, P. Beckwith and Pochi Yeh, presented at O-E LASE'89, Los Angeles, CA, January 15-20, 1989.

"Multimode Fiber Gyro Using a Mutually Pumped Conjugator," Ian McMichael, Paul Beckwith, and Pochi Yeh, presented at the Annual Meeting of the Optical Society of America, Santa Clara, CA, October 31 - November 4, 1988.

* "Recent Advances in Photorefractive Nonlinear Optics," Pochi Yeh, invited paper presented at the Laser Materials and Laser Spectroscopy Meeting, Shanghai, China, July 25 (1988).

---

* Works only partially supported by this contract.

## 2.0 PROGRESS

### 2.1 Phase-Conjugate Fiber-Optic Gyros

Under this contract we demonstrated that the correction of modal scrambling by phase-conjugation allows for the construction of fiber gyros using multimode fibers. In this section we review our progress in this area and we describe the construction of an all fiber device using a diode laser. Difficulties in obtaining operation of the mutually pumped phase conjugator at diode laser wavelengths precluded measurements of the all-fiber gyro's sensitivity.

Phase-conjugate fiber-optic gyros (PCFOG's) use phase conjugation to compensate for reciprocal phase changes due to thermal and mechanical effects on the fiber, while at the same time allowing for the measurement of the nonreciprocal phase shift produced by rotation.[1,2] Where the best standard fiber-optic gyros require polarization-preserving fibers and couplers to avoid polarization scrambling that is a source of noise and signal fading, the PCFOG can avoid this problem by using polarization-preserving phase conjugation.[3] This has the advantage of allowing for the use of inexpensive nonpolarization preserving, and even multimode fibers and components.[3-5] Our first objective was to demonstrate that the PCFOG is sensitive to the nonreciprocal phase shift produced by the Sagnac effect and can be used to sense rotation. A proof of concept experiment was set up for this objective using an externally-pumped crystal of barium titanate as the phase conjugator. This experiment, reported in Ref. 6, provided the first demonstration of rotation sensing with a PCFOG. In this proof of concept demonstration the length of the fiber-optic coil, and therefore the sensitivity of the gyro, was limited by the coherence length of the laser. To solve this problem we set up a PCFOG consisting of a Michelson interferometer in which the light beams from two arms travel as clockwise and counterclockwise beams respectively, in the same fiber optic coil and reflect from the same self-pumped phase-conjugator. We reported the demonstration of rotation sensing with this PCFOG in Ref. 7. Again, since phase conjugation can correct for modal scrambling, a PCFOG can use multimode fibers. However, complete correction of modal scrambling requires a polarization-preserving conjugator,[5] and the corresponding experimental setup of a PCFOG is complicated. To solve this problem we set up a PCFOG using a multimode fiber coil, a nonpolarization-preserving conjugator,[4] and a spatial filter to discriminate against the

portion of the light reflected by the conjugator that does not correct for modal scrambling. This experiment, reported in Ref. 8, provided the first demonstration of rotation sensing with a PCFOG using multimode fiber.

The demonstrations of PCFOG's noted above used a quarter-wave retarder for biasing. This biasing technique is known to be a source of noise and drift. The preferred biasing technique in interferometric fiber-optic gyros is to use a fast (faster than the roundtrip time in the fiber coil) phase modulation at one end of the fiber coil. In our first demonstrations of PCFOG's it was not possible to use this technique due to the requirement of mutual coherence between the two beams entering the photorefractive phase conjugator. However, the recently discovered mutually pumped phase conjugators (MPPC's)[9-11] provided a solution to this problem. The MPPC's have the unique ability to generate the conjugates of two beams that are mutually incoherent. To test this concept we set up the PCFOG shown in Fig. 1 using the bird-wing MPPC.[11] Light from a laser was coupled onto a rotating table by a single mode polarization-preserving fiber SMPPF. The light exiting from the fiber was split into two components by the polarizing beamsplitter PBS. One component traveled in a multimode fiber MMF, and both components eventually became the pumping beams for the bird-wing MPPC in a crystal of $BaTiO_3$. Although the coherence length of the laser was much shorter than the path length difference between the components entering the $BaTiO_3$ crystal, the MPPC was able to generate the conjugates of the two components.

Figure 2 shows representative gyro signals obtained from detectors D1 and D2. For the upper trace, the gyro was first stationary, then it was rotated clockwise, stopped, and then rotated counterclockwise for several cycles with an amplitude of approximately 6°/s. The experimentally measured phase shift was in good agreement with the predicted phase shift. The background noise level with the gyro stationary is shown in the lower trace (vertical scale is 10 times more sensitive).

Measurements indicated that the noise shown in Fig. 2 was associated with the bulk optical setup. To solve this problem, the all fiber PCFOG shown in Fig. 3 was constructed. Light from a single mode diode laser operating at 830 nm was coupled into a single mode fiber using a tapered fiber tip. This fiber was spliced to the first coupler which is used to split off light returning from the fiber coil for detection by a pin photodetector. The first fiber coupler is spliced to a second fiber coupler that splits

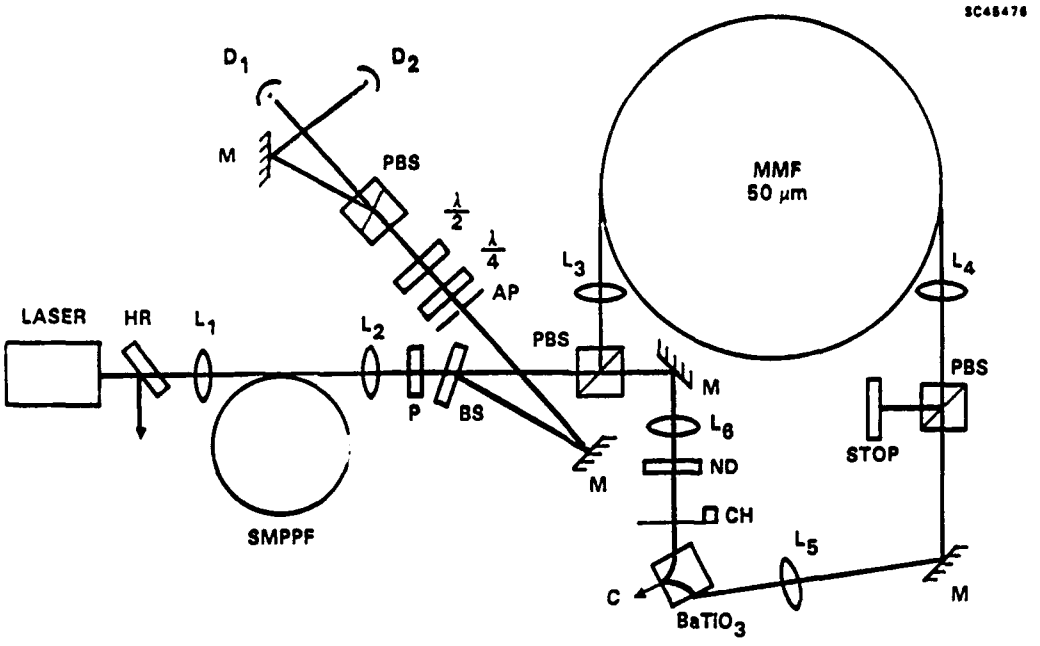


Fig. 1 PCFOG using the bird-wing MPPC.

SC45475

SIGNAL $\propto D_1 - D_2$
CHOPPER FREQUENCY 200 Hz

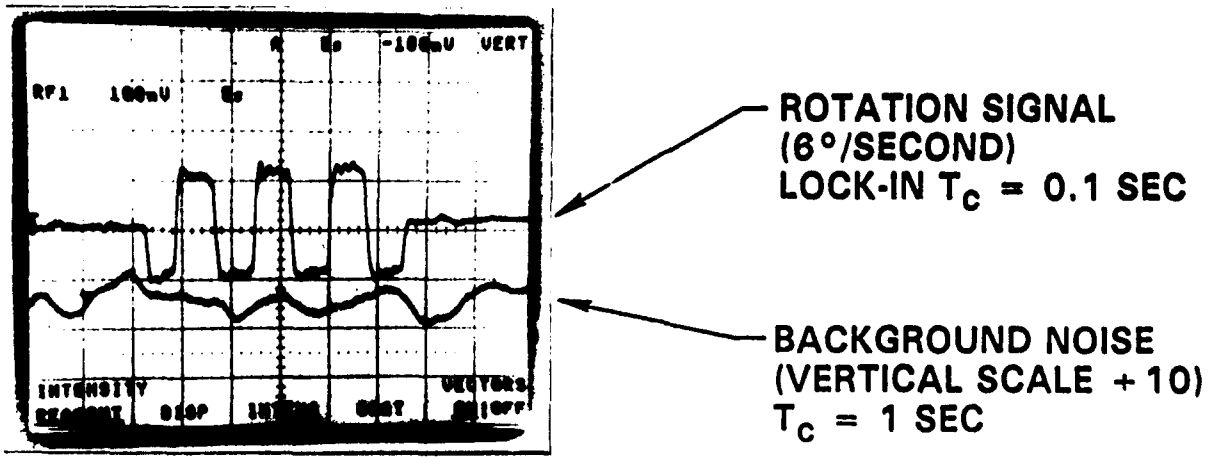


Fig. 2 Gyro Signals.

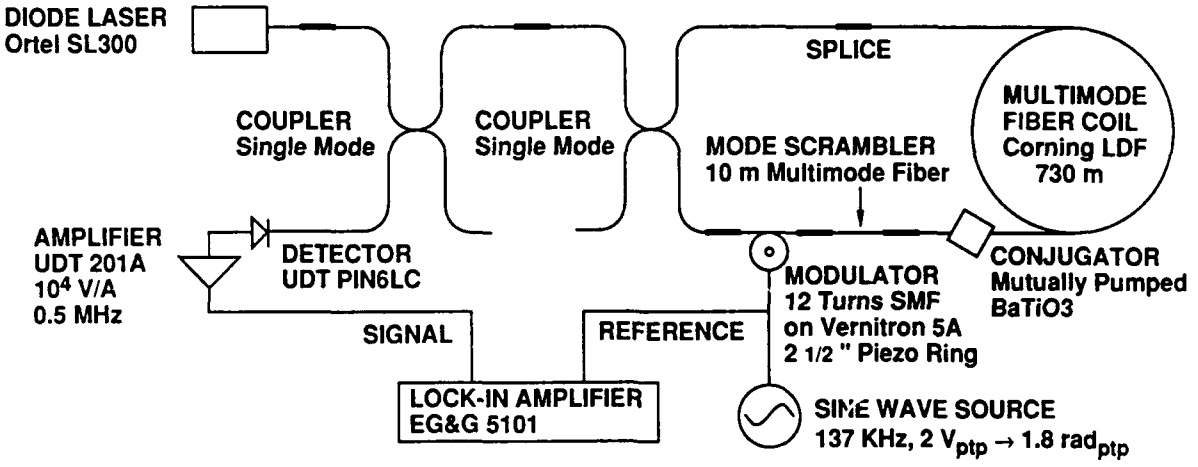


Fig. 3 All-fiber PCFOG.

light from the laser into the two counterpropagating waves in the fiber coil. A phase modulator consisting of 12 turns of single mode fiber on a PZT cylinder was used to provide a bias for phase sensitive detection with the lock-in amplifier. The conjugator was a single crystal of $BaTiO_3$ used in the mutually pumped configuration shown in Fig. 4. Operation at 830 nm was demonstrated using this configuration. A section of multimode fiber was used for mode scrambling prior to the conjugator to avoid problems with polarization changes that could give rise to signal fading. Difficulties in obtaining operation of the conjugator at 830 nm with only 200 μW's available at the fiber output precluded measurements with the all-fiber gyro.

## 2.2 Hologram Sharing in Mutually Pumped Phase-Conjugators

Early theories suggested that mutually pumped phase conjugators (MPPC's) form as a result of self-oscillation in an optical four-wave mixing process.[12] However, experimental evidence has since shown that fanning plays an important role and that mutually pumped phase conjugation does not seem to be a self-oscillation process. As detailed in Ref. 13 (Appendix 4.2) we have developed a model based on a coupled-mode analysis of the grating formation process showing that the amplification coefficient for mutually conjugated beams is twice that possible for any other scattered beams. This result provides a quantitative basis for the hologram sharing model of MPPC formation.

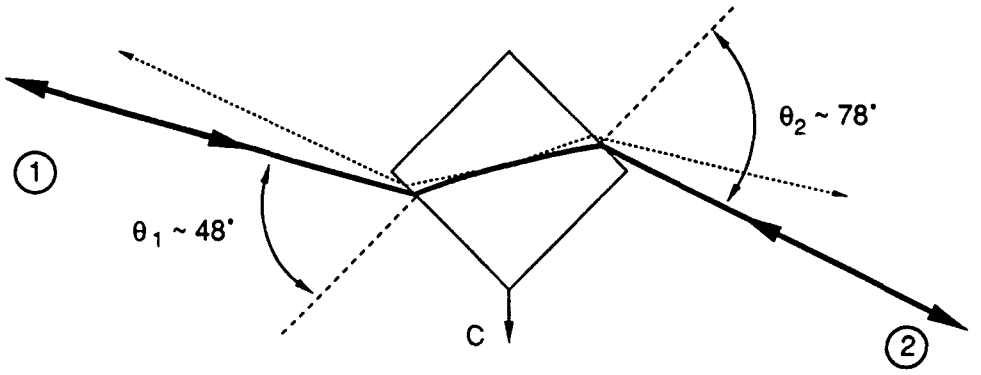


- PC REFLECTIVITY > 34 % (IN BOTH DIRECTIONS)
- POSSIBLE USES: 1) EFFICIENT PC LOCKING OF DIODE LASERS
  2) CONJUGATOR IN MULTI-MODE FIBER GYRO OPERATING AT 830 nm (GO 5544)

Fig. 4 MPPC at 830 nm.

## 2.3 Seeding and Grating Phase in Mutually Pumped Phase Conjugators

Mutually pumped phase conjugators (MPPC's) have as a distinguishing characteristic the ability to conjugate two mutually incoherent pumping beams simultaneously. This property makes them ideal candidates for applications in communications, laser locking, fiber optic gyros and optical information processing where coherence limitations can be a problem. When two pump beams enter a photorefractive material, an MPPC is generated as a result of competition between multiple gratings that form between each pump beam and its own amplified scattering. When one particular set of gratings is common to both pump beams, it dominates over all the other gratings being formed. This grating diffracts each pump beam into a conjugate beam for the other pump beam. One question that has remained unanswered to this point has been, what determines the phase of the grating being formed between the two mutually incoherent pump beams? From the above description, one might expect that, in the absence of any other determining factors, the phase of the photorefractive grating should be determined solely by the phase of the amplified scattering which is responsible for its formation. As detailed in Ref. 14 (Appendix 4.3), we have examined this question through the introduction of a seed beam into an MPPC along a path precisely opposite to that taken by one of its two pump beams. By varying the intensity of the seed beam we sought to

determine the conditions under which the phase of the grating would be determined by the phase of the injected seed beam. Our expectation was that when the seed beam was stronger than the scattering, the phase of the grating forming the MPPC would be determined by the phase of the injected seed beam.

The experimental setup we used for injection seeding an MPPC in barium titanate ($BaTiO_3$) is shown schematically in Fig. 5. An argon ion laser operating at 514.5 nm without an intracavity etalon provided the two pump beams (2 and 4) for the MPPC (MPPC1). The MPPC was arranged in a double phase-conjugate mirror configuration.[9,15] This configuration was chosen for its relative simplicity as only one interaction region is responsible for the conjugation process. The pump beams were mutually incoherent by virtue of having traveled over paths that differed in length by more than the 3 cm coherence length of the laser. The conjugate beams from MPPC1 are labeled 1 and 3. A bird-wing conjugator[11] (MPPC2) was used to ensure optimal alignment and spatial overlap of the injected seed beam with the grating forming in MPPC1. To monitor the phase fronts of the conjugate beams, an interferometer was set up between each conjugate beam and a reference beam from the laser. The resulting fringe patterns were monitored by detectors D1 and D2. To determine the extent to which the phase of the seed beam was controlling the phase of the MPPC grating, a PZT mounted mirror was used to vary the phase of the seed beam.

As shown in Fig. 6, phase changes in the seed beam generated by movement of the PZT clearly translate into corresponding changes in the phase of the MPPC grating as evidenced by the fringe movement detected by both D1 and D2.

In Fig. 7 a Fourier transform of the beat signal detected by D1 during movement of the PZT is presented. For seed/pump injection levels above $10^{-6}$ there is clear evidence of linkage between the phase of the seed beam and the phase of the MPPC grating. Other measurements we performed placed an upper limit of $10^{-8}$ on the self-scatter/pump intensity ratio. In light of this result, the failure of seed/pump beam ratios below $10^{-6}$ to influence the phase of the grating has yet to be explained.

## 2.4 Diffraction Properties of Multiple-Beam Photorefractive Gratings

Many applications of photorefractive media depend on their ability to transfer intensity and phase information in real time among a variety of incident optical beams.

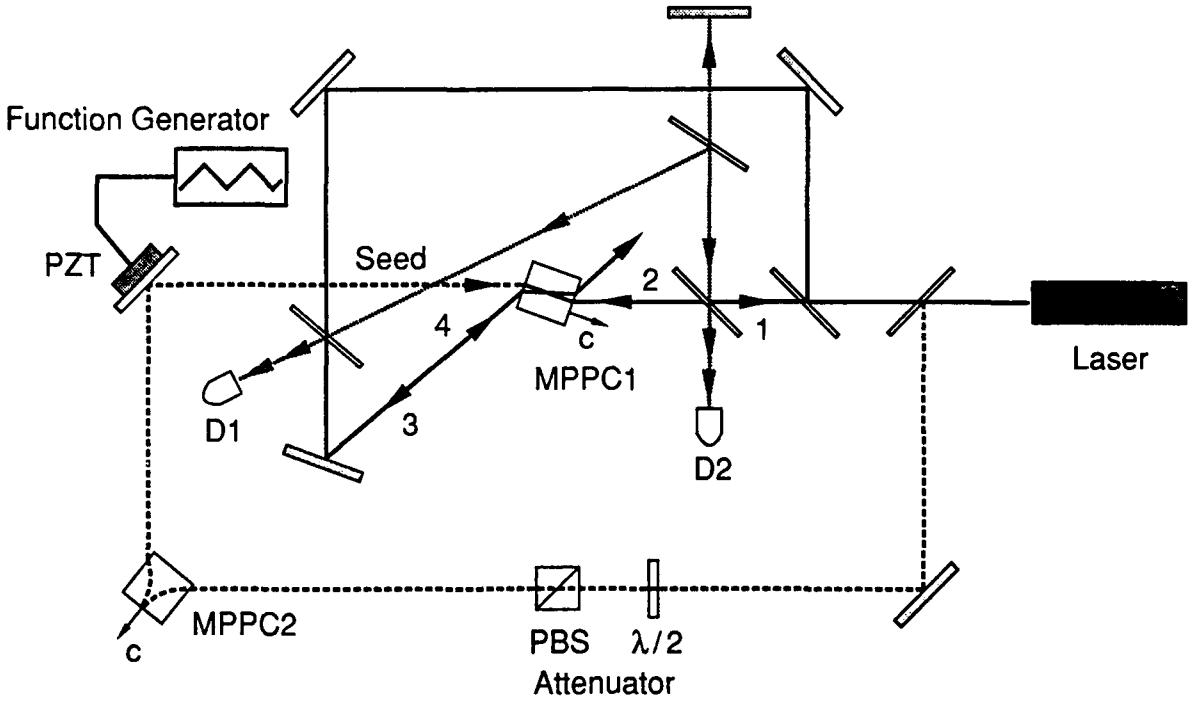


Fig. 5 Experimental setup for injection seeded MPPC.

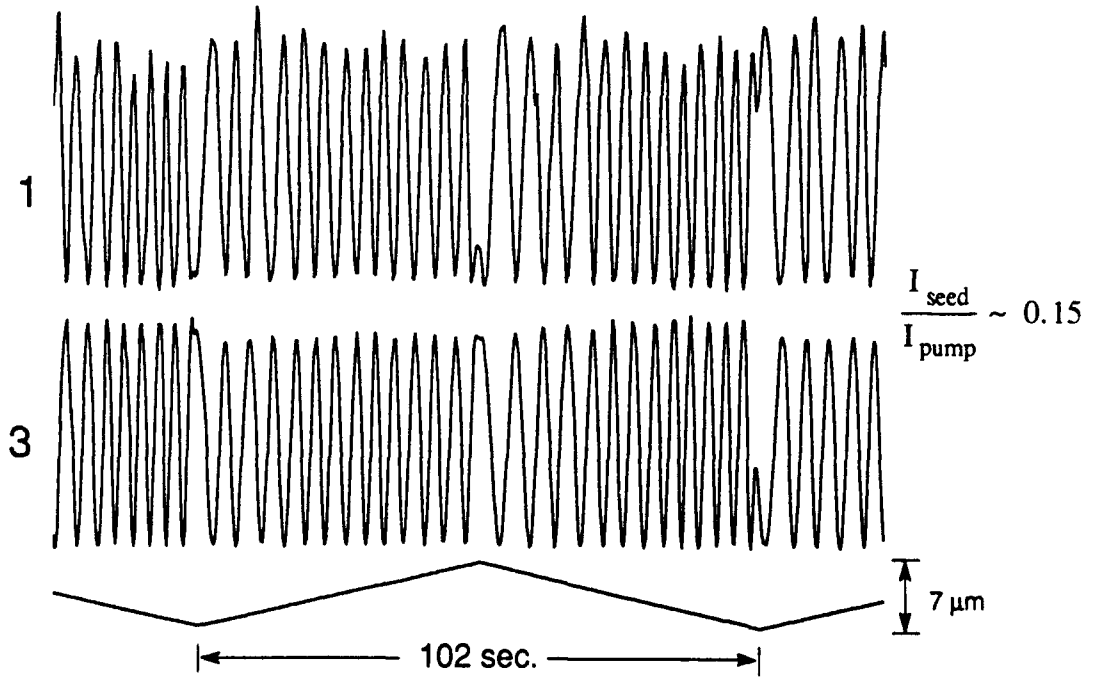


Fig. 6 Beat signal detected by D1 and D2.

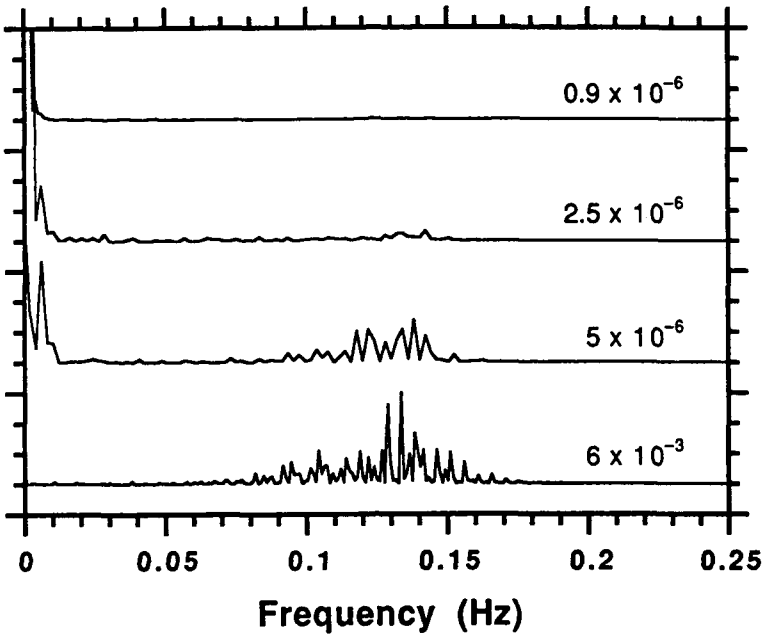


Fig. 7 FFT of signals taken by D1 for seed-to-pump ratios of $0.9 \times 10^{-6}$ to $6 \times 10^{-3}$.

This multibeam interaction occurs through holographic gratings written in the material by the interfering incident beams. We constructed an analytical model to solve the interaction of N mutually incoherent pairs of beams in a photorefractive medium. The details of this work can be found in Ref. 16 (Appendix 4.4). In short, using our model we examined the dynamics of a simultaneous read-write process using multiple beams of comparable intensity. Because of the mediating presence of multiple beams, a complete energy transfer between two write beams occurs in a finite thickness of the photorefractive crystal. This is in contrast to the infinite thickness required in the standard two-beam coupling case. We also found that the diffraction efficiency of the energy transfer process is a nonlinear function of the read-beam intensity. That is, for strong coupling and readout in the direction that enhances the grating being read, the maximum diffraction efficiency occurs when the read beam is more intense than the write beams. The diffraction efficiency is also nonreciprocal with respect to readout from the two input ports.

## 2.5 Diffraction Properties of Fixed Gratings in Photorefractive Media

While holograms in photorefractive media can be manipulated dynamically, stored holograms are partially erased by the reading beam each time information is retrieved. There are situations, such as in computer memory systems[17] or in optical perceptrons,[18-21] where it is desirable to have photorefractive holograms that can be fixed by physical processes so that they are not subject to erasure during readout. It is important to note in these cases that energy coupling between the reading beam and the diffracted beam occurs not only because of the fixed grating but also because of a photorefractive grating formed by these two beams.[22] Thus, diffraction in photorefractive media with fixed gratings is different from simple Bragg scattering. In Ref. 23 (Appendix 4.5) we examine, theoretically, just how different the diffraction process can be in photorefractive materials with fixed holograms. In determining the effect of the photoinduced grating it is important to note that because it is formed by incident and scattered beams it has exactly the same grating wave vector as the fixed volume grating. Thus the photoinduced grating is either in phase or 180° out of phase with the fixed grating[24] depending on the direction of incidence. This leads to a strengthened or weakened grating and nonreciprocal diffraction.

## 2.6 Diffraction Efficiency of Strong Volume Holograms

Volume holograms have attracted growing interest for information-storage applications owing to their potentially large storage capacity. In most situations the coupled-mode analysis of volume holograms established by Kogelnik[25] accurately describes the diffraction behavior of a thick hologram and predicts a diffraction efficiency $\eta$ that is a periodic function of the index perturbation amplitude-thickness product. Typically only the increasing part of the first period of $\eta$ is observed. However, as the grating amplitude and/or the thickness of the grating is increased, further coupling between the write beams is expected to result in a reversal of the energy transfer direction to yield a drop in the diffraction efficiency. As described in Ref. 26 (Appendix 4.6) we have been able to observe this effect in a photorefractive barium titanate ($BaTiO_3$) crystal. The use of photorefractive crystals for this purpose is particularly appropriate since the dynamic nature of photorefraction allows the time evolution of the grating development and erasure process to be observed.

From observation of the diffraction efficiency we can gauge the maximum number of holograms that can be recorded in a given crystal. Typical numbers obtained from our measurements were on the order of $10^6$. Unfortunately, such a large number is difficult to realize in practice because of the additional constraint placed by incoherent erasure during the sequential exposure process used to achieve the superimposed set of holograms used for optical storage.

## 2.7 Optical Pattern Classifier with Perceptron Learning

Processing information in neural networks differs from conventional applications in that the interconnections play the dominant role rather than acting as mere communication pathways. As described in the previous section, holographic techniques, in particular volume holograms, offer the most compact means of storing information. In the case of neural networks that information is in the form of interconnection patterns.[27] As detailed fully in Ref. 18 (Appendix 4.7) we have implemented a novel learning machine which implements the Perceptron algorithm for pattern dichotomy.[20] The optical system performs the weight storage and update functions for learning using coherent means and, in particular, makes novel use of the Stokes' principle to achieve truly subtractive as well as additive weight changes. This precludes the need for biases which were typically used in previous incoherent implementations.[20]

## 3.0 REFERENCES

1. C.J. Bord'e, in Experimental Gravitation and Measurement Theory , P. Meystre and M.O. Scully, Eds. (Plenum, New York, 1983) 269.

2 B. Fischer and S. Sternklar, Appl. Phys. Lett. **47**, 1 (1985).

3. I. McMichael, M. Khoshnevisan and P. Yeh, Opt. Lett. **11**, 525 (1986).

4. K. Kyuma, A. Yariv, and S. Kwong, Appl. Phys. Lett. **49**, 617 (1986).

5. I. McMichael, P. Yeh, and P. Beckwith, Opt. Lett. **12**, 507 (1987).

6. P. Yeh, I. McMichael, and M. Khoshnevisan, Appl. Opt. **25**, 1029 (1986).

7. I. McMichael and P. Yeh, Opt. Lett. **11**, 686 (1986).

8. I. McMichael, P. Beckwith and P. Yeh, Opt. Lett. **12**, 1023 (1987).

9. S. Weiss, S. Sternklar and B. Fischer, Opt. Lett. **12**, 114 (1987); S. Sternklar, S. Weiss, M. Segev and B. Fischer, Opt. Lett. 11, 528 (1986).

10. R.W. Eason and A.M.C. Smout, Opt. Lett. **12**, 51 (1987); A.M.C. Smout and R.W. Eason, Opt. Lett. 12, 498 (1987).

11. M.D. Ewbank, Opt. Lett. **13**, 47 (1988).

12. M. Cronin-Golomb, Ph.D. Dissertation (Caltech, 1983).

13. Pochi Yeh, Appl. Opt. **28**, 1961 (1989).

14. W.R. Christian, R. Saxena, and I. McMichael, submitted to J. Opt. Soc. Am. B (1991)

15. S. Sternklar, S. Weiss and B. Fischer, Opt. Eng. **26**, 423 (1987).

16. R. Saxena, F. Vachss, I. McMichael, and Pochi Yeh, J. Opt. Soc. Am. B **7**, 1210 (1990).

17. P.J. van Heerden, Appl. Opt. **2**, 393 (1963).

18. J.Hong, S. Campbell, and P. Yeh, Appl. Opt. **29**, 3019 (1990).

19. J. Hong, S. Campbell, and P. Yeh, "Optical learning machine for pattern classification," in Digest of Optical Society of America Annual Meeting (Optical Society of America, Washington, D.C., 1989), paper WJ3.

20. D. Psaltis, D. Brady, and K. Wagner, Appl. Opt. **27**, 1752 (1988).

21. E.G. Paek, J. Wullert, and J.S. Patel, Opt. Lett. **14**, 1303 (1989).

22. D.L. Staebler and J.J. Amodei, J. Appl. Phys. **43**, 1042 (1972).

23. Claire Gu and Pochi Yeh, J. Opt. Soc. Am. B **7**, 2339 (1990).

24. T. Chang and P. Yeh, Proc. Soc. Photo-Opt. Instrum. Eng. **739**, 109 (1987).

25. H. Kogelnik, Bell Syst. Tech. J. **48**, 2909 (1969).

26. J.H. Hong, Pochi Yeh, D. Psaltis and D. Brady, Opt. Lett. **15**, 344 (1990).

27. A. Yariv and S. Kwong, Opt. Lett. **11**, 186 (1986).

## Appendix 4.1

## PHASE CONJUGATE FIBER-OPTIC GYRO

# PHASE-CONJUGATE FIBER-OPTIC GYROS

SC5544.FR

IAN MCMICHAEL, WILLIAM CHRISTIAN, PAUL BECKWITH
MONTE KHOSHNEVISAN, and POCHI YEH

ROCKWELL INTERNATIONAL SCIENCE CENTER
THOUSAND OAKS, CALIFORNIA

RESEARCH SUPPORTED BY THE OFFICE OF NAVAL RESEARCH
CONTRACT NO. N00014-88-C-0230

Rockwell International
Science Center

# FIBER-OPTIC GYROS



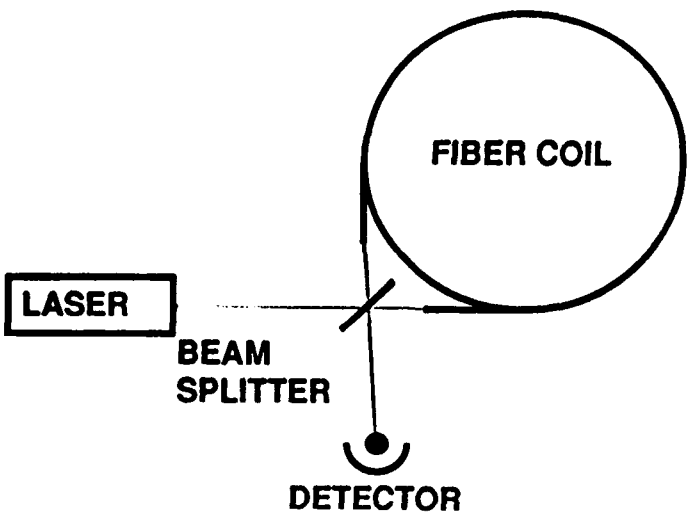


## SAGNAC EFFECT

$$\phi_S = 2\pi R\underline{L}\Omega/\lambda c$$

- LONG FIBER FOR HIGH SENSITIVITY
- NONMECHANICAL
- LEVERAGES CURRENT TECHNOLOGY

Rockwell International
Science Center

# PCFOG CONCEPT



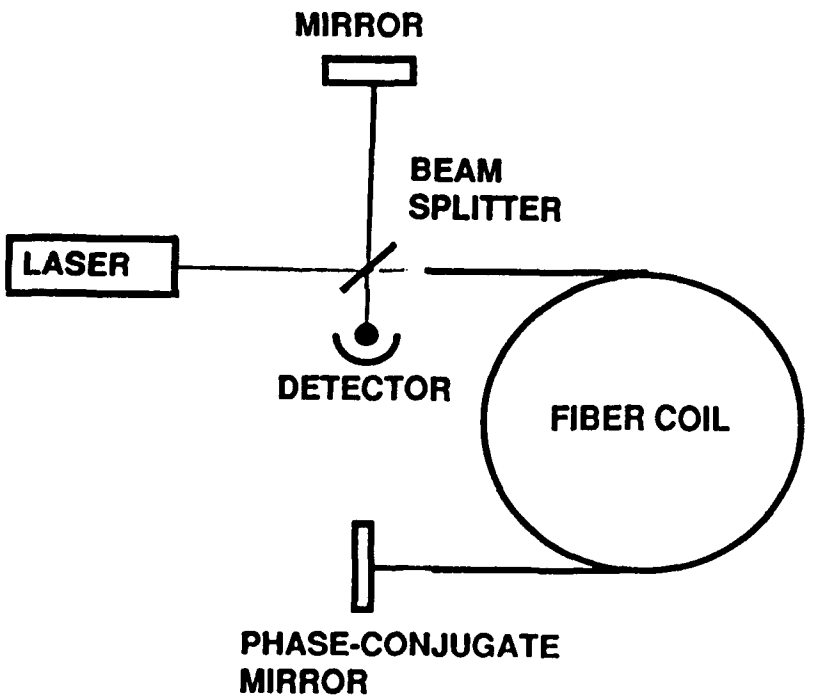


## PHASE CONJUGATION

- CORRECTS FOR MODAL SCRAMBLING
- ALLOWS THE USE OF MULTIMODE FIBER

- Demo

Rockwell International
Science Center

# BACKGROUND



-SINGLE-MODE POLARIZATION-PRESERVING FIBER-OPTIC GYRO

W. Burns, R. Moeller, C. Villarruel, and M. Abebe, Opt. Lett. 8, 540(1983).

-PHASE-CONJUGATE FIBER-OPTIC GYROS (SINGLE-MODE FIBER)

B. Fischer and S. Sternklar, Appl. Phys. Lett. 47, 1(1985).
P. Yeh, I. McMichael, and M. Khoshnevisan, Appl. Opt. 25, 1029(1986).

-CORRECTION OF MODAL SCRAMBLING BY PHASE CONJUGATION

I. McMichael, M. Khoshnevisan, and P. Yeh, Opt. Lett. 11, 525(1986).
K. Kyuma, A. Yariv, and S. Kwong, Appl. Phys. Lett. 49, 617(1986).
I. McMichael, P. Yeh, and P. H. Beckwith, Opt. Lett. 12, 507(1987).

# MULTIMODE FIBER GYRO USING A MUTUALLY PUMPED PHASE CONJUGATOR



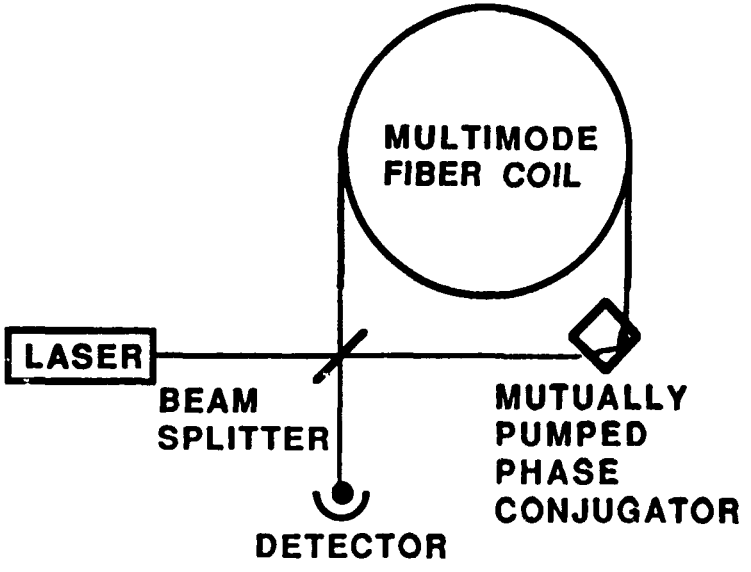


MUTUALLY PUMPED PHASE CONJUGATION

- WORKS WITH INCOHERENT PUMPS
- ALLOWS BIASING BY FAST PHASE MOD
- STATIONARY GRATING DURING ACCEL

RESEARCH SUPPORTED BY ONR CONTRACT NO. NOOO14-88-C-0230

Rockwell International
Science Center

# MULTIMODE FIBER-OPTIC GYRO USING A MUTUALLY-PUMPED PHASE CONJUGATOR



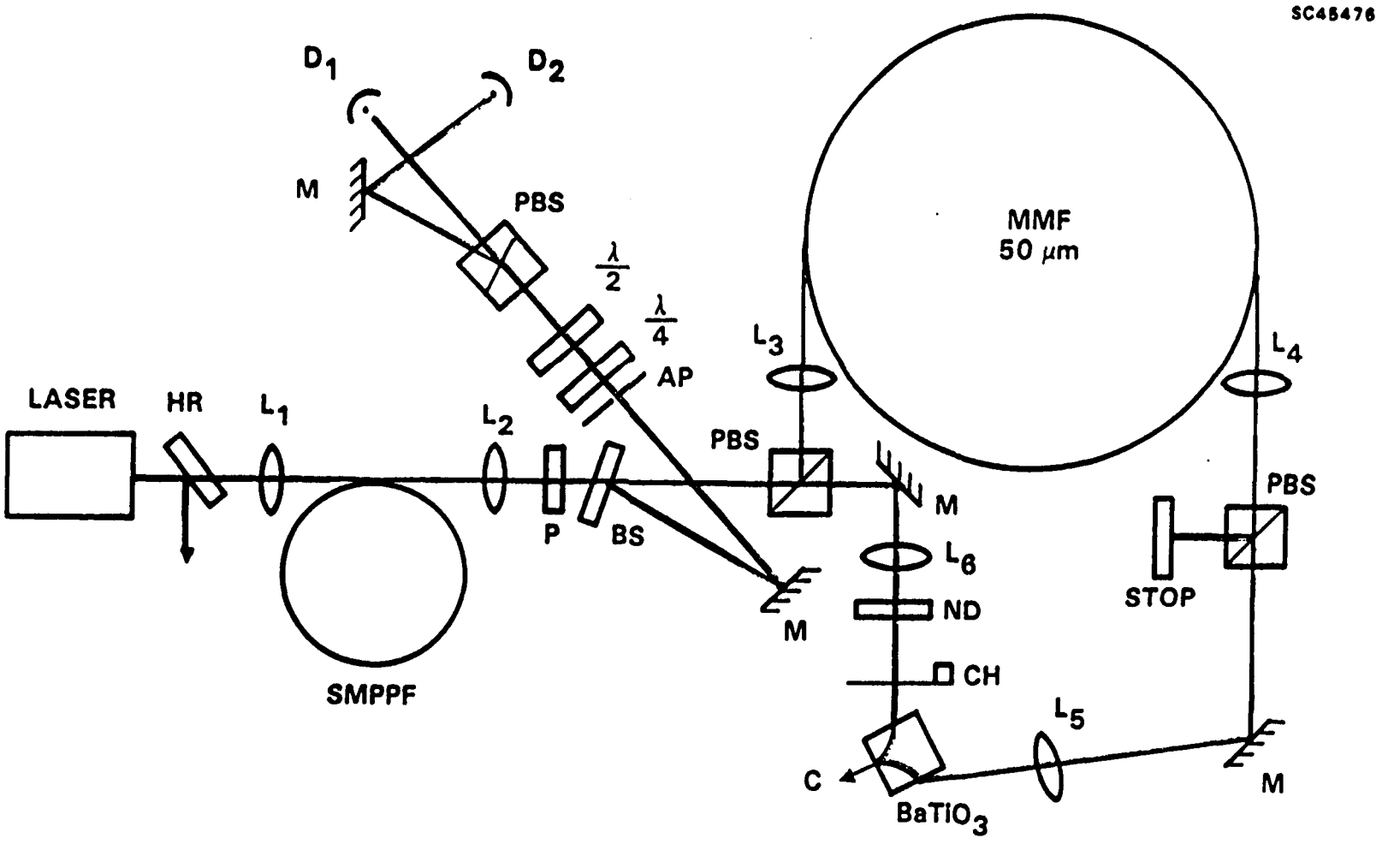


Rockwell International
Science Center

# DEMONSTRATION OF ROTATION SENSING

SC5544.FR

SC45475

SIGNAL $\alpha$ $D_1 - D_2$
CHOPPER FREQUENCY 200 Hz

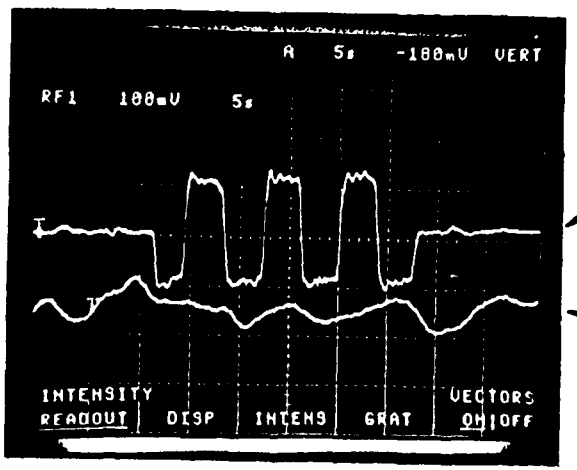


ROTATION SIGNAL
(6°/SECOND)
LOCK-IN $T_c$ = 0.1 SEC

BACKGROUND NOISE
(VERTICAL SCALE + 10)
$T_c$ = 1 SEC

~ 1 mrad

Rockwell International
Science Center

# ALL FIBER PHASE-CONJUGATE GYRO



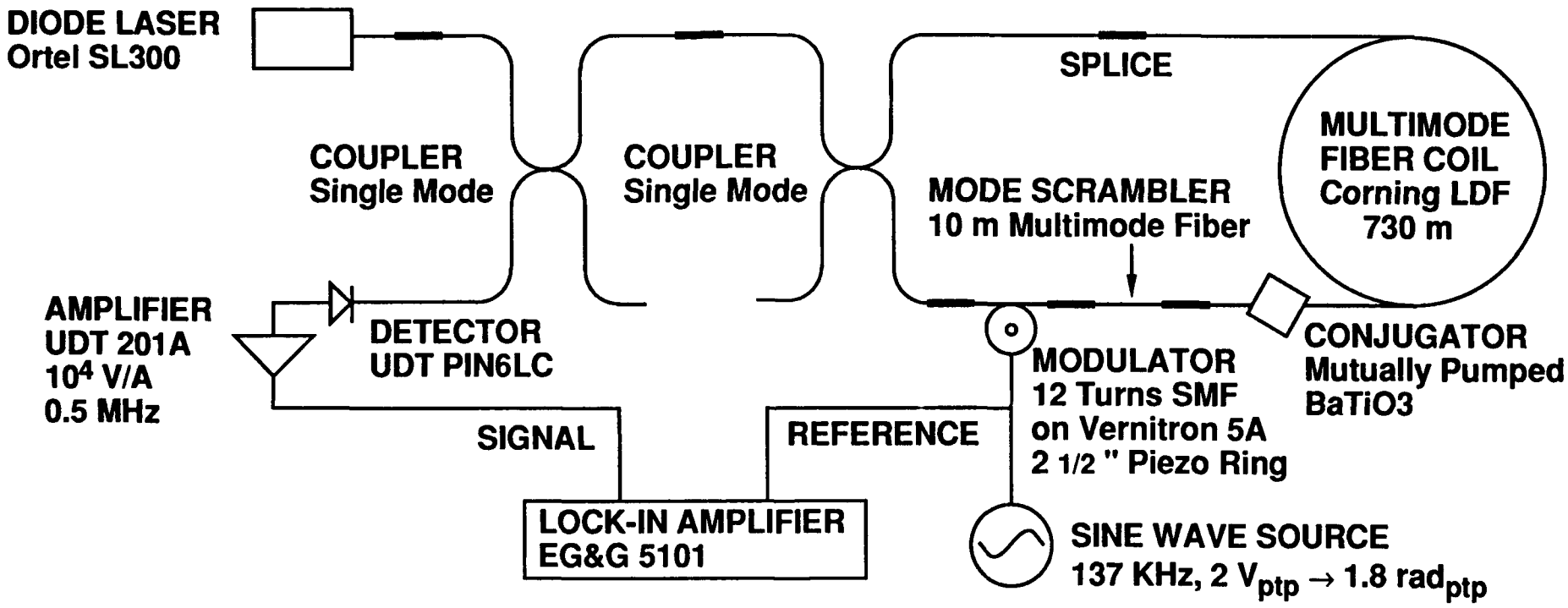


- GYRO CONSTRUCTED WITHOUT CONJUGATOR
- HUGE BIAS AND BIAS DRIFT (~10,000 °/hr) WITHOUT CONJUGATOR
- CONJUGATOR PRESENTLY BEING INSTALLED
- LASER SINGLE MODE FREQUENCY STABILITY MAY BECOME AN ISSUE

• RESEARCH SUPPORTED BY ONR CONTRACT NO. N00014-88-C-0230

# SUMMARY



PHASE CONJUGATION

- CORRECTS FOR MODAL SCRAMBLING
- ALLOWS FOR THE USE OF MULTIMODE FIBER

MUTUALLY PUMPED PHASE CONJUGATION

- WORKS WITH MUTUALLY INCOHERENT BEAMS
- ALLOWS FOR THE USE OF FAST PHASE MODULATION

DEMONSTRATION OF FOG USING MPPC

- PHASE NOISE DUE TO BULK OPTICS
- ALL FIBER DESIGN

## Appendix 4.2

# COUPLED-MODE THEORY OF HOLOGRAM SHARING IN MUTUALLY PUMPED PHASE CONJUGATORS

Rockwell International
Science Center

Reprinted from Applied Optics

# Coupled-mode theory of hologram sharing in mutually pumped phase conjugators

Pochi Yeh

Rockwell International Science Center, P.O. Box 1085, Thousand Oaks, California 91360.
Received 16 February 1989.
Sponsored by Iam-Choon Khoo, Pennsylvania State University.
0003-6935/89/111961-04$02.00/0.


*A coupled-mode theory is developed for photorefractive hologram sharing in mutually pumped phase conjugators. The theory shows that the spatial gain coefficients for the mutually conjugated beams are twice as large as those of other scattered beams.*

Mutually pumped phase conjugators (MPPCs) are nonlinear optical devices in which two incident laser beams can

mutually pump each other and produce phase-conjugated beams inside photorefractive crystals. Such phase conjugations have been observed in barium titanate photorefractive crystals.[1-4] Some of the earlier researchers suggested that MPPC is a result of self-oscillation in the optical four-wave mixing process.[5] Such a model, unfortunately, does not seem to explain the phase conjugation nature of the process. To illustrate this, the author may want to point out that the self-oscillation model using plane waves does not explain why the conical scattered lights collapse as soon as the wavefronts of the incident beams deviate from the planar ones. In addition, the experimental observation in various photorefractive crystals indicates that fanning plays an important role[6] and that MPPC does not seem to be a self-oscillation process. In fact, MPPC behaves much like a stimulated scattering process which occurs in high gain media. Experimental studies also indicate that most of the MPPCs require a gain length product of much higher than that predicted by the self-oscillation model. Recently, a resonator model[7] was proposed by the author and his co-workers to explain the physical mechanism of the phase conjugation process. According to this model, internal bidirectional ring oscillations occur inside the photorefractive crystals. Cross readout of the holograms produces the mutually phase conjugated waves. Both of these models require the onset of oscillations. The author presents a coupled mode theory of the hologram-sharing model which does not require the presence of internal oscillation or self-oscillation.

The hologram-sharing model proposed earlier,[2,4] provides a very good explanation of the phenomenon of mutually pumped phase conjugation in photorefractive crystals. The model is based on the fact that cross washout of index gratings generally occurs except when two sets of beams share the common hologram. Although the model gives a very clear picture of the physical mechanisms involved in MPPC, no quantitative results are given to describe the growth of the phase conjugated waves. In this Communication, we present a coupled-mode analysis for the hologram sharing model of the mutually pumped phase conjugators.

Referring to Fig. 1, let us consider the interaction of two sets of beams in a photorefractive medium. Beams 1 and 2 are mutually coherent; beams 3 and 4 are also mutually coherent. But beams 2 and 3 (or 2 and 4) are mutually incoherent. The electric field can be written as

$$E = \sum_{j=1}^{4} A_j \exp[i(\omega_j t - \mathbf{k}_j \cdot \mathbf{r})], \tag{1}$$

where $A_1, A_2, A_3, A_4$ are the complex amplitude of the four waves, $\omega_1, \omega_2, \omega_3, \omega_4$ are the angular frequencies, and $\mathbf{k}_1, \mathbf{k}_2, \mathbf{k}_3, \mathbf{k}_4$ are the wave vectors. The frequencies of the beam satisfy the following condition:

$$\omega_1 = \omega_2 \neq \omega_3 = \omega_4. \tag{2}$$

This condition indicates that beams 1 and 2 are mutually coherent; beams 3 and 4 are also mutually coherent. In addition, these two sets of beams are mutually incoherent. Inside the photorefractive medium, these four beams intersect and form volume holograms. We assume that beams 1 and 2 enter the medium at the face $z = 0$, and beams 3 and 4 enter the medium from the backface $z = L$. If we assume that the frequencies are very different so that $(\omega_3 - \omega_1)\tau \gg 1$ (where $\tau$ is the photorefractive grating decay time), the fundamental component of the index grating can be written

$$\Delta n = \tfrac{1}{2} n_1 \exp(i\phi) \frac{A_1^* A_2 \exp(-i\mathbf{K}_{21} \cdot \mathbf{r}) + A_3^* A_4 \exp(-i\mathbf{K}_{43} \cdot \mathbf{r})}{I_0} + \text{c.c.} \tag{3}$$

where $I_0$ is proportional to the total intensity and is given by

$$I_0 = |A_1|^2 + |A_2|^2 + |A_3|^2 + |A_4|^2, \tag{4}$$

and $\mathbf{K}_{21}$ and $\mathbf{K}_{43}$ are the grating wave vectors

$$\mathbf{K}_{21} = \mathbf{k}_2 - \mathbf{k}_1, \qquad \mathbf{K}_{43} = \mathbf{k}_4 - \mathbf{k}_3, \tag{5}$$

and c.c. denotes the complex conjugate term. We note that there are only two contributions to the index grating since beams 1 and 2 are incoherent with respect to beams 3 and 4. If $\mathbf{K}_{21}$ is distinct from $\mathbf{K}_{43}$, the coupled-mode equations can be written

$$\begin{aligned}
\frac{d}{dz} A_1 &= -\tfrac{1}{2}\gamma_{21} |A_2|^2 A_1 / I_0, \\
\frac{d}{dz} A_2 &= \tfrac{1}{2}\gamma_{21} |A_1|^2 A_2 / I_0, \\
\frac{d}{dz} A_3 &= -\tfrac{1}{2}\gamma_{43} |A_4|^2 A_3 / I_0, \\
\frac{d}{dz} A_4 &= \tfrac{1}{2}\gamma_{43} |A_3|^2 A_4 / I_0,
\end{aligned} \tag{6}$$

where $\gamma_{21}$ and $\gamma_{43}$ are coupling constants. In deriving the coupled-mode equations, we assume that the photorefractive medium operates by diffusion only so that $\phi = \pi/2$. In addition, we neglect the material absorption. We notice that there are two sets of two-beam coupled-mode equations in Eq. (6). In other words, the two sets of beams undergo two-beam coupling independent of each other, except for the denominator $I_0$ which accounts for the cross washout of the gratings due to the presence of the other set of beams. In the usual two-wave mixing (2WM), $I_0$ is either $|A_1|^2 + |A_2|^2$ or $|A_3|^2 + |A_4|^2$. The $I_0$ in Eqs. (6) is, however, given by Eq. (4), which can be as big as a factor of 2 larger for beams with similar intensities. The cross washout is a result of two gratings sharing the same volume of photorefractive medium.

When $\mathbf{k}_4 = -\mathbf{k}_1$ and $\mathbf{k}_2 = -\mathbf{k}_3$, the wave vectors of the two gratings are identical, i.e.,

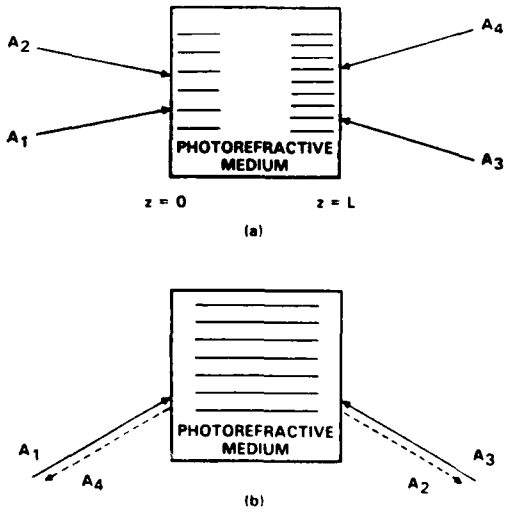


Fig. 1. Hologram sharing in photorefractive crystals.

$$\mathbf{K}_{21} = \mathbf{K}_{43}. \tag{7}$$

The coupled-mode equations can be written

$$\begin{aligned}
\frac{d}{dz}A_1 &= -\tfrac{1}{2}\gamma[A_2^*A_1 + A_4^*A_3]A_2/I_0,\\
\frac{d}{dz}A_2 &= \tfrac{1}{2}\gamma[A_1^*A_2 + A_3^*A_4]A_1/I_0,\\
\frac{d}{dz}A_3 &= -\tfrac{1}{2}\gamma[A_4^*A_3 + A_2^*A_1]A_4/I_0,\\
\frac{d}{dz}A_4 &= \tfrac{1}{2}\gamma[A_3^*A_4 + A_1^*A_2]A_3/I_0,
\end{aligned} \tag{8}$$

where $\gamma = \gamma_{21} = \gamma_{43}$ is the coupling constant. We notice that there are two terms on the right side of each equation in Eq. (8). Each term represents Bragg scattering from one grating. Since these two gratings have the same wave vector, they contribute equally to the Bragg scattering. The magnitude of the grating is, however, determined by the algebraic sum of the two complex numbers $A_1^*A_2$ and $A_3^*A_4$. If, in addition,

$$A_4 = \rho A_1^*, \qquad A_2 = \rho A_3^*, \tag{9}$$

where $\rho$ is an arbitrary constant, the two terms in the brackets in Eq. (8) are identical, and the coupled equations become

$$\begin{aligned}
\frac{d}{dz}A_1 &= -\gamma|A_2|^2A_1/I_0, \quad \frac{d}{dz}A_3 = -\gamma|A_4|^2A_3/I_0,\\
\frac{d}{dz}A_2 &= \gamma|A_1|^2A_2/I_0, \quad \frac{d}{dz}A_4 = \gamma|A_3|^2A_4/I_0.
\end{aligned} \tag{10}$$

Let us assume that beams 2 and 4 are the ones that get amplified due to two-beam coupling (i.e., $\gamma > 0$). We now examine the spatial growth of beams 2 and 4. The exponential growth constant for these two beams in Eqs. (10) is twice as large as that of the same beams in Eqs. (6) as a result of the hologram sharing. This factor of 2 is reminiscent of the theoretical proof of the phase conjugated nature of SBS.[8,9] It was shown that the gain coefficient for the conjugated wave in SBS is twice that of any other scattered wave.[10] In fact the spatial gain constant shown in Eqs. (10) is exactly the same as that of the usual 2WM. The cross washout, which lowers the gain coefficient by a factor of 2 for other scattered light, disappears as a result of the hologram sharing. In photorefractive media such as $BaTiO_3$ or SBN, the exponential gain coefficient can be as large as 40 $cm^{-1}$.[11] Thus, in a sample of 1 cm, the ratio between the gain of mutually phase conjugated beams and that of the randomly scattered beams can be as large as a factor of exp(20). This enormous factor indicates that the mutually phase conjugate beams are the dominant ones in terms of spatial growth and that the conjugated beams can be generated from the noise.

We now consider the effect of transverse spatial variation (i.e., $A_i$ terms are functions of $x,y$) on the process of phase conjugation. For plane waves with $A_i$ = constants, Eqs. (7) and (9) alone do not uniquely yield phase conjugation. In fact, given a set of incident wave vectors, Eq. (7) yields an infinite set of solutions for $\mathbf{k}_2$ and $\mathbf{k}_4$. These wave vectors are cylindrically symmetric with respect to an axis along the direction of $(\mathbf{k}_1 - \mathbf{k}_3)$. Thus for plane waves (with $A_i$ independent of $x,y$), conical scattering may have exactly the same gain coefficient as the conjugated wave provided that their amplitudes satisfy Eq. (9). This explains the arcs that are often observed in attempts to build mutually pumped phase conjugators. Let $\mathbf{k}_2'$ and $\mathbf{k}_4'$ be an arbitrary set of these solutions. For plane waves, $A_2 \exp[i(\omega_2 t - \mathbf{k}_2' \cdot \mathbf{r})]$ and $A_4 \exp[i(\omega_3 t - \mathbf{k}_4' \cdot \mathbf{r})]$ are also solutions of the wave equation because $\mathbf{A}_i$ terms are independent of $\mathbf{k}_i$. This, however, is no longer true for waves with transverse spatial variation. For these waves, the complex amplitudes and wave vectors are related by[12]

$$\nabla^2 A + 2i(\mathbf{k} \cdot \nabla)A = 0. \tag{11}$$

For incident waves with nonplanar wavefronts and spatial amplitude variations, $A_1$ and $A_3$ are complex functions of $x$ and $y$. If Eqs. (9) are satisfied for all $x$ and $y$, they uniquely determined the mutually phase conjugated waves. As a result of the constraint by Eq. (11), $A_2(x,y) \exp[i(\omega_2 t - \mathbf{k}_2' \cdot \mathbf{r})]$ and $A_4(x,y) \exp[i(\omega_4 t - \mathbf{k}_4' \cdot \mathbf{r})]$ are no longer acceptable solutions of the wave equation. According to this argument, spatial wavefront variation plays an important role in the fidelity of mutual phase conjugation. Experimentally, it was found that the fidelity of mutual phase conjugation increases drastically as soon as the wavefronts of the incident waves deviate from the planar one.[6]

In photorefractive crystals such as $BaTiO_3$ or SBN, mutually pumped phase conjugation starts from the scattering of the two incident beams (beams 1 and 3) [see Fig. 1(b)]. These scattered waves are represented by $A_2$ and $A_4$ in Eq. (1). As a result of photorefractive coupling, these scattered waves will be amplified in the medium.

Initially these scattered waves $A_2$ and $A_4$ may have arbitrary wavefronts. These scattered waves may be decomposed into two parts:

$$\begin{aligned}
A_2(0) &= \rho A_3^*(0) + A_2'(0),\\
A_4(L) &= \rho A_1^*(L) + A_4'(L),
\end{aligned} \tag{12}$$

where $A_2'(0)$ and $A_4'(L)$ represent the portions which are orthogonal to the conjugate waves. Here we recall that these amplitudes are also functions of $x$ and $y$. As indicated earlier, these nonconjugated parts have smaller gain coefficients compared with the conjugated parts. Although these nonconjugated parts may be significant in the beginning, the conjugated parts dominate at the end due to the exponential growth. Thus in high gain media such as $BaTiO_3$ and SBN, the mutually phase conjugated beams are often many orders of magnitude higher than other scattered beams.

Although the present analysis assumes only one interaction region, the result can be easily extended to include two or multiple interaction regions. In some of the mutually pumped phase conjugation which involves two or more spatial regions of interaction,[2-5] specular reflection and total internal reflection play an important role in maximizing the grating strength and matching the Bragg angles. It is important to note that in some cases the specular reflection from the surfaces may interfere with the hologram and disrupt the process of phase conjugation. The analysis of this effect is beyond the scope of this paper.

Summarizing: A coupled-mode theory is developed for the hologram sharing model of MPPC. The theory predicts that the amplification coefficient for the mutually phase conjugated beams is twice that of other scattered beams and provides a quantitative basis for the hologram sharing model.

The author acknowledges helpful discussions with M. D. Ewbank, T. Y. Chang, and J. Feinberg (USC). This work is supported in part by the Office of Naval Research under contract N00014-88-C-0230.



## References


1. S. Weiss, S. Sternklar, and B. Fischer, "Double Phase-Conjugate Mirror: Analysis, Demonstration, and Applications," Opt. Lett. **12**, 114–116 (1987).
2. M. D. Ewbank, "Incoherent Beams Sharing Photorefractive Holograms," in *Technical Digest, Topical Meeting on Photorefractive Materials, Effects, and Devices, Vol. 17* (Optical Society of America, Washington DC, 1987), pp. 179–182.
3. R. W. Eason and A. M. C. Smout, "Bistability and Noncommutative Behavior of Multiple-Beam Self-Pulsing and Self-Pumping in $BaTiO_3$," Opt. Lett. **12**, 51–53 (1987); A. M. C. Smout and R. W. Eason, "Analysis of Mutually Incoherent Beam Coupling in $BaTiO_3$," Opt. Lett. **12**, 498–500 (1987).
4. M. D. Ewbank, "Mechanism for Photorefractive Phase Conjugation Using Incoherent Beams," Opt. Lett. **13**, 47–49 (1988).
5. M. Cronin-Golomb, Ph.D. Dissertation (Caltech, 1983).
6. M. D. Ewbank (Rockwell International) and J. Feinberg, (U. Southern California); private communication.
7. P. Yeh, T. Y. Chang, and M. D. Ewbank, "Model for Mutually Pumped Phase Conjugation," J. Opt. Soc. Am. **5**, 1743–1750 (1988).
8. B. Ya. Zeldovich, V. I. Popovichev, V. V. Ragulskii, and F. S. Faizullov, "Connection Between the Wavefronts of the Reflected and Exciting in SBS," Zh Ekap. Teor. Fiz. Pis. Red. **15**, 160–163 (1972) [JETP Lett. **15**, 109–112 (1972)].
9. R. W. Hellwarth, "Theory of Phase Conjugation by Stimulated Scattering in a Waveguide," J. Opt. Soc. Am. **68**, 1050–1056 (1978).
10. B. Ya Zeldovich, N. F. Pilipetskii, and V. V. Shkunov, *Optical Phase Conjugation* (Academic, New York, 1983), pp. 135–167.
11. F. Laeri, T. Tschudi, and J. Albers, "Coherent cw Image Amplifiers and Oscillators Using Two-Wave Interaction in a $BaTiO_3$ Crystal," Opt. Comm. **47**, 387–390 (1983).
12. See, for example, A. Yariv and P. Yeh, "Optical Waves in Crystals," (Wiley, New York, 1984), p. 52.

Appendix 4.3

# SEEDING AND GRATING PHASE IN MUTUALLY PUMPED PHASE CONJUGATORS

# Seeding and Grating Phase in Mutually Pumped Phase Conjugators

**William R. Christian, Ragini Saxena and Ian McMichael**

**Rockwell International Science Center, Thousand Oaks, California 91360**

We present theoretical and experimental studies of mutually pumped phase conjugation when a seed beam is injected that is the conjugate of one of the pumping beams. Good agreement exists between the theoretical and the experimental functional dependencies of the conjugate reflectivities on seed beam intensity. However, the calculated gain is lower than that measured by two-beam coupling by nearly a factor of 2. We found that the seed-to-pump intensity ratio needs to exceed approximately $10^{-6}$, greater than 100 times the scattering, before the phase of the grating in the MPPC would follow the phase of the seed beam when it was varied by using a moving mirror.

## 1. Introduction

Optical phase conjugation has been an active field of research for nearly two decades.[1] One of the more unusual additions to the list of photorefractive phase conjugators in recent years has been a group of conjugators known as mutually pumped phase conjugators.[2–9] Mutually pumped phase conjugators (MPPCs) have as a distinguishing characteristic the ability to conjugate two mutually incoherent pumping beams simultaneously. This property makes them ideal candidates for applications in communications, laser locking, fiber optic gyros, and optical information processing where coherence limitations can be a problem. Phase conjugation in an MPPC begins with competition between a multitude of gratings that form between each pump beam and its own amplified scattering. One particular set of these gratings is common to both pump beams. This doubly reinforced grating dominates over all the other gratings being formed. It diffracts each pump beam into a conjugate beam for the other pump beam. If this description of the conjugation process is correct, then one might expect that, in the absence of any other determining factors, the phase of the photorefractive grating will be determined solely by the relative phase between each pumping beam and its scattering. In this paper, we examine how grating formation is influenced by the injection of a seed beam into the MPPC along a path precisely opposite to that taken by one of the two pump beams. We show that the phase of the seed beam determines the phase of the grating if the seed intensity is above that of the scattered light present in the MPPC. A theoretical derivation, based on the work of Cronin-Golomb et al.,[5] is presented for comparison with our experimental results.

## 2. THEORETICAL ANALYSIS

The geometry for the nonlinear interaction responsible for MPPC is shown in Fig. 1. Input beams $A_2$ and $A_4$ are a pair of mutually incoherent beams that enter the photorefractive crystal from opposite sides ($z = L$ and $z = 0$ respectively). Imperfections in the crystal scatter both incident beams. Due to the photorefractive effect,[10] interference of each beam with its

coherent scattered light creates a multitude of randomly oriented index gratings. The particular grating that scatters incident beam $A_2$ into the phase-conjugate replica of beam $A_4$ (labelled as beam $A_3$ in Fig. 1) must also, by the principle of time-reversal, scatter beam $A_4$ into the phase-conjugate replica of beam $A_2$ (labelled as beam $A_1$ in Fig. 1). This particular grating is reinforced by both the incident beams and dominates the competition to eliminate the other gratings.[9] This nonlinear interaction is described by Degenerate Four-Wave Mixing (DFWM) with appropriate boundary conditions. DFWM in photorefractive media in transmission geometry is described by the following set of coupled equations:[5]

$$\frac{dA_1}{dz} = \frac{\gamma}{I_o} ( A_1 A_4^* + A_2^* A_3 ) A_4 - \alpha A_1$$

$$\frac{dA_2^*}{dz} = \frac{\gamma}{I_o} ( A_1 A_4^* + A_2^* A_3 ) A_3^* + \alpha A_2^*$$

$$\frac{dA_3}{dz} = - \frac{\gamma}{I_o} ( A_1 A_4^* + A_2^* A_3 ) A_2 + \alpha A_3$$

$$\frac{dA_4^*}{dz} = - \frac{\gamma}{I_o} ( A_1 A_4^* + A_2^* A_3 ) A_1^* - \alpha A_4^* \qquad (1)$$

where $A_n$ is the complex electric field amplitude of the n th beam at steady-state, $\alpha$ is the linear amplitude absorption coefficient, and the z axis is taken normal to the surface of the medium. $I_o$ is the total beam intensity equal to $\sum_{m=1}^{4} |A_m|^2$ and $\gamma$ is the complex amplitude coupling constant that is equal to $\frac{i\omega n_1 e^{-i\phi}}{2c \cos\theta}$. Here $n_1$ is the amplitude and $\phi$ is the phase of the photorefractive index change. $\omega$ is the frequency and $\theta$ is the angle made by the beams with the z axis. In this paper, we consider charge transport by diffusion only, so that $\phi = 90°$, and $\gamma$ is a real, positive quantity. The difference in sign of $\gamma$ in Eqs. (1) when compared to the coupled equations of Ref. 5 is due to our choice of positive charge carriers for the photorefractive effect.[11] This change was necessary because the charge carriers in barium

titanate, the material used in our experimental work, are positive.[12]

The coupled Eqs. (1) with appropriate boundary conditions describe a seeded MPPC in a photorefractive medium, where linear absorption and depletion of the incident beams have been taken into account. The equation for each beam has contributions from two terms: one term due to diffraction from the grating the beam wrote itself (the usual two-beam coupling term ), and the second term that arises due to cross-readout of the grating written by the other pair of coherent beams (the four-wave mixing term). Both phase-conjugate beams 1 and 3 are amplified as they propagate through the interaction region.

We assume that linear absorption is small in the photorefractive medium under consideration, so that $\alpha L << 1$, where L is the interaction length. The boundary conditions appropriate for MPPC are the nonzero intensities of the two input beams at the opposite faces of the nonlinear medium, i.e. $I_2(L), I_4(0) \neq 0$, while the self-generated, phase-conjugate beam $A_3$ is zero at its input: $I_3(L) = 0$. However, for seeded MPPC, we consider beam $A_1$ to be nonzero at its input, i.e. $I_1(0) \neq 0$. The problem then becomes analogous to phase-conjugation by FWM in photorefractive media, and we use the solutions obtained by Cronin-Golomb et al.,[5] for our study. The phase-conjugate reflection coefficients in the two arms are defined as the amplitude ratios: $\rho \equiv A_3(0)/A_4^*(0)$ and $\sigma \equiv A_1(L)/A_2^*(L)$ and are given by[5]

$$\rho = \frac{2c \tanh \mu L}{Q - \Delta \tanh \mu L}$$

$$\sigma = \frac{2c \tanh \mu L}{Q + \Delta \tanh \mu L} \qquad (2)$$

where c, $\Delta$, Q and $\mu$ are defined as

$$c \equiv A_1 A_2 + A_3 A_4$$

$$\Delta \equiv I_2(L) - I_1(0) - I_4(0)$$

$$Q \equiv (\Delta^2 + 4|c|^2)^{1/2}$$

$$\mu \equiv \gamma Q / (2I_o)$$

$$I_o \equiv I_2(L) + I_1(0) + I_4(0)$$

Note that $\Delta$, $I_o$ and $\gamma L$ are known from the boundary conditions for the problem, while the integration constant c is proportional to the output intensities of the beams and is yet to be determined. The phase-conjugate intensity reflectivities in the two arms are defined as $R \equiv |\rho|^2$ and $S \equiv |\sigma|^2$. An examination of Eqs. (2) reveals that R and S ( and also Q and $\mu$) are functions of $|c|^2$ only, and not any linear combinations of c and c*. Hence the problem is solved once $|c|^2$ is determined. $|c|^2$ is given by the roots of the transcendental equation[5]

$$[\,|c|^2 - I_1(0)\, I_2(L)]\,(Q - \Delta T)^2 + 4\,|c|^2\, T^2\, I_2(L)\, I_4(0) - 4\,|c|^2\, T\, Q\, I_4(0) = 0 \qquad (4)$$

where $T \equiv \tanh(\mu L)$.

Figure 2 is a plot of the steady-state phase-conjugate reflectivities R and S in both the arms as a function of the seed beam intensity $I_1(0)$. The product of the coupling constant and the interaction length ($= \gamma L$) is taken to be 2.26, and the input intensity of the two beams is assumed to be equal; i.e., $I_2(L) = I_4(0) \equiv 1$. For a weak seed beam with intensity of the order of $I_1(0) \leq 10^{-6}$, the phase-conjugate reflectivities in the two arms of the MPPC are hardly affected by the presence of the seed beam. For larger seed beam intensity, the phase-conjugate reflectivity in the arm that is directly seeded increases monotonically with the seed beam intensity. This is true even if we were to subtract out the contribution of the seed, $I_1(0)$, from the phase-conjugate signal, S. In the arm not seeded directly, the phase-conjugate reflectivity at first increases until $I_1(0) \sim 0.1$. Further increase of the seed beam reduces R.

To understand the behavior of the phase-conjugate reflectivities as a function of seed beam intensity $I_1(0)$, we plot the intensities of the four beams as a function of distance into the crystal using the following expressions[5]

$$I_1(z) = I_{12}(z)\,\frac{d_2 - d_1\, I_{34}(z)}{1 - I_{12}(z)\, I_{34}(z)}$$

$$I_2(z) = \frac{d_2 - d_1\, I_{34}(z)}{1 - I_{12}(z)\, I_{34}(z)}$$

$$I_3(z) = I_{34}(z)\ \frac{d_1 - d_2\, I_{12}(z)}{1 - I_{12}(z)\, I_{34}(z)}$$

$$I_4(z) = \frac{d_1 - d_2\, I_{12}(z)}{1 - I_{12}(z)\, I_{34}(z)} \qquad (5)$$

Here $d_1 = I_1(0) + I_4(0)$, $d_2 = I_2(L)$ and the intensity ratios $I_{12} \equiv |A_{12}|^2$ and $I_{34} \equiv |A_{34}|^2$ are given by[5]

$$A_{12}(z) = -\frac{1}{2\,c^*}\ \frac{S_-\, D^2\, e^{2\mu z} - S_+}{D^2\, e^{2\mu z} - 1}$$

$$A_{34}(z) = \frac{1}{2\,c^*}\ \frac{S_-\, E^2\, e^{2\mu z} - S_+}{E^2\, e^{2\mu z} - 1} \qquad (6)$$

where the constants D and E are given by: $D^2 = [\,2|c|^2 + S_+\, I_2(L)]\, \exp(-2\mu L) / [\,2|c|^2 + S_-\, I_2(L)]$, $E^2 = S_+ \exp(-2\mu L) / S_-$, with $S_\pm \equiv \Delta \pm Q$. Once again, a knowledge of $|c|^2$ alone is sufficient for calculating the intensities as a function of distance. The value of $|c|^2$ is obtained by solving the transcendental equation (4) with the given boundary conditions.

The results of our calculations are shown in Figs. 3a - 3d, in which we have plotted the intensities of the four beams as a function of normalized distance, for seed beam intensities of 0, 0.01, 0.1 and 0.5 respectively. Similar to the choice of parameters for Fig. 2, the two input beam intensities are equal: $I_2(L) = I_4(0) = 1$, and $\gamma L = 2.26$. The curves corresponding to the two input beams are shown by the solid lines, while those corresponding to the two self-generated phase-conjugate beams are shown by dashed lines. The case of $I_1(0) = 0$ (Fig. 3a) corresponds to MPPC with no seed, and equations (5), (6) for the beam intensities are still valid, but the algebraic equation (4) for $|c|^2$ simplifies to: $T = Q / [\, I_2(L) + I_4(0)]$. The scattered field of each beam is zero at the two input planes ($z = 0$ and $z = L$), and in Fig. 3a, there is little amplification of the scattered beams while propagating in the medium of length L because the photorefractive coupling constant is small. In the presence of a small seed beam ($I_1(0) = 0.01$), input beam 4 transfers energy more efficiently to its coherently scattered beam 1 by two-beam coupling. As a result, this coherent beam pair has comparable intensities near the output

plane z = L, and reflectivity S increases with $I_1(0)$. Due to the photorefractive nature of the index grating written by beams 1 and 4, maximum grating amplitude occurs near z = L. Incoherent readout of this large grating by input beam 2 at z = L helps to diffract energy of beam 2 into its scattered beam 3. As a result, reflectivity R also increases with an increase of $I_1(0)$. As the seed is further increased, the maximum of the grating written by beams 1 and 4 moves to the left (towards z = 0). This is because larger seeds require shorter distances for the two beams to become equal in intensity. The maximum reflectivity for R occurs for a seed level of approximately $I_1(0) = 0.1$ (see Fig. 2). This coincides with $I_1 \approx I_4$ at the center of the interaction region (see Fig. 3c).

## 3. EXPERIMENTAL STUDY

Our experimental setup for injection seeding an MPPC in barium titanate ($BaTiO_3$) is shown schematically in Figure 4. An argon ion laser operating at 514.5 nm without an intracavity etalon provided the two pump beams (labeled 2 and 4) for MPPC1. MPPC1 was arranged in a double phase-conjugate mirror configuration.[2] This configuration was chosen for its relative simplicity as only one interaction region is responsible for the conjugation process. The pump beams were mutually incoherent by virtue of having traveled over paths that differed in length by more than the 3 cm coherence length of the laser. The conjugate beams are labeled 1 and 3 in accordance with the terminology used in our theory section. A seed beam was directed into MPPC1 using a bird-wing conjugator[4] (MPPC2). The bird-wing was formed by the transmitted portion of pump beam 2 from MPPC1 and an attenuated beam from the laser at a point where the beams were mutually incoherent. This configuration ensured optimal alignment and spatial overlap of the seed beam with the grating that was forming in MPPC1. The attenuator (a half-wave plate, polarizing beamsplitter combination) was used to adjust the intensity of the seed beam entering the bird-wing conjugator. For some measurements we required a higher power seed beam than was obtainable from the bird-wing conjugator alone. To increase power in the seed beam we used amplification by two-wave

mixing in a third $BaTiO_3$ crystal (not shown) positioned in the seed beam's path between MPPC2 and the PZT mounted mirror. Care was taken to ensure that the seed beam was coherent with pump beam 4 (see Fig. 4) so that a grating would form in the crystal at the same location as the grating being formed by self scattering.

To examine the effects of seeding on the phase fronts of the two conjugate beams, an interferometer was set up between each conjugate beam and a reference beam from the argon ion laser as shown in Figure 5. Beam paths in each interferometer were arranged so that conjugate and reference beams would be mutually coherent when combined. The resulting circular fringe patterns were then monitored by detectors D1 and D2. Figure 6 shows the fringe pattern that was observed for conjugate beam 3 with and without seeding. In this case, two 5 mW (1 mm diameter) pump beams were used to form the conjugator and a 0.4 mW beam was used for seeding ($I_{seed}/I_{pump} = 0.08$). Note that introduction of the seed beam did not noticeably disturb the phase front of the conjugate beam. Furthermore, varying the path taken by the seed beam to the conjugator using a piezoelectric translator (PZT) did not distort the phase front of the conjugate beam as long as the motion was slower than the response time for movement of the photorefractive grating (approximately 1 fringe/sec). Instead it led to motion of the fringes as the photorefractive grating moved to keep in step with the phase of the seed beam. This is shown clearly in Fig. 7 where we have plotted the travel of the PZT against the motion of the fringe patterns detected by D1 and D2.

Variation of the phase-conjugate reflectivity in both arms of MPPC1 as a function of seed beam intensity is shown in Fig. 8. The data have been corrected to take into account both Fresnel and absorption losses. Absorption in our $BaTiO_3$ crystal was $\alpha = 1.4\ cm^{-1}$ at 514.5 nm. The solid line is a theoretical fit to the data using $\gamma L = 2.26$ for the coupling factor. There is good agreement between the functional dependence predicted by the theory and that measured in the experiment. However, a two-wave mixing (TWM) gain measurement between the seed beam and pump beam 4 (see Fig. 4) yielded $\gamma L = 4$ when neither the orientation of the crystal nor the positioning of the beams was changed from that used in the seeded MPPC experiment. The discrepancy between $\gamma L$ for TWM and MPPC has been noted before[13] but to

our knowledge, it has not been explained. It could account for the observation that phase conjugators with equal intensity inputs never attain the 100% reflectivities that are predicted for them by calculations using values of $\gamma L$ obtained through TWM measurements.

To determine the minimum seed intensity necessary to influence grating formation in the MPPC, we proceeded in the following manner. The path taken by the seed beam to the conjugator was varied by applying a sawtooth signal to the PZT shown in Fig. 4. The PZT moved 7 μm in 100 seconds causing the fringes observed by D1 and D2 to move at a rate of 0.13 Hz when the grating was locked to the seed beam. By taking a fast Fourier transform (FFT) of the signals from detectors D1 and D2, the seed levels at which the 0.13 Hz frequency component was present were easily discernable. A series of FFTs taken for seed-to-pump intensity ratios ranging from $6 \times 10^{-3}$ to $0.9 \times 10^{-6}$ is shown in Figure 9. The only difference between these traces was in the power of the seed beam entering the conjugator.

If scattering determines the phase of the grating in the absence of the seed beam, then the level of scattering along the seed path should place a lower bound on the seed intensity required to control the phase of the grating. To determine the amount of self scattering present without seeding we performed the following experiment. First detector D2 was moved over a meter away from MPPC1 along the path taken by the conjugate beam it had been monitoring. Two 1 mm pinholes were then placed in the beam path, one close to the conjugator and the other just in front of the detector. This arrangement served to select only that portion of the scattered light that contributed to MPPC grating formation. Next, all beams entering the crystal were blocked and the MPPC gratings were erased by a strong beam split off from the pump laser. Following grating erasure, only the pump beam entering the conjugator from the left (see Fig. 4) was unblocked. Figure 10, which shows the signal recorded by D2, illustrates the buildup of fanning from scattering along the path normally taken by the conjugate signal of the MPPC. To the resolution of our detection apparatus (0.1 nW) no scatter signal was observed prior to the buildup of fanning. This places an upper limit of $10^{-8}$ on the scattering-to-pump intensity ratio. This is two orders of magnitude below the minimum seed level required to influence grating formation in the crystal. The reason for this difference is not presently understood.

## 4. CONCLUSIONS/DISCUSSION

We have studied the behavior of a mutually pumped phase conjugator when a seed beam is injected into the conjugator that is the conjugate of one of the pumping beams. There is good agreement between the functional dependencies of the conjugate reflectivities on seed beam intensity as predicted by the theory and as measured in the experiment. However, the gain obtained from the theoretical fit to the data is lower than that measured by two-beam coupling by nearly a factor of 2. To our knowledge this discrepancy remains unexplained and may be the reason that MPPC's have not obtained the high reflectivities that measurements of two-beam coupling would imply.

It seems reasonable that the phase of the grating in an unseeded MPPC is determined by the phase of that portion of the scattering that is conjugate to the pumping beams, and therefore that the phase of the grating would be influenced by a seed beam when its intensity exceeded that of the scattering. This is qualitatively supported by our experiments, but not quantitatively. The scattering that was conjugate to the pumping beams was measured to be less than $10^{-8}$ of the pumping intensity, whereas our measurements indicated that the seed beam to pump beam intensity ratio needed to exceed approximately $10^{-6}$ before the phase of the grating followed the phase of the seed beam when it was varied at a rate that was slower than the photorefractive response time. This ability to control the phase of the grating in a MPPC using a weak seed beam may be used to provide a nonmechanical method for biasing and modulation in phase-conjugate interferometers.

## 5. ACKNOWLEDGEMENTS

This research has been primarily supported by the Office of Naval Research under contract N0014-88-C-0230.

1. *Optical Phase Conjugation*, R. A. Fisher, Ed., (Academic, NY, 1983).

2. S.Weiss, S. Sternklar, and B. Fischer, Opt. Lett. **12**, 114 (1987); S. Sternklar, S. Weiss and B. Fischer, Opt. Eng. **26**, 423 (1987).

3. R. W. Eason and A. M. C. Smout, Opt. Lett. **12**, 51 (1987); A. M. C. Smout and R. W. Eason, Opt. Lett. **12**, 498 (1987).

4. M. D. Ewbank, Opt. Lett. **13**, 47 (1988).

5. M. Cronin-Golomb, B. Fischer, J. O. White and A. Yariv, IEEE J. Quantum Electron. **QE-20**, 12 (1984).

6. P. Yeh, T. Y. Chang and M. D. Ewbank, J. Opt. Soc. Am. **B5**, 1743 (1988).

7. Q. C. He, IEEE J. Quantum Electron. **QE-24**, 2507 (1988).

8. P. Yeh, Appl. Opt. **28**, 1961 (1989).

9. M. D. Ewbank, R.A. Vazquez, R.R. Neurgaonkar, and J. Feinberg. J. Opt. Soc. Am. **B7**, 2306 (1990).

10. See, for example, P. Gunter and J.-P Huignard, eds., *Photorefractive Materials and their Applications I* (Springer-Verlag, Berlin, 1988).

11. K. R. MacDonald and J. Feinberg, J. Opt. Soc. Am., **73**, 548 (1983).

12. J. Feinberg, D. Heiman, A.R. Tanguay, Jr., and R.W. Hellwarth, J. Appl. Phys. **51**, 1297 (1980); erratum **52**, 537 (1981).

13. B. Fischer, S. Sternklar and S. Weiss, IEEE J. Quantum Electron. **25**, 550 (1989).

# Figure Captions



Fig. 1. Geometry for mutually pumped phase conjugator.

Fig. 2. Steady-state phase-conjugate reflectivities R and S as a function of seed beam intensity $I_1$ for $\gamma L = 2.26$ and equal input pump intensities $[I_2(L) = I_4(0) = 1]$.

Fig. 3. Four beam interactions in the MPPC with initial pump beam intensities equal $[I_2(L) = I_4(0) = 1]$, $\gamma L = 2.26$, L = 1 cm., for seed beam intensities of (a) 0; (b) 0.01; (c) 0.1; and (d) 0.5

Fig. 4. Experimental setup for external seeding of an MPPC. Pump beams 2 and 4 from an argon ion laser form MPPC1 which generates phase-conjugate beams 1 and 3. Seeding through a bird-wing conjugator (MPPC2) ensures optimum overlap of the injected seed beam with the grating in MPPC1. An attenuator (half-wave plate and polarizer) provides control of seed beam intensity while a PZT mounted mirror varies the phase of the seed beam.

Fig. 5. Experimental setup for external seeding of an MPPC including interferometers used to monitor the phase fronts of phase conjugate beams 1 and 3. As shown, detectors D1 and D2 monitor beams 3 and 1 respectively.

Fig. 6. Interferogram of the phase front of phase conjugate beam 3 taken with (a) no seed beam; (b) a 0.4 mW seed beam; and (c) a 0.4 mW seed beam with a sawtooth signal applied to the PZT causing fringe movement at 0.27 Hz.

Fig. 7. Beat signal detected by D1 and D2 when the seed beam phase is changed by a 7 μm movement of the PZT mounted mirror in the seed beam path. Seed-to-pump beam intensity ratio is 0.15 in this case.

Fig. 8. Phase conjugate reflectivities R and S as a function of seed beam intensity.

Fig. 9. FFT of signals taken by D1 for seed-to-pump intensity ratios ranging from $0.9 \times 10^{-6}$ to $6 \times 10^{-3}$ when the signal applied to the PZT creates a 0.13 Hz movement of fringes in the interferogram.

Fig. 10. Scattering and fanning buildup signal monitored by detector D2.

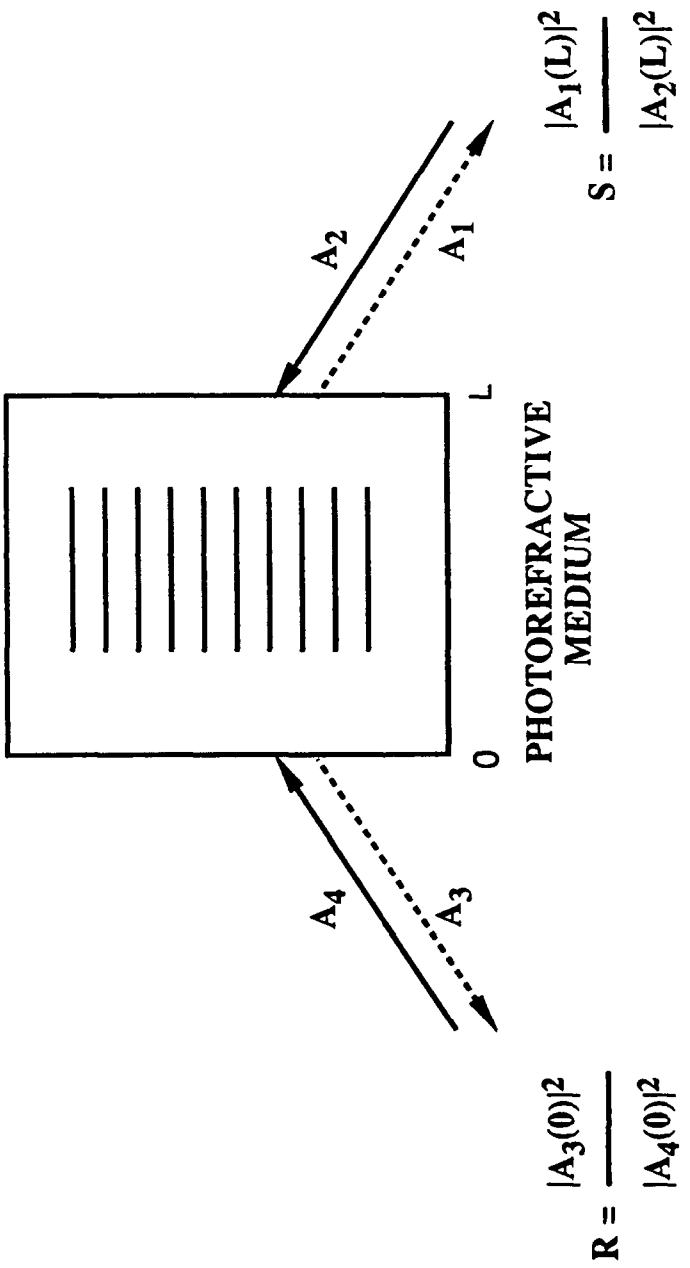
$A_2$
$A_1$
$S = \frac{|A_1(L)|^2}{|A_2(L)|^2}$
L
PHOTOREFRACTIVE MEDIUM
0
$A_4$
$A_3$
$R = \frac{|A_3(0)|^2}{|A_4(0)|^2}$

Fig. 1

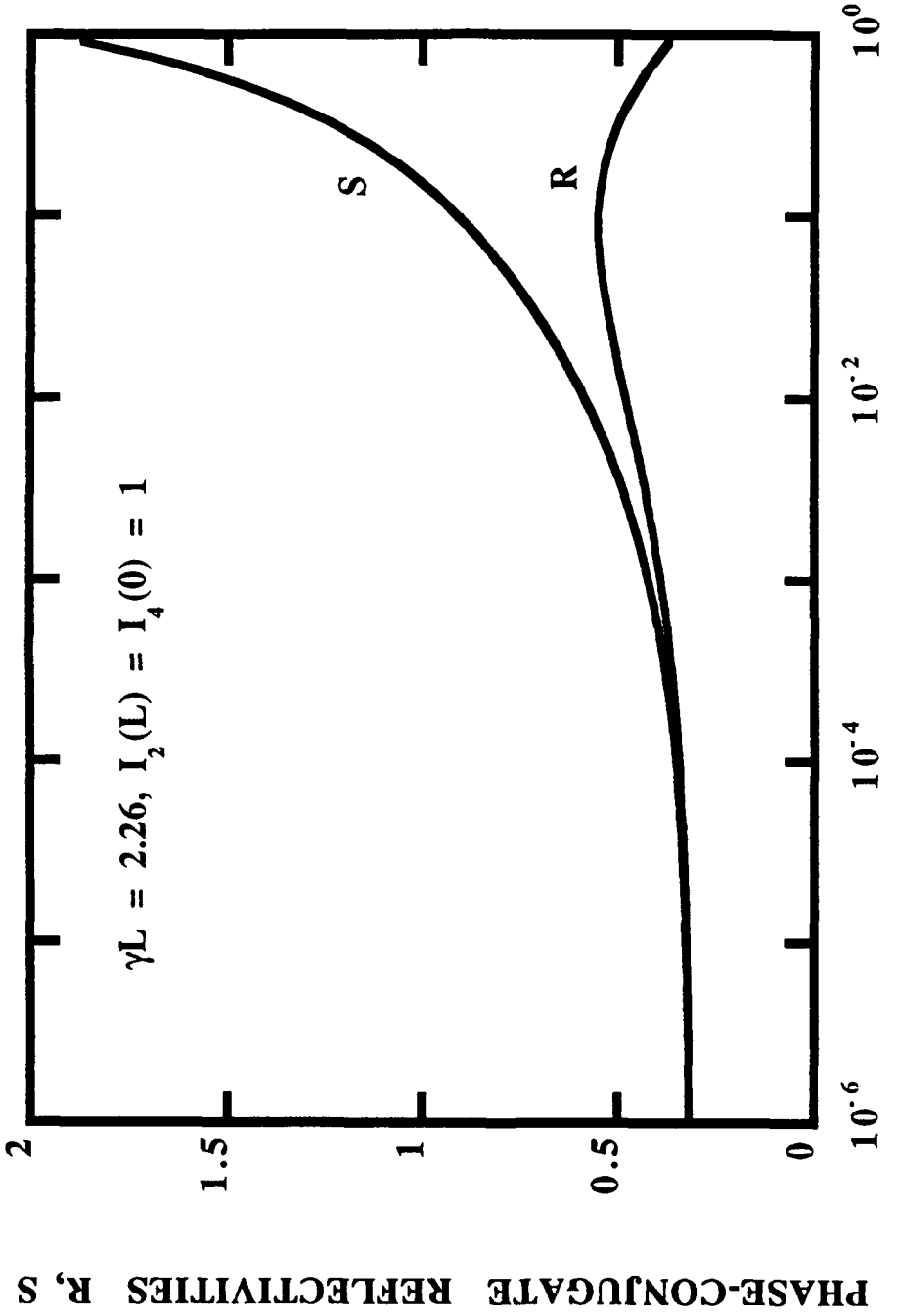
PHASE-CONJUGATE REFLECTIVITIES R, S
2
1.5
1
0.5
0
$\gamma L = 2.26$, $I_2(L) = I_4(0) = 1$
S
R
$10^{0}$
$10^{-2}$
$10^{-4}$
$10^{-6}$
NORMALIZED SEED INTENSITY $I_1(0) / I_4(0)$

Fig. 2

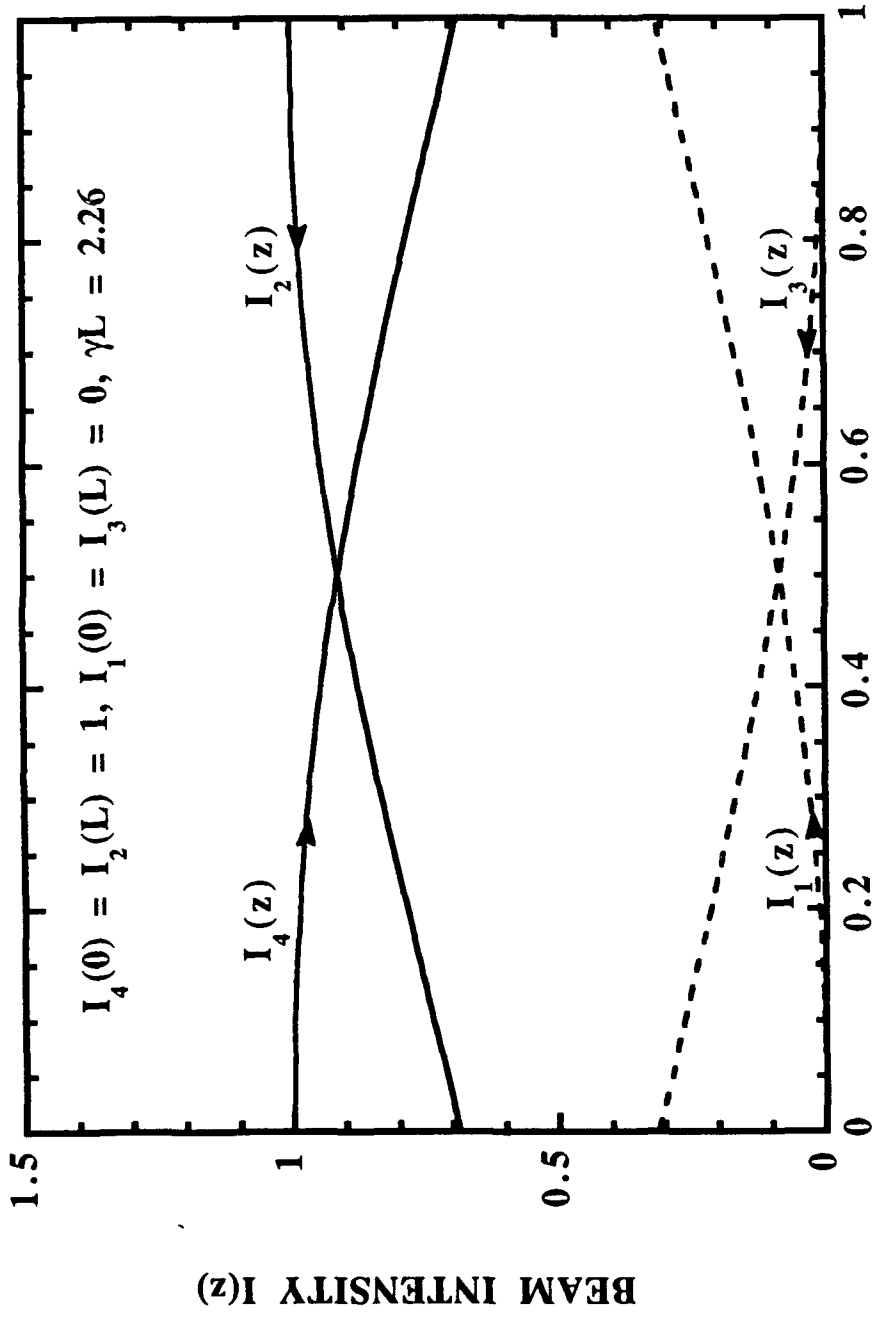
$I_4(0) = I_2(L) = 1, I_1(0) = I_3(L) = 0, \gamma L = 2.26$
$I_2(z)$
$I_4(z)$
$I_3(z)$
$I_1(z)$
BEAM INTENSITY I(z)
1.5
1
0.5
0
0
0.2
0.4
0.6
0.8
1
NORMALIZED DISTANCE z

Fig. 3a

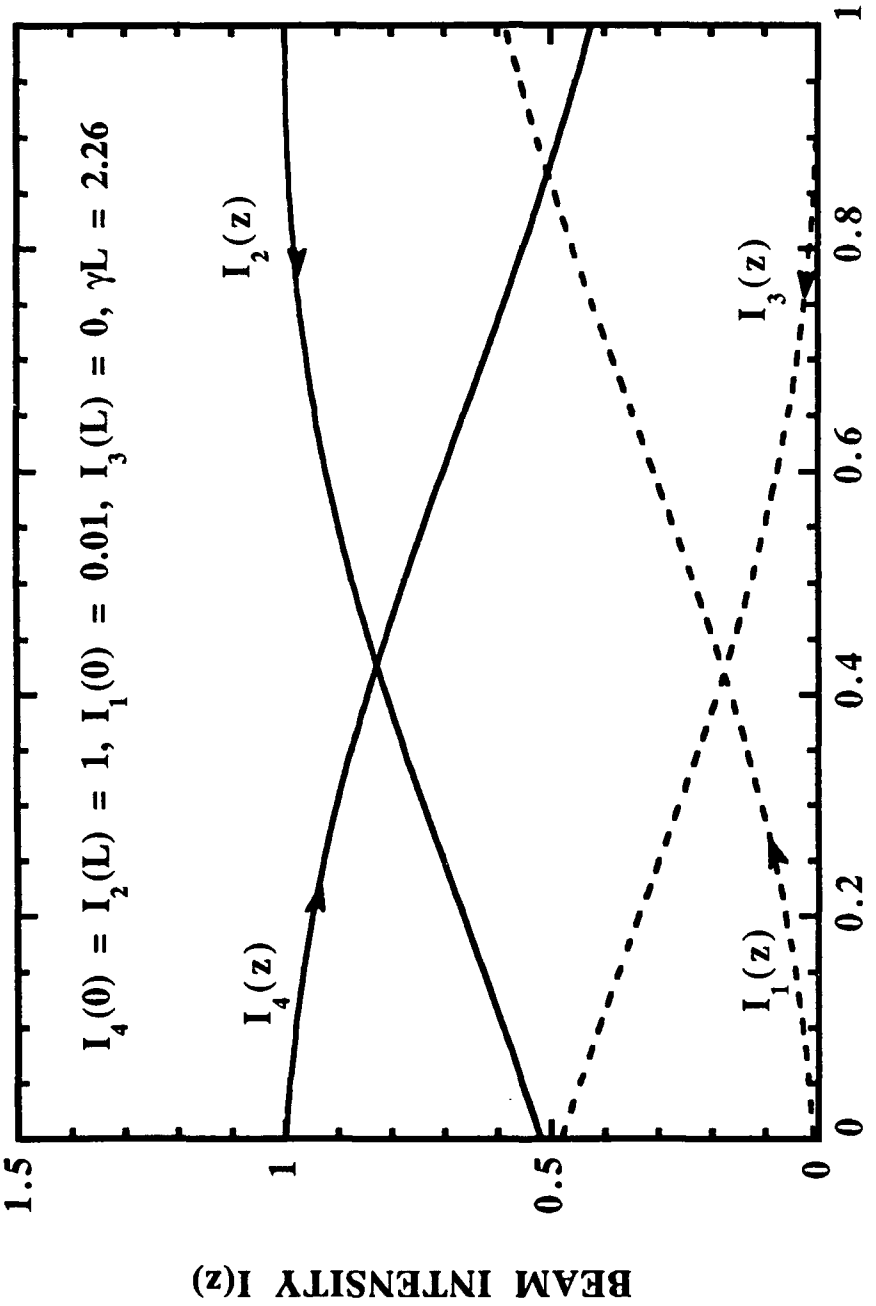
$I_4(0) = I_2(L) = 1,\ I_1(0) = 0.01,\ I_3(L) = 0,\ \gamma L = 2.26$
$I_2(z)$
$I_4(z)$
$I_3(z)$
$I_1(z)$
BEAM INTENSITY I(z)
1.5
1
0.5
0
0
0.2
0.4
0.6
0.8
1
NORMALIZED DISTANCE z

Fig. 3b

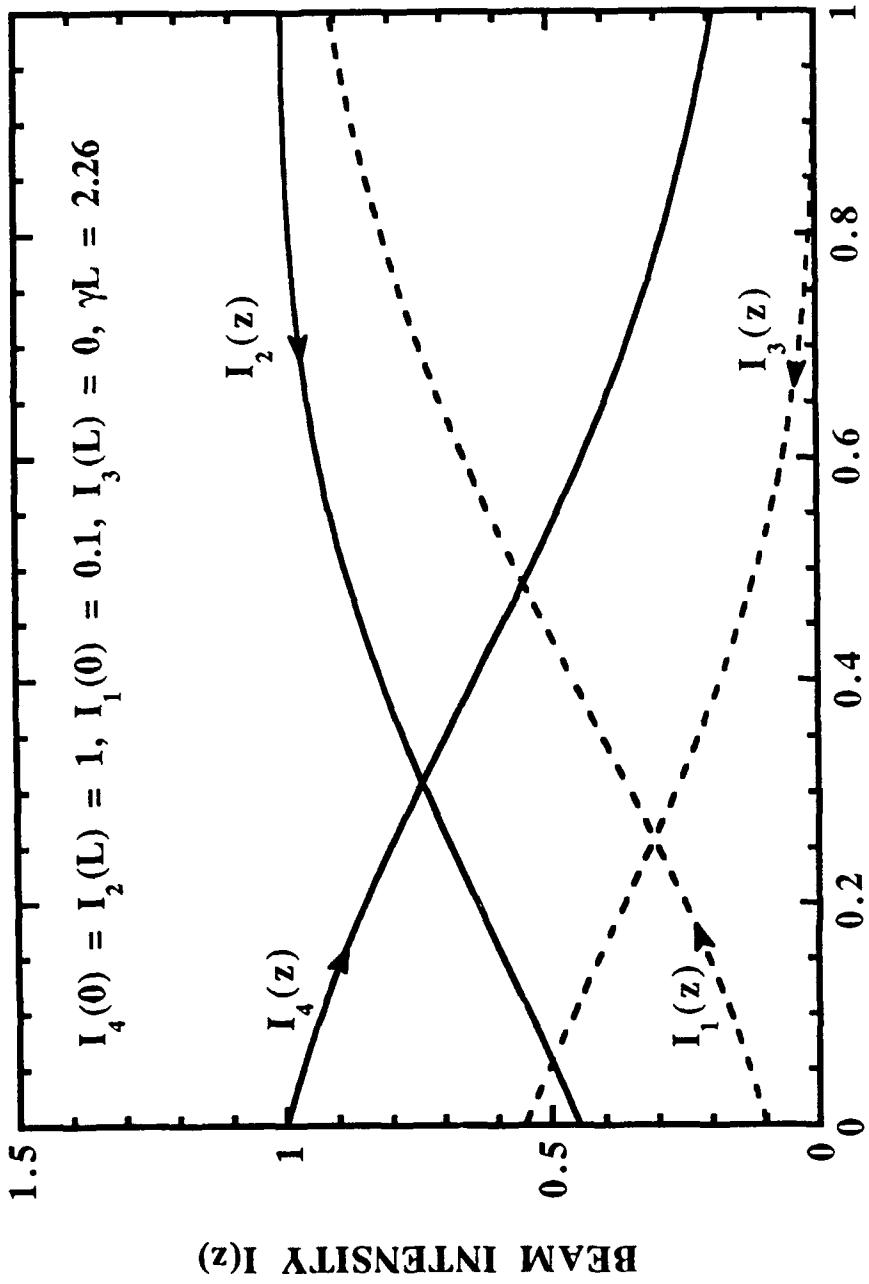
$I_4(0) = I_2(L) = 1,\ I_1(0) = 0.1,\ I_3(L) = 0,\ \gamma L = 2.26$
$I_2(z)$
$I_3(z)$
$I_4(z)$
$I_1(z)$
BEAM INTENSITY I(z)
1.5
1
0.5
0
0
0.2
0.4
0.6
0.8
1
NORMALIZED DISTANCE z

Fig. 3c

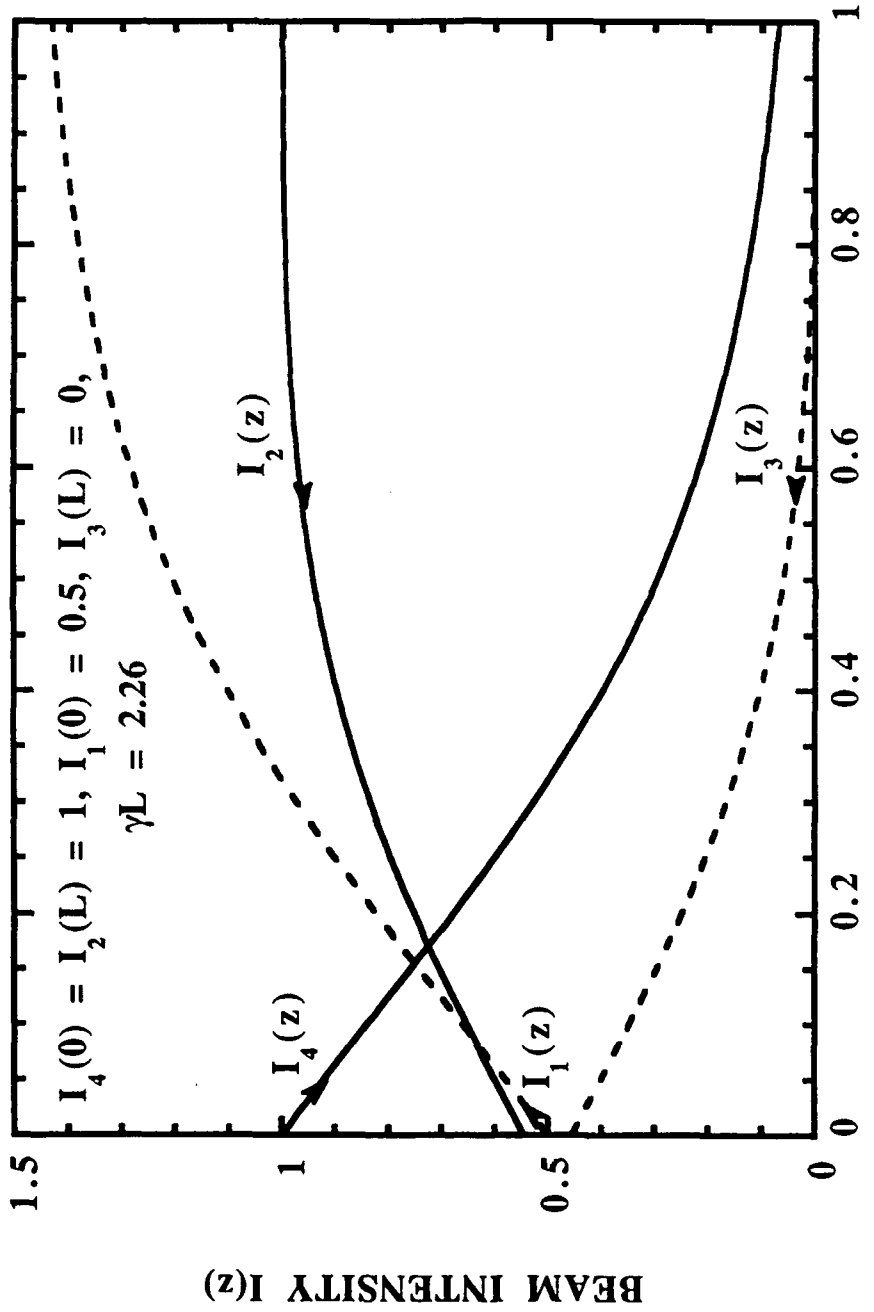
$I_4(0) = I_2(L) = 1,\ I_1(0) = 0.5,\ I_3(L) = 0,$
$\gamma L = 2.26$
$I_2(z)$
$I_3(z)$
$I_4(z)$
$I_1(z)$
BEAM INTENSITY $I(z)$
1.5
1
0.5
0
0
0.2
0.4
0.6
0.8
1
NORMALIZED DISTANCE z

Fig. 3d

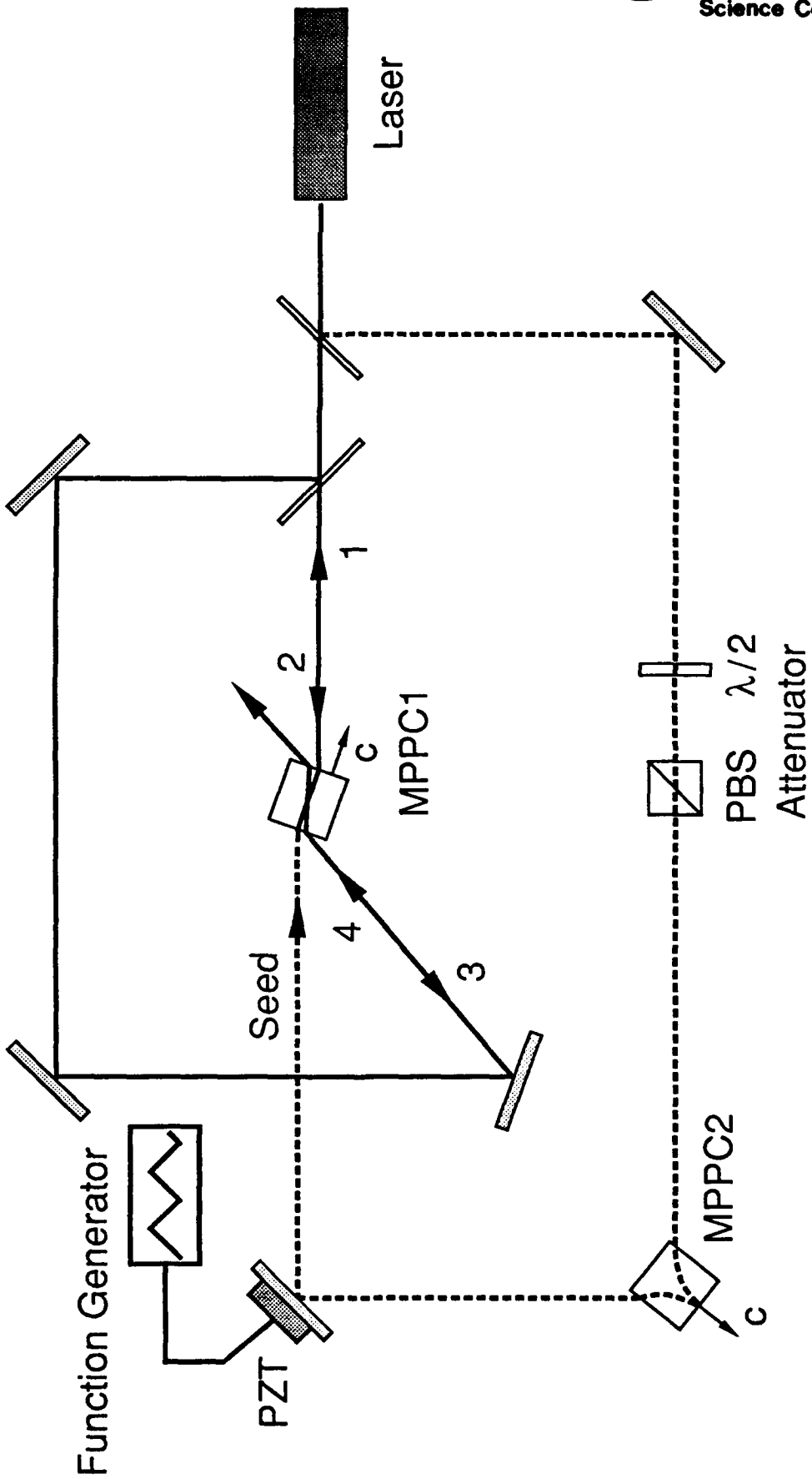
Laser
1
2
c
MPPC1
PBS
λ/2
Attenuator
Seed
4
3
Function Generator
PZT
MPPC2
c

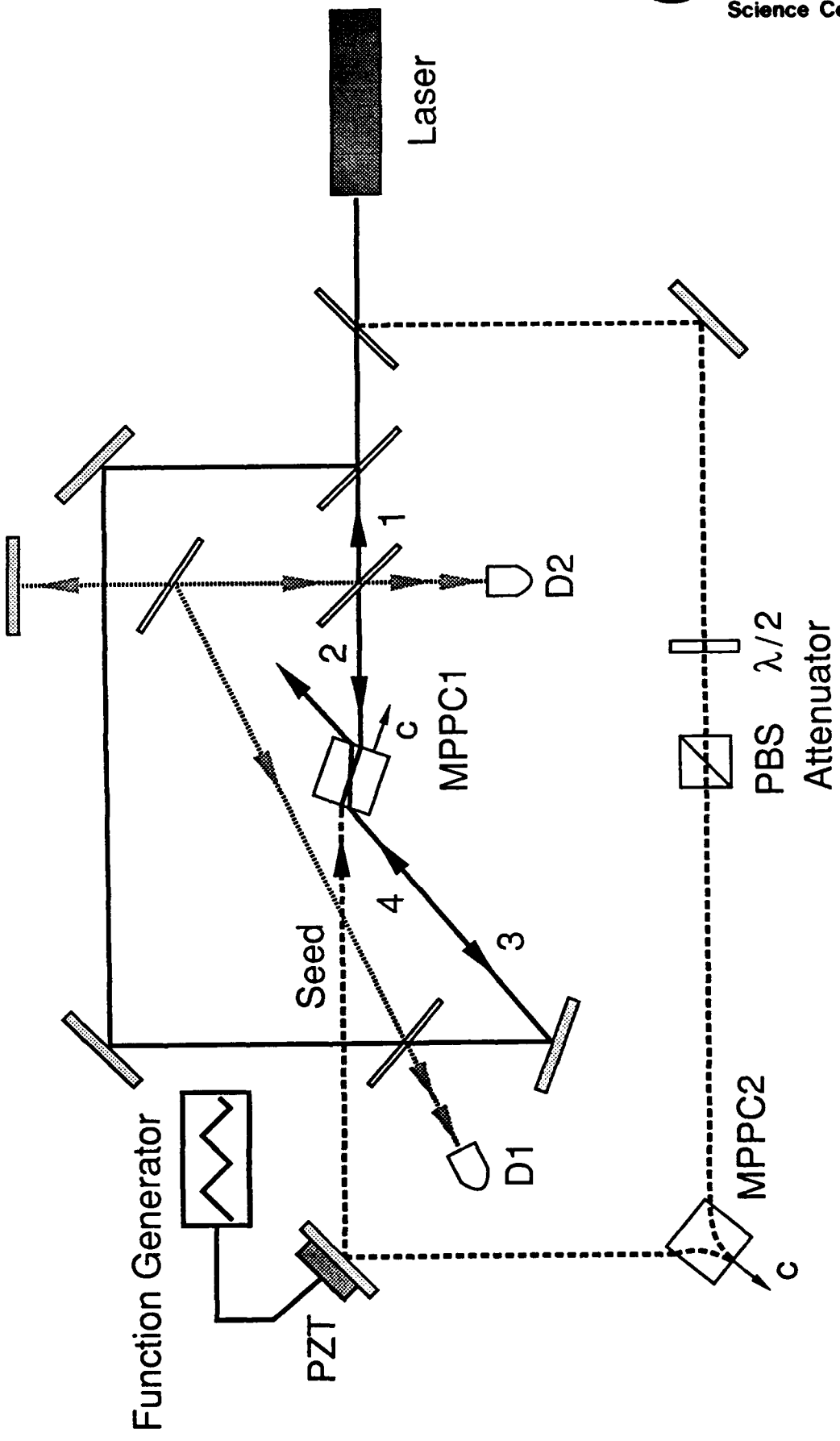
Laser
1
D2
2
c
MPPC1
PBS
λ/2
Attenuator
Seed
4
3
D1
MPPC2
c
Function Generator
PZT

(b)

(a)

(c)

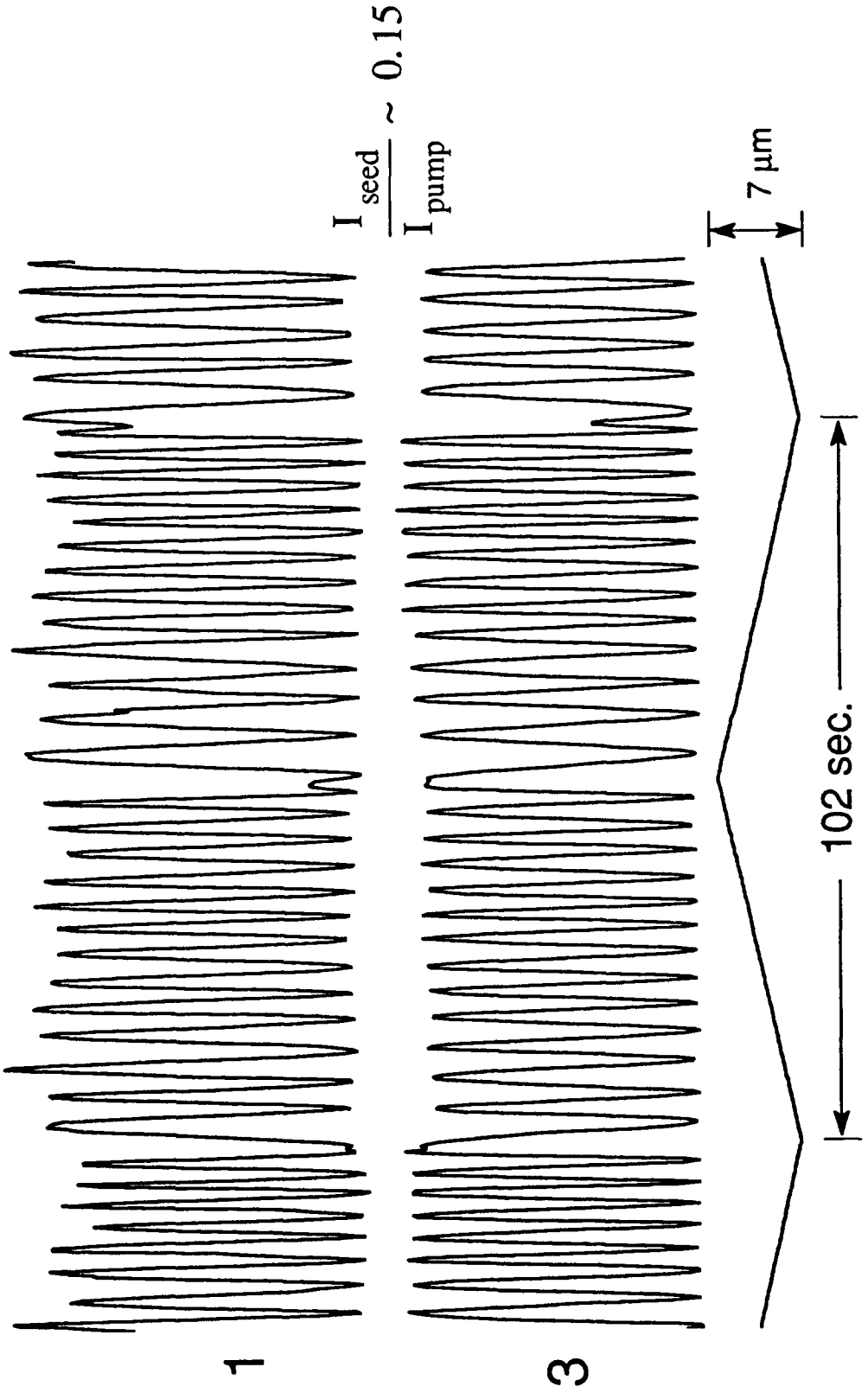
$\frac{I_{seed}}{I_{pump}} \sim 0.15$
7 μm
102 sec.
1
3

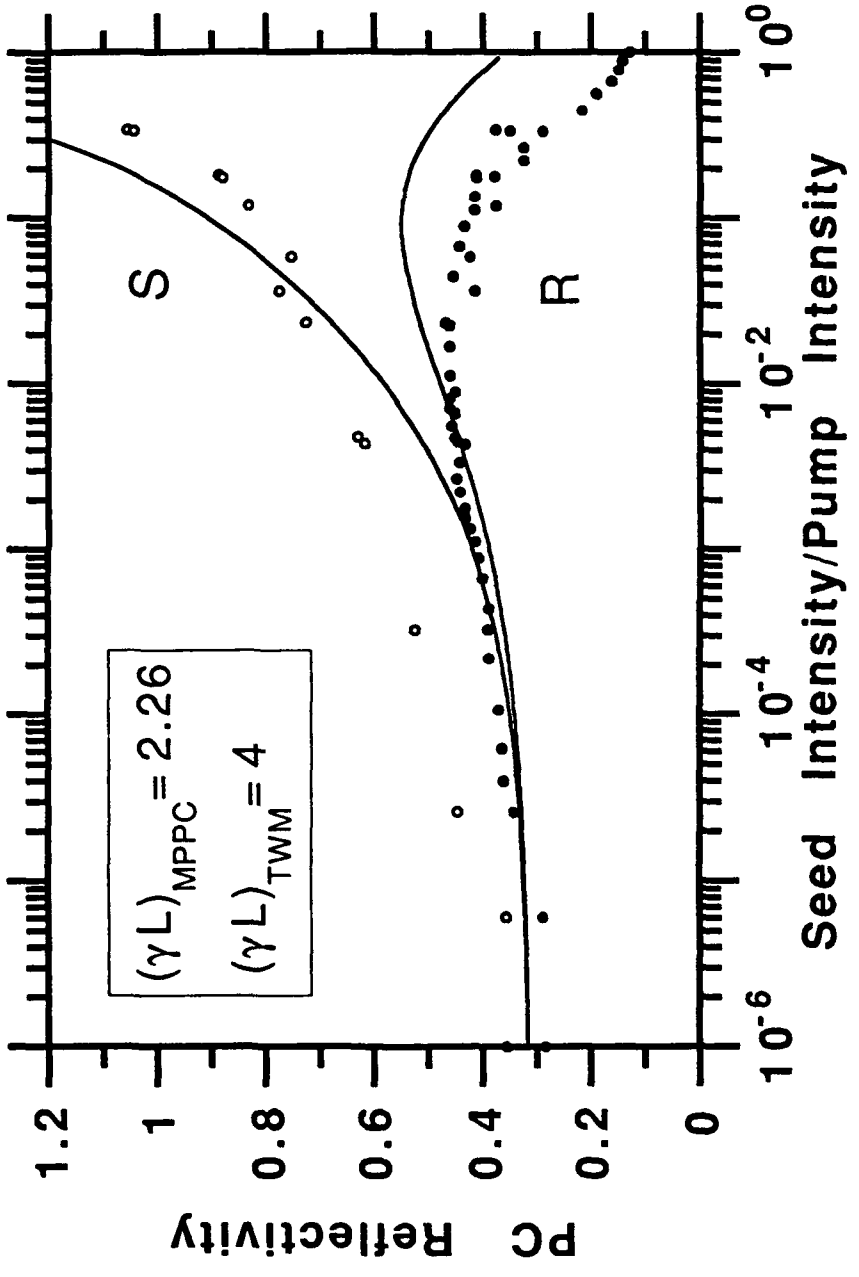
PC Reflectivity
1.2
1
0.8
0.6
0.4
0.2
0
$10^{-6}$
$10^{-4}$
$10^{-2}$
$10^{0}$
Seed Intensity/Pump Intensity
S
R
$(\gamma L)_{MPPC} = 2.26$
$(\gamma L)_{TWM} = 4$

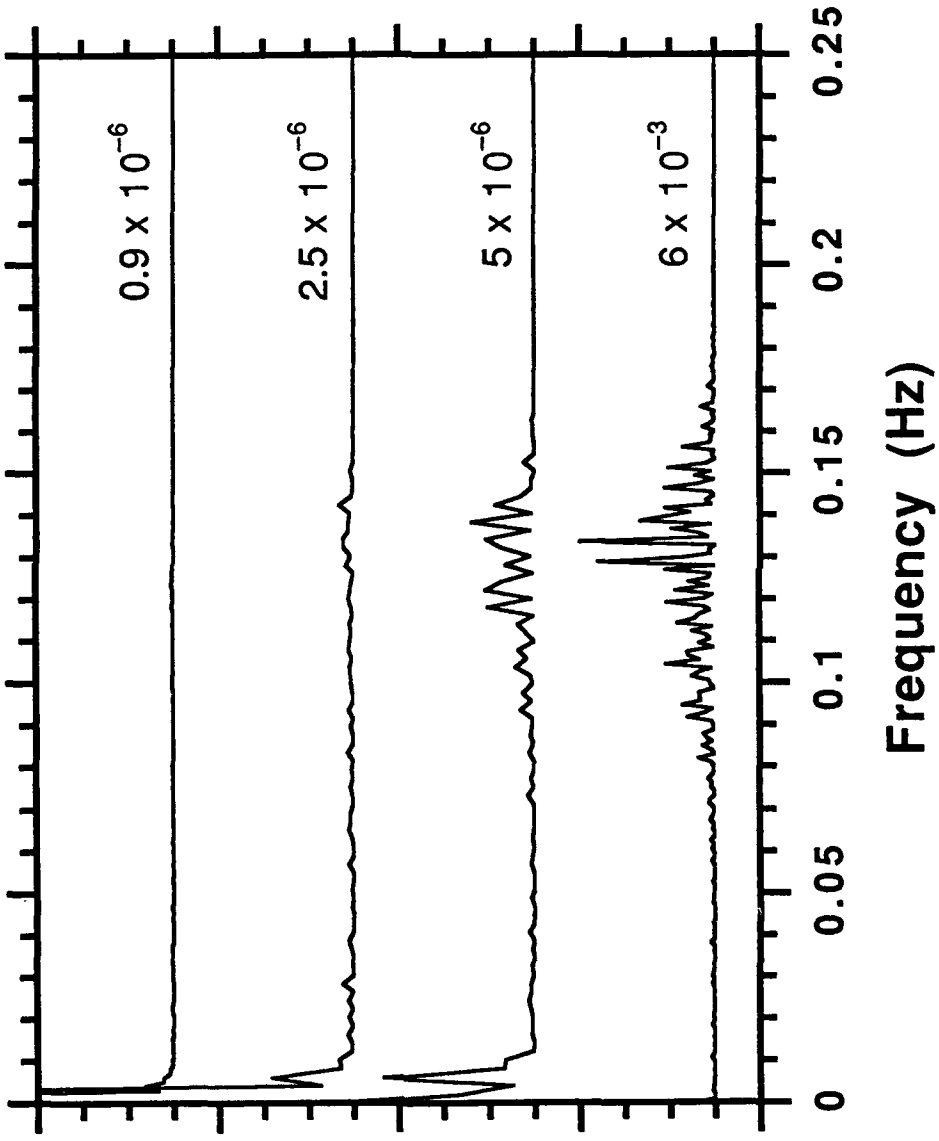
0.9 x 10^-6
2.5 x 10^-6
5 x 10^-6
6 x 10^-3
0
0.05
0.1
0.15
0.2
0.25
Frequency (Hz)

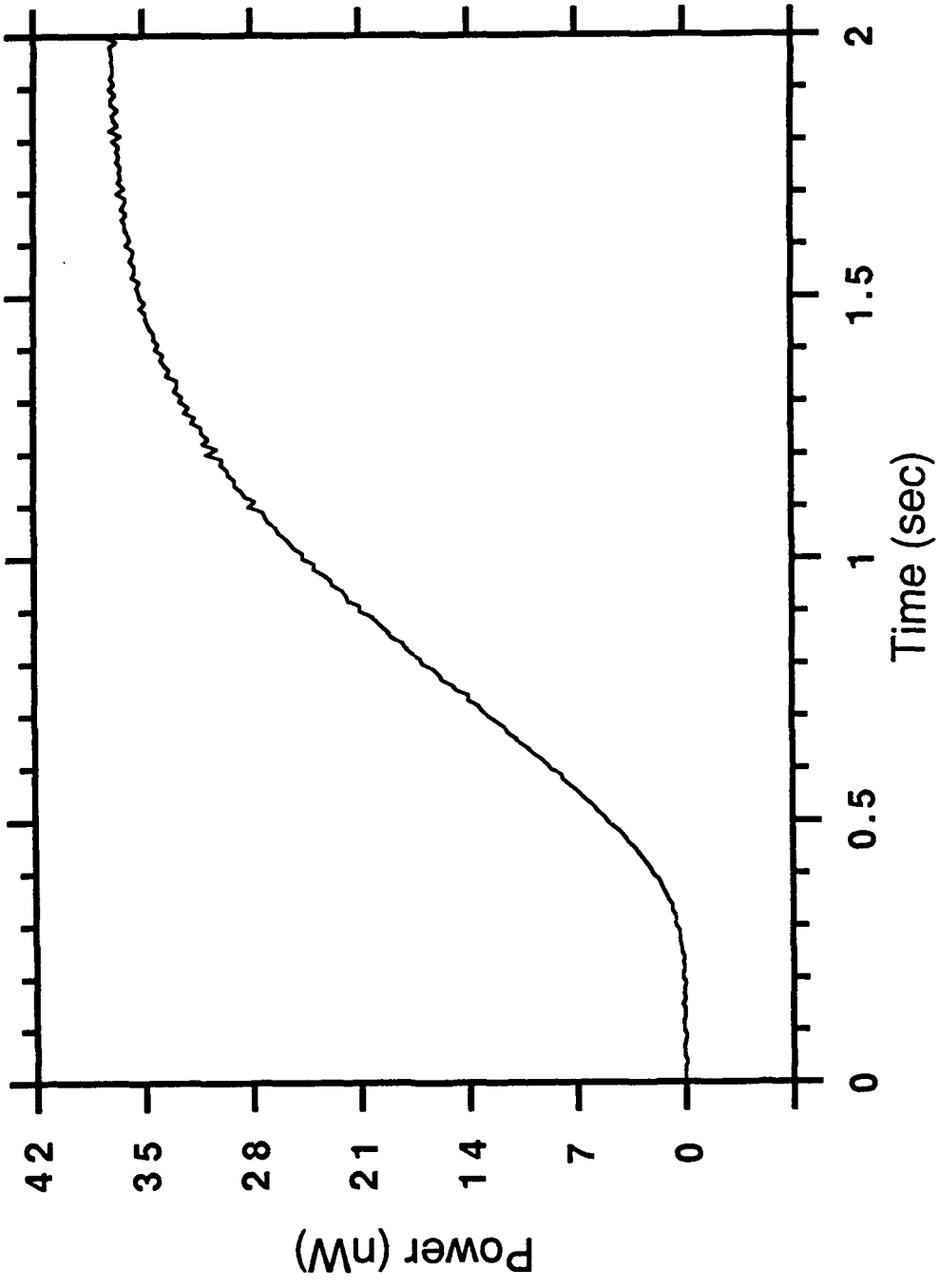
Power (nW)
42
35
28
21
14
7
0
0
0.5
1
1.5
2
Time (sec)

## Appendix 4.4

# DIFFRACTION PROPERTIES OF MULTIPLE-BEAM PHOTOREFRACTIVE GRATINGS

Reprinted from Journal of the Optical Society of America B



# Diffraction properties of multiple-beam photorefractive gratings

R. Saxena, F. Vachss, I. McMichael, and P. Yeh

*Rockwell International Science Center, Thousand Oaks, California 91360*

Received October 30, 1989; accepted February 22, 1990

We have analytically solved the problem of $N$ mutually incoherent pairs of beams in photorefractive media, each pair of which shares a common grating. The results are applied to study simultaneous read–write of dynamic photorefractive holograms with beams of comparable intensity. The diffraction efficiency is shown to be a nonlinear function of the read-beam intensity and is nonreciprocal with respect to readout from the two input ports. A complete energy transfer between the two write beams occurs in a finite thickness of the photorefractive crystal, in contrast to the infinite thickness required in the standard two-beam coupling case.

## INTRODUCTION

Most applications of photorefractive media in nonlinear-optical processing depend on these materials' ability to transfer intensity and phase information in real time among the various incident optical beams. This multibeam interaction occurs through holographic gratings written in the material by the interfering incident beams. While a variety of beam-coupling scenarios have been proposed, by far the most commonly used are the standard two-wave[1–3] and four-wave[4,5] mixing geometries illustrated in Figs. 1(a) and 1(b), respectively. This is at least partly a result of the fact that analytic solutions for the interacting beam amplitudes can be obtained for two-wave[3,6–8] and four-wave[4,9] mixing by using transmission reflection geometries in photorefractive media with negligible absorption. In the four-wave mixing case, the analysis is greatly simplified because the beams interact through a single shared grating. Numerical techniques are required for studying the effects of bulk absorption on two-beam coupling in reflection geometry[10] and on four-wave mixing in either geometry.[11,12] The descriptions of higher-order multibeam processes, in general, will also require more cumbersome numerical approaches.

In this paper we describe such a class of multiple-beam interactions in photorefractive materials with linear absorption for which relatively simple analytic solutions exist. Specifically, we shall consider a system of $N$ pairs of mutually incoherent beams incident upon a photorefractive material as shown in Fig. 2(a). We shall show that when these beams are oriented so that the $N$ holographic gratings written by all the pairs of beams coincide, the amplitude of the overall shared grating may be derived analytically and then used to obtain explicit expressions for the amplitudes of all the $2N$ interacting beams. The case of $N = 2$ would describe the two-wavelength photorefractive optical interconnect by McRuer *et al.*[13] With suitable boundary conditions, the results of this case are also applied to study simultaneous read–write of dynamic photorefractive holograms with beams of comparable intensity. Enhanced readout occurs because of beam coupling during display, and the diffraction efficiency is shown to be nonreciprocal with respect to readout from the two input ports. In particular, we shall show that this form of multibeam interaction permits complete energy transfer between beams in a finite depth of material, in contrast to the behavior seen in the canonical two-wave mixing geometry.

## THEORETICAL FORMULATION

The schematic representation for coupling of $N$ mutually incoherent pairs of beams in photorefractive media is shown in Fig. 2(a). $A_n$ and $B_n$ are two coherent laser beams of the $n$th pair that are symmetrically incident at an angle $\theta_n$ on a photorefractive crystal of thickness $L$. The electric field amplitudes of the beams in one direction may be written as

$$E_{A_n}(\mathbf{r}, t) = \tfrac{1}{2}A_n(x)\exp[i(\mathbf{k}_{A_n}\cdot\mathbf{r} - \omega_n t)] + \text{c.c.}, \quad (1)$$

where $A_n$ is the complex amplitude of the $n$th field at steady state and $\mathbf{k}_{A_n}$ is the wave vector in the medium. To describe the fields in the other direction, $A$ is replaced by $B$, and we have assumed that all the beams are plane polarized in the same direction. Each beam pair is incoherent with the other pairs, and the wave vectors $\mathbf{k}_{A_n}$ and $\mathbf{k}_{B_n}$ are such that each beam can still Bragg diffract off the gratings written by the other beam pairs. The $x$ axis is taken normal to the surface of the medium, and the complex amplitudes are assumed to be functions of $x$ due to absorption and energy transfer by beam coupling. We assume that the frequency difference between any two pairs of beams, $\Delta\omega_{mn} \equiv \omega_m - \omega_n$, is much larger than the inverse of the response time $\tau$ of the medium, i.e., $\Delta\omega_{mn} \gg \tau^{-1}$. Then the medium cannot respond to these fast oscillations in the intensity, and beams of different frequency will not write a grating. The time-averaged intensity then simplifies to

$$I(\mathbf{r}) = \tfrac{1}{2}\sum_n \{|A_n|^2 + |B_n|^2 + [A_n B_n^* \exp(i\mathbf{K}_n\cdot\mathbf{r}) + \text{c.c.}]\}, \quad (2)$$

where the grating vectors are defined by $\mathbf{K}_n \equiv \mathbf{k}_{A_n} - \mathbf{k}_{B_n}$. Hence the intensity contains an interference term from each pair, summed over all such pairs. This interference pattern induces a spatial modulation of the refractive index of the medium by means of the photorefractive effect

0740-3224/90/071210-06$02.00 

Rockwell International
Science Center
Vol. 7, No. 7/July 1990/J. Opt. Soc. Am. B 1211

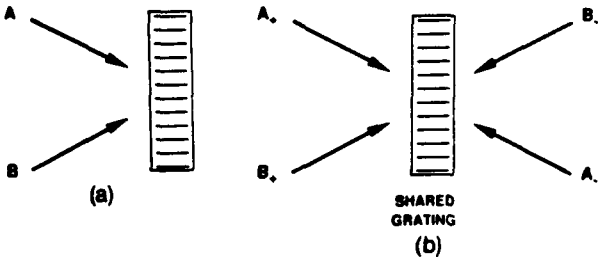


Fig. 1. Schematic representation of (a) two-wave mixing and (b) four-wave mixing in photorefractive media.

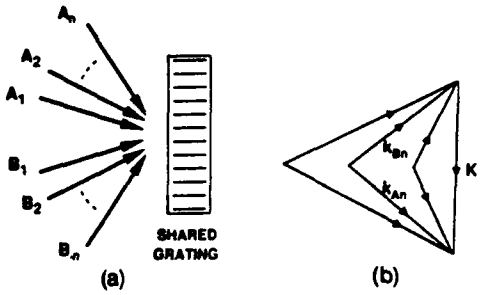


Fig. 2. (a) Schematic representation of multibeam coupling in photorefractive media. (b) Vector diagram showing the Bragg condition.

that has the form

$$n = n_b + \frac{\Delta n}{2I_0}\left[e^{i\phi}\exp(i\mathbf{K}\cdot\mathbf{r})\sum_n A_n B_n^* + c.c.\right], \tag{3a}$$

where

$$I_0 \equiv \sum_n (|A_n|^2 + |B_n|^2) \tag{3b}$$

and we have assumed that the Bragg condition is satisfied for all beam pairs: $K_n \equiv \mathbf{K}$ [see Fig. 2(b)]. Under these conditions, the gratings formed by all beam pairs combine to form a single grating that couples all the beams. Here $n_b$ is the background refractive index of the photorefractive medium in the absence of light, $\Delta n$ is the amplitude of the index grating at the fundamental harmonic of the grating vector, and $\phi$ represents the spatial phase shift of the index gratings with respect to the light intensity pattern. We have assumed that the photoionization cross section, the recombination coefficient, and the background refractive index of the photorefractive medium are essentially the same for all the incident frequencies so that $\Delta n$ and $\phi$ depend only on the material properties and on the magnitude and the direction of the grating vector $\mathbf{K}$.

To describe the propagation and the coupling of the waves in the nonlinear medium, we start with the wave equation, use the slowly varying envelope approximation, and ignore terms that are quadratic in the index change to arrive at the following coupled equations for the complex field amplitudes:

$$\frac{dA_n}{dx} = \gamma G B_n - \alpha A_n,$$

$$\frac{dB_n}{dx} = -\gamma^* G^* A_n - \alpha B_n, \tag{4}$$

where $\alpha$ is the field absorption coefficient and $\gamma$ is the complex coupling coefficient that is given by

$$\gamma \equiv \frac{i\omega\Delta n\, e^{i\phi}}{2c\cos\theta}, \tag{5}$$

while $G$ represents the normalized amplitude of the overall shared grating:

$$G \equiv \sum_n A_n B_n^*/I_0. \tag{6}$$

We have ignored the small frequency differences between the waves and taken $\omega_n \approx \omega$ for all the waves, and we have assumed that $\theta_n \approx \theta$, leading to the same coupling constant for all the beam pairs. For typical values of 1-$\mu$m grating period and 1-mm thickness of the photorefractive grating, the frequencies of the various beam pairs can differ by a few tens of gigahertz and their angles differ by a few milliradians for the Bragg phase-matching condition to be still satisfied, so that assuming the same coupling constant for all the beam pairs seems reasonable. In the next section we obtain general analytic solutions to the coupled amplitude equations (4) for arbitrary input beam amplitudes.

## GENERAL ANALYTIC SOLUTIONS FOR MULTIWAVE MIXING

We restrict our attention to charge transport by diffusion in the photorefractive crystal. Choosing $\phi = \pi/2$, we see from Eq. (5) that $\gamma$ is a real, negative quantity, which we denote by $-\Gamma$ ($\Gamma = \pi\Delta n/\lambda\cos\theta$, where $\lambda$ is the free-space wavelength). The linear absorption terms can be eliminated by the transformation: $a_n \equiv A_n e^{\alpha x}$, $b_n \equiv B_n e^{\alpha x}$. The coupled equations in terms of the new variables are

$$\frac{da_n}{dx} = -\Gamma g b_n,$$

$$\frac{db_n}{dx} = \Gamma g^* a_n, \tag{7}$$

where $g$ is redefined in terms of the new variables: $g \equiv \Sigma_n g_n/i_0$, with $g_n \equiv a_n b_n^*$ and $i_0 \equiv I_0\exp(2\alpha x)$. Note that $i_0$ remains constant as the beams propagate through the nonlinear medium. We define another normalized variable as $f \equiv \Sigma_n f_n/i_0$, where $f_n \equiv (|a_n|^2 - |b_n|^2)$, and the nonlinear, coupled equations for the global variables $f$ and $g$ are given by

$$\frac{d|g|^2}{dx} = 2\Gamma|g|^2 f,$$

$$\frac{df}{dx} = -4\Gamma|g|^2. \tag{8}$$

Equations (8) can be decoupled since $(f^2 + 4|g|^2)$ is a conserved quantity, which we take equal to the constant $C^2$. The value of $C$ will be determined from the boundary conditions for the beams at the input. The resulting equation for $f$, $df/dx = -\Gamma(C^2 - f^2)$, can be solved to yield

$$f(x) = -C\tanh(C\Gamma x - D). \tag{9a}$$

where the integration constants $C$ and $D$ are given by

$$C^2 \equiv f^2(0) + 4|g(0)|^2, \qquad D \equiv \frac{1}{2}\ln\frac{C + f(0)}{C - f(0)} \tag{9b}$$

and the solution for the magnitude of the overall shared grating is

$$|g(x)| = \frac{C}{2}\,\mathrm{sech}(C\Gamma x - D). \tag{9c}$$

If $D \approx 0$ and $C \approx 1$ (this will be true for the dynamic hologram described in the next section when the two write beams are of equal intensity and the read beam is much weaker than either of the write beams), then Eq. (9c) shows that the strength of the overall shared grating is maximum at the input plane and falls off exponentially with increasing distance for large coupling strength ($\Gamma x \gg 1$). This behavior is expected because, for equal-intensity write beams, the fringe contrast—and hence the photorefractive index grating—is maximum at the input plane. To determine the phase of the overall shared grating, we express $g$ in polar form: $g \equiv |g|\exp(i\phi_g)$. Since $\Gamma$ and $f$ are real quantities, we find from Eqs. (7) that $d\phi_g/dx = 0$, indicating that the phase of the overall shared grating is uniform throughout the interaction region and equal to its value at the input plane, $\phi_g(0)$. Having determined the solutions for the global variables $f(x)$ and $g(x)$, we now consider the coupled equations for the variables $f_n$ and $g_n$ that are characteristic of each individual beam pair:

$$\frac{dg_n}{dx} = \Gamma g f_n,$$

$$\frac{df_n}{dx} = -2\Gamma g^* g_n + \text{c.c.} \tag{10}$$

If we define each complex grating in the following manner: $g_n \exp[-i\phi_g(0)] \equiv r_n + is_n$, then the above set of coupled equations transforms into the following:

$$\frac{dr_n}{dx} = \Gamma|g|f_n,$$

$$\frac{ds_n}{dx} = 0,$$

$$\frac{df_n}{dx} = -4\Gamma|g|r_n. \tag{11}$$

Equations (11) show that in the complex plane rotated by $\phi_g(0)$, the imaginary part of $g_n$ remains constant at its initial value. The coupled equations for the intensities of the beams of a given pair are given by

$$\frac{di_{a_n}}{dx} = -2\Gamma|g|r_n,$$

$$\frac{di_{b_n}}{dx} = 2\Gamma|g|r_n, \tag{12}$$

where $i_{a_n} \equiv |a_n|^2$ and $i_{b_n} \equiv |b_n|^2$. Once the solution of $r_n$ is determined from Eqs. (11), it may be substituted into Eqs. (12) along with $|g|$ to solve finally for the intensities of the various beams. Following exactly the same procedure as for solving the global variables and simplifying, we obtain the following expression for the intensity of beam A of the $n$th pair:

$$\begin{aligned} i_{a_n}(x) = i_{a_n}(0) &- \frac{i_{a_n}(0) - i_{b_n}(0)}{2} \\ &\times [1 + \tanh(C\Gamma x - D)\tanh D \\ &- \mathrm{sech}(C\Gamma x - D)\,\mathrm{sech}\,D] \\ &- [i_{a_n}(0)i_{b_n}(0)]^{1/2}\cos[\phi_{g_n}(0) - \phi_g(0)] \\ &\times [\tanh(C\Gamma x - D)\,\mathrm{sech}\,D \\ &+ \mathrm{sech}(C\Gamma x - D)\tanh D], \end{aligned} \tag{13}$$

where $\phi_{g_n}(0)$ is the phase of the complex grating $g_n$ at the input plane: $g_n \equiv |g_n|\exp(i\phi_{g_n})$. The intensity of beam B for the same pair is given by the relation $i_{b_n}(x) = i_{a_n}(0) + i_{b_n}(0) - i_{a_n}(x)$. We shall now apply the general solutions developed in this section to study special cases of interest in the following two sections.

## SIMULTANEOUS READ–WRITE OF PHOTOREFRACTIVE HOLOGRAMS

We now consider simultaneous illumination of the photorefractive crystal by two beam pairs 1 and 2, the boundary conditions being that both beams of pair 1 are nonzero at the input ($x = 0$), while only beam $A_2$ is nonzero at the input for the second pair [i.e., $A_2(0) \neq 0$, $B_2(0) = 0$]. Bragg diffraction of $A_2$ off the grating written by beam pair 1 generates the beam $B_2$ in the nonlinear medium, and we study its diffraction efficiency for a variety of different situations. In previous theoretical studies of volume holograms in photorefractive crystals,[6-8,14-16] recording and replay of the photorefractive holograms are treated as two separate processes, and readout is accomplished with a weak beam (assumed to be weak enough not to perturb the grating being read). In this section we consider simultaneous write–read of volume phase holograms with beams of comparable intensity.

Note that the beam interaction under consideration in this section is formally identical to the forward four-wave mixing geometry studied by Khyzniak *et al.*[17] and Fischer *et al.*[18] In Ref. 17 the authors studied the phase-conjugate nature of the fourth beam generated by the nonlinear interaction of the three, noncoplanar interfering beams of equal frequency, whereas in Ref. 18 the authors examined photorefractive coupling of two beams with general polarization, which led to four coupled equations for the various components of the beams' electric fields. In this section we study the diffraction efficiency of the read beam in the limiting case of coplanar propagation vectors for all the beams.

Consider the index grating written by equal-intensity write beams $A_1$ and $B_1$. Now suppose that this grating is read by beam $A_2$, so that beam $B_2$ is zero in the input plane. This implies that at the input plane, the phase of the overall shared grating is equal to the phase of the grating resulting from beam pair 1; i.e., $\phi_g(0) = \phi_{g1}(0)$.

Hence the solutions in Eq. (13) simplify to

$$I_{A1}(x) = I_{A1}(0)e^{-2\alpha x}[1 - \tanh D\,\mathrm{sech}(C\Gamma x - D) - \mathrm{sech}\,D\tanh(C\Gamma x - D)],$$
$$I_{A2}(x) = \tfrac{1}{2}I_{A2}(0)e^{-2\alpha x}[1 + \mathrm{sech}\,D\,\mathrm{sech}(C\Gamma x - D) - \tanh D\tanh(C\Gamma x - D)], \quad (14)$$

where we have expressed the solutions in terms of the original variables. If we define the diffraction efficiency $\eta$ of beam $A_2$ as the intensity ratio $I_{B_2}(L)/I_{A_2}(0)$, where $L$ is the crystal thickness, then $\eta$ is given by the expression

$$\eta = \frac{e^{-2\alpha L}}{2}[1 + \tanh D\tanh(C\Gamma L - D) - \mathrm{sech}\,D\,\mathrm{sech}(C\Gamma L - D)]. \quad (15)$$

As can be seen from Eqs. (9b), the parameters $C$ and $D$ are determined by the intensities of the input beams. Hence, because of coupling during readout, the diffraction efficiency is now a nonlinear function of the read-beam intensity, besides having the usual dependence on the write-beam intensities. For large coupling strengths such that $(C\Gamma L - D) \gg 1$, and negligible absorption losses, we have

$$I_{A_1}(L) \approx I_{A_1}(0)(1 - \mathrm{sech}\,D),$$
$$I_{A_2}(L) \approx \tfrac{1}{2}I_{A_2}(0)(1 - \tanh D),$$
$$\eta \approx \tfrac{1}{2}(1 + \tanh D). \quad (16)$$

Since the maximum value of $\tanh D$ is 1, $\eta$ can in principle attain the value of 100%. This is a consequence of the grating's being written by the pair of write beams 1 and of the self-induced grating being written by the read beam $A_2$ and its diffracted beam being in phase with each other. If we reverse the sign of the coupling constant $\Gamma$, then Eq. (15) transforms into

$$\eta = \frac{e^{-2\alpha L}}{2}[1 - \tanh D\tanh(C\Gamma L + D) - \mathrm{sech}\,D\,\mathrm{sech}(C\Gamma L + D)], \quad (17)$$

so that for strong coupling $\eta \approx 1/2(1 - \tanh D)$. The maximum value of $\eta$ in this case can only be 50% when $\tanh D \approx 0$. For equal intensity of the write beams, changing the sign of $\Gamma$ is equivalent to reading the grating from the other input port $[I_{A_2}(0) = 0, I_{B_2}(0) \neq 0]$. In this case, the grating written by the pair of write beams 1 and the self-induced grating written by the read beam $B_2$ and its diffracted beam are out of phase with each other $(\phi_{g_1} - \phi_{g_2} = \pi)$, leading to a decrease in the diffraction efficiency. Hence our results show the nonreciprocal nature of readout of gratings in the presence of coupling. Similar results were obtained qualitatively by Staebler and Amodei[6] for fixed gratings when they used the coupled-wave theory of Kogelnik[16] and treated record and replay as two separate stages.

If the read beam is much weaker than either of the write beams, then from Eq. (9b), $C \approx \pm 1$ and $D \approx 0$. Since we chose beam coupling to be such that $A_1$ is depleted and $B_1$ is amplified in the process of writing the index grating, our choice of the value of $C$ is limited to +1. Consequently Eqs. (14) and (15) reduce to

$$I_{A_1}(L) \approx I_{A_1}(0)e^{-2\alpha L}[1 - \tanh(\Gamma L)],$$
$$I_{B_1}(L) \approx I_{A_1}(0)e^{-2\alpha L}[1 + \tanh(\Gamma L)],$$
$$\eta \approx \frac{e^{-2\alpha L}}{2}[1 - \mathrm{sech}(\Gamma L)]. \quad (18)$$

The solutions for the write beams with negligible absorption are identical to those by Vahey,[7] who assumed a phenomenological expression for the index modulation. Note that for weak read beams the diffraction efficiency is independent of the read-beam intensity and remains constant if the sign of the coupling constant is reversed. Hence the nonlinearity and the nonreciprocity in $\eta$ are observed only when the read beam has an intensity comparable with that of the write beams. For small coupling strengths ($\Gamma L \ll 1$) and negligible absorptive losses ($\alpha = 0$), the diffraction efficiency has a quadratic dependence on $\Gamma L$: $\eta \approx \Gamma^2 L^2/4$. For strong coupling and negligible absorption, the maximum value of $\eta$ is 50% for readout from either input port, which is smaller than the maximum diffraction efficiency that can be obtained with a strong read beam. Hence for strong coupling and readout in the right direction to enhance $\eta$, there exists a range of values for the read beam intensity for which it is actually advantageous to read with a beam that is more intense than the write beams.

Figure 3 is a plot of the diffraction efficiency as a function of the read-beam intensity, as given by approximations (16). The equal intensity of the write beams is taken to be unity: $I_{A_1}(0) = I_{B_1}(0) = 1$, and the absorption losses are assumed to be negligible: $\alpha = 0$. With this choice of input beam intensities, the index change $\Delta n$ in Eq. (5) will be determined by the nonlinear material equations.[1,2] For small coupling strengths ($\Gamma L \approx 1$) and weak read beam $[I_{A_2}(0) < I_{A_1}(0), I_{B_1}(0)]$, the diffraction efficiency is independent of the read-beam intensity. Increase of the read-beam intensity above the write-beam intensities serves to erase the grating being read, and the diffraction efficiency falls to zero. For strong coupling, the behavior of $\eta$ is different—the diffraction efficiency is ~50% for weak read beams increases as the read beam becomes stronger than the write beams, reaches a broad

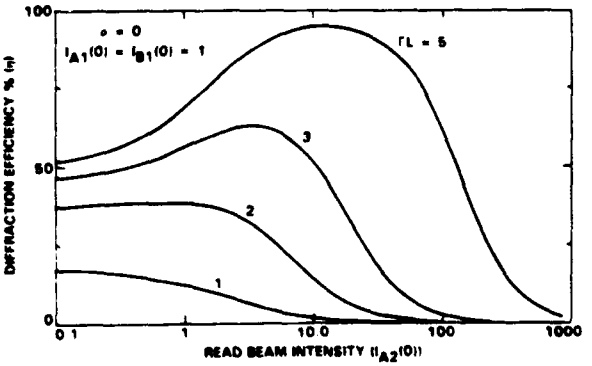


Fig. 3. Diffraction efficiency $\eta$ as a function of read-beam intensity $I_{A_2}(0)$ for various coupling strengths $\Gamma L$. The normalized, equal intensities of the write beams are unity: $I_{A_1}(0) = I_{B_1}(0) = 1$.

maximum, and eventually falls to zero when $I_{A_2}(0) \gg I_{A_1}(0), I_{B_1}(0)$.

To understand the nonlinear behavior of the diffraction efficiency with the read-beam intensity that occurs at strong coupling, we have plotted the intensities of the four beams as a function of the distance propagated in the medium in Fig. 4. The absorption losses are assumed to be negligible ($\alpha = 0$), and the coupling is assumed to be strong ($\Gamma = 5$ cm$^{-1}$, $L = 1$ cm). As in Fig. 3, the equal intensity of the write beams (solid curves) is taken to be unity, and the intensities of beam pair 2 (dashed curves) are normalized by the read-beam intensity at the input, $I_{A_2}(0)$, with $I_{B_2}(0) = 0$. For these input intensities, grating 1 has its maximum amplitude near the input plane, while grating 2 is zero. For strong coupling there can be a complete energy transfer between the write beams, and when this happens the grating formed by the write beams reduces to zero. This particular propagation distance is a sensitive function of the read-beam intensity. For a weak read beam, which does not perturb the grating written by beam pair 1, total energy transfer requires long interaction lengths, as is typical of two-beam coupling in photorefractive media and is shown in Fig. 4(a) for $I_{A_2}(0) = 0.01$. As scattering of read beam $I_{A_2}$ off grating 1 generates beam $I_{B_2}$, grating 2 slowly builds up. An examination of the curves reveals that, near the exit plane, grating 1 is zero and only grating 2 is finite, but it is very weak owing to the cross-washout factor $I_0$ in the denominator. Hence the maximum diffraction efficiency of the read beam is 50%. As the intensity of the read beam increases, grating 2 can build up to a magnitude comparable with that of grating 1, and, since the two gratings are in phase, the overall shared grating strength increases, leading to a stronger coupling of the beams in a given pair. The propagation distance for total depletion of $I_{A_1}(0)$ decreases as $I_{A_2}(0)$ is increased, being approximately half of the interaction length when all three input beams have equal intensities [Fig. 4(b)]. Beyond this distance, scattering of $I_{B_1}$ off grating 2 begins to restore the depleted beam $I_{A_1}$, and grating 1 is rebuilt. Consequently, there are now two in-phase gratings near the exit plane, leading to a larger diffraction efficiency. Since scattering of $I_{B_1}$ increases with the intensity of read beam, grating 1 rebuilds to a bigger amplitude with increasing $I_{A_2}$ and hence higher $\eta$ [Fig. 4(c)]. However, if $I_{A_2}(0) \gg I_{A_1}(0), I_{B_1}(0)$ [Fig. 4(d)], then grating 1 is small near the input plane and grating 2 is zero. Consequently, depletion of $I_{A_1}$ occurs slowly, almost near the end of the interaction region, so that grating 1 no longer has a chance to rebuild. Once again only a single grating, grating 2, contributes to the overall shared grating near the exit plane, leading to a decrease in $\eta$. For still higher read-beam intensities, grating 1 becomes small near the input plane so that diffraction of read beam becomes negligible throughout the interaction region and $\eta$ reduces to zero. Thus the nonlinear behavior of the diffraction efficiency with read-beam intensity arises because of the photorefractive nature of the index gratings—the grating strength depends on the local beam ratios and not on the absolute intensities of the beams.

Figure 5 is the same set of curves as in Fig. 3 but for negative coupling constant $\Gamma$, which corresponds to readout from the other input port. In this case, the two gratings are out of phase, so that there is no enhancement of the

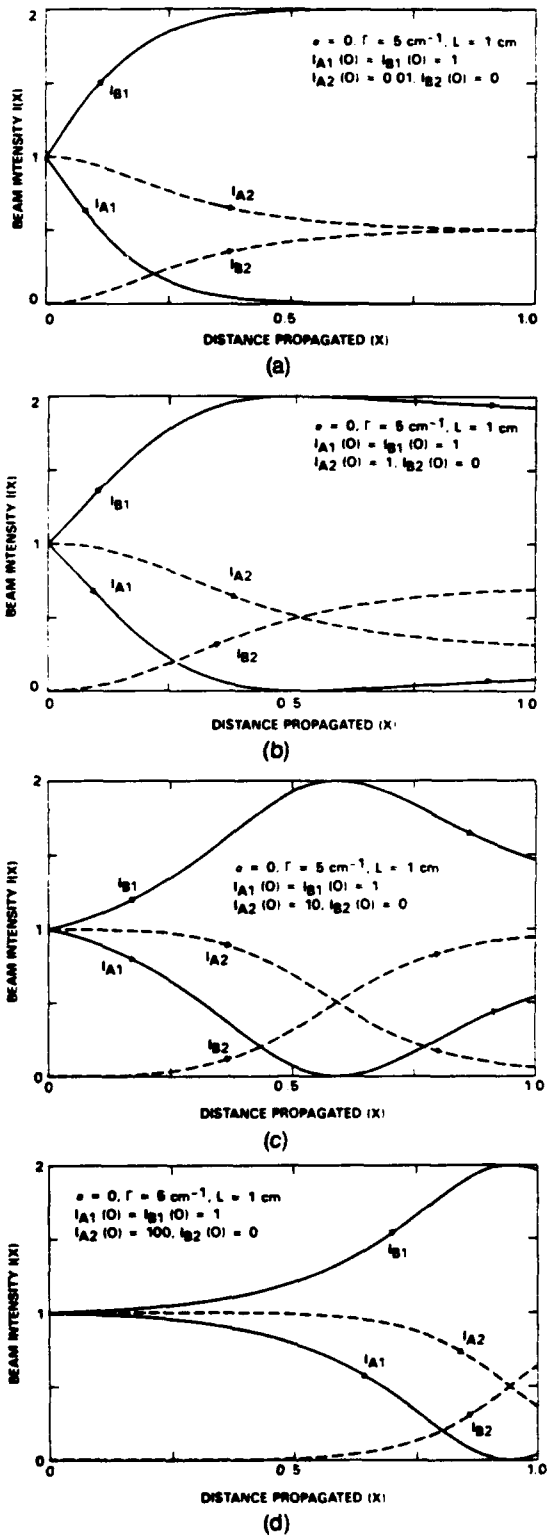


Fig. 4. Intensities $I(x)$ of the four beams as a function of the depth $x$ within the medium. The absorption coefficient $\alpha$ is taken to be zero, the coupling coefficient $\Gamma$ is equal to 5 cm$^{-1}$, and the interaction length $L$ is 1 cm. The normalized, equal intensities of the write beams (shown as solid curves) are unity: $I_{A_1}(0) = I_{B_1}(0) = 1$ and $I_{B_2}(0) = 0$. The read beam $I_{A_2}(0)$ has the following intensity corresponding to each figure: (a) 0.01, (b) 1, (c) 10, (d) 100.

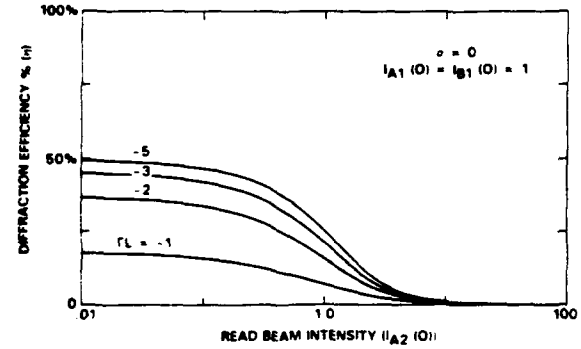


Fig. 5. Diffraction efficiency $\eta$ as a function of read-beam intensity $I_{A_2}(0)$ for various negative coupling strengths $\Gamma L$. The normalized, equal intensities of the write beams are unity: $I_{A_1}(0) = I_{B_1}(0) = 1$.

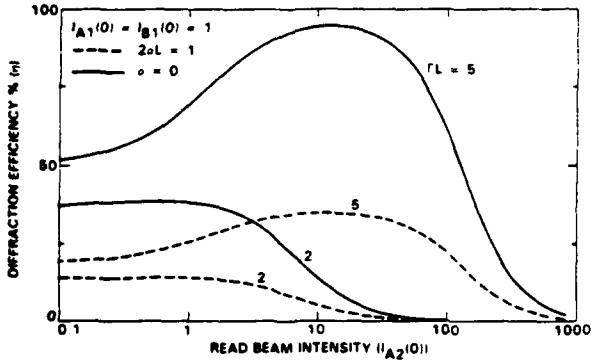


Fig. 6. Diffraction efficiency $\eta$ as a function of read-beam intensity $I_{A_2}(0)$ in the presence of absorption (dashed curves, $2\alpha L = 1$). The normalized, equal intensities of the write beams are unity: $I_{A_1}(0) = I_{B_1}(0) = 1$.

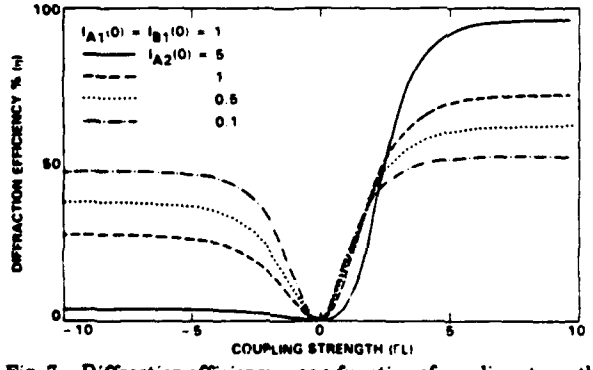


Fig. 7. Diffraction efficiency $\eta$ as a function of coupling strength $\Gamma L$ for various read-beam intensities $I_{A_2}(0)$. The normalized, equal intensities of the write beams are unity: $I_{A_1}(0) = I_{B_1}(0) = 1$, and absorptive losses are assumed to be negligible ($\alpha = 0$).

diffraction efficiency for any intensity of the read beam. As predicted by Eq. (17), the maximum diffraction efficiency is only 50% at large coupling strengths.

The effects of finite absorptive losses are shown in Fig. 6; the product of the power absorption coefficient and the crystal thickness is taken to be unity. The dependence of $\eta$ on $I_{A_2}(0)$ remains the same, but the magnitude of diffraction efficiency is reduced by the factor $e^{-2\alpha L}$.

Figure 7 is a plot of the diffraction efficiency $\eta$ versus the normalized coupling strength $\Gamma L$ for negligible absorption and equal intensity of write beams, $I_{A_1}(0) = I_{B_1}(0) = 1$. The asymmetry in $\eta$ is negligible for a weak read beam and becomes appreciable only when $I_{A_2}(0) \geq I_{A_1}(0)$, $I_{B_1}(0)$.

## CONCLUSIONS

We have solved analytically the problem of $N$ mutually incoherent pairs of beams in photorefractive media, each of which shares a common grating. The results are applied to study simultaneous read–write of dynamic photorefractive holograms with beams of comparable intensity. Because of the mediating presence of multiple beams, a complete energy transfer between the two write beams occurs in a finite thickness of the photorefractive crystal. The diffraction efficiency is shown to be a nonlinear function of the read-beam intensity: for strong coupling and readout in the direction that enhances the grating being read, the maximum diffraction efficiency occurs when the read beam is more intense than the write beams. The diffraction efficiency is also shown to be nonreciprocal with respect to readout from the two input ports.

## ACKNOWLEDGMENT

This research is supported, in part, by the U.S. Office of Naval Research under contract N00014-88-C-0230

## REFERENCES

1. G. C. Valley, J. Opt. Soc. Am. B **1**, 868 (1984).
2. Ph. Refreiger, L. Solymar, H. Rajbenbach, and J. P. Huignard, J. Appl. Phys. **58**, 45 (1985).
3. P. Yeh, IEEE J. Quantum Electron **25**, 484 (1989).
4. M. Cronin-Golomb, J. O. White, B. Fischer, and A. Yariv, Opt. Lett. **7**, 313 (1982); M. Cronin-Golomb, B. Fischer, J. O. White, and A. Yariv, IEEE J. Quantum Electron. **QE-20**, 12 (1984).
5. P. Yeh, Appl. Opt. **28**, 1961 (1989).
6. D. L. Staebler and J. J. Amodei, J. Appl. Phys. **43**, 1042 (1972).
7. D. W. Vahey, J. Appl. Phys. **46**, 3510 (1975).
8. N. V. Kukhtarev, V. B. Markov, S. G. Odulov, M. S. Soskin, and V. L. Vinetskii, Ferroelectrics **22**, 961 (1979).
9. A. Bledowski, W. Krolikowski, and A. Kujawski, IEEE J. Quantum Electron. **QE-22**, 1547 (1986); N. V. Kukhtarev, T. I. Semenets, K. H. Ringhofer, and G. Tomberger, Appl. Phys. B **41**, 259 (1986).
10. Y. H. Ja, Opt. Quantum Electron. **14**, 547 (1982).
11. Y. H. Ja, Opt. Quantum Electron. **15**, 539 (1983).
12. M. R. Belić, Phys. Rev. A **31**, 3169 (1985); M. R. Belić and M. Lax, Opt. Commun. **56**, 197 (1985).
13. R. McRuer, J. Wilde, L. Hesselink, and J. Goodman, Opt. Lett. **14**, 1174 (1989).
14. G. T. Sincerbox and G. Roosen, Appl. Opt. **22**, 690 (1983).
15. J. M. Heaton, P. A. Mills, E. G. S. Paige, L. Solymar, and T. Wilson, Opt. Acta **31**, 885 (1984).
16. H. Kogelnik, Bell Syst. Tech. J. **48**, 2909 (1969).
17. A. Khyzniak, V. Kondilenko, Y. Kucherov, S. Lesnik, S. Odulov, and M. Soskin, J. Opt. Soc. Am. A **1**, 169 (1984).
18. B. Fischer, J. O. White, M. Cronin-Golomb, and A. Yariv, Opt. Lett. **11**, 239 (1986).

## Appendix 4.5

## DIFFRACTION PROPERTIES OF FIXED GRATINGS IN PHOTOREFRACTIVE MEDIA

# Diffraction properties of fixed gratings in photorefractive media

**Claire Gu and Pochi Yeh**

*Rockwell International Science Center, Thousand Oaks, California 91360*

Received May 8, 1990; accepted August 2, 1990

The diffraction properties of fixed volume gratings, including the effect of additional photorefractive energy coupling between the incident wave and the diffracted wave, are considered. Both transmission gratings and reflection gratings are treated. Analytical solutions for phase gratings are derived, and numerical solutions for absorption gratings are also obtained. The results are presented and discussed.

## INTRODUCTION

Photorefractive materials such as $BaTiO_3$, $LiNbO_3$, $Sr_xBa_{1-x}Nb_2O_6$, and $Bi_{12}SiO_{20}$ (BSO) are, by far, the most efficient media for the recording of dynamic holograms.[1] In these media information can be stored, retrieved, and erased by light. In addition to the holographic properties, energy coupling occurs between the recording beams and also between the reading beam and the scattered beam. This is known as two-wave mixing[2] (TWM). The unique properties of beam coupling and high diffraction efficiency can be employed for many applications in optical computing,[3] including information storage,[4] image processing,[5,6] reconfigurable optical interconnections,[7,8] and implementation of neural networks.[9-11]

While the holograms in photorefractive media can be manipulated dynamically, the stored holograms are partially erased by the reading beam each time the information is retrieved. There are situations in which it is desirable to have photorefractive holograms that can be fixed by physical processes. These fixed holograms are not subject to erasure during readout.[12-16] For example, it is desirable to fix the photorefractive holograms at the end of the learning cycles in optical perceptrons.[17-20] After it is fixed, a trained perceptron will perform pattern classification without its memory fading. It is important to note that energy coupling between the reading beam and the scattered beam occurs not only because of the fixed grating but also because of the photorefractive grating formed by these two beams.[21] The diffraction is therefore different from that of simple Bragg scattering. Previously, Bragg diffraction from fixed gratings and photorefractive beam coupling were treated separately.[22,23] In this paper we investigate, theoretically, the diffraction properties of these fixed holograms in photorefractive media, taking into account the effect of the photoinduced index gratings. In the following discussions we assume that the relaxation time of the fixed grating is much longer than the time needed to form a new photorefractive grating and that diffusion is the dominant mechanism for the transportation of charge carriers.

## THEORETICAL FORMULATION

Consider a fixed volume grating inside a photorefractive medium with a well-defined grating wave vector $\mathbf{K}$. A plane wave is incident upon the fixed volume grating along a direction that satisfies the Bragg condition (see Fig. 1). As a result of the Bragg scattering, a plane wave along a new direction is generated. These two plane waves can be written as

$$E_j = A_j \exp[i(\omega t - \mathbf{k}_j \cdot \mathbf{r})], \tag{1}$$

where $j = 1, 2, \omega$ is their common frequency and $\mathbf{k}_j$ is the corresponding wave vector. Conservation of momentum requires that

$$\mathbf{k}_2 = \mathbf{k}_1 \pm \mathbf{K}. \tag{2}$$

It is important to note that the photorefractive grating induced by the interference intensity pattern, formed by the incident beam and the scattered beam, has exactly the same grating wave vector $\mathbf{K}$. The photoinduced grating is either in phase or 180° out of phase with the fixed grating[24] (when we assume a phase grating), depending on the direction of incidence. This leads to a strengthened or weakened grating and nonreciprocal diffraction. The nonreciprocity was observed in thick color-center holograms.[25] A similar effect was also analyzed and observed in Kerr media.[26,27]

The total index grating can be written as

$$n = n_0 + n_p \cos \mathbf{K} \cdot \mathbf{r} - i n_a (1 + \cos \mathbf{K} \cdot \mathbf{r}) + \left[\frac{n_1}{2} \exp(i\phi) \frac{A_1^* A_2}{I_0} \exp(-i\mathbf{K} \cdot \mathbf{r}) + \text{c.c.}\right], \tag{3}$$

where $n_0$ is the index of refraction in the absence of gratings, $n_p$ and $n_a$ represent the amplitudes of the fixed phase and absorption gratings, respectively (here we have assumed that there is no phase shift between the phase and absorption gratings, for simplicity), $n_1$ together with the modulation depth represent the amplitude of the index grating formed by the incident wave and the diffracted

0740-3224/90/122339-08$02.00 

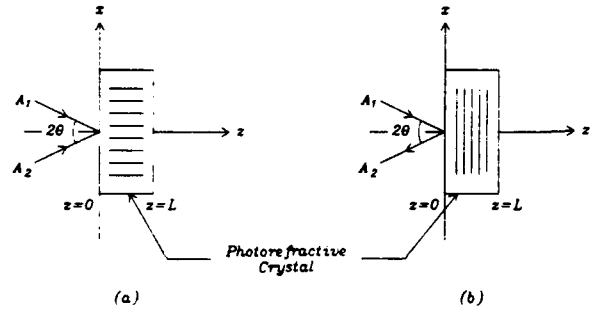


Fig. 1. Schematic drawings of incident and scattered beams in the case of (a) transmission gratings and (b) reflection gratings.

wave by the photorefractive effect, $\phi$ is the spatial phase shift between the index grating and the interference pattern, and $I_0$ is the sum of intensities of the two waves:

$$I_0 = |A_1|^2 + |A_2|^2. \tag{4}$$

All these amplitudes, $n_p$, $n_a$, and $n_1$, are real numbers. In photorefractive crystals for which diffusion is the dominant mechanism for charge transportation, $\phi$ is either $\pi/2$ or $-\pi/2$, depending on the direction of the $c$ axis.

The coupled-mode equations can be derived by substituting Eq. (3) for the index of refraction in the wave equation. For simplicity we assume that the grating wave vector is along the $x$ direction, the angle between the two waves is $2\theta$, and the $z$ component of $\mathbf{k}_j$ is $\beta_j$. For the slow-varying approximation

$$\left|\frac{d^2}{dz^2}A_j\right| \ll \left|\beta_j \frac{d}{dz}A_j\right| \tag{5}$$

and the equality

$$|\mathbf{k}_j|^2 = (\omega^2/c^2)n_0^2, \tag{6}$$

we can write the coupled-mode equations as

$$2i\beta_1 \frac{d}{dz}A_1 = \frac{\omega^2}{c^2}\left[n_0 n_1 e^{-i\phi}\frac{|A_2|^2}{I_0}A_1 + (n_0 n_p - in_0 n_a)A_2 - 2in_0 n_a A_1\right], \tag{7}$$

$$2i\beta_2 \frac{d}{dz}A_2 = \frac{\omega^2}{c^2}\left[n_0 n_1 e^{i\phi}\frac{|A_1|^2}{I_0}A_2 + (n_0 n_p - in_0 n_a)A_1 - 2in_0 n_a A_2\right], \tag{8}$$

where $c$ is the speed of light in vacuum. These two equations will be used in the following analysis for various interaction configurations.

In Eq. (3), fixed gratings are represented by the terms $n_p \cos \mathbf{K}\cdot\mathbf{r}$ and $-in_a(1 + \cos \mathbf{K}\cdot\mathbf{r})$. The term $n_p \times \cos \mathbf{K}\cdot\mathbf{r}$ is a pure phase grating, while the term $-in_a(1 + \cos \mathbf{K}\cdot\mathbf{r})$ represents an absorption grating. The term in square brackets, which is dependent on the product of the two wave amplitudes, represents the photoinduced grating. The coupling of these two waves depends on their directions of propagation. The diffraction properties of fixed gratings in photorefractive media are thus divided according to the categories transmission phase, transmission absorption, reflection phase, and reflection absorption gratings.

**Transmission Phase Gratings ($n_a = 0, \beta_1\beta_2 > 0$)**

For transmission gratings, the $z$ component of the two-wave vectors are of the same sign. Without loss of generality, we take

$$\beta_1 = \beta_2 = (2\pi/\lambda)n_0 \cos\theta. \tag{9}$$

With Eq. (9), the coupled-mode equations can be written in the form

$$\frac{d}{dz}A_1 = -\frac{\Gamma}{2}\frac{|A_2|^2}{I_0}A_1 - i\left(\kappa - i\frac{\alpha}{4}\right)A_2 - \frac{\alpha}{2}A_1, \tag{10}$$

$$\frac{d}{dz}A_2 = \frac{\Gamma^*}{2}\frac{|A_1|^2}{I_0}A_2 - i\left(\kappa - i\frac{\alpha}{4}\right)A_1 - \frac{\alpha}{2}A_2, \tag{11}$$

where $\Gamma$ is the complex photorefractive coupling coefficient for TWM, $(\kappa - i\alpha/4)$ is the complex Bragg coupling coefficient, and $\alpha$ is the absorption constant:

$$\Gamma = i\frac{2\pi n_1}{\lambda\cos\theta}e^{-i\phi}, \tag{12}$$

$$\kappa = \frac{\pi n_p}{\lambda\cos\theta}, \tag{13}$$

and

$$\alpha = \frac{4\pi n_a}{\lambda\cos\theta}. \tag{14}$$

The coupled equations (10) and (11) can be written in terms of intensities and phases of the two waves. We write

$$A_1 = \sqrt{I_1}\exp(-i\psi_1), \tag{15}$$

$$A_2 = \sqrt{I_2}\exp(-i\psi_2), \tag{16}$$

and assume that the medium is lossless, i.e., $n_a = \alpha = 0$. Equations (10) and (11) can be separated into

$$\frac{d}{dz}I_1 = -\gamma\frac{I_1 I_2}{I_1 + I_2} - 2\kappa \sin\Delta\psi\sqrt{I_1 I_2}, \tag{17}$$

$$\frac{d}{dz}I_2 = \gamma\frac{I_1 I_2}{I_1 + I_2} + 2\kappa \sin\Delta\psi\sqrt{I_1 I_2} \tag{18}$$

and

$$\frac{d}{dz}\psi_1 = \beta\frac{I_2}{I_1 + I_2} + \kappa\cos\Delta\psi\sqrt{I_2/I_1}, \tag{19}$$

$$\frac{d}{dz}\psi_2 = \beta\frac{I_1}{I_1 + I_2} + \kappa\cos\Delta\psi\sqrt{I_1/I_2}, \tag{20}$$

where

$$\Delta\psi = \psi_2 - \psi_1 \tag{21}$$

and

$$\gamma = \frac{2\pi n_1}{\lambda\cos\theta}\sin\phi, \tag{22}$$

$$\beta = \frac{\pi n_1}{\lambda \cos\theta} \cos\phi. \tag{23}$$

Note that $\gamma$ and $\beta$ are related to $\Gamma$ by $\Gamma = \gamma + i2\beta$. In photorefractive crystals that operate by pure diffusion, $\beta = 0$. Since wave $A_2$ is generated by Bragg scattering of wave $A_1$ from the fixed grating, the phase of $A_2$ is automatically locked to that of $A_1$. Thus the possible solutions to Eqs. (19) and (20) are

$$\Delta\psi = \pi/2 \tag{24}$$

and

$$\Delta\psi = -\pi/2. \tag{25}$$

With the boundary condition $A_2(0) = 0$, we find that $\Delta\psi = \pi/2$ is a proper solution by examining the phase of $A_2$ in Eq. (11). Substituting $\Delta\psi = \pi/2$ into Eqs. (17) and (18), we obtain

$$\frac{d}{dz} I_1 = -\gamma \frac{I_1 I_2}{I_1 + I_2} - 2\kappa\sqrt{I_1 I_2}, \tag{26}$$

$$\frac{d}{dz} I_2 = \gamma \frac{I_1 I_2}{I_1 + I_2} + 2\kappa\sqrt{I_1 I_2}. \tag{27}$$

Since $I_1 + I_2$ is a constant, Eqs. (26) and (27) are mathematically identical to those for nonlinear optical Bragg scattering and can be solved exactly.[26] The solutions, subject to the boundary condition $A_2(0) = 0$, are written

$$I_1(z) = I_0 \cos^2 u, \tag{28}$$

$$I_2(z) = I_0 \sin^2 u, \tag{29}$$

where $I_0$ is the incident intensity and $u$ is given by[26]

$$\tan u = \frac{\tan[\kappa z(1 - b^2)^{1/2}]}{(1 - b^2)^{1/2} - b \tan[\kappa z(1 - b^2)^{1/2}]}, \tag{30}$$

with

$$b = \gamma/(4\kappa). \tag{31}$$

The intensity of the diffracted wave as a function of $z$ was investigated in a previous study[26] for various values of $b$. The parameter $b$ is a measure of the strength of the photorefractive grating relative to the fixed grating. It is important to note that $b$ in this paper is independent of the intensity, whereas $b$ is proportional to $I_0$ in Kerr media.

The diffraction efficiency is a nonlinear function of $b$. For a crystal with interaction length $L$, the diffraction efficiency is

$$\eta = \frac{I_2(L)}{I_0} = \sin^2 u(z = L). \tag{32}$$

When $b \gg 1$ and $\kappa L b \gg 1$, the asymptotic form of $\eta$ can be written as

$$\eta = 1 - \frac{1}{4b^2}[1 - 4b^2 \exp(-2\kappa L b)]^2$$

$$= 1 - \frac{1}{4b^2}[1 - 8b^2 \exp(-2\kappa L b)]. \tag{33}$$

The asymptotic form for $b \to -\infty$ can be written as

$$\eta = \frac{1}{4b^2}\left[1 + \frac{1}{4b^2} - 2\exp(-2\kappa L|b|)\right]. \tag{34}$$

Here we note that the expressions are slightly different from those that appeared in Eqs. (18) and (19) of Ref. 26. Figure 2 depicts the diffraction efficiency as a function of $b$ for different values of $\kappa L$. For $b > 0$ the photorefractive grating is in phase with the fixed grating. When $\kappa L$ is small the presence of the photoinduced grating strengthens the grating, and the diffraction efficiency increases as a function of $b$. When $\kappa L = \pi/2$ the diffraction efficiency is 1 at $b = 0$ (no photoinduced grating). The diffraction efficiency decreases as $b$ increases from $b = 0$, reaches a minimum at $b \approx 0.89$, and then increases to 1 when $b$ is extremely large. When $\kappa L > \pi$, the diffraction efficiency will oscillate between 0 and 100% within $|b| < 1$. This oscillatory behavior can also be seen in Fig. 2 of Ref. 26, since $I_1$ and $I_2$ are periodic functions of $z$ for $-1 < b < 1$. The sign of the parameter $b$ depends on the direction of incidence. Thus if $b$ is positive for an incident angle of $\theta$, it will be negative when the beam is incident at an angle of $-\theta$. The different values of $\eta$ for $+b$ and $-b$ reflect nonreciprocal diffractions caused by TWM. In other words, the diffraction efficiency of fixed gratings in photorefractive media depends on the direction of incidence at Bragg angles.

Figure 3 shows the grating amplitude as a function of $z$. When $b > 0$, e.g., $b = 1$, the photoinduced grating is in phase with the fixed grating; therefore the grating is strengthened. When $b < 0$, e.g., $b = -1$, the photoinduced grating is out of phase with the fixed grating; therefore the grating is weakened. From the curve for $b = 10$, we notice that at the beginning the photoinduced grating is in phase with the fixed grating; therefore the grating is strengthened. At the point in space where all the incident power is converted into a diffracted beam, i.e., $I_2 = I_0$ and $I_1 = 0$, the photoinduced grating disappears. After this point the photoinduced grating is out of phase with the fixed grating. Physically, this is equivalent to the case in which the beam is incident from the other input port (i.e., at $-\theta$). When the photoinduced grating cancels the fixed grating, there is no more diffraction, and thus the grating amplitude stays 0. The curve for $b = -10$ is the same as the curve for $b = 10$ after the point $\eta = 100\%$.

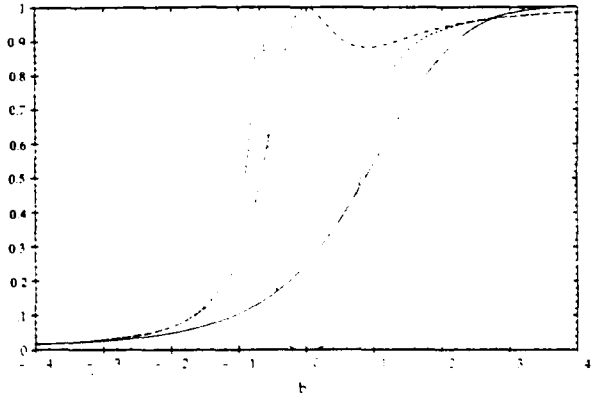


Fig. 2. Diffraction efficiency as a function of $b$ for transmission phase gratings with different values of $\kappa L$. Solid curve, $\kappa L = \pi/6$; dotted-dashed curve, $\kappa L = \pi/2$; dashed curve, $\kappa L = \pi$.

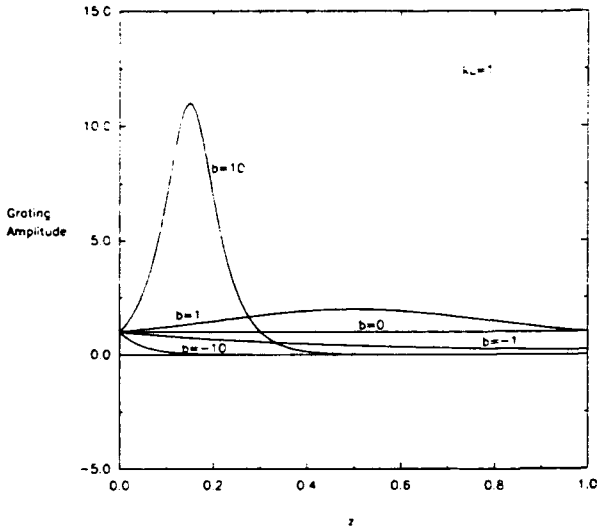


Fig. 3. Grating amplitudes as functions of $z$ for $b$ equal to 10, 1, 0, −1, and −10 in the case of transmission phase gratings.

Photorefractive media and Kerr media[26] can be distinguished by the different expressions for $b$, i.e., Eq. (31) in this paper and Eq. (16) in Ref. 26. In Kerr media $b$ is a function of intensity; therefore the diffraction efficiency depends on the incident intensity nonlinearly. In photorefractive media there is no such nonlinearity.

**Transmission Absorption Gratings ($n_p = 0$, $\beta_1\beta_2 > 0$)**
Nonreciprocal diffractions also occur in the case of absorption gratings. When $\alpha \neq 0$, the coupled-mode equations (10) and (11) cannot be easily solved analytically; however, nonreciprocal behavior can still be seen in the numerical solutions. We have solved the coupled-mode equations (10) and (11) by using the fifth-order Runge–Kutta method with adaptive step size. In the general case, the parameter $b$ is defined as

$$b = \frac{\gamma}{[(4\kappa)^2 + \alpha^2]^{1/2}}. \tag{35}$$

Figure 4 shows the intensities of the incident and diffracted beams as functions of $z$ for various values of $b$, where the fixed grating is a pure absorption grating ($\kappa = 0$). Similar to the case of phase gratings, diffraction from one input port ($b > 0$) is enhanced and that from the other input port ($b < 0$) is suppressed, as compared with the case when TWM disappears ($b = 0$). The diffraction efficiency as a function of $b$ is plotted in Fig. 5 for various values of $\alpha L$. We note that the nonreciprocity in absorption gratings is quite strong.

For fixed gratings with both phase and absorption variations, the diffraction property is a combination of that of the pure phase and pure absorption gratings. As an example, we give the numerical solutions for $\kappa = \cos(\pi/30)$ and $\alpha = 4\sin(\pi/30)$. Figure 6 shows the intensities of the incident and diffracted beams as functions of $z$ for various values of $b$, and Fig. 7 shows the diffraction efficiency as a function of $b$ for various values of $L$. In the numerical calculations, the units of $\kappa$, $\alpha$, and $z$ are chosen arbitrarily, since $\kappa z$ and $\alpha z$ are dimensionless. Again, the diffraction is nonreciprocal.

**Reflection Phase Gratings ($n_a = 0$, $\beta_1\beta_2 < 0$)**
For reflection gratings, the $z$ components of the two wave vectors are of opposite sign. They are given by

$$\beta_1 = -\beta_2 = (2\pi/\lambda)n_0 \cos\theta. \tag{36}$$

With Eqs. (7) and (8), the coupled-mode equations can be written in the form

$$\frac{d}{dz}A_1 = -\frac{\Gamma}{2}\frac{|A_2|^2}{I_0}A_1 - i\left(\kappa - i\frac{\alpha}{4}\right)A_2 - \frac{\alpha}{2}A_1, \tag{37}$$

$$\frac{d}{dz}A_2 = -\frac{\Gamma^*}{2}\frac{|A_1|^2}{I_0}A_2 + i\left(\kappa - i\frac{\alpha}{4}\right)A_1 + \frac{\alpha}{2}A_2. \tag{38}$$

Following similar steps as in transmission phase gratings, the coupled equations for the intensities of the two waves can be found as

$$\frac{d}{dz}I_1 = -\gamma\frac{I_1 I_2}{I_1 + I_2} - 2\kappa\sqrt{I_1 I_2}, \tag{39}$$

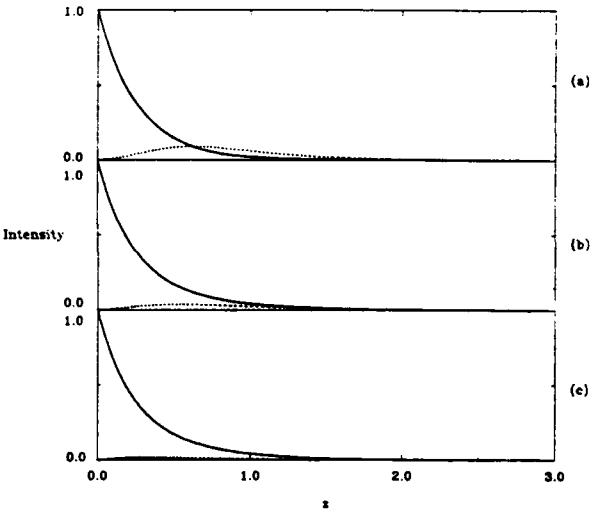


Fig. 4. Intensities of the incident and diffracted beams as functions of $(\alpha/4)z$ for transmission absorption gratings ($\kappa = 0$) with various values of $b$. Solid curves, $I_1$; dotted curves, $I_2$. (a) $b = 1$, (b) $b = 0$, (c) $b = -1$.

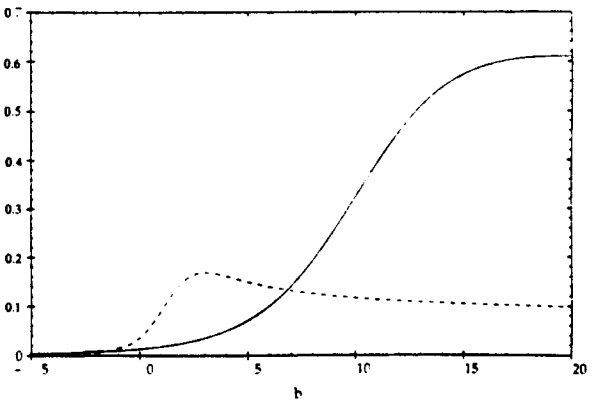


Fig. 5. Diffraction efficiency as a function of $b$ for transmission absorption gratings ($\kappa = 0$) with various values of $\alpha L$. Solid curve, $\alpha L = 0.2\pi$; dotted curve, $\alpha L = 0.4\pi$; dashed curve, $\alpha L = 0.8\pi$.

Rockwell International
Science Center

Vol. 7, No. 12/December 1990/J. Opt. Soc. Am. B 2343

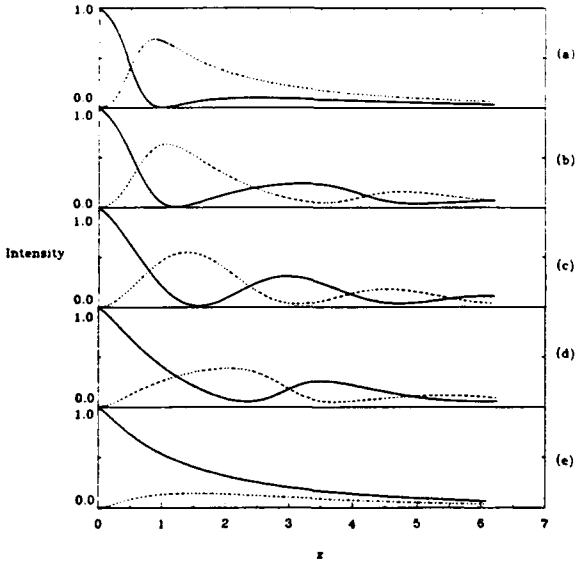


Fig. 6. Intensities of the incident and diffracted beams as functions of $z$ for fixed gratings with both phase and absorption variations [$\kappa = \cos(\pi/30) = 0.9945$, $\alpha = 4\sin(\pi/30) = 0.4181$] and various values of $b$. Solid curves, $I_1$; dotted curves, $I_2$. (a) $b = 1$, (b) $b = 0.5$, (c) $b = 0$, (d) $b = -0.5$, (e) $b = -1$. The units of $\kappa$, $\alpha$, and $z$ are chosen arbitrarily, since $\kappa z$ and $\alpha z$ are dimensionless.

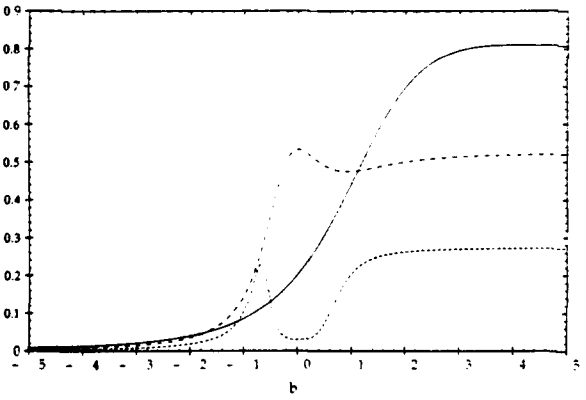


Fig. 7. Diffraction efficiency as a function of $b$ for fixed gratings with both phase and absorption variations [$\kappa = \cos(\pi/30) = 0.9945$, $\alpha = 4\sin(\pi/30) = 0.4181$] and various values of $L$. Solid curve, $L = \pi/6$; dotted–dashed curve, $L = \pi/2$; dashed curve, $L = \pi$. The units of $\kappa$, $\alpha$, and $L$ are chosen arbitrarily, since $\kappa z$ and $\alpha z$ are dimensionless.

$$\frac{\mathrm{d}}{\mathrm{d}z} I_2 = -\gamma \frac{I_1 I_2}{I_1 + I_2} - 2\kappa\sqrt{I_1 I_2}. \tag{40}$$

In deriving Eqs. (39) and (40), we used $\phi = \pi/2$ and $\Delta\psi = \pi/2$, which is one of the two solutions ($\Delta\psi = \pi/2$ or $\Delta\psi = -\pi/2$) for the equations of phase change.

Equations (39) and (40) can be solved analytically. The solutions with the boundary condition $I_2 = 0$ at $z = L$ are given by

$$I_1(z) = C\cosh^2 u, \tag{41}$$

$$I_2(z) = C\sinh^2 u, \tag{42}$$

where $C$ is the transmitted intensity at $z = L$, and $u$ is related to $z$ by

$$\frac{e^{2u}}{[\cosh(2u) + b\sinh(2u)]^b} = \exp[-2\kappa(1 - b^2)(z - L)], \tag{43}$$

where $b$ was given by Eq. (31). Equation (43) must be handled with care when $|b| = 1$. The solution for $u$ as a function of $z$ when $b = 1$ can be written

$$u = 2\kappa(L - z) - \tfrac{1}{4} + \tfrac{1}{4}e^{-4u}, \tag{44}$$

whereas, when $b = -1$,

$$u = 2\kappa(L - z) + \tfrac{1}{4} - \tfrac{1}{4}e^{4u}. \tag{45}$$

Figure 8 shows the intensities as functions of $z$ for $b = 1$, $b = 0$, and $b = -1$. We note that backward coupling of energy is enhanced for the case when $b > 0$.

The diffraction efficiency is given by the expression

$$\eta = \frac{I_2(0)}{I_1(0)} = \tanh^2 u(z = 0). \tag{46}$$

Given a $\kappa L, u(0)$ can be solved from Eq. (43). For example, when $b = 1$, according to Eq. (44), $u(0)$ is given by

$$u = 2\kappa L - \tfrac{1}{4} + \tfrac{1}{4}e^{-4u}. \tag{47}$$

We note that when $\kappa L > \frac{1}{8}$ $u(0)$ is positive, and $e^{-4u}$ becomes extremely small when $2\kappa L - \frac{1}{4} > \frac{1}{4}$. Therefore, when $\kappa L > \frac{1}{4}, u(0) \approx 2\kappa L - \frac{1}{4}$ and $\eta \approx \tanh^2(2\kappa L - \frac{1}{4})$. The diffraction efficiency approaches 100% exponentially as $2\kappa L - \frac{1}{4} \gg 1$; i.e., $\kappa L \gg \frac{5}{8}$. Figure 9(a) shows the diffraction efficiency as a function of $\kappa L$ for $b = 0$, $b = \pm 1$, and also for $b = \pm 2$. When $b = 0$, $\eta = \tanh^2 \kappa L$. When $b \gg 1$ and $\kappa L b \gg 1$, the asymptotic expression for the diffraction efficiency is

$$\eta = 1 - 2b\exp(-2\kappa L b). \tag{48}$$

We note that the diffraction efficiency approaches 100%

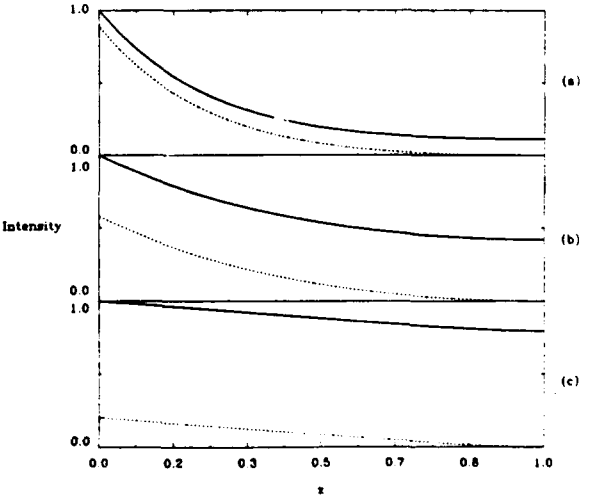


Fig. 8. Intensities of incident and diffracted beams as functions of $z$ for reflection phase gratings ($\kappa = 1, \alpha = 0$). (a) $b = 1$, (b) $b = 0$, (c) $b = -1$.

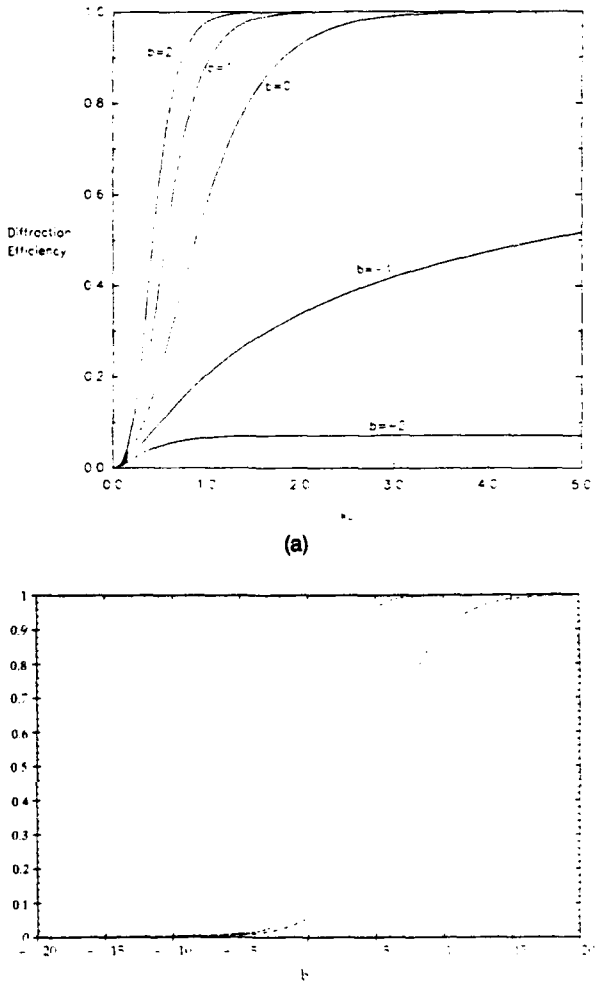


Fig. 9. (a) Diffraction efficiency for reflection phase gratings as a function of $\kappa L$ for $b$ equal to 0, $\pm 1$, and $\pm 2$. (b) Diffraction efficiency as a function of $b$ for reflection phase gratings with various values of $\kappa L$. Dotted curve, $\kappa L = \frac{1}{8}$; dotted-dashed curve, $\kappa L = \frac{1}{4}$; dashed curve, $\kappa L = \frac{1}{2}$.

exponentially as $b$ increases. When $b \to -\infty$, the asymptotic expression for the diffraction efficiency is

$$\eta = \frac{1}{4b^2}[1 - 2\exp(-2\kappa L|b|)]. \tag{49}$$

As $2\kappa L|b| \gg 1$, $\eta = \frac{1}{4}b^2$ for all $\kappa L$. Figure 9(b) shows the diffraction efficiency as a function of $b$ for various values of $\kappa L$. Comparison of Figs. 9 and 2 reveals that the diffraction is nonreciprocal for both transmission and reflection gratings. The oscillatory behavior in Fig. 2 does not occur in Fig. 9 because the intensities in Eqs. (41) and (42) are not periodic functions of $z$.

Figure 10 shows the grating amplitude as a function of $z$. Similar to the case of codirectional diffractions, the photoinduced grating is in phase with the fixed grating when $b > 0$ and out of phase when $b < 0$, and therefore strengthens or weakens the fixed grating, respectively. We note from Fig. 10 that the grating amplitude for $b = 1$ and that for $b = -1$ are not symmetric with respect to the value that corresponds to $b = 0$. This is because the photoinduced grating is proportional to $|A_1 A_2|/(I_1 + I_2)$, which depends on the sign of $b$ as well as its absolute value, as shown in Fig. 8. This asymmetric behavior also occurs in the transmission phase gratings, as shown in Fig. 3.

**Reflection Absorption Gratings ($n_p = 0, \beta_1\beta_2 < 0$)**

For absorption gratings, closed-form solutions of the coupled equations are not easily available. The diffraction properties of these gratings can be studied by using numerical techniques. We solved the coupled-mode equations (37) and (38) numerically with a nonzero absorption constant. Since the photoinduced grating depends only on the modulation depth, Eqs. (37) and (38) are scaling invariant. In other words, if $A_1$ and $A_2$ are solutions to Eqs. (37) and (38), $cA_1$ and $cA_2$ are also solutions to these

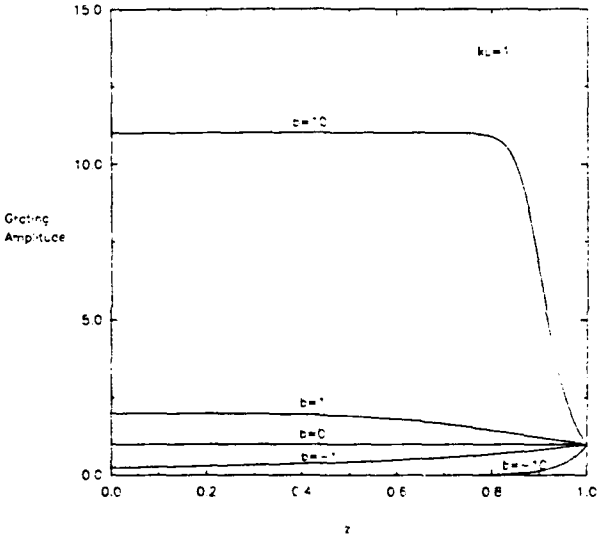


Fig. 10. Grating amplitudes as functions of $z$ for $b$ equal to 10, 1, 0, $-1$, and $-10$, in the case of reflection phase gratings.

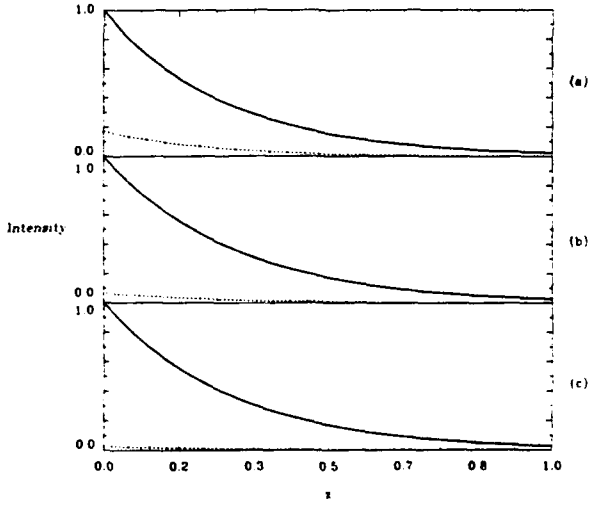


Fig. 11. Intensities of incident and diffracted beams as functions of $z$ for reflection absorption gratings ($\kappa = 0, \alpha = 4$). (a) $b = 1$, (b) $b = 0$, (c) $b = -1$.

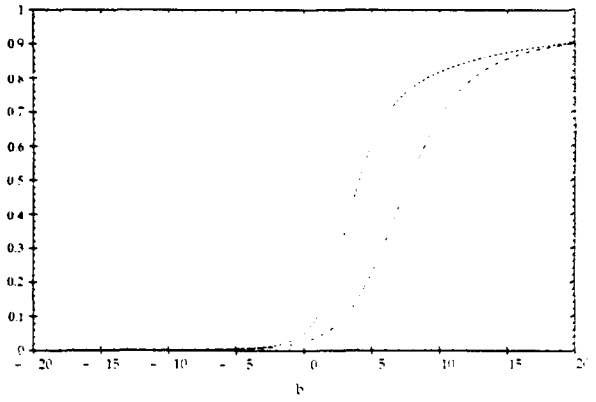


Fig. 12. Diffraction efficiency as a function of $b$ for reflection absorption gratings ($\kappa = 0$) with various values of $\alpha L$. Dotted curve, $\alpha L = \frac{2}{3}$; dotted-dashed curve, $\alpha L = 1$; dashed curve, $\alpha L = 2$.

two equations, where $c$ is a complex constant. Therefore we can reduce the two-point boundary-value problem to the one-point one. Numerical integration starts from $z = L$, where $A_2 = 0$ and $A_1$ is set to be 1. As we go from $z = L$ to $z = 0$, complex $A_1(z)$ and $A_2(z)$ are obtained. Then the intensities $I_1(z)$ and $I_2(z)$ are normalized by taking the normalized $I_1(0)$ to be 1.

For the case of a pure absorption grating ($\kappa = 0$), Fig. 11 shows the intensities as functions of $z$. We note that $I_2$ grows from 0 as the diffracted beam propagates from $z = L$ to $z = 0$. Because of absorption, the growth is slower than that for phase gratings. The incident beam $I_1$ decays as it propagates from $z = 0$ to $z = L$ because of both energy exchange with $I_2$ and absorption. Figure 12 shows the diffraction efficiency as a function of $b$ for various values of $\alpha L$. The diffraction property is similar to that in the absence of absorption (Fig. 9), except that because of the loss in the medium the diffraction efficiency cannot reach 100%. The nonreciprocity, in the case of absorption gratings, can be explained by the phase shift between the photoinduced phase grating and the interference pattern. The fixed absorption grating provides a source for generating the second beam when the incident beam satisfies the Bragg condition.

## CONCLUSION

In conclusion, we analyzed the diffraction properties of fixed gratings in photorefractive media with the consideration of TWM between the incident and the diffracted waves. Both codirectional and contradirectional diffractions were solved, including the presence of both phase and absorption gratings. The results indicate that fixed gratings in photorefractive media exhibit strong optical nonreciprocity, which cannot be explained without considering TWM. Since the photorefractive grating depends on the modulation depth instead of the intensities, there is no optical nonlinearity like that which appeared in the Kerr media.[26] Our analysis can be applied not only to fixed photorefractive gratings but also to those that may be fabricated artificially.

In this paper we considered only diffraction properties of fixed gratings with exact Bragg match, and the photorefractive media were assumed to be in the regime of pure diffusion. Bragg mismatch ($\Delta k \neq 0$) as well as arbitrary phase shift ($\phi \neq \pi/2$) are important issues that will affect the diffraction properties of fixed gratings in photorefractive media.

## ACKNOWLEDGMENTS

We thank R. Saxena for technical discussions. This work is supported, in part, by U.S. Office of Naval Research contract N00014-88-C-0230.

## REFERENCES AND NOTES

1. See, for example, G. C. Valley and P. Yeh, eds., Feature on Photorefractive Materials, Effects, and Devices, J. Opt. Soc. Am. B **5**, 1681–1821 (1988). Many papers on photorefracts are included.
2. See, for example, P. Yeh, "Two-wave mixing in nonlinear media," IEEE J. Quantum Electron. **25**, 484–519 (1989).
3. See, for example, P. Yeh, A. E. Chiou, J. Hong, P. Beckwith, T. Chang, and M. Khoshnevisan, "Photorefractive nonlinear optics and optical computing," Opt. Eng. **26**, 328–343 (1989).
4. P. J. van Heerden, "Theory of optical information storage in solids," Appl. Opt. **2**, 393–400 (1963).
5. A. E. T. Chiou and P. Yeh, "Parallel image subtraction using a phase-conjugate Michelson interferometer," Opt. Lett. **11**, 306–308 (1986).
6. T. Y. Chang, P. H. Beckwith, and P. Yeh, "Real-time optical image subtraction using dynamic holographic interference in photorefractive media," Opt. Lett. **13**, 586–588 (1988).
7. P. Yeh, A. E. T. Chiou, and J. Hong, "Optical interconnections using photorefractive dynamic holograms," Appl. Opt. **27**, 2093–2096 (1988).
8. A. Chiou and P. Yeh, "Energy efficiency of optical interconnections using photorefractive holograms," Appl. Opt. **29**, 1111–1117 (1990).
9. H. Lee, X. G. Gu, and D. Psaltis, "Volume holographic interconnections with maximal capacity and minimal cross talk," J. Appl. Phys. **65**, 2191–2194 (1989).
10. D. Psaltis, X. G. Gu, and D. Brady, "Holographic implementations of neural networks," in *An Introduction to Neural and Electronic Networks*, S. F. Zornetzer, J. L. Davis, and C. Lau, eds. (Academic, New York, 1990), pp. 339–348.
11. D. Psaltis, D. Brady, X. G. Gu, and S. Lin, "Holography in artificial neural networks," Nature (London) **343**, 325–330 (1990).
12. D. L. Staebler and J. J. Amodei, "Thermally fixed holograms in $LiNbO_3$," Ferroelectrics **3**, 107–113 (1972).
13. F. Micheron and G. Bismuth, "Electrical control of fixation and erasure of holographic patterns in ferroelectric materials," Appl. Phys. Lett. **20**, 79–81 (1972).
14. F. Micheron, C. Mayeux, and J. C. Trotier, "Electrical control in photoferroelectric materials for optical storage," Appl. Opt. **13**, 784–787 (1974).
15. D. von der Linde, A. M. Glass, and K. F. Rodgers, "High-sensitivity optical recording in KTN by two-photon absorption," Appl. Phys. Lett. **26**, 22–24 (1975).
16. A. Delboulbe, C. Fromont, J. P. Herriau, S. Mallick, and J. P. Huignard, "Quasi-nondestructive readout of holographically stored information in photorefractive $Bi_{12}SiO_{20}$ crystals," Appl. Phys. Lett. **55**, 713–715 (1989).
17. J. Hong, S. Campbell, and P. Yeh, "Optical pattern classifier with perceptron learning," Appl. Opt. **29**, 3019–3025 (1990).
18. J. Hong, S. Campbell, and P. Yeh, "Optical learning machine for pattern classification," in *Digest of Optical Society of America Annual Meeting* (Optical Society of America, Washington, D.C., 1989), paper WJ3.
19. D. Psaltis, D. Brady, and K. Wagner, "Adaptive optical networks using photorefractive crystals," Appl. Opt. **27**, 1752–1759 (1988).
20. E. G. Paek, J. Wullert, and J. S. Patel, "Holographic implementation of a learning-machine based on a multicategory perceptron algorithm," Opt. Lett. **14**, 1303–1305 (1989).

21. D. L. Staebler and J. J. Amodei, Coupled-wave analysis of holographic storage in $LiNbO_3$," J. Appl. Phys. **43**, 1042–1049 (1972).
22. H. Kogelnik, "Coupled wave theory for thick hologram gratings," Bell Syst. Tech. J. **48**, 2909–2945 (1969).
23. R. Saxena, F. Vachss, I. McMichael, and P. Yeh, "Diffraction properties of multiple-beam photorefractive gratings," J. Opt. Soc. Am. B **7**, 1210–1215 (1990).
24. T. Chang and P. Yeh, "Dark rings from photorefractive conical diffraction in a $BaTiO_3$ crystal," Proc. Soc. Photo-Opt. Instrum. Eng. **739**, 109–116 (1987).
25. N. A. Vainos, S. L. Clapham, and R. W. Eason, "Multiplexed permanent and real-time holographic recording in photorefractive BSO," Appl. Opt. **28**, 4381–4385 (1989).
26. P. Yeh and M. Khoshnevisan, "Nonlinear-optical Bragg scattering in Kerr media," J. Opt. Soc. Am. B **4**, 1954–1957 (1987). We believe that there may be a slight error in this reference (typesetting error in the asymptotic form of the diffraction efficiency for $b \gg 1$).
27. F. Vachss, I. McMichael, M. Khoshnevisan, and P. Yeh, "Enhanced acousto-optic diffraction in electrostrictive media," J. Opt. Soc. Am. B **7**, 859–867 (1990).

## Appendix 4.6

## DIFFRACTION EFFICIENCY OF STRONG VOLUME HOLOGRAMS

a reprint from Optics Letters

Rockwell International
Science Center

# Diffraction efficiency of strong volume holograms

**John H. Hong and Pochi Yeh**

*Rockwell International Science Center, 1049 Camino dos Rios, A25A, Thousand Oaks, California 91360*

**Demetri Psaltis and David Brady**

*Department of Electrical Engineering, California Institute of Technology, 116-81, Pasadena, California 91125*

Received September 22, 1989; accepted January 2, 1990

We investigate the diffraction efficiency of strong volume holograms in which the coupling parameter is several times that needed for maximum diffraction efficiency. We discuss the implications of our findings on photorefractive implementations of various neural network systems.

The study of volume gratings has led to useful applications in many areas of optics, including integrated optics, acousto-optics, and holography. In most situations the coupled-mode analysis of volume holograms established by Kogelnik[1] accurately describes the diffraction behavior of a thick hologram and predicts a diffraction efficiency that is a periodic function of the index perturbation amplitude–thickness product. The diffraction efficiency $\eta$ from a volume index grating with the direction of the readout beam tuned for the Bragg condition is given by

$$\eta = \exp(-\alpha d/\cos\theta)\sin^2(\pi\Delta n d/\lambda\cos\theta), \qquad (1)$$

where $\alpha$ is the absorption coefficient, $d$ is the thickness of the hologram, $\Delta n$ is the amplitude of the index perturbation, and $\theta$ is the angle of incidence of the readout beam with respect to the normal to the surface of the hologram (we assume an unslanted grating); $\theta$ and $\lambda$ are assumed to be measured inside the medium. Typically the amplitude of $\Delta nd$ realized in most holographic materials is such that only the increasing part of the first period of $\eta$ is observed. As the grating amplitude and/or the thickness of the grating is increased beyond this regime, further coupling between the two waves results in a reversal of the energy-transfer direction to yield a drop in the diffraction efficiency as predicted by Eq. (1).

We have been able to observe this effect in a photorefractive barium titanate ($BaTiO_3$) crystal. The use of photorefractive crystals for such a purpose is particularly appropriate since the dynamic nature of photorefraction allows us to record easily and accurately the temporal evolution of $\Delta n$, the index change. For example, by monitoring $\eta$ during the holographic recording process, we are able to observe the functional dependence of $\eta$ on $\Delta nd$ from $\Delta nd = 0$ to saturation. Although $\eta$ cannot exceed unity, a large saturation value of $\Delta nd$ is desirable because it corresponds to a large dynamic range for hologram recording, which in turn implies that a large number of holograms may be recorded. By monitoring the time dependence of $\eta$, we are able to estimate the saturation value of $\Delta nd$ in our $BaTiO_3$ sample and calculate the storage capacity of the crystal for dense holographic interconnections. Such interconnections are useful in parallel information-processing applications such as artificial neural networks.[2,3]

In a photorefractive crystal the steady-state value of $\Delta n$ is proportional to the modulation depth of the intensity interference pattern responsible for writing the hologram. Hence, by manipulating the intensities of the writing beams, one can monitor the functional relationship between $\Delta n$ and the diffraction efficiency. For a fixed writing-beam modulation depth, the entire range of index perturbation amplitudes from zero to the maximum attainable value can be scanned by performing a transient experiment in which one of the two writing beams is abruptly turned on and then turned off after permitting the grating to saturate. One beam is left on to ensure a zero-grating initial condition and also to provide an erasure mechanism after the other beam is turned off. Since the diffraction efficiency is a periodic function of $\Delta n$, for a sufficiently large saturation value of $\Delta n$ the diffracted intensity will oscillate as a function of time during both formation and decay of the grating. The theoretical predictions of the temporal behavior of the index grating amplitude and its associated diffraction efficiency are plotted in Figs. 1(a) and 1(b), respectively. We see that the larger the saturation value of $\Delta n$, the more oscillations are present in $\eta$. The plots are shown for two values of the strength parameter given by $\phi = \pi\Delta nd/\lambda\cos\theta$. The saturation value of $\Delta n$ can be easily controlled by adjustment of the writing-beam intensities.

We have written holograms in single-crystal $BaTiO_3$ using an argon-ion laser ($\lambda = 514.5$ nm) with a read beam derived from a He–Ne laser ($\lambda = 633$ nm). The experimental apparatus, shown in Fig. 2, is described below. The writing beam was polarized in the ordinary direction with respect to the crystal in order to preclude beam-coupling effects so that a uniform grating could be written in the crystal. The width of the writing beam was approximately 1 mm, and the power levels that were used are indicated in Fig. 3. The readout beam (≈1-mm width, power level ~95 $\mu$W) is a He–Ne beam at $\lambda = 633$ nm that is polarized in the extraordinary direction and aligned at the Bragg angle

0146-9592/90/060344-03$2.00/0 

Rockwell International
Science Center
March 15, 1990 / Vol. 15, No. 6 / OPTICS LETTERS 345

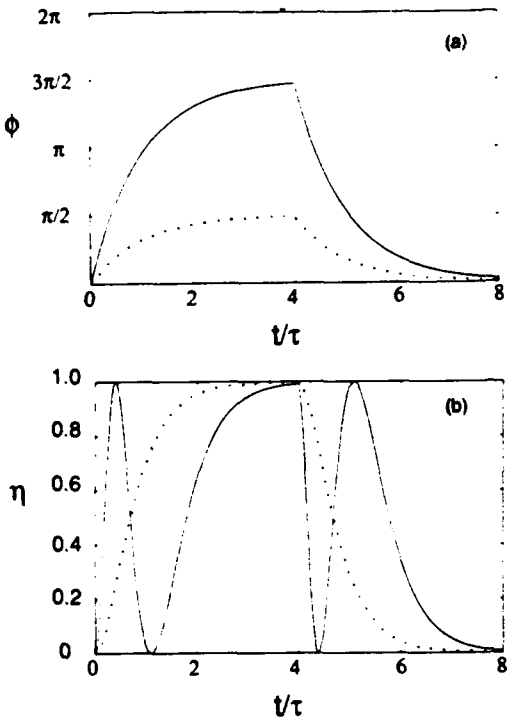


Fig. 1. Theoretical predictions of the temporal behavior of the strength parameter and diffraction efficiency during hologram development and erasure. Plots are given for two steady-state value of $\phi$: $\phi_{max} = \pi/2$ (dotted curve) and $\phi_{max} = 3\pi/2$ (solid curve). The time is shown in units of the photorefractive time constant. (a) Growth and decay of the strength parameter $\phi$. (b) Normalized diffraction efficiency during growth and decay of the grating [corresponding to depth parameter plots of (a)].

of the hologram. This combination of ordinary–extraordinary polarizations for the write–read beams gives maximum diffraction efficiency with minimum coupling. The relative intensities of the two writing beams can be adjusted with the variable attenuator realized by a wave plate–polarizing beam splitter combination. The 4-mm-thick $BaTiO_3$ crystal is a special-cut variety whose orientation was selected to access the large $r_{42}$ coefficient [the $c$ axis is oriented 30° from the cut face; see Fig. 2(b)].[4] The special crystal cut effectively gives a large dynamic range for the index variation $\Delta n$ that we can write.

The two writing beams were first turned on, and the readout-beam direction was adjusted for maximum diffraction efficiency. The intensity of one of the writing beams (#1) could be varied with a wave plate–polarizer combination. After shutting off beam #1 and waiting until the hologram was completely erased by the other beam, we abruptly turned beam #1 on again. After a steady state was achieved in the diffracted intensity, beam #1 was again shut off. The temporal evolution of the diffracted power exhibited oscillatory behavior, indicating that the $\Delta n$ was varied through several peaks of the diffraction efficiency curve during the development and erasure of the hologram. The experiment was repeated for several different write-beam intensity ratios. The diffraction efficiency record for a near-unity beam intensity ratio exhibited the largest number (3) of oscillations [Fig. 3(c) corresponds to the near-unity beam intensity ratio hologram, and Fig. 3(a) corresponds to the smallest beam ratio hologram; note that the latter exhibits no oscillations during either formation or decay]. The oscillatory behavior compares favorably with the theoretical plots of Fig. 1, except that the experimental oscillations do not dip down to zero and the maxima have different values. This may be due to two-wave mixing between the reading beam and its diffracted component, the small but finite two-wave mixing between the two writing beams, and/or imperfections in the overlap between the hologram and the read beam. The maximum diffraction efficiency in each case was ~25%, which differs from the ideal unity value owing to absorption, reflection losses, scattering, and position errors in setting the readout beam so that it maximally overlaps with the grating.

Volume holograms have long attracted interest for information-storage applications owing to their potentially large storage capacity and more recently as an interconnection device for neural networks. In such applications, holograms are superimposed within the same crystal volume where, for example, the reference beam can be angularly multiplexed to distinguish between the various holograms. The corresponding index perturbation of such a superposition can be expressed by

$$\Delta n(\mathbf{r}) \propto \sum_{m=1}^{M} f_m(\mathbf{r}), \tag{2}$$

where $f_m(\mathbf{r})$ is the contribution of the $m$th hologram and $\mathbf{r}$ is the spatial coordinate within the volume. It is important to gauge the maximum number of holograms, $M$, that can be recorded in a given crystal. Although other constraints such as that due to geome-

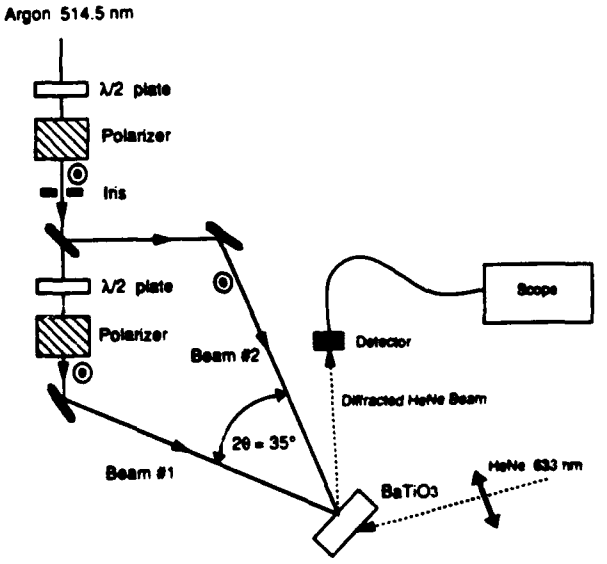


Fig. 2. Apparatus for writing and probing deep holograms.

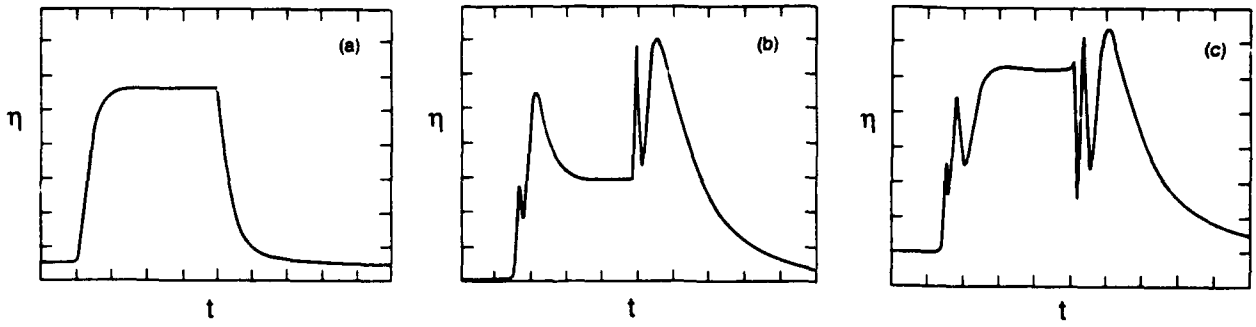


Fig. 3. Diffraction efficiencies recorded during writing and erasure of gratings. The peak diffraction efficiency in each case is approximately 25 ± 3% (diffraction efficiency is defined as the ratio of the input readout power to the diffracted power); the horizontal scale is 793.5 msec/division. (a) $P_1 = 24$ mW, $P_2 = 2.1$ mW; (b) $P_1 = 27.8$ mW, $P_2 = 10.8$ mW; (c) $P_1 = 20.7$ mW, $P_2 = 20.8$ mW.

try exist,[2,3] we are interested in the limit on $M$ as dictated by the finite dynamic range of photorefractive crystals. In particular, we use the maximum index modulation that we observed in our strong hologram experiments in conjunction with a reasonable figure for the smallest index modulation that can be detected to calculate the dynamic range that is available in $BaTiO_3$.

As is shown in Fig. 3(c), a hologram recorded at unity modulation depth in our $BaTiO_3$ sample achieved the third maximum of the diffraction efficiency function given in Eq. (1). This result implies a saturation strength parameter of $\phi_{max} = 5\pi/2$ (for an approximate interaction length of $d = 4$ mm, which is the crystal thickness, this value of $\phi$ corresponds to $\Delta n = 1.67 \times 10^{-4}$). Given a minimum allowable diffraction efficiency per hologram of $\eta_{min}$, the minimum allowable value for the strength parameter can be found in the small perturbation regime of Eq. (1) to be $\phi_{min} \approx (\eta_{min})^{1/2}$, where $\eta_{min}$ is determined from noise sources in the apparatus such as scattering and detector noise. Although the specific value of $\eta_{min}$ is dependent on the measurement environment (e.g., scattering and detector noise), the value of $\eta_{min} = 0.01\%$ (1-mW/cm$^2$ read beam resulting in a 100-nW/cm$^2$ diffracted beam) is reasonable. The ratio of these two numbers gives the index amplitude dynamic range,

$$R = \frac{\phi_{max}}{\phi_{min}} = \frac{5\pi/2}{(\eta_{min})^{1/2}} \approx 10^3. \tag{3}$$

Turning now to the multiple-hologram case, this dynamic range must be greater than or equal to the average amplitude excursions of the total superposition $\Delta n(\mathbf{r})$ given by relation (2) (normalized by the amplitude of each component of the sum) in order to maintain accuracy. In almost all cases of interest, the individual terms of the sum of relation (2) are mutually uncorrelated, so that the normalized amplitude excursion is $M^{1/2}$. Equating the dynamic range to $M^{1/2}$ yields $\phi_{max} = \phi_{min} M^{1/2}$, from which we get $M_{max} = R^2 \approx 10^6$, the maximum number of holograms that can be supported. Unfortunately, such a large number is difficult to realize in practice because of the additional constraint placed by incoherent erasure during the sequential exposure process used to achieve the superimposed set of holograms of relation (2). In particular, it is shown in Ref. 5 that the exposure schedule that must be followed in order to yield a set of holograms with equal amplitudes results in a strength parameter equal to $\phi_{max}/M$ for each component. Under this constraint the maximum number of holograms is determined by the detectability of each component, so that

$$\frac{\phi_{max}}{M} = \phi_{min}, \tag{4}$$

which yields $M_{max} = R \approx 10^3$. This value is consistent with the discussions and experiments found in Refs. 6 and 7.

This research is supported in part by the U.S. Office of Naval Research under contract N00014-88-C-0230. At the California Institute of Technology this research is supported by the Defense Advanced Research Projects Agency and the U.S. Air Force Office of Scientific Research.

## References

1. H. Kogelnik, Bell Syst. Tech. J. **48**, 2909 (1969).
2. P. J. Van Heerden, Appl. Opt. **2**, 393 (1963).
3. H. Lee, X. Gu, and D. Psaltis, J. Appl. Phys. **65**, 2191 (1989).
4. Y. Fainman, E. Klancnik, and S. H. Lee, Opt. Eng. **25**, 228 (1986).
5. D. Psaltis, K. Wagner, and D. Brady, Appl. Opt. **27**, 1752 (1988).
6. W. J. Burke, D. L. Staebler, W. Phillips, and G. A. Alphonse, Opt. Eng. **17**, 308 (1978).
7. F. Mok, M. Tackitt, and H. M. Stoll, in *Digest of Annual Meeting of the Optical Society of America* (Optical Society of America, Washington, D.C., 1989), p. 76.

Appendix 4.7

# OPTICAL PATTERN CLASSIFIER WITH PERCEPTRON LEARNING

SC5544.FR

Rockwell International
Science Center

a reprint from Applied Optics

# Optical pattern classifier with Perceptron learning

John H. Hong, Scott Campbell, and Pochi Yeh

An optical realization of a single layer pattern classifier is described in which Perceptron learning is implemented to train the system weights. Novel use of the Stokes's principle of reversability for light is made to realize both additive and subtractive weight modifications necessary for true Perceptron learning. This is achieved by using a double Mach-Zehnder interferometer in conjunction with photorefractive hologram recording. Experimental results are given which show the high quality subtractive changes that can be made.

## I. Introduction

The processing of information in neural networks differs from conventional approaches in that the interconnections play the dominant role rather than acting as mere communication pathways. The fact that this interconnection intensive computation can be achieved using optical techniques was realized by many, holographic techniques being the most promising because of the potentially high capacity that is achievable.[1-3] The volume hologram in particular offers the most compact means of storing interconnection patterns.[3] Although the interconnection pattern can be computed and fixed in such holograms for prescribed tasks in which the problem parameters do not change, the idea of a neural network that can be adapted on-line to solve problems is especially appealing.

Shown in Fig. 1 is a diagram depicting the most basic one-layer network with $N$ input elements and one output. The weighted sum of the input pattern elements is thresholded to yield the output

$$y = g\left(\sum_{i=1}^{N} w_i x_i\right), \qquad g(z) = \begin{cases} 1 \text{ if } z > 0 \\ 0 \text{ otherwise} \end{cases} \tag{1}$$

where $g(z)$ is the thresholding nonlinearity, $w_i$ is the $i$th weight, and $x_i$ is the $i$th element of the input pattern. Such a system can be used to dichotomize a set of patterns into two prescribed classes, and more complex, multiple layered networks can be built up using this as the basic building block. Also, extensions to multicategory pattern classification can be achieved by having a matrix of weights and a multiplicity of output units as is discussed in Sec. III.

The authors are with Rockwell International Science Center, P.O. Box 1085, Thousand Oaks, California 91360.

Received 25 August 1989.
0003-6935/90/203019-07$02.00/0.



Simple learning algorithms can be characterized by the update equation:

$$w_i(p+1) = w_i(p) + \alpha(p) x_i(p), \tag{2}$$

where $w_i(p)$ is the $i$th weight at time $p$, $x_i(p)$ is the $i$th element of the pattern shown at time $p$, and $\alpha(p)$ is a multiplier that depends on the particular learning algorithm. This includes most deterministic algorithms, where some kind of a descent procedure is involved and incremental changes are made to the set of weights during each iteration. For perceptron learning,[4]

$$\alpha(p) = \begin{cases} 0 \text{ if output } y(p) \text{ was correct} \\ 1 \text{ if } y(p) = 0 \text{ but should have been 1} \\ -1 \text{ if } y(p) = 1 \text{ but should have been 0.} \end{cases} \tag{3}$$

The threshold bias can be absorbed into the patterns by choosing one element of each pattern to be always equal to a nonzero constant.[4] Note, that both additive and subtractive changes to the weights $w_i$ must be made to implement the algorithm directly. Although multiple layer networks require more complex routines such as Back Propagation, most algorithms share the common requirement of bipolar weight changes.

## II. Optical Implementation

The basic components to implement the network described above are an input device to convert the patterns into the appropriate format (e.g., electrical to optical, incoherent to coherent optical), an interconnection device, and a thresholding device for the output unit. The function of the interconnections in this context is to simply compute the inner product between the input pattern $x_i$ and the weights $w_i$. Volume holograms can be used to implement such functions[5] in a way that is extendable to the multiple category case (i.e., multiple inner products). Consider the arrangement shown in Fig. 2 where a holographic medium is positioned at the Fourier plane of lens $L1$. The input pattern is displayed in the spatial light modulator (SLM), which is positioned at the front focal plane of

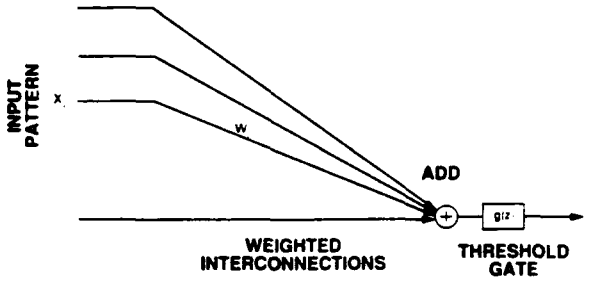


Fig. 1. One layer neural network.

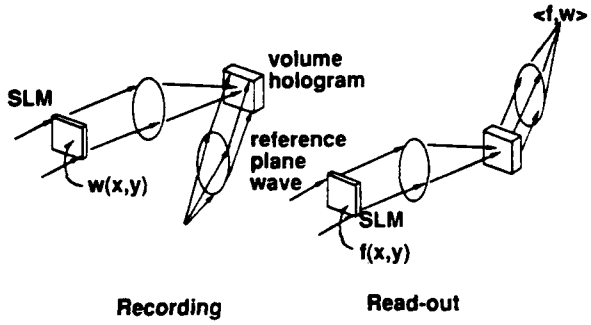


Fig. 2. Inner product computation using volume hologram.

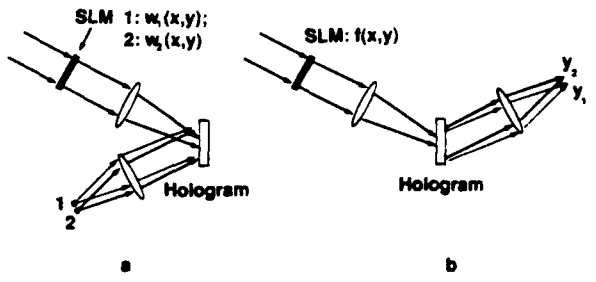


Fig. 3. Multiple output holographic system: (a) recording (point source 1 is activated when $w_1(x,y)$ is in SLM and point source 2 is activated when $w_2(x,y)$ is in SLM); (b) read-out ($y_1 = \langle w_1, f \rangle$ and $y_2 = \langle w_2, f \rangle$).

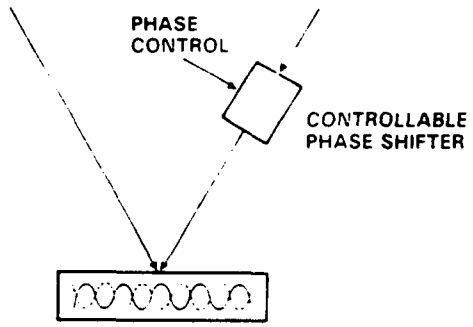


Fig. 4. Grating phase control using phase shifting device.

the same lens. A hologram is exposed with a pattern $w(x,y)$ in the SLM and a reference plane wave as shown. After development, another pattern $f(x,y)$ is loaded into the SLM. The light passing through the SLM is diffracted by the hologram and the diffracted amplitude can be shown to be the inner product between the two patterns $w$ and $f$.[5] Clearly, this is an overkill since the same function could have been achieved with a planar hologram. However, in the multiple category case where a number of different inner products need to be computed simultaneously, the added dimension afforded by the volume hologram is necessary; unless one resorts to spatial multiplexing of the planar hologram.[5,6] Multiple category classification is achieved by what is essentially an angular multiplexing of the volume hologram. This is shown in Fig. 3 where multiple holograms are written using the various reference plane waves. For the moment, we focus on the single output case and discuss generalizations for the multiple category problem in Sec. III.

By virtue of their dynamic nature, photorefractive crystals are ideal candidates for the holographic medium. In addition, crystals such as $LiNbO_3$, $BaTiO_3$ and SBN are by far the most efficient holographic media requiring relatively low optical intensity levels (e.g., 1 W/cm$^2$); the most efficient photorefractive crystals exhibit photosensitivities approaching that of photographic film. The holographic process records both modulus and phase of patterns and, thus, holographic interconnection techniques can be used to store bipolar valued weights and adaptable changes, which are either subtractive or additive, are possible.

The Perceptron implementation reported by Psaltis *et al.*[2] employed photorefractive crystal for adaptable interconnections but used incoherent erasure to achieve subtractive weight changes. In their system, the photorefractive crystal was placed at the image plane of the SLM and a device (movable piezoelectric mirror) was used to provide either a coherent reference or an incoherent one. For additive changes to the hologram, a coherent reference was provided so that the hologram is strengthened, but for subtractive changes, the reference beam was made to be incoherent with respect to the object beam so that nonuniform incoherent erasure resulted. This is roughly equivalent to providing a weight bias in which erasure will result in subtraction. Such methods involving incoherent erasure do not fully take advantage of the phase sensitive nature of holography.

To accurately implement the learning algorithm described by Eq. 2 and to exploit the hologram's coherent capability just described, a method by which both subtractive as well as additive changes to the weights can be made must be devised. Physically, such a method would amount to a multiple exposure hologram in which each exposure results in a grating (index grating in the case of photorefractive crystals) whose phase is either 0 or $\pi$ (relative phase difference is $\pi$). An obvious method of achieving this is shown in Fig. 4 in which two coherent waves intersect in a medium to create a holographic grating. One of the beams passes through a phase shifting device (e.g., an electrooptic

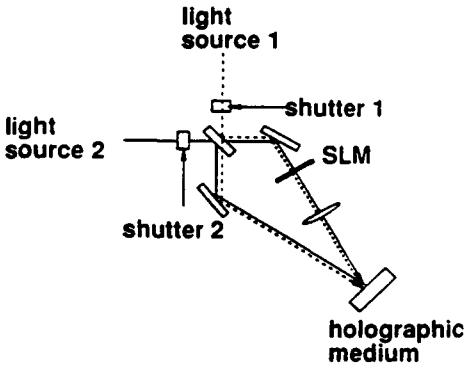


Fig. 5. Holographic phase control using Stokes' principle of reversibility.

phase modulator, liquid crystal phase modulating device, piezoelectric movable mirror) to acquire a phase of either 0 or $\pi$ relative to the other writing beam. After writing a hologram with one phase setting, holographic subtraction can be performed by using the other phase setting in the subsequent exposure and addition can be performed by using the original phase setting. Such phase shifting devices, however, may suffer from inaccuracies and also performance may degrade with time depending on various device characteristics (e.g., backlash in piezo mirrors, voltage inaccuracies in phase modulation devices (electrooptic, liquid crystal). Also, the continuous phase variability of these devices is an overkill in the present application in which only two phase settings, 0 and $\pi$, are required. In this paper, we describe a system that relies on a fundamental principle in optics known as the Stokes' principle of reversability[7,8] and a pair of shutters for the phase control.

The basic principle of operation of the phase control system can be described with the help of Fig. 5. This configuration is known as a double Mach-Zehnder interferometer because both input ports are used. The beam from laser source 1 (marked by the dotted line) is split into two paths by the dielectric beam splitter to intersect within the holographic medium to create a grating. Another laser source (which can be derived from laser source 1 or a separate laser with the same nominal wavelength) is positioned so that the directions of the beams transmitted and reflected by the beam splitter traverse precisely the same paths as those resulting from source 1. The Stokes' principle governs the relationship between the reflection and transmission coefficients seen by source 1 (call them $r$ and $t$, respectively) and those seen by source 2 ($r'$ and $t'$). Simple arguments[7] using this principle lead to the result

$$t = t' \text{ and } rt^* + r't^* = 0. \tag{4}$$

Note that since the amplitude of the hologram due to source 1 is proportional to $rt^*$ and that due to source 2 is proportional to $r't^*$, the two gratings are mutually $\pi$ out of phase. Of course, the accuracy of this result is dependent on how well the beams can be aligned. Such a phase shift of $\pi$ has been employed for the parallel subtraction of images.[7]

To quantify the accuracy that can easily be obtained in the laboratory, we performed the experiment sketched out in Fig. 6. An argon ion laser beam ($\lambda$ = 514.5 nm, coherence length ~1 cm) was split into two paths containing shutters. Each of the two beams (serving as the light sources 1 and 2 of Fig. 5) is directed into another beam splitter whose transmitted and reflected components are recombined with an output beam splitter. This part of the apparatus is the double Mach-Zehnder interferometer mentioned earlier. The combined result is viewed along a line with a linear detector array to give the scanned image intensity distributions shown in Fig. 7. When shutter 1 is on (and 2 is off), the distribution is nearly $\pi$ out of phase with that corresponding to shutter 2 on (and 1 off); we

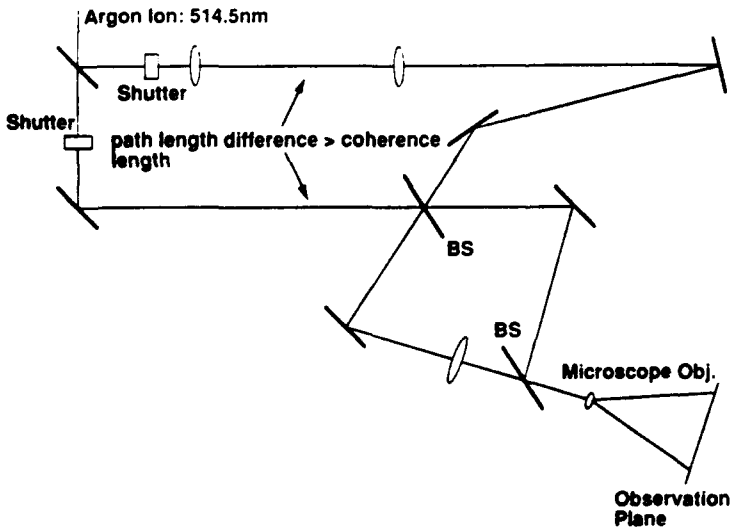


Fig. 6. Experiment to view holographic fringes.

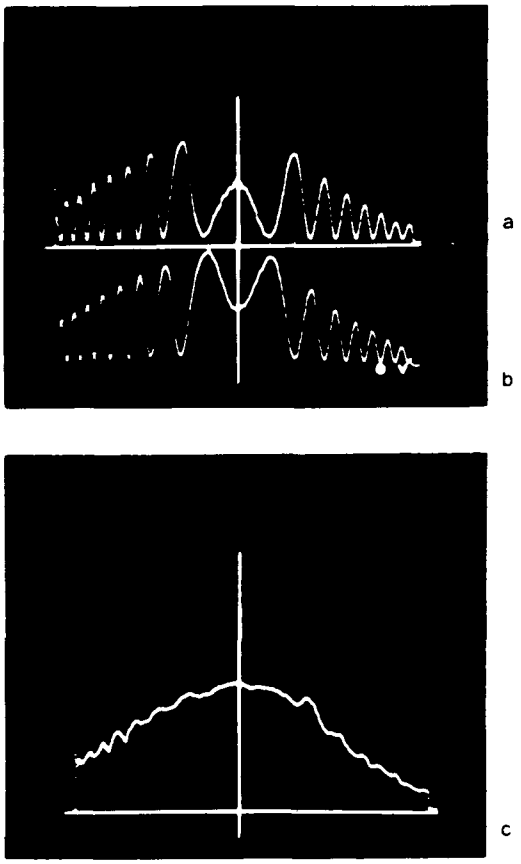


Fig. 7. Scanned image of intensity grating: (a) shutter 1 on; (b) shutter 2 on; and (c) both shutters on.

estimate that the error is to within 3° due to alignment errors and also measurement errors. As expected, when both shutters are on, the result shown in Fig. 7(c) is a fringe-less distribution with the nonuniformity due to the gaussian nature of the laser beams.

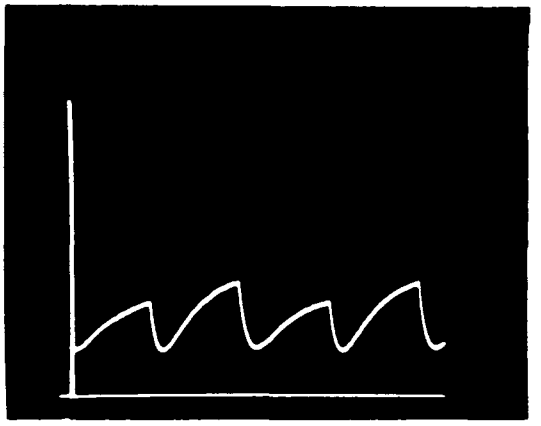

Fig. 9. Monitored diffraction efficiency (see text).

To investigate actual subtraction of index holograms with the described apparatus, we used photorefractive $BaTiO_3$ (6 mm × 6 mm × 2 mm) as the holographic medium in the arrangement shown in Fig. 8. Again, two beams derived from the same Argon laser served as the two light sources controlled by shutters 1 and 2. The writing beam sources were of ordinary polarization with respect to the crystal to minimize effects due to beam coupling.[9] The crystal was placed at the position where the two writing beams intersect to form a photorefractive grating and the diffraction efficiency of the resulting hologram was monitored with a read beam supplied by a He–Ne laser ($\lambda$ = 633 nm). First, a hologram was exposed with shutter 1 open and 2 closed. As soon as the hologram reached nearly full strength, shutter 1 was closed and 2 opened to allow the new hologram to develop. This sequence was repeated and the diffracted read beam intensity recorded as shown in Fig. 9. As is apparent, as soon as shutter 1 is closed and 2 is opened, the diffracted intensity diminshed to reach a complete null after which it rises again to reach saturation. This phenom-

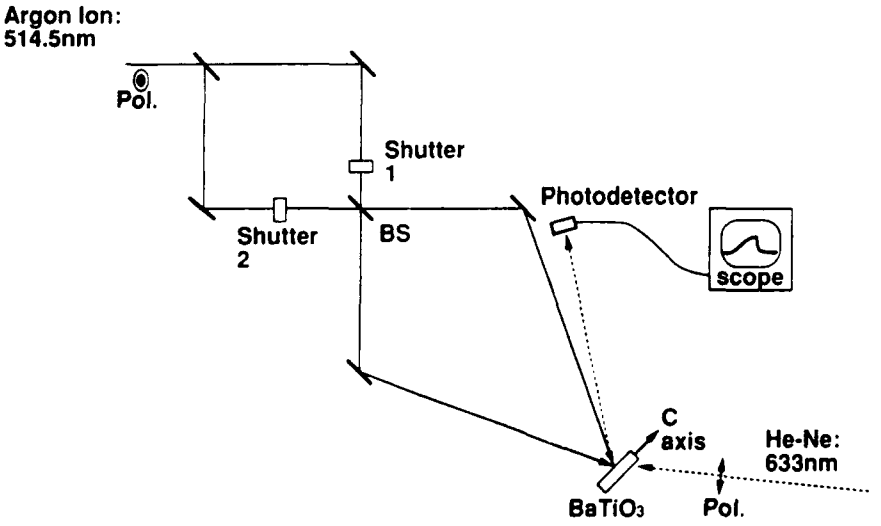


Fig. 8. Experiment to view subtraction of holograms using a $BaTiO_3$ crystal.

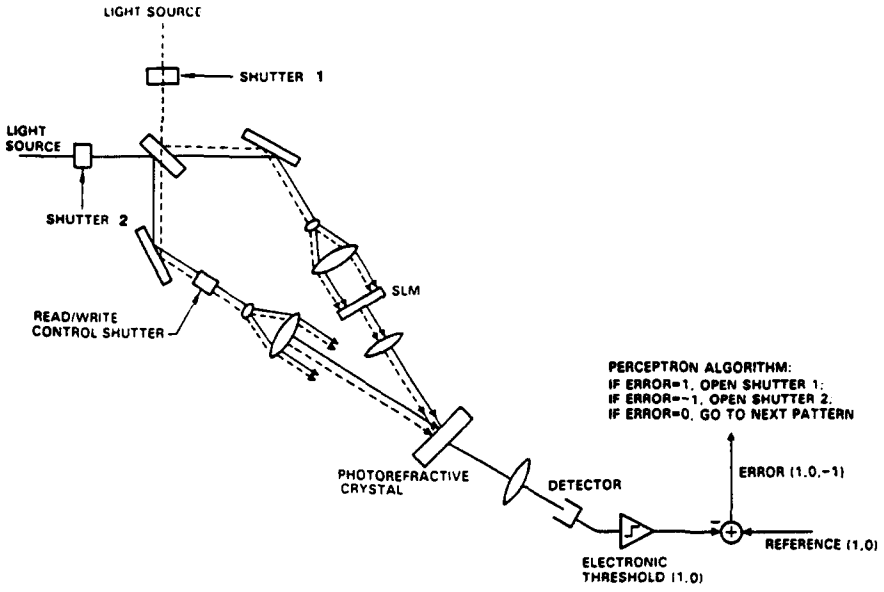


Fig. 10. Optical pattern classifier.

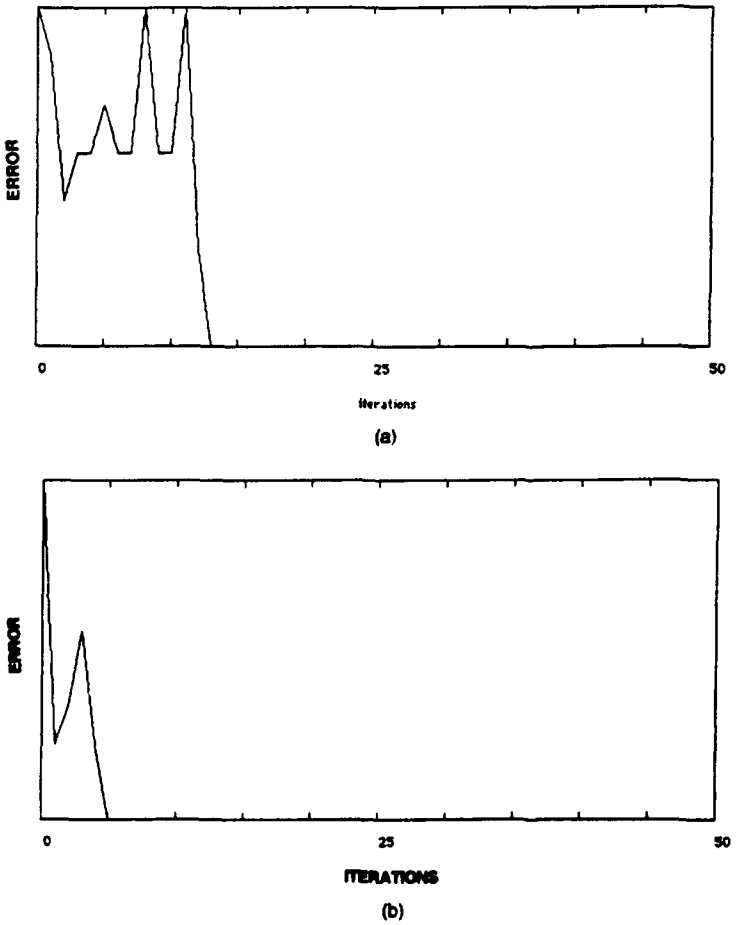


Fig. 11. Computer simulation learning curves (classification error shown as function of number of iterations): (a) photorefractive system with $\tau/10$ exposure time; and (b) ideal Perceptron system.

enon is due entirely to the fact that the newly exposed hologram because shutter 2 is $\pi$ out of phase with respect to the initial hologram, which results from shutter 1 being open (the quenching of the hologram is actually aided in part by incoherent erasure).

We now describe the overall optical system, shown in Fig. 10, in which an arrangement to allow for multiple exposures of a photorefractive hologram is diagramed. This setup uses the holographic phase control method just described. If the SLM contains a picture whose amplitude distribution is given by $a(x',y')$, the grating amplitude written in the crystal due to source 1 can be described by

$$\Gamma_1(x,y) = K(1 - \exp(-t_1/\tau))\,\frac{A(x,y)}{I_0 + |A(x,y)|^2}, \tag{5}$$

where $\tau$ is the time constant of the medium (assuming intensity is kept constant for all exposures), $t_1$ is the exposure time, $A(x,y)$ is the Fourier transform of $a(x',y')$, $I_0$ is the reference beam intensity, and $K$ is a constant determined by the characteristics of the particular crystal. If, without changing the picture, source 1 is turned off and source 2 is turned on, the new grating can be shown to be proportional to the first with the opposite sign. In particular, if the second exposure time duration is $t_2$, then

$$\Gamma(x,y) = K|(1 - \exp(-t_1/\tau))\exp(-t_2/\tau) - (1 - \exp(-t_2/\tau))|\,\frac{A(x,y)}{I_0 + |A(x,y)|^2}. \tag{6}$$

True subtractive weight changes are thus possible without the use of external phase shifters.

Note, in Eq. 6 that as the new out of phase hologram is being written, the initial hologram is partially erased due to the presence of the writing beams (incoherent erasure). This will modify the actual learning algorithm that is used in the following way. The weight update equation in comparison with the ideal rule of Eq. 2 is given by

$$w_i(p+1) = \exp(-t_e/\tau)w_i(p) + [1 - \exp(-t_e/\tau)]a(p)x_i(p), \tag{7}$$

where $t_e$ is the exposure time, so that the old weight distribution is diminished slightly as new holograms are written. This forgetting effect actually may prove to be beneficial in the optical implementation where the amplitude of the hologram has a finite dynamic range, since it helps to somewhat normalize the weight values during learning to keep the crystal from saturating. The output of the photodetector is given by

$$y(p) = |\langle w_i(p), x_i(p)\rangle|^2. \tag{8}$$

System simulations were performed using Eqs. 7 and 8 as the model, and the learning curve thus obtained is shown in Fig. 11(a), which verifies that, with the described modifications, the Perceptron training scheme works well. The result of the example shown in Fig. 11(a) was obtained for the task of dichotomizing a set of twelve randomly chosen binary patterns, each with thirty-two elements. The forgetting factor that was used was 0.9 (= $\exp(-t_e/\tau)$, so that an exposure time of $\sim\tau/10$ was assumed, where $\tau$ is the photorefractive response time constant. Sequencing through the entire set of patterns once is considered as one iteration of the algorithm. A comparison simulation of the original Perceptron algorithm is shown in Fig. 11(b) [same conditions as those in Fig. 11(a)].

### III. Multiple Category System

The extension of this concept to the multiple category case, which requires a multiplicity of output lines as opposed to a single output sufficient for dichotomies, is

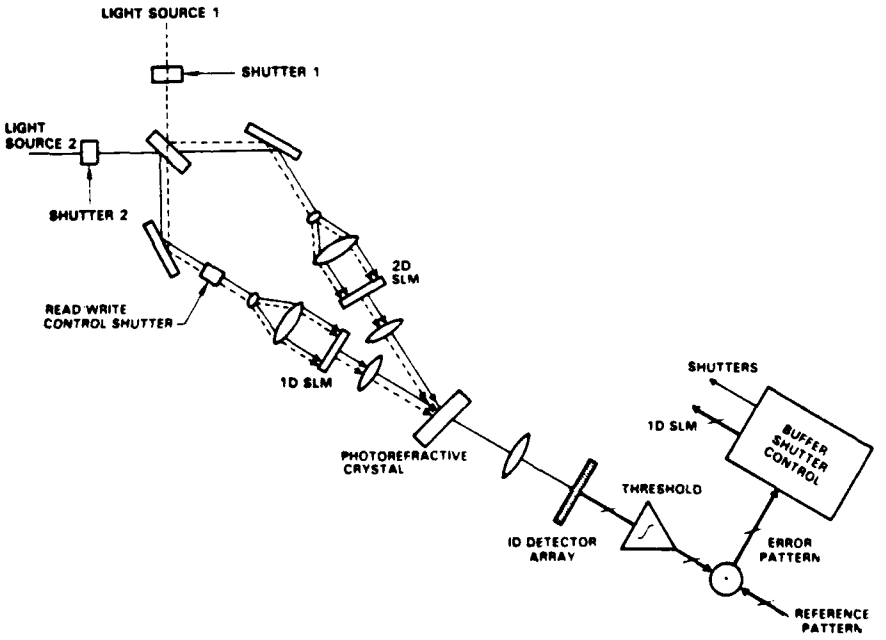


Fig. 12. Multiple category pattern classifier.

shown in Fig. 12, where the single detector and the reference beam shutter have been replaced by a detector array/shutter combination and an SLM/shutter combination, respectively. Here, the reference for each pattern is no longer a single plane wave but a set of plane waves dictated by the collection of openings in the 1-D SLM. Initially, the crystal contains no holograms and interconnections are built up by simply exposing the hologram with light source 1 with the pattern in the 2-D SLM and its associated reference pattern in the 1-D SLM. The process is repeated for each pattern in the training set. After the initialization, the first pattern is loaded into the 2-D SLM and the reference beam shutter is closed to interrogate the system. The reconstructed output pattern is then compared against the desired output pattern to yield the error vector. The algorithm must now be performed in two steps; first, only those portions of the 1-D SLM corresponding to the positive portions of the error vector are opened and light source 1 is turned on to strengthen certain interconnections following the Perceptron recipe. Then, only those portions corresponding to negative elements of the error vector are loaded into the 1-D SLM and light source 2 is turned on to weaken the appropriate weights. The buffer needed to store the error result needed for this function is especially simple and can be integrated into the detector array/amplifier assembly. The subtractive capability allows for a more exact implementation of the learning algorithms, even for the multiple category case.

## IV. Summary

We have described a new implementation of a learning machine which implements the Perceptron algorithm for pattern dichotomy. The optical system implements the weight storage and update functions using coherent means and, in particular, makes novel use of the Stokes' principle to achieve truly subtractive as well as additive weight changes, precluding the need for biases which are typically used in incoherent implementations as discussed earlier. The preliminary experimental results show that high quality subtractions are possible and the computer simulations will be verified by actual optical system operation in future work.

This work is supported, in part, by the Office of Naval Research contract N00014-88-C-0230.

## References

1. D. Z. Anderson and D. M. Lininger, "Dynamic Optical Interconnects: Volume Holograms as Optical Two-Port Operators," Appl. Opt. **26**, 5031–5038 (1987).
2. D. Psaltis, D. Brady, and K. Wagner, "Adaptive Optical Networks Using Photorefractive Crystals," Appl. Opt. **27**, 1752–1759 (1988).
3. A. Yariv and S. Kwong, "Associative Memories Based on Message-Bearing Optical Modes in Phase Conjugate Resonators," Opt. Lett. **11**, 186–188 (1986).
4. R. O. Duda and P. E. Hart, *Pattern Classification and Scene Analysis* (Wiley, New York 1973).
5. D. Psaltis, C. H. Park, and J. Hong, "Higher Order Associative Memories and Their Optical Implementations," Neural Networks **1**, 149–163 (1988).
6. H. J. Caulfield, "Parallel $N^4$ Weighted Optical Interconnections," Appl. Opt. **26**, 4039–4040 (1987).
7. P. Yeh, T. Y. Chang, and P. H. Beckwith, "Real-time optical image subtraction using dynamic holographic interference in photorefractive media," Opt. Lett. **13**, 586–588 (1988).
8. J. H. Hong, P. Yeh and S. Campbell, "Trainable Optical Network for Pattern Recognition," in *Technical Digest, Topical Meeting on Optical Computing* (Optical Society of America, Washington, DC, 1989), p. 307.
9. See, for example, P. Yeh, "Two-Wave Mixing in Nonlinear Media," IEEE J. Quantum Electron. **QE-25**, 484–519 (1989).

## Appendix 4.8

## TWO-WAVE MIXING IN NONLINEAR MEDIA

Rockwell International
Science Center

SC5544.FR

J-QE/25/3//25875

# Two-Wave Mixing in Nonlinear Media

Pochi Yeh

Reprinted from
IEEE JOURNAL OF QUANTUM ELECTRONICS
Vol. 25, No. 3, March 1989

# Two-Wave Mixing in Nonlinear Media

POCHI YEH, SENIOR MEMBER, IEEE

*(Invited Paper)*

*Abstract*—**The coupling of two electromagnetic waves in various nonlinear media is treated. The nonlinear media considered include photorefractive crystals, Kerr media, etc. The theory, some of the experiments, and several applications are described.**

## I. Introduction

TWO-WAVE mixing (sometimes referred to as two-beam coupling) is an exciting area of research in nonlinear optics. This area involves the use of nonlinear optical media for the coupling of two electromagnetic waves, especially the energy exchange between them.

Two-wave mixing is a physical process which takes advantage of the nonlinear response of some materials to the illumination of electromagnetic radiation. For example, let us consider the interference pattern formed by two laser beams in a nonlinear medium. Such a pattern is characterized by a spatial variation (usually periodic) of the intensity. If the medium responds nonlinearly, then an index variation is induced in the medium. The process of forming an index variation pattern inside a nonlinear medium using two-beam interference is similar to that of hologram formation. Such an index variation pattern is often periodic and is called a volume grating. When the two waves propagate through the grating induced by them, they undergo Bragg scattering [1]. One beam scatters into the other and vice versa. Such scatterings are reminiscent of the read-out process in holography [2].

Energy exchange between two electromagnetic waves in nonlinear media has been known for some time. Stimulated Brillouin scattering (SBS) and stimulated Raman scattering (SRS) are the best examples [3]. Both of these processes require relatively high intensities for efficient coupling. Recent interest in two-wave mixing arises from the strong nonreciprocal energy exchange at relatively lower intensities between two coherent laser beams in a new class of materials called photorefractive crystals. In addition, these materials are very efficient for the generation of phase-conjugated waves [4]–[6]. Materials such as barium titanate ($BaTiO_3$) and strontium barium niobate ($Sr_xBa_{1-x}Nb_2O_6$, SBN) are by far the most efficient nonlinear media for the generation of phase-conjugate waves, as well as the coupling of two laser beams using relatively low light intensities (e.g., 1 W/cm$^2$). Optical phase conjugation via four-wave mixing in nonlinear media also involves the formation of a volume index grating. The main difference between two-wave mixing and phase conjugation via four-wave mixing is that in four-wave mixing, a third beam is used to read out the volume hologram, whereas in two-wave mixing, the same beams read the mutually-induced volume hologram. To satisfy the Bragg condition, this third beam must be counterpropagating relative to one of the two beams that are involved in the formation of the volume hologram. In two-wave mixing, the Bragg condition is automatically satisfied.

In this paper, we first describe briefly the physics of the photorefractive effect. A coupled-mode theory is then developed to analyze the coupling of two coherent electromagnetic waves inside a photorefractive medium. Both codirectional and contradirectional coupling are considered. The coupled-mode theory is then extended to consider the case of nondegenerate two-wave mixing. This is followed by a discussion of the fundamental limit of the speed of photorefractive effect. The concept of an artificial photorefractive effect is then introduced. In the section that follows, we consider the coupling of two polarized beams inside photorefractive cubic crystals. The formulation is focused on the cross-polarization two-beam coupling in semiconductors such as GaAs. In Section IV, we treat the coupling of two electromagnetic waves inside a Kerr medium and discuss the electrostrictive Kerr effect. A new concept of nonlinear Bragg scattering is introduced. We also point out the similarity among various kinds of two-wave mixing, including SBS and SRS. In the last section, we discuss several applications of two-wave mixing. These include photorefractive resonators, optical nonreciprocity, resonator model of self-pumped phase conjugators, real-time holography, and nonlinear optical information processing.

## II. Photorefractive Materials

The photorefractive effect is a phenomenon in which the local index of refraction is changed by the spatial variation of the light intensity. Such an effect was first discovered in 1966 [7]. The spatial index variation leads to a distortion of the wavefront, and such an effect was referred to as "optical damage." The photorefractive effect has since been observed in many electrooptic crystals, including $LiNbO_3$, $BaTiO_3$, SBN, BSO, BGO, GaAs, InP,

Manuscript received May 20, 1988; revised July 24, 1988. This work was supported in part by the Office of Naval Research under Contracts N00014-85-C-0219, N00014-85-C-0557, N00014-88-C-0230, and N00014-88-C-0231.

The author is with the Rockwell International Science Center, Thousand Oaks, CA 91360.

IEEE Log Number 8825875.

etc. It is generally believed that the photorefractive effect arises from optically-generated charge carriers which migrate when the crystal is exposed to a spatially-varying pattern of illumination with photons having sufficient energy. Migration of the charge carriers due to drift or diffusion produces a space-charge separation, which then gives rise to a strong space-charge field. Such a field induces refractive index change via the Pockels' effect. This simple picture of the photorefractive effect explains several interesting steady-state optical phenomena in these media.

### A. Kukhtarev-Vinetskii's Model

Although there are several models for the photorefractive effect [8]–[11], the Kukhtarev-Vinetskii model is the most widely accepted one [8], [9]. In this model, the photorefractive materials are assumed to contain donor and acceptor traps. These traps which arise from the imperfections in the crystal, create intermediate electronic energy states in the bandgap of the insulators. When photons with sufficient energy are present, electronic transitions due to photoexcitations take place. As a result of the transitions, charge carriers are excited into the conduction band and the ionized donors become empty trap sites. The rate of carrier generation is $(sI + \beta)(N_D - N_D^+)$, whereas the rate of trap capture is $\gamma_R N N_D^+$. Here, $s$ is the cross section of photoionization, $\beta$ is the rate of thermal generation, $\gamma_R$ is the carrier-ionized trap recombination rate, and $N$ and $N_D^+$ stand for the concentration of the carriers and ionized traps. $N_D$ is the density of the donor traps.

The space-charge field produced by the migration of the charge carriers is determined by the following set of equations:

$$\frac{\partial}{\partial t} N = \frac{\partial}{\partial t} N_D^+ - \frac{1}{e} \nabla \cdot \vec{J} \tag{1}$$

$$\frac{\partial}{\partial t} N_D^+ = (sI + \beta)(N_D - N_D^+) - \gamma_R N N_D^+ \tag{2}$$

$$\vec{J} = e\mu N\left(\vec{E} - \frac{kT}{e} \nabla \log N\right) + pI\vec{c} \tag{3}$$

$$\nabla \cdot (\epsilon \vec{E}^{sc}) = e(N_A + N - N_D^+) \tag{4}$$

where $\vec{c}$ is the unit vector along the $c$ axis of the crystal, $I$ is the light intensity, $N_A$ is the acceptor concentration, $\mu$ is the mobility, $T$ is temperature, $k$ is the Boltzmann constant, $n$ is the index of refraction, $\epsilon$ is the dielectric tensor, $pI$ is the photovoltaic current, and $p$ is the photovoltaic constant. $\vec{E}^{sc}$ stands for the space-charge field. $\vec{E}$ is the total field which includes $\vec{E}^{sc}$ and any external or internal fields (such as chemical or internal ferroelectric fields).

As a result of the presence of the space-charge field, a change in the index of refraction is induced via the linear electrooptic effect [1] (Pockels effect):

$$\Delta\left(\frac{1}{n^2}\right)_{ij} = r_{ijk} \vec{E}_k^{sc} \tag{5}$$

where $r_{ijk}$ is the electrooptic coefficient (with $i, j, k = x, y, z$).

### B. Degenerate Two-Wave Mixing

We now consider the interaction of two laser beams inside a photorefractive medium (see Fig. 1). If the two beams are of the same frequency, a stationary interference pattern is formed. Let the electric field of the two waves be written

$$E_j = A_j e^{i(\omega t - \vec{k}_j \cdot \vec{r})} \qquad j = 1, 2 \tag{6}$$

where $A_1$, $A_2$ are the wave amplitudes, $\omega$ is the angular frequency, and $\vec{k}_1$, $\vec{k}_2$ are the wave vectors. For simplicity, we also assume that both beams are polarized perpendicular to the plane of incidence (i.e., $s$-polarized).

Within a factor of proportionality, the intensity of the electromagnetic radiation can be written

$$I = |E|^2 = |E_1 + E_2|^2. \tag{7}$$

Using (6) for the electric field, the intensity can be written

$$I = |A_1|^2 + |A_2|^2 + A_1^* A_2 e^{-i\vec{K}\cdot\vec{r}} + A_1 A_2^* e^{i\vec{K}\cdot\vec{r}} \tag{8}$$

where

$$\vec{K} = \vec{k}_2 - \vec{k}_1. \tag{9}$$

The magnitude of the vector $\vec{K}$ is $(2\pi/\Lambda)$, where $\Lambda$ is the period of the fringe pattern. The intensity [(8)] represents a spatial variation of optical energy inside the photorefractive medium. According to Kukhtarev's model, such an intensity pattern will generate and redistribute photocarriers. As a result, a space-charge field is created in the medium. This field induces a volume index grating via the Pockels effect. In general, the index grating will have a spatial phase shift relative to the interference pattern [8]. The index of refraction including the fundamental component of the intensity-induced gratings can be written

$$n = n_o + \frac{n_1}{2} e^{i\phi} \frac{A_1^* A_2}{I_o} \exp(-i\vec{K} \cdot \vec{r}) + \text{c.c.} \tag{10}$$

where

$$I_o = I_1 + I_2 = |A_1|^2 + |A_2|^2. \tag{11}$$

$n_o$ is the index of refraction when no light is present, $\phi$ is real, and $n_1$ is a real and positive number. Here again, for the sake of simplicity, we assume a scalar grating. The phase $\phi$ indicates the degree to which the index grating is shifted spatially with respect to the light interference pattern. In photorefractive media that operate by diffusion only (i.e., no external static field), e.g., $BaTiO_3$, the magnitude of $\phi$ is $\pi/2$ with its sign depending on the direction of the $c$ axis. $\vec{K}$ is the grating wave vector and $I_o$ is the sum of the intensities. The parameter $n_1$ depends on the grating spacing and its direction, as well as on the material properties of the crystal, e.g., the electrooptic coefficient. Expressions for $n_1 e^{i\phi}$ can be found in [9] and [10].

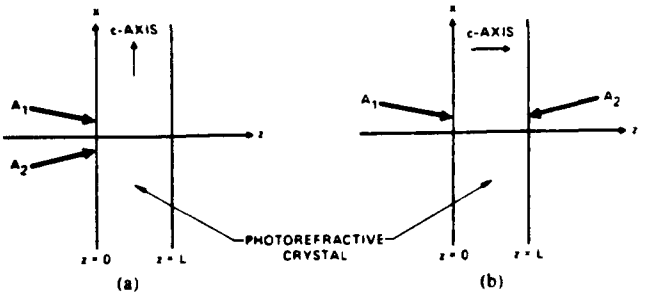


Fig. 1. (a) Schematic drawing of codirectional two-wave mixing. (b) Schematic drawing of contradirectional two-wave mixing.

The finite spatial phase shift between the interference pattern and the induced volume index grating has been known for some time [8], [12]. The presence of such a phase shift allows for the possibility of nonreciprocal steady-state transfer of energy between the beams [9], [13]–[15]. To investigate the coupling, we substitute (10) for the index of refraction and $E = E_1 + E_2$ for the electric field into the following wave equation:

$$\nabla^2 E + \frac{\omega^2}{c^2} n^2 E = 0 \tag{12}$$

where $c$ is the velocity of light.

We assume that both waves propagate in the $xz$ plane. Generally speaking, if the beams are of finite extent (i.e., comparable to the intersection of the beams), the amplitudes may depend on both $x$ and $z$. Here we assume, for the sake of simplicity, that the transverse dimension of the beams is of infinite extent so that the boundary condition requires that the wave amplitudes $A_1$ and $A_2$ be functions of $z$ only (see Fig. 1). We will solve for the steady states so that $A_1$ and $A_2$ are also taken to be time-independent.

Using the slowly-varying approximation, i.e.,

$$\left|\frac{d^2}{dz^2} A_j\right| \ll \left|\beta_j \frac{d}{dz} A_j\right| \qquad j = 1, 2$$

we obtain

$$2i\beta_1 \frac{d}{dz} A_1 = \frac{\omega^2 n_o n_1}{c^2 I_o} e^{-i\phi} A_2^* A_2 A_1$$

$$2i\beta_2 \frac{d}{dz} A_2 = \frac{\omega^2 n_o n_1}{c^2 I_o} e^{i\phi} A_1^* A_1 A_2 \tag{13}$$

where $\beta_1$ and $\beta_2$ are the $z$ components of the wave vectors $\vec{k}_1$ and $\vec{k}_2$ inside the medium, respectively. The energy coupling depends on the relative sign of $\beta_1$ and $\beta_2$. Thus, two-wave mixing is divided into the following two categories.

*1) Codirectional Two-Wave Mixing ($\beta_1\beta_2 > 0$):* Referring to Fig. 1(a), we consider the case when the two laser beams enter the medium from the same side at $z = 0$. Without loss of generality, we assume that

$$\beta_1 = \beta_2 = k \cos(\theta/2) = \frac{2\pi}{\lambda} n_o \cos(\theta/2) \tag{14}$$

where $\theta$ is the angle between the beam inside the medium, and $n_o$ is the index of refraction of the medium.

Substituting (14) for $\beta_1$ and $\beta_2$ in (13), and using $(\omega/c) = 2\pi/\lambda$, we obtain

$$\frac{d}{dz} A_1 = -i \frac{\pi n_1}{\lambda I_o \cos(\theta/2)} e^{-i\phi} |A_2|^2 A_1 - \frac{\alpha}{2} A_1$$

$$\frac{d}{dz} A_2 = -i \frac{\pi n_1}{\lambda I_o \cos(\theta/2)} e^{i\phi} |A_1|^2 A_2 - \frac{\alpha}{2} A_2 \tag{15}$$

where we have added terms that account for the attenuation and $\alpha$ is the bulk absorption coefficient.

We now write

$$A_1 = \sqrt{I_1} \exp(-i\psi_1)$$

$$A_2 = \sqrt{I_2} \exp(-i\psi_2) \tag{16}$$

where $\psi_1$ and $\psi_2$ are phases of the complex amplitudes $A_1$ and $A_2$, respectively. Using (16) and (11), the coupled equation (15) can be written as

$$\frac{d}{dz} I_1 = -\gamma \frac{I_1 I_2}{I_1 + I_2} - \alpha I_1$$

$$\frac{d}{dz} I_2 = \gamma \frac{I_1 I_2}{I_1 + I_2} - \alpha I_2 \tag{17}$$

and

$$\frac{d}{dz} \psi_1 = \beta \frac{I_2}{I_1 + I_2}$$

$$\frac{d}{dz} \psi_2 = \beta \frac{I_1}{I_1 + I_2} \tag{18}$$

where

$$\gamma = \frac{2\pi n_1}{\lambda \cos(\theta/2)} \sin\phi \tag{19}$$

$$\beta = \frac{\pi n_1}{\lambda \cos(\theta/2)} \cos\phi. \tag{20}$$

The solutions for the intensities $I_1(z)$ and $I_2(z)$ are [16]

$$I_1(z) = I_1(0) \frac{1 + m^{-1}}{1 + m^{-1} e^{\gamma z}} e^{-\alpha z} \tag{21}$$

$$I_2(z) = I_2(0) \frac{1 + m}{1 + m e^{-\gamma z}} e^{-\alpha z} \tag{22}$$

where $m$ is the input intensity ratio

$$m = \frac{I_1(0)}{I_2(0)}. \tag{23}$$

Note that in the absence of absorption ($\alpha = 0$), $I_2(z)$ is an increasing function of $z$ and $I_1(z)$ is a decreasing function of $z$, provided $\gamma$ is positive. The sign of $\gamma$ depends on the direction of the $c$ axis. As the result of the coupling for $\gamma > 0$ in Fig. 1, beam 2 gains energy from beam 1. If this two-wave mixing gain is large enough to overcome

the absorption loss, then beam 2 is amplified. Such an amplification is responsible for the fanning and stimulated scatterings of laser beams in photorefractive crystals [17].

With $I_1(z)$, $I_2(z)$ known, the phases $\psi_1$ and $\psi_2$ can be obtained by a direct integration of (18). Substituting (21) and (22) into (18) for $I_1$ and $I_2$, respectively, we obtain

$$\psi_2(z) - \psi_2(0) = \int_0^z \frac{\beta\, dz'}{1 + m^{-1}e^{\gamma z'}}. \tag{24}$$

Note that this photorefractive phase shift is independent of the absorption coefficient $\alpha$. Carrying out the integration in (24), we obtain

$$\psi_2(z) - \psi_2(0) = \frac{\beta}{\gamma} \ln\left(\frac{1 + m}{1 + me^{-\gamma z}}\right). \tag{25}$$

From (18), we note that

$$\frac{d}{dz}(\psi_1 + \psi_2) = \beta. \tag{26}$$

Thus, $\psi_1(z)$ can be written

$$\begin{aligned}\psi_1(z) - \psi_1(0) &= \beta z - [\psi_2(z) - \psi_2(0)] \\ &= -\frac{\beta}{\gamma} \ln\left(\frac{m + 1}{m + e^{\gamma z}}\right).\end{aligned} \tag{27}$$

If we refer to $A_2$ as the signal beam, then a useful parameter is the gain

$$g = \frac{I_2(L)}{I_2(0)} = \frac{1 + m}{1 + me^{-\gamma L}} e^{-\alpha L} \tag{28}$$

where we recall that $m$ is the intensity ratio at input face ($z = 0$). Fig. 2 plots the gain as a function of the length of interaction $L$ for various values of $m$.

*2) Contradirectional Two-Wave Mixing:* We now consider the case when the two beams enter the medium from opposite faces, as shown in Fig. 1(b). In codirectional two-wave mixing, the sum of the beam power is a constant of integration provided the medium is lossless, whereas in contradirectional two-wave mixing, the difference of the beam power (i.e., net Poynting power flow) is a constant. In addition, the coupled-mode equation which governs the wave amplitudes is also different from that of codirectional coupling. This leads to qualitative differences in the energy exchange between the two waves in two cases.

Let

$$\beta_1 = -\beta_2 = k \cos(\theta/2) = \frac{2\pi}{\lambda} n_o \cos(\theta/2) \tag{29}$$

where $\theta/2$ is the angle between each of the beams and the $z$ axis. Substitution of (29) for $\beta_1$ and $\beta_2$ in (13) yields a similar set of coupled equations. Using (16), such a set of coupled equations becomes

$$\begin{aligned}\frac{d}{dz} I_1 &= -\gamma \frac{I_1 I_2}{I_1 + I_2} - \alpha I_1 \\ \frac{d}{dz} I_2 &= -\gamma \frac{I_1 I_2}{I_1 + I_2} + \alpha I_2\end{aligned} \tag{30}$$

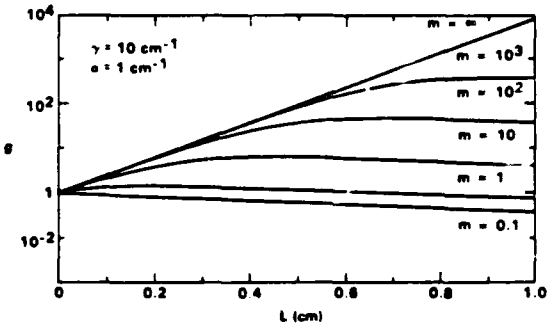


Fig. 2. Gain versus $L$ for various values of $m$.

and

$$\begin{aligned}\frac{d}{dz}\psi_1 &= \beta \frac{I_2}{I_1 + I_2} \\ \frac{d}{dz}\psi_2 &= -\beta \frac{I_1}{I_1 + I_2}\end{aligned} \tag{31}$$

where $\beta$ and $\gamma$ are phase and intensity coupling constants and are given by

$$\begin{aligned}\gamma &= \frac{2\pi n_1}{\lambda \cos(\theta/2)} \sin\phi \\ \beta &= \frac{\pi n_1}{\lambda \cos(\theta/2)} \cos\phi.\end{aligned}$$

Comparing with (17) and (18), we notice the sign difference in these equations for beam 2.

The solutions for (30) and (31) can be obtained in closed form for the case when $\alpha = 0$ (i.e., lossless). In the lossless case, we note that the Poynting power flow along $+z$ is conserved, i.e.,

$$\frac{d}{dz}(I_1 - I_2) = 0 \tag{32}$$

and the solution of (30) with $\alpha = 0$ is [18]

$$\begin{aligned}I_1(z) &= -C + \sqrt{C^2 + B\exp(-\gamma z)} \\ I_2(z) &= C + \sqrt{C^2 + B\exp(-\gamma z)}\end{aligned} \tag{33}$$

where $B$ and $C$ are constants and are related to the boundary condition. $B$ and $C$ can be expressed in terms of any two of the four boundary values $I_1(0)$, $I_2(0)$, $I_1(L)$ and $I_2(L)$, where $L$ is the length of interaction. In terms of $I_1(0)$ and $I_2(0)$, $B$ and $C$ are given by

$$\begin{aligned}B &= I_1(0)\, I_2(0) \\ C &= [I_2(0) - I_1(0)]/2.\end{aligned} \tag{34}$$

In practice, it is convenient to express $B$ and $C$ in terms of the incident intensities $I_1(0)$ and $I_2(L)$. In this case, $B$ and $C$ become

$$\begin{aligned}B &= I_1(0)\, I_2(L) \frac{I_1(0) + I_2(L)}{I_2(L) + I_1(0)\exp(-\gamma L)} \\ C &= \frac{1}{2} \frac{I_2^2(L) - I_1^2(0)\exp(-\gamma L)}{I_2(L) + I_1(0)\exp(-\gamma L)}.\end{aligned} \tag{35}$$

According to (30), both $I_1(z)$ and $I_2(z)$ are increasing functions of $z$, provided $\gamma$ is negative. The transmittance for both waves, according to (34) and (35), are

$$t_1 = \frac{I_1(L)}{I_1(0)} = \frac{1 + m^{-1}}{1 + m^{-1}\exp(\gamma L)}$$

$$t_2 \equiv \frac{I_2(0)}{I_2(L)} = \frac{1 + m}{1 + m\exp(-\gamma L)} \tag{36}$$

where $m$ is the incident intensity ratio $m \equiv I_1(0)/I_2(L)$. Note that $t_1 < 1$ and $t_2 > 1$ for positive $\gamma$. The sign of $\gamma$ depends on the direction of the $c$ axis. It is interesting to note that these expressions for transmittance are formally identical to those of the codirectional coupling, even though the spatial variations of $I_1(z)$ and $I_2(z)$ with respect to $z$ are very different. Note that $t_1$ and $t_2$ are related by $t_2 = t_1 \exp(\gamma L)$.

The relative phase of the two waves is obtained by solving (30) in cooperation with (33), and is given by

$$\psi_2 - \psi_1 = -\tfrac{1}{2}\beta z + \text{constant} \tag{37}$$

where $\beta$ is the phase coupling constant. The relative phase varies linearly with $z$, and thus leads to a change in the grating wave vector by $\beta/2$ along the $z$ direction (i.e., the grating wave vector becomes $\vec{K} - \frac{1}{2}\beta\hat{z}$).

The nonreciprocal transmittance of photorefractive media may have important applications in many optical systems. It is known that in linear optical media, the transmittance of a layered structure (including absorbing material) is independent of the side of incidence (the so-called left and right incidence theorem). Right now, with the photorefractive material available, it is possible to make a "one-way" window which favors transmission from one side only. These applications will be addressed later in Section V-C.

The solutions of (33) did not take into account the effect of the bulk absorption of light. The attenuation due to finite absorption coefficient is reflected by the $-\alpha I_1$ term on the right-hand side of the first equation in (30), and the $+\alpha I_2$ term on the RHS of the other equation. With these two additional terms accounting for bulk absorption, closed-form solutions are not available [19]. However, (30) can still be integrated numerically. It is found that a very good approximate solution is

$$I_1^a(z) = I_1^{a=0}(z)\exp(-\alpha z)$$

$$I_2^a(z) = I_2^{a=0}(z)\exp[\alpha(z - L)]. \tag{38}$$

The approximation is legitimate provided $\alpha \ll |\gamma|$.

Fig. 3 illustrates the intensity variation with respect to $z$ for the case when $\gamma = -10^{-1}$ cm, $\alpha = 1.6$ cm$^{-1}$, and $L = 2.5$ mm. If the loss were neglected (i.e., $\alpha = 0$), the transmittance would be $t_1 = 1.81$ and $t_2 = 0.15$. With $\alpha = 1.6$ cm$^{-1}$, the transmittances become $t_1 = 1.27$ and $t_2 = 0.1$, according to a numerical integration. The approximate solution [(38)] would lead to $t_1 = 1.21$ and $t_2 = 0.10$. Note that even with the presence of absorption, the transmittance can still be greater than unity.

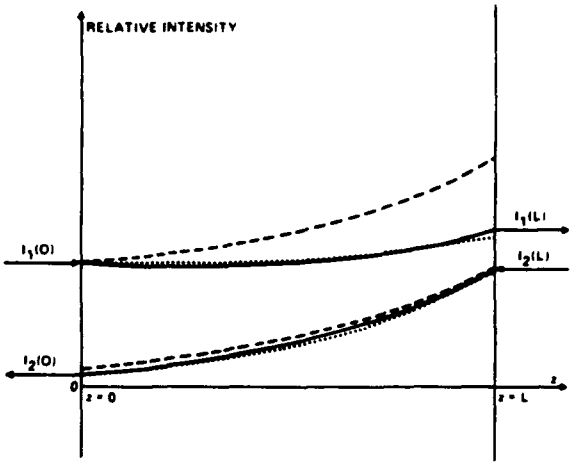


Fig. 3. Intensity variation with respect to $z$ in photorefractive crystals. The coupling constant is taken as $\gamma = -10$ cm$^{-1}$ and interaction length $L$ is 2.5 mm. The dashed curves are for the lossless case (i.e., $\alpha = 0$). The solid curves are obtained by numerical integration including the loss ($\alpha = 1.6$ cm$^{-1}$). The dotted curves are the approximate solution (38).

By using the approximation solution [(38)], the transmittances become

$$t_1 = \frac{1 + m^{-1}}{1 + m^{-1}\exp(\gamma L)}\exp(-\alpha L)$$

$$t_2 = \frac{1 + m}{1 + m\exp(-\gamma L)}\exp(-\alpha L). \tag{39}$$

There are two extreme cases worth mentioning. In the case when $I_2(L) \gg I_1(0)$, $m \ll 1$, the transmittances become $t_1 \approx \exp[(-\gamma - \alpha)L]$ and $t_2 \approx \exp(-\alpha L)$, whereas in the case when $I_1(0) \gg I_2(L)$, $m \gg 1$, the transmittances are $t_1 \approx \exp(-\alpha L)$ and $t_2 \approx \exp[(\gamma - \alpha)L]$.

### C. Nondegenerate Two-Wave Mixing

When the frequencies of the two laser beams are different, the interference fringe pattern is no longer stationary. A volume index grating can still be induced provided the fringe pattern does not move too fast. The amplitude of the index modulation decreases as the speed of the fringe pattern increases. This is related to the finite time needed for the formation of index grating in the photorefractive medium. In the next section, we will consider the fundamental limit of the speed of photorefractive effect.

Let $\omega_1$ and $\omega_2$ be the frequency of the two beams. The electric field of these two beams can be written

$$E_j = A_j e^{i(\omega_j t - \vec{k}_j \cdot \vec{r})} \qquad j = 1, 2 \tag{40}$$

where $\vec{k}_1$ and $\vec{k}_2$ are the wave vectors and $A_1$, $A_2$ are the wave amplitudes. The intensity of the electromagnetic radiation, similar to that given by (8), can be written

$$I = |A_1|^2 + |A_2|^2 + A_1^* A_2 e^{i(\Omega t - \vec{K} \cdot \vec{r})} + A_1 A_2^* e^{-i(\Omega t - \vec{K} \cdot \vec{r})} \tag{41}$$

where

$$\Omega = \omega_2 - \omega_1$$

$$\vec{K} = \vec{k}_2 - \vec{k}_1. \tag{42}$$

Such an intensity distribution represents a traveling fringe pattern at a speed of

$$v = \frac{\Omega}{K} = \frac{\Omega\Lambda}{2\pi} \tag{43}$$

where $\Lambda$ is the period of the fringe pattern.

The index of refraction including the fundamental component of the intensity-induced grating can be written

$$n = n_o + \frac{n_1}{2}\left\{e^{i\phi}\frac{A_1^* A_2}{I_o}\exp\left[i(\Omega t - \vec{K}\cdot\vec{r})\right] + \text{c.c.}\right\} \tag{44}$$

where

$$I_o = I_1 + I_2 \equiv |A_1|^2 + |A_2|^2. \tag{45}$$

$\phi$ is real and $n_1$ is a real and positive number. Here again, for the sake of simplicity, we assume a scalar grating. The phase $\phi$ indicates the degree to which the index grating is shifted spatially with respect to the light interference pattern. According to [20], $\phi$ and $n_1$ can be written, respectively, as

$$\phi = \phi_o - \tan^{-1}(\Omega\tau) \tag{46}$$

and

$$n_1 = \frac{2}{(1 + \Omega^2\tau^2)^{1/2}}\Delta n_s \tag{47}$$

where $\tau$ is the decay time constant of the holograph grating, $\Delta n_s$ is the saturation value of the photoinduced index change, and $\phi_o$ is a constant phase shift related to the nonlocal response of the crystal under fringe illumination. Both parameters $\Delta n_s$ and $\phi_o$ depend on the grating spacing ($2\pi/K$) and its direction, as well as on the material properties of the crystal, e.g., the electrooptic coefficients. Expressions for $\Delta n_s$ and $\phi_o$ can be found in [9] and [10]. In photorefractive media, e.g., $BaTiO_3$, that operate by diffusion only (i.e., no external static field), the magnitude of $\phi_o$ is $\pi/2$ with its sign depending on the orientation of the $c$ axis (note that these crystals are acentric).

Following the procedure similar to the one used in the previous section, coupled equations for the intensities $I_1(z)$, $I_2(z)$ and the phases $\psi_1(z)$, $\psi_2(a)$ are obtained. They are formally identical to those of the degenerate case, i.e., (17) and (18) for codirectional coupling and (30) and (31) for contradirectional coupling. The intensity coupling constant $\gamma$, however, is now a function of the frequency detuning $\Omega$.

For crystals such as $BaTiO_3$ that operate by diffusion only, the coupling constant can be written, according to (19), (46), and (47), as

$$\gamma = \gamma_o/\left[1 + (\Omega\tau)^2\right] \tag{48}$$

where $\gamma_o$ is the coupling constant for the case of degenerate two-wave mixing (i.e., $\Omega = \omega_1 - \omega_2 = 0$) and is given by

$$\gamma_o = \frac{4\pi\Delta n_s}{\lambda\cos\theta}. \tag{49}$$

In deriving (48), we have used $\pi/2$ for $\phi_o$ in (46).

The two-wave mixing gain can be written

$$g \equiv \frac{I_2(L)}{I_2(0)} = \frac{1 + m}{1 + me^{-\gamma L}}e^{-\alpha L} \tag{50}$$

where we recall that $m$ is the input beam ratio $m = I_1(0)/I_2(0)$ and $L$ is the length of interaction.

Fig. 4 shows the signal gain [(50)] as a function of the frequency detuning $\Omega\tau$ for various values of $m$. We note that for the case of pure diffusion, signal gain decreases as $\Omega\tau$ increases. This is true for both codirectional and contradirectional coupling. When $\Omega\tau \gg 1$, the intensity coupling constant $\gamma$ decreases significantly. The time constant $\tau$ depends on materials as well as on the intensity of the laser beams. The fundamental limit of such a time constant $\tau$ is discussed next.

### *D. Speed of Photorefractive Effect—Grating Formation Time*

As mentioned earlier, photorefractive crystals such as $BaTiO_3$, $Sr_xBa_{1-x}Nb_2O_6$ (SBN), $Bi_{12}SiO_{20}$ (BSO), etc., are by far the most efficient media for the generation of phase-conjugated optical waves using relatively low light intensities (1–10 W/cm$^2$). In addition, these materials also exhibit several interesting and important phenomena such as self-pumped phase conjugation, two-beam energy coupling, and real-time holography. All of these phenomena depend on the formation of volume index gratings inside the crystals [8], [9].

One of the most important issues involved in device applications is the speed of the grating formation (or the time constant $\tau$). Such a speed of the light-induced index gratings has been investigated theoretically using Kukhtarev's model and others, as well as experimentally in various crystals [8]–[10], [21]. The issue of fundamental limit of the speed of photorefractive effect has been a subject of great interest recently. Using Kukhtarev's model, let us examine the four fundamental processes involved in the photorefractive effect in sequence: 1) photoexcitation of carriers, 2) transport, 3) trap, and 4) Pockels effect. The photorefractive effect is a macroscopic phenomenon and requires the generation and transport of a large number of charge carriers. We note that without the presence of charge carriers, photorefractive gratings can never be formed, and no matter how fast the carriers can move (even at the speed of light, $3 \times 10^8$ m/s), the formation of index grating is still limited by the rate of carrier generation. Therefore, although each of the four processes involved imposes a theoretical limit on the response time of photorefractive effect, the fundamental limit of the speed of photorefractive effect is determined by the pho-

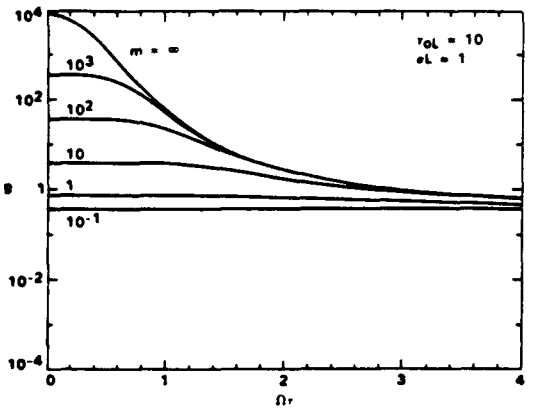


Fig. 4. Signal gain $g$ as a function of $\Omega\tau$ for various values of $m$.

toexcitation of carriers and not by the carrier transport. In other words, the charge carriers must be generated before they can be transported. Any finite time involved in the transport process can only lengthen the formation time of the grating. From this point of view, the fundamental limit may also be called the photon-flux limit, or simply the photoexcitation limit. Although the fundamental limit can be derived from (1)–(4) of Kukhtarev's model, it has been recently derived using a relatively simple method [22]. Such a fundamental limit has been confirmed experimentally [23]. In the limit when the crystal is illuminated with infinite intensity, the speed of the photorefractive effect will be limited by the charge transport process [24].

Assuming that the separation of a pair of charge particles requires the absorption of at least one photon, we can calculate the energy required to form a given volume index grating. To illustrate this, let us consider the photorefractive effect in $BaTiO_3$. Generally speaking [10], an efficient beam coupling would require a charge carrier density of approximately $10^{16}$ cm$^{-3}$. Such a charge separation would require the absorption of at least $10^{16}$ photons in a volume of 1 cm$^3$. Using a light intensity of 1 W in the visible spectrum, the photon flux would be approximately $10^{19}$/s. Thus, assuming a quantum efficiency of 100 percent, it takes at least 1 ms just to deposit enough photons to create the charge separation. The actual grating formation time can be much longer because not all of the charge carriers are trapped at the appropriate sites.

According to the model described in [22], the minimum time needed for the formation of an index grating, which provides a coupling constant of $\gamma$, is given by

$$t = \left(\frac{h\nu}{e}\right)\left(\frac{\lambda}{\Lambda}\right)\left(\frac{\gamma}{\alpha_p}\right)\frac{2}{\pi\eta}\cdot\frac{\epsilon}{In^3r} \qquad (51)$$

where $h\nu$ is the photon energy, $e$ is electronic charge, $\lambda$ is wavelength of light, $\Lambda$ is the grating period, $\alpha_p$ is photorefractive absorption coefficient, $\eta$ is the quantum efficiency, $\epsilon$ is dielectric constant, $r$ is the relevent electrooptic coefficient, and $I$ is the intensity of light. Note that the time constant is directly proportional to the coupling constant $\gamma$ and is inversely proportional to the light intensity. Equation (51) is the expression for the minimum time required for the formation of an index grating which provides a coupling constant $\gamma$.

A figure-of-merit for photorefractive material is often defined as

$$Q = \frac{n^3r}{\epsilon}. \qquad (52)$$

Table I lists such parameters for some photorefractive materials. Using such a parameter, the photon-limited time for the index grating formation becomes

$$t = \left(\frac{h\nu}{e}\right)\left(\frac{\lambda}{\Lambda}\right)\left(\frac{\gamma}{\alpha_p}\right)\frac{2}{\pi\eta IQ}. \qquad (53)$$

Here, we note that this photon-limited time is inversely proportional to the material's figure-of-merit and is proportional to the coupling constant $\gamma$.

We now discuss this photon-limited time for the formation of an index grating which yields a coupling constant of 1 cm$^{-1}$. For materials such as $BaTiO_3$, SBN, BSO, and GaAs, the figure-of-merit $Q$ is of the order of 1 (see Table I) in MKS units (M$^2$/FV). In many of the experiments reported recently, $h\nu$ is approximately 2 eV, $(\lambda/\Lambda)$ is of the order of 0.1. We further assume that the photoexcitation absorption coefficient is 0.1 cm$^{-1}$ and that the quantum efficiency $\eta$ is 100 percent. Using these parameters and a light intensity of 1 W/cm$^2$, (53) yields a photon-limited time constant of 0.15 ms. This is the minimum time required for the formation of an index grating which can provide a two-wave mixing coupling constant of 1 cm$^{-1}$. By virtue of its photoexcitation nature, the photorefractive effect is relatively slow at low intensities because of the finite time required to absorb the photons. Table II shows the comparison between the measured time constants with the calculated minimum time from (53). The only way to speed up the photorefractive process is by using higher intensities. Fig. 5 plots this minimum time constant for $BaTiO_3$ (or GaAs) as a function of intensity.

The photoexcitation process imposes a fundamental limit on the speed of photorefractive effect at a given power level. The time constant given by (51) here is the absolute minimum time required to generate a volume grating of given index modulation. We assume that the transport is instantaneous and the quantum efficiency is unity. Thus the derived time constant is the absolute minimum time. Any finite time involved in the transport process can only slow down the photorefractive process.

The fundamental limit discussed here can also provide important guidelines for many workers in the area of material research. For example, if we compare it with the experimental results, we find that the time constant of some materials (e.g., $BaTiO_3$, SBN) is two orders of magnitude larger than the fundamental limit. Thus, the calculation of such a fundamental limit and a simple comparison point out the room for improvement by either increasing the photorefractive absorption or the quantum ef-

TABLE I
FIGURE-OF-MERIT FOR SOME PHOTOREFRACTIVE MATERIALS [22]

| Materials | $\lambda$ $\mu$m | $r$ pm/V | $n$ | $\epsilon/\epsilon_0$ | $Q^a$ pm/V$\epsilon_0$ | $Q$(MKS) |
|---|---|---|---|---|---|---|
| $BaTiO_3$ | 0.5 | $r_{42} = 1640$ | $n_e = 2.4$ | $\epsilon_1 = 3600$ | 6.3 | 0.71 |
| SBN | 0.5 | $r_{33} = 1340$ | $n_e = 2.3$ | $\epsilon_3 = 3400$ | 4.8 | 0.54 |
| GaAs | 1.1 | $r_{12} = 1.43$ | $n_e = 3.4$ | $\epsilon = 12.3$ | 4.7 | 0.53 |
| BSO | 0.6 | $r_{41} = 5$ | $n = 2.54$ | $\epsilon = 56$ | 1.5 | 0.17 |
| $LiNbO_3$ | 0.6 | $r_{33} = 31$ | $n_e = 2.2$ | $\epsilon_3 = 32$ | 10.3 | 1.16 |
| $LiTaO_3$ | 0.6 | $r_{33} = 31$ | $n_e = 2.2$ | $\epsilon_3 = 45$ | 7.3 | 0.83 |
| $KNbO_3$ | 0.6 | $r_{42} = 380$ | $n = 2.3$ | $\epsilon_3 = 240$ | 19.3 | 2.2 |

[a] The figure-of-merit $Q$ depends on the configuration of interaction.

TABLE II
COMPARISON OF MEASURED TIME CONSTANTS $\tau$ AND THE FUNDAMENTAL LIMIT $t$

| Materials | $\lambda$ $\mu$m | $\Lambda$ $\mu$m | $\alpha_p$ cm$^{-1}$ | $\gamma$ cm$^{-1}$ | $\tau^a$ s | $\tau^b$ s | Remarks |
|---|---|---|---|---|---|---|---|
| GaAs | 1.06 | 1.0 | 1.2 | 0.4 | $80 \times 10^{-6}$ | $45 \times 10^{-6}$ | (25) |
| GaAs:Cr | 1.06 | 1.1 | 4.0 | 0.6 | $53 \times 10^{-6}$ | $31 \times 10^{-6}$ | (26) |
| $BaTiO_3$ | 0.515 | 1.3 | 1.0 | 20.0 | 1.3 | $2 \times 10^{-1}$ | (27) |
| BSO | 0.568 | 23.0 | 0.13 | 10.0 | $15 \times 10^{-3}$ | $2 \times 10^{-1}$ | (28) |
| SBN | 0.515 | 1.5 | 0.1 | 0.6 | 2.5 | $6 \times 10^{-1}$ | (29) |
| SBN:Ce | 0.515 | 1.5 | 0.7 | 14.0 | 0.8 | $2 \times 10^{-1}$ | (29) |

[a] $\tau$ and $t$ are time constants at incident intensity of 1 W/cm$^2$.
[b] $t$ is the calculated time constant by using (53) and assuming a quantum efficiency of 1.

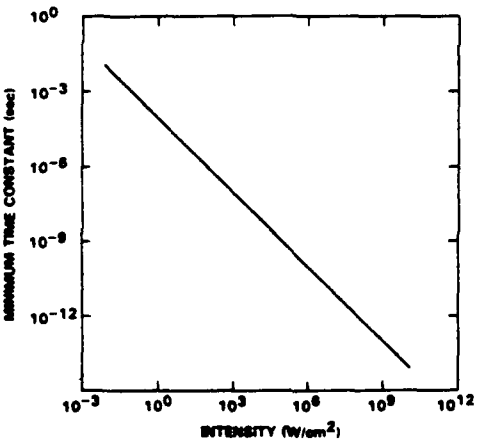


Fig. 5. Fundamental limit of the speed of photorefractive effect of $BaTiO_3$ (or GaAs) with coupling constant of 1 cm$^{-1}$.

ficiency. There are some materials (e.g., GaAs) whose photorefractive response is close to the fundamental limit, leaving no more room for further improvement by any means (e.g., heat treatment, doping, or reduction.) Recently, highly-reduced crystals of $KNbO_3$ were prepared which exhibit a photorefractive response time very close to the fundamental limit [23].

In summary, the photorefractive effect is a macroscopic phenomenon. It involves the transport of a large number of charge carriers for the formation of any finite grating. The fundamental limit is the minimum time needed for the generation of these carriers. The speed is fundamentally limited by the finite time needed to absorb a large number of photons at a given power level. By counting the total number of photons needed for the formation of an index grating, the photon-limited time constant is derived. This time constant is inversely proportional to the light intensity. We further estimated this minimum time constant for some typical photorefractive crystals. Such a fundamental limit provides important guidelines for researchers in the areas of device application and material research.

## III. PHOTOREFRACTIVE TWO-WAVE MIXING IN CUBIC CRYSTALS

Photorefractive two-beam coupling in electrooptic crystals has been studied extensively for its potential in many applications. Much attention has been focused on materials such as $BaTiO_3$, BSO, SBN, etc., because of their large coupling constants (see, for example, Table II). Although these oxide materials are very efficient for two-beam coupling, they are very slow in response at low operating powers [22]. Recently, several experimental investigations have been carried out to study two-wave mixing in cubic crystals such as GaAs, which responds much faster than any of the previously mentioned oxides at the same operating power [25], [26].

In addition to the faster temporal response, the optical isotropy and the tensor nature of the electrooptic coefficients of cubic crystals allow for the possibility of cross-polarization coupling. Such cross-polarization two-wave mixing is not possible in $BaTiO_3$ and SBN because of the optical anisotropy, which leads to velocity mismatch. The velocity mismatch also exists in BSO crystals because of

Rockwell International
Science Center
IEEE JOURNAL OF QUANTUM ELECTRONICS, VOL. 25, NO. 3, MARCH 1989

the circular birefringence. A number of special cases of two-wave mixing have been analyzed. Recently, a general theory of photorefractive two-wave mixing in cubic crystals was developed [30]. Such a theory predicts the existence of cross-polarization signal beam amplification. These cross-polarization couplings have been observed in GaAs crystals [31]–[33]. In what follows, we describe the coupled-mode theory of photorefractive two-wave mixing in cubic crystals, especially those with point group symmetry of $\bar{4}3m$. The theory shows that cross-polarization two-wave mixing is possible in cubic crystals such as GaAs. Exact solutions of coupled mode equations are obtained for the case of codirectional coupling.

### A. Coupled-Mode Theory

Referring to Fig. 6, we consider the intersection of two polarized beams inside a cubic photorefractive crystal. Since the crystal is optically isotropic, the electric field of the two beams can be written as

$$\vec{E} = (\vec{s}A_s + \vec{p}_1 A_p)\exp(-i\vec{k}_1 \cdot \vec{r}) + (\vec{s}B_s + \vec{p}_2 B_p)\exp(-i\vec{k}_2 \cdot \vec{r}) \quad (54)$$

where $\vec{k}_1$ and $\vec{k}_2$ are wave vectors of the beams, $\vec{s}$ is a unit vector perpendicular to the plane of incidence, and $\vec{p}_1$, $\vec{p}_2$ are unit vectors parallel to the plane of incidence and perpendicular to the beam wave vectors, respectively. Since each beam has two polarization components, there are four waves involved and $A_s$, $A_p$, $B_s$, and $B_p$ are amplitudes of the waves. All of the waves are assumed to have the same frequency. In addition, we assume that the crystal does not exhibit optical rotation.

In the photorefractive crystal (from $z = 0$ to $z = L$), these two beams generate an interference pattern,

$$\vec{E}^*\vec{E} = A_s^*A_s + A_p^*A_p + B_s^*B_s + B_p^*B_p + [(A_sB_s^* + A_pB_p^*\vec{p}_1 \cdot \vec{p}_2) \cdot \exp(i\vec{K} \cdot \vec{r}) + \text{c.c.}] \quad (55)$$

where $\vec{K} = \vec{k}_2 - \vec{k}_1$ is the grating wave vector, and c.c. represents the complex conjugate. We note that there are two contributions to the sinusoidal variation of the intensity pattern. As a result of the photorefractive effect, a space-charge field $E^{sc}$ is formed which induces a volume index grating via the Pockels effect,

$$(\Delta\epsilon)_{ij} = -\epsilon_0 n^4 r_{ijk} E_k \quad (56)$$

where $\epsilon_0$ is the dielectric permittivity of vacuum, $n$ is the index of refraction of the crystal, $r_{ijk}$ is the electrooptic coefficient, and $E_k$ is the k component ($k = x, y, z$) of the space-charge field. The fundamental component of the induced grating can be written

$$\Delta\epsilon = -\epsilon_0\epsilon_1[(A_sB_s^* + A_pB_p^*\cos\theta) \cdot \exp(i\vec{K} \cdot \vec{r} + \phi) + \text{c.c.}])/I_o \quad (57)$$

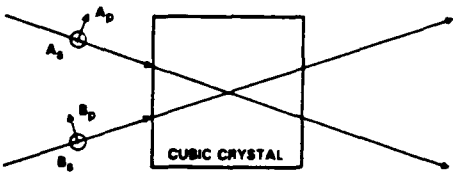


Fig. 6. Schematic drawing of photorefractive two-beam coupling in cubic crystals.

where $\epsilon_1$ is a $3 \times 3$ tensor, $\phi$ is the spatial phase shift between the index grating and the intensity pattern, $\theta$ is the angle between the beams inside the crystal, and $I_o$ is given by

$$I_o = A_s^*A_s + A_p^*A_p + B_s^*B_s + B_p^*B_p. \quad (58)$$

For cubic crystals with point group symmetry of $\bar{4}3m$, $\epsilon_1$ is given by

$$\epsilon_1 = n^4 r_{41}\begin{pmatrix} 0 & E_z & E_y \\ E_z & 0 & E_x \\ E_y & E_x & 0 \end{pmatrix} \quad (59)$$

where $r_{41} = r_{231} = r_{312} = r_{123}$, and $E_x$, $E_y$, and $E_z$ are the three components of the amplitude of the space-charge field.

Substitution of the index grating equation (56) into Maxwell's wave equation leads to the following set of coupled equations:

$$\frac{d}{dz}A_s = \frac{i}{2\beta_1}e^{i\phi}[\Gamma_{ss}B_s + \Gamma_{sp_2}B_p] \cdot (A_sB_s^* + A_pB_p^*\cos\theta)/I_o$$

$$\frac{d}{dz}B_s = \frac{i}{2\beta_2}e^{-i\phi}[\Gamma_{ss}A_s + \Gamma_{sp_1}A_p] \cdot (A_s^*B_s + A_p^*B_p\cos\theta)/I_o$$

$$\frac{d}{dz}A_p = \frac{i}{2\beta_1}e^{i\phi}[\Gamma_{p_1s}B_s + \Gamma_{p_1p_2}B_p] \cdot (A_sB_s^* + A_pB_p^*\cos\theta)/I_o$$

$$\frac{d}{dz}B_p = \frac{i}{2\beta_2}e^{-i\phi}[\Gamma_{p_2s}A_s + \Gamma_{p_2p_1}A_p] \cdot (A_s^*B_s + A_p^*B_p\cos\theta)/I_o \quad (60)$$

where

$$\Gamma = \omega^2\mu\epsilon_0\epsilon_1 \quad (61)$$

and

$$\Gamma_{ij} = \langle i|\Gamma|j\rangle \qquad i, j = \vec{s}, \vec{p}_1, \vec{p}_2 \quad (62)$$

and $\beta_1$, $\beta_2$ are the $z$ components of the wave vectors.

As indicated by the subscripts, $\Gamma_{ij}$'s are the coupling constants between the $i$th and $j$th polarized waves. Thus, $\Gamma_{ss}$ and $\Gamma_{p_1p_2}$ are the parallel coupling constants, and $\Gamma_{sp_1}$, $\Gamma_{sp_2}$ are the cross-coupling constants.

A similar set of equations had been derived by previous workers and exact solutions were obtained for the case of codirectional parallel coupling [34]. Here we focus our attention on the case of cross-polarization coupling. In cross-polarization coupling, the $s$ component of beam 1 is coupled with the $p$ component of beam 2, and the $p$ component of beam 1 is coupled with the $s$ component of beam 2.

### B. Codirectional Cross Coupling

To illustrate the use of the coupled equation (60), in the case of codirectional cross coupling, we consider a special case in which the crystal orientation does not allow the parallel coupling to occur. Such a two-beam coupling configuration is shown in Fig. 7(a). The two beams enter the crystal in such a way that the grating wave vector is along the [110] direction of the crystal. In this configuration, the unit vector $\vec{s}$ is parallel to [001] and the unit vectors $p_1$, $p_2$ are perpendicular to [001]. The amplitude of the induced index grating $\epsilon_1$ can thus be written, according to (59),

$$\epsilon_1 = \frac{1}{\sqrt{2}} n^4 r_{41} \begin{pmatrix} 0 & 0 & 1 \\ 0 & 0 & 1 \\ 1 & 1 & 0 \end{pmatrix} E^{sc} \tag{63}$$

where $E^{sc}$ is the amplitude of the space-charge field.

According to (63) and (62), and after a few steps of algebra, the coupling constants can be written

$$\Gamma_{ss} = \Gamma_{p_1p_2} = 0 \tag{64}$$

$$\Gamma_{sp_1} = \Gamma_{p_1s} = \Gamma_{sp_2} = \Gamma_{p_2s} = (2\pi/\lambda)^2 n^4 r_{41} E^{sc} \cos(\theta/2) \tag{65}$$

where we assume that the beams enter the crystal symmetrically such that

$$\beta_1 = \beta_2 = (2\pi/\lambda) n \cos(\theta/2). \tag{66}$$

We now substitute (65) and (66) into the coupled equation (60). This leads to

$$\begin{aligned} \frac{d}{dz} A_s &= -\gamma B_p (A_s B_s^* + A_p B_p^* \cos\theta)/I_o \\ \frac{d}{dz} B_s &= \gamma A_p (A_s^* B_s + A_p^* B_p \cos\theta)/I_o \\ \frac{d}{dz} A_p &= -\gamma B_s (A_s B_s^* + A_p B_p^* \cos\theta)/I_o \\ \frac{d}{dz} B_p &= \gamma A_s (A_s^* B_s + A_p^* B_p \cos\theta)/I_o \end{aligned} \tag{67}$$

where we have taken $\phi = \pi/2$, and $\gamma$ is real and is given by

$$\gamma = \tfrac{1}{2}(2\pi/\lambda) n^3 r_{41} E^{sc}. \tag{68}$$

We notice from the coupled equation (67) that there are two contributions to the holographic index grating. The relative phase of these two contributions is very important because it determines whether these two parts enhance or destroy the index grating. Such a relative phase is determined by the relative phases of the four amplitudes. Thus, the energy exchange among the four waves depends on the input polarization states.

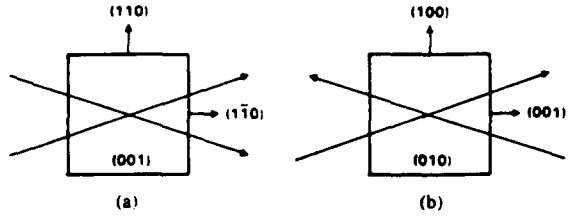


Fig. 7. (a) A configuration for codirectional cross polarization coupling in a cubic crystal of point group symmetry $\bar{4}3m$. (b) a configuration for contradirectional cross polarization coupling in the same class of crystals.

We now derive the solutions of these coupled equations. According to (67), the total intensity $I_o$ is a constant (i.e., independent of $z$). Thus, it is convenient to normalize the beam amplitudes such that $I_o = 1$. Here, remember that we neglect the material absorption in the coupled equation. We will obtain the closed form solutions of these coupled equations for the case of no absorption. In the case when the material absorption cannot be neglected, the solutions are obtained by simply multiplying an exponential factor accounting for the absorption. This is legitimate provided that all four waves have the same attenuation coefficient.

To obtain the solutions of the coupled equation (67), it is useful to employ some of the constants of integration which are given by

$$A_s A_s^* + B_p B_p^* = c_1 \tag{69}$$

$$A_p A_p^* + B_s B_s^* = c_2 \tag{70}$$

$$A_s A_p^* + B_s^* B_p = c_3 \tag{71}$$

$$A_s B_s - A_p B_p = c_4. \tag{72}$$

Using a change of variable similar to that used in [34] and [35], the coupled equations can be written

$$\frac{d}{dz} g = -\gamma (g^2 c_2 \cos\theta + g\sigma^* - c_1) \tag{73}$$

$$\frac{d}{dz} f = \gamma (f^2 c_1 \cos\theta + f\sigma - c_2) \tag{74}$$

where

$$f = A_p/A_s, \qquad g = B_p/B_s \tag{75}$$

$$\sigma = c_3 - c_3^* \cos\theta. \tag{76}$$

Equations (73) and (74) can be integrated, and the results are

$$f = A_p/A_s = [-\sigma + q \tanh(-q\gamma z/2 + C)]/(2c_1 \cos\theta)$$

$$g = B_p/B_s = [-\sigma^* + q^* \tanh (q^*\gamma z/2 + C')]/(2c_2 \cos\theta) \quad (77)$$

with

$$q^2 = 4c_1c_2 + \sigma^2 \quad (78)$$

where $C$ and $C'$ are constants of integration which are determined by the boundary condition at $z = 0$.

Once $f$ and $g$ are known, the intensity of all four waves is given by

$$|A_p|^2 = \frac{|f|^2c_1 - |fg|^2c_2}{1 - |fg|^2}$$

$$|B_p|^2 = \frac{|g|^2c_2 - |fg|^2c_1}{1 - |fg|^2}$$

$$|A_s|^2 = \frac{|A_p|^2}{|f|^2} = \frac{c_1 - |g|^2c_2}{1 - |fg|^2}$$

$$|B_s|^2 = \frac{|B_p|^2}{|g|^2} = \frac{c_2 - |f|^2c_1}{1 - |fg|^2}. \quad (79)$$

We now consider a special case of particular interest in which the cubic crystal is sandwiched between a pair of cross polarizers. Such a configuration is useful to eliminate unwanted background radiation which often causes noises in the detection of signals. The boundary conditions in this case may be taken as

$$A_p(0) = B_p(0) = 0. \quad (80)$$

Using (71) and (75)–(78), we have $f(0) = g(0) = 0$, $c_3 = 0$, and $\sigma = 0$, and the solutions become

$$f = -\frac{q \tanh (q\gamma z/2)}{2c_2 \cos\theta}$$

$$g = \frac{q \tanh (q\gamma z/2)}{2c_2 \cos\theta} \quad (81)$$

where $q = 2\sqrt{c_1c_2}$.

Taking $\theta = 0$, and using (79), the intensity of the four waves becomes

$$|A_s|^2 = c_1 \frac{1}{1 + \tanh^2 (q\gamma z/2)}$$

$$|A_p|^2 = c_2 \frac{\tanh^2 (q\gamma z/2)}{1 + \tanh^2 (q\gamma z/2)}$$

$$|B_s|^2 = c_2 \frac{1}{1 + \tanh^2 (q\gamma z/2)}$$

$$|B_p|^2 = c_1 \frac{\tanh^2 (q\gamma z/2)}{1 + \tanh^2 (q\gamma z/2)} \quad (82)$$

where $c_1 = |A_s(0)|^2$, $c_2 = |B_s(0)|^2$. Fig. 8(a) shows the variation of these intensities as functions of position for the case of $c_2/c_1 = 0.1$. We note that for strong coupling ($\gamma L >> 1$), one-half of the incident pump energy $A_s(0)$ is coupled to the $p$ component of the signal beam $B_p$, and one-half of the incident signal energy $B_s(0)$ is coupled to the $p$ component of the pump beam. As a result of the opposite signs in the wave amplitudes ($f < 0$), the two contributions to the index grating tend to cancel each other. Thus, when the energy of the $p$ components reaches one half of the incident energies, the coupling ceases.

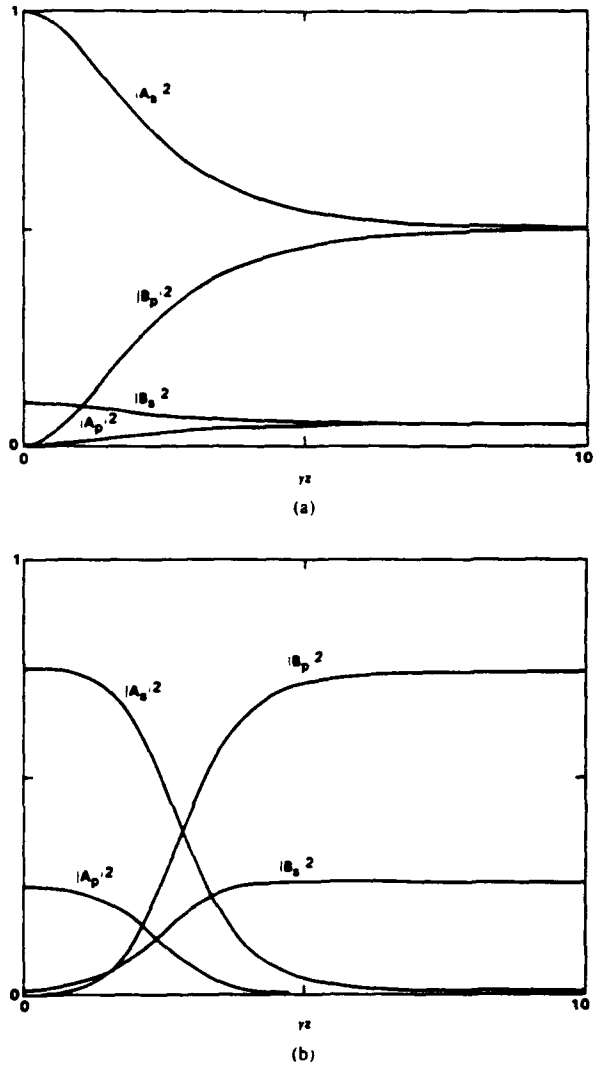


Fig. 8. Intensity of the four waves are plotted as functions of distance for various interaction situations. (a) Both incident beams are $s$-polarized (i.e., $(A_p(0) = B_p(0) = 0$, $c_2/c_1 = 0.1)$. (b) The pump beam is linearly polarized at an azimuth angle of 30° relative to the $s$ direction, and the signal beam is $s$-polarized, $c_2/c_1 = 0.01$.

It is possible that the $p$ component of the signal beam $B_p$ receives most of the incident pump energy $A_s$. Fig. 8(b) illustrates a case in which the pump beam has both $s$ and $p$ components, whereas the signal beam is $s$-polarized. We note that for strong coupling ($\gamma L >> 1$), most of the energy of the $s$ component of the pump beam is coupled to the $p$ component of the signal beam. The nonreciprocal transfer of energy is very similar to that of conventional two-wave mixing.

The exact solutions of (77) and (79) are useful when the coupling is strong ($\gamma L >> 1$) and the energy exchange is significant. For the case of weak coupling ($\gamma L << 1$), or very little pump depletion, we may assume that the pump beam amplitudes ($A_s$, $A_p$) remain virtually unchanged throughout the interaction. Under these conditions, the coupled equations become

$$\frac{d}{dz} B_s = \gamma a B_p + \gamma b B_s$$

$$\frac{d}{dz} B_p = \gamma c B_p + \gamma d B_s \tag{83}$$

where $a$, $b$, $c$, and $d$ are dimensionless constants and are given by

$$a = |A_p|^2 \cos\theta / I_o$$

$$b = A_p A_s^* / I_o$$

$$c = A_s A_p^* \cos\theta / I_o$$

$$d = |A_s|^2 / I_o. \tag{84}$$

We note that the magnitude of all four of these constants is less than unity.

The coupled equation (83) can be easily integrated and the results are

$$B_s(z) = \left\{[bB_s(0) + aB_p(0)] \exp[(b + c)\gamma z] + [cB_s(0) - aB_p(0)]\right\}/(b + c)$$

$$B_p(z) = \left\{c[bB_s(0) + aB_p(0)] \exp[(b + c)\gamma z] - b[cB_s(0) - aB_p(0)]\right\}/[a(b + c)] \tag{85}$$

where $B_s(0)$ and $B_p(0)$ are the amplitudes of the signal beams at $z = 0$.

If we set $B_p(0) = 0$ in (85), we obtain

$$B_s(z) = B_s(0)[be^{(b+c)\gamma z} + c]/(b + c)$$

$$B_p(z) = B_s(0)bc[e^{(b+c)\gamma z} - 1]/[a(b + c)]. \tag{86}$$

If we assume further that $\gamma z << 1$, (86) can be written approximately as

$$B_s(z) = B_s(0) + B_s(0) \frac{A_p A_s^*}{I_o} \gamma z$$

$$B_p(z) = B_s(0) \frac{|A_s|^2}{I_o} \gamma z. \tag{87}$$

We note that the amplitude of $B_s$ may increase or decrease depending on the polarization state of the pump beam $A$, whereas the amplitude $B_p$ is an increasing function of $\gamma z$.

In the above derivation, a spatial phase shift between the index grating and the intensity pattern was assumed to be exactly $\pi/2$, which corresponds to the case of pure diffusion (i.e., no externally-applied static electric field). In the event when the spatial phase shift is not $\pi/2$, (69)–(72) are still valid and exact solutions are still available. They are given by

$$f = A_p/A_s = [-\sigma + q \tanh(ieq\gamma z/2 + C)]/(2c_1 \cos\theta) \tag{88}$$

$$g = B_p/B_s = [-\sigma^* + q^* \tanh(ie^* q^* \gamma z/2 + C')]/(2c_2 \cos\theta) \tag{89}$$

where $e$ is an exponential factor given by

$$e = \exp(i\phi). \tag{90}$$

We note that the solutions are formally identical to the previous case, except the complex phase factors $ie^*$ and $-ie$ in the argument of the transcendental function. Deviation from $\sigma = \pi/2$ is known to occur in nondegenerate two-wave mixing [see (46)]. Such a deviation for the case of degenerate two-wave mixing has been observed in oxide crystals such as $BaTiO_3$ and $Sr_{0.6}Ba_{0.4}Nb_2O_6$ [36].

For the special case of particular interest in which the cubic crystal is sandwiched between a pair of cross polarizers, the boundary conditions are given by (8). Using (71) and (75)–(78), we have $f(0) = g(0) = 0$, $c_3 = 0$, and $\sigma = 0$, and the solutions become

$$f = \frac{q \tanh(ieq\gamma z/2)}{2c_1 \cos\theta}$$

$$g = \frac{q \tanh(ie^* q\gamma z/2)}{2c_2 \cos\theta} \tag{91}$$

where $q = 2\sqrt{c_1 c_2}$.

Consider the special case of $\phi = 0$. The solutions (91) become

$$f = \frac{iq \tan(q\gamma z/2)}{2c_1 \cos\theta}$$

$$g = \frac{iq \tan(q\gamma z/2)}{2c_2 \cos\theta} \tag{92}$$

Taking $\theta = 0$, and using (79), the intensity of the four waves becomes

$$|A_s|^2 = c_1 \cos^2(q\gamma z/2)$$

$$|A_p|^2 = c_2 \sin^2(q\gamma z/2)$$

$$|B_s|^2 = c_2 \cos^2(q\gamma z/2)$$

$$|B_p|^2 = c_1 \sin^2(q\gamma z/2) \tag{93}$$

where $c_1 = |A_s(0)|^2$, $c_2 = |B_s(0)|^2$. Note that the intensities of these waves are periodic functions of $z$. This is distinctly different from the case when $\phi = \pi/2$. The case of $\phi = 0$ corresponds to a pure local response of the material. Although the energy is exchanged back and forth between $A_s$ and $B_p$ as well as between $A_p$ and $B_s$, there is no nonreciprocal energy transfer. In other words, there is no unique direction of energy flow as compared with the case when $\phi \neq 0$. For cases with $0 < |\phi| < \pi$, nonreciprocal energy transfer is possible according to our so-

lutions (88) and (89) with maximum energy transfer at $\phi = \pm\pi/2$.

### C. Contradirectional Cross Coupling

Referring to Fig. 7(b), we consider a case of contradirectional coupling which does not permit the parallel coupling to occur. The two beams enter the crystal in such a way that the grating wave vector is along the [001] direction of the crystal. In this configuration, the unit vector $\vec{s}$ is parallel to [010] and the unit vectors $\vec{p}_1$, $\vec{p}_2$ are perpendicular to [010]. The amplitude of the induced index grating $\epsilon_1$ can thus be written, according to (59),

$$\epsilon_1 = n^4 r_{41} \begin{pmatrix} 0 & 1 & 0 \\ 1 & 0 & 0 \\ 0 & 0 & 0 \end{pmatrix} E^{sc} \tag{94}$$

where $E^{sc}$ is the amplitude of the space-charge field.

According to (62) and (94), and after few steps of algebra, the coupling constants can be written

$$\Gamma_{ss} = \Gamma_{p_1p_2} = 0$$

$$\Gamma_{sp_1} = \Gamma_{p_1s} = \Gamma_{sp_2} = \Gamma_{p_2s} = n^4 r_{41} E^{sc} \cos(\theta/2) \tag{95}$$

where we assume that the beams enter the crystal symmetrically [see Fig. 7(b)] such that

$$\beta_1 = -\beta_2 = -(2\pi/\lambda) n \cos(\theta/2). \tag{96}$$

We now substitute (95) and (96) into the coupled equation (60). This leads to

$$\frac{d}{dz} A_s = \gamma B_p (A_s B_s^* + A_p B_p^* \cos\theta)/I_o$$

$$\frac{d}{dz} B_s = \gamma A_p (A_s^* B_s + A_p^* B_p \cos\theta)/I_o$$

$$\frac{d}{dz} A_p = \gamma B_s (A_s B_s^* + A_p B_p^* \cos\theta)/I_o$$

$$\frac{d}{dz} B_p = \gamma A_s (A_s^* B_s + A_p^* B_p \cos\theta)/I_o \tag{97}$$

where we have taken $\phi = \pi/2$, and $\gamma$ is real and is given by

$$\gamma = \tfrac{1}{2}(2\pi/\lambda) n^3 r_{41} E^{sc}. \tag{98}$$

Notice that the coupled mode equation (97) is similar to that of (67), except for the signs. The difference in signs is due to the direction of propagation of the pump beam ($A_s$, $A_p$). As a result of this difference, the total intensity $I_o$ is no longer a constant. According to (97), $(A_s^* A_s + A_p^* A_p - B_s^* B_s - B_p^* B_p)$, which is proportional to the net Poynting power flow along the $+z$ direction, is a constant [37]. There are other constants of integration. These include

$$A_s^* A_s - B_p^* B_p = c_1$$

$$A_p^* A_p - B_s^* B_s = c_2$$

$$A_s A_p^* - B_s B_p^* = c_3$$

$$A_s B_s - A_p B_p = c_4. \tag{99}$$

Because $I_o$ is not a constant, the integration of the coupled equation (97) is not as simple as that of (67). As of now, there is no closed form solution available. However, numerical techniques can be used to integrate the coupled equations.

For the case of no pump depletion, we may treat $A_s$ and $A_p$ as constants. In this case, the coupling equations for $B_s$ and $B_p$ are identical to those of the codirectional coupling, and the solutions are given by (85) and (86).

In summary, we have derived a general theory of the coupling of polarized beams in cubic photorefractive crystals. As a result of the optical isotropy of the crystal and the tensor nature of the holographic photorefractive grating, cross-polarization energy coupling occurs. Exact solutions for the case of codirectional coupling are obtained. Such cross-polarization coupling may be useful for the suppression of background noises.

### D. Cross-Polarization Two-Beam Coupling in GaAs Crystals

Cross-polarization two-beam coupling has been observed in GaAs crystals recently. The experimental results are in good agreement with the coupled-mode theory presented earlier [31]–[33].

In a contradirectional two-beam coupling experiments as described in [33], a 1.15 $\mu m$ beam from a He–Ne laser is split into two by a beam splitter. The two beams intersect inside a liquid-encapsulated Czochralski (LEC) grown, undoped, semiinsulating GaAs crystal from opposite sides of the (001) faces [see Fig. 7(b)]. The intersecting angle of two beams is approximately 168°. The wave vector of the induced index grating is along the [001] crystalline direction.

One beam, $B$, is polarized along the [010] direction ($s$-polarization) using a polarizer, which fits the condition of $B_p(0) = 0$. The other beam, $A$, is transmitted through another polarizer (along the [100] direction), followed by a half-wave plate, which is used to vary the polarization of the pump beam. The power of beams $A$ and $B$ is 80 mW/cm$^2$ and 1 mW/cm$^2$, respectively. The GaAs crystal is 5 mm thick. The gain coefficient of the crystal measured with the regular beam-coupling configuration is about 0.1/cm. These values fit well with the conditions of no beam $A$ depletion and $\gamma L \ll 1$, which are used to derive (87). A mechanical chopper, which operates at 100 Hz, is used to modulate beam $A$. An analyzer is placed in front of a Ge photodetector. The analyzer is used so that the intensity of both the $s$ and $p$ components of transmitted beam $B$ can be measured. The signal from the photodetector was amplified by a current amplifier, whose output can be used as the dc component of $|B_s(L)|^2$. A lock-in amplifier is used to measure the ac component of $|B_s(L)|^2$ and $|B_p(L)|^2$.

According to (87), the beam intensities can be written

$$|B_s(L)|^2 = |B_s(0)|^2[1 + (\sin 2\psi)\gamma L] \quad (100)$$

$$|B_p(L)|^2 = |B_s(0)|^2[(\cos\psi)^4(\gamma L)^2] \quad (101)$$

where $|B_s(0)|^2$ is the intensity of beam $B$ at $z = 0$ and $\psi$ is the angle between the $\vec{s}$ vector and the polarization direction of beam $A$. In addition, we have used the intensity of beam $A$ to be approximately equal to $I_o$ and neglected the $(\gamma L)^2$ term in the first equation of (87). There are several interesting features in (87) which should be pointed out. $|B_s(L)|^2$ may increase or decrease depending on the polarization state of the pump beam $A$, whereas $|B_p(L)|^2$ is an increasing function of $\gamma L$. Both $|B_s(L)|^2$ and $|B_p(L)|^2$ are independent of $\theta$. The ac component of $|B_s(L)|^2$ has a function of $\sin 2\psi$ which has a maximum at $\psi = 45°$ and a minimum of $\psi = 135°$, whereas $|B_p(L)|^2$ is a function of $(\cos\psi)^4$ and has maxima at $\psi = 0$ and 180°. These features have been validated with experimental data [33].

In addition, it is observed that the maximum value of $|B_p(L)|^2$ is smaller than the maximum ac component of $|B_s(L)|^2$ by a factor of 0.052. From (100) and (101), it is clear that the factor of 0.52 is $\gamma L$. This leads to $\gamma = 0.104$/cm, which is practically the same as the $\gamma$ of the sample measured by a regular beam-coupling technique.

In codirectional interaction configurations, the output of a CW Nd:YAG laser beam was used [31]. A laser beam operating at 1.06 $\mu$m was split into two by a beam splitter and then recombined inside a semiinsulating (undoped) GaAs crystal. The beam diameter of both beams was about 1 mm just before entering the crystal. The intensities of the pump and the probe were about 1 W/cm$^2$ and 10 mW/cm$^2$, respectively, and the angle between the beams was 90° outside the crystal. A neutral density filter was used in the probe beam to achieve the desired intensity ratio between the pump and the probe. The half-wave plate $\lambda/2$ was used in the pump beam to control the initial mixture of the $s$ and $p$ components. Also, a chopper was used to modulate the pump beam at about 100 Hz. Finally, the probe beam transmitted through the crystal was analyzed by a polarizing beam splitter, and the $p$ and $s$ components were simultaneously monitored independently by two photodetectors. Various polarization states of the pump beam were achieved by rotating the half-wave plate, while both $|B_s(L)|^2$ and $|B_p(L)|^2$ were monitored simultaneously. There is good agreement between the experimental data and the theoretical calculations.

The coupling coefficient can be calculated from (100) and (101). One can solve for the coupling $\gamma L$ by taking the ratio of the measured value of $|B_s(L)|^2$ and $|B_p(L)|^2$ at $\psi = 0$. Using the measured interaction length $L$ of 0.5 cm, we have calculated the cross-polarization coupling coefficient $\gamma$ to be about 0.4 cm$^{-1}$. This value is consistent with the gain coefficient measured for parallel-polarization coupling in the same sample. According to the theory, the gain coefficients for both parallel- and cross-polarization coupling should be the same. The coupling coefficient of $\gamma = 2.6$ cm$^{-1}$ has been observed recently in a sample of GaAs crystal [38]. Using moving fringes in the GaAs/Cr crystal, an even higher coupling coefficient of $\gamma = 6 \sim 7$ cm$^{-1}$ has also been reported [39]. Such coupling coefficients allow the possibility of net gain (amplification) in two-wave mixing.

## IV. Kerr Media

In the above discussion, we notice that the nonlocal response (i.e., $\phi \neq 0$) in photorefractive media plays a key role in the nonreciprocal energy transfer. The existing materials such as $BaTiO_3$, $LiNbO_3$, SBN, BSO, BGO, etc. are very slow and are also effective only for visible light. Photorefractive crystals such as GaAs, CdTe, GaP, InP, and other semiconductors are faster and are also effective in the near-IR spectral region [25], [26]. However, for high-power laser application, these solids are no longer useful. Gases or fluids, because of their optical isotropy and local response, have never been considered as candidate materials for degenerate two-wave mixing. In what follows, we show that nonlocal response in gases or fluids can be artificially induced by applying an external field or simply by moving the media. Using such a concept, gases or fluids become the best candidate materials for high power laser beam coupling. Energy coupling also occurs in stationary media when the frequencies of the two beams are properly detuned, as in SBS and SRS.

### A. Two-Wave Mixing in Kerr Media

The concept of using moving gratings in local media for energy coupling was first proposed in 1973 by a group of Soviet scientists [41]–[44]. It was recognized that a spatial phase shift between the index grating and the light intensity pattern can be induced by moving the grating relative to the medium. Such a spatial phase shift is a result of the inertia (temporal) of the hologram formation process and leads to a nonreciprocal energy transfer. If the formation time of the hologram is finite, a spatial phase shift occurs when the intensity pattern is moving relative to the medium. In addition to the phase shift, such a motion also leads to a decrease in the depth of modulation of the induced index grating. Several possibilities of achieving such a spatial phase shift have been proposed. These include moving the medium itself relative to a thermally induced grating [41], using the Lorentz force to move free-carrier grating in a semiconducting medium [45], and nondegenerate two-wave mixing in which a frequency shift between the beams results in a moving grating [46]–[49]. It is important to note that a temporal phase shift itself is not enough for energy coupling. The induced index grating must be physically shifted in space relative to the intensity pattern in order to achieve energy coupling.

It is known that the Kerr effect in gases or fluids is a local effect. In media with local response ($\phi = 0$), there is no steady-state transfer of energy between two lasers of the same frequency. In what follows, we will show that nonlocal response can be induced by moving the Kerr medium relative to the beams. Such an induced nonlocal re-

sponse is only possible when the material response time $\tau$ is finite.

The propagation of electromagnetic waves in media possessing a strong Kerr effect is one subject of long and sustained interest. A number of interesting phenomena manifest themselves at high incident beam powers. This includes self-phase modulation, mode-locking and self-focusing. The effect is described by a dependence of the index of refraction on the electric field according to

$$n = n_o + n_2\langle E^2\rangle \tag{102}$$

where $n_o$ is the index of refraction, $n_2$ is the Kerr coefficient (see Appendix A), and $\langle E^2\rangle$ is the time average of the varying electric field.

Consider the case of degenerate two-wave mixing. The time average of the electric field, is given by

$$\langle E^2\rangle = E_o^2[1 + \cos(\vec{K}\cdot\vec{r})] \tag{103}$$

where we assume $E_o = A_1 = A_2$. The index of refraction, according to (102) and (103), is given by

$$n = n_o + n_2E_o^2[1 + \cos(\vec{K}\cdot\vec{r})]. \tag{104}$$

Comparing (104) with (103), we note that the response is local and there can be no energy coupling, even if $n_2$ is complex.

Using the interference of two beams with different frequencies, a moving fringe pattern can be obtained inside the medium. As a result of the finite temporal response of the material, a spatial phase shift exists between the induced index grating and the intensity pattern. Such a finite phase shift leads to energy transfer between the beams. Coupled-mode analysis has been used to study the beam coupling in these media [40]. In what follows, we describe the coupling of two beams with different frequencies in the codirectional configuration.

Inside the Kerr medium, the two waves form an interference pattern which corresponds to a spatially periodic variation of the time-averaged field $\langle E^2\rangle$. In a Kerr medium, such a periodic intensity produces a volume grating. Thus, the problem we address is most closely related to the phenomenon of self-diffraction from an induced grating. The formulation of such a problem is very similar to that of the holographic two-wave coupling in photorefractive crystals [8], [9], [12]. However, there exists a fundamental difference between these two types of two-wave mixing. In photorefractive media, the index modulation is proportional to the contrast of the interference fringes, whereas in Kerr media the index modulation is directly proportional to the field strength. Thus, in Kerr media the coupling strength is proportional to the beam intensities, whereas in photorefractive media the coupling strength is determined by the ratio of beam intensities.

Let the electric field of the two waves be written

$$E_j = A_j\exp[i(\omega_j t - \vec{k}_j\cdot\vec{r})] \qquad j = 1, 2 \tag{105}$$

where $\omega_j$'s are the frequencies and $\vec{k}_j$'s are the wave vectors. In (105), we assume for simplicity that both waves are $s$-polarized and the medium is isotropic. We further assume that no optical rotation is present in the material. $A_1$ and $A_2$ are the amplitudes and are taken as functions of $z$ only for a steady-state situation. The $z$ axis is taken normal to the surface of the medium (see Fig. 9).

In the Kerr medium (from $z = 0$ to $z = L$), these two waves generate an interference pattern. Such a pattern is traveling if $\omega_1 \neq \omega_2$. This interference pattern is described by $\langle E^2\rangle$, where $E$ is the total electric field

$$E = E_1 + E_2 \tag{106}$$

and the averaging is taken over a time interval $T$ such that

$$\omega_1 T \gg 1, \quad \omega_2 T \gg 1 \tag{107}$$

and

$$|\omega_2 - \omega_1|T \ll 1. \tag{108}$$

Using $\langle E^2\rangle = \frac{1}{2}\,\mathrm{Re}\,[E^*E]$ and (105) and (106), we obtain

$$\langle E^2\rangle = \tfrac{1}{2}\{|A_1|^2 + |A_2|^2 + A_1^*A_2e^{i(\Omega t - \vec{K}\cdot\vec{r})} + A_1A_2^*e^{-i(\Omega t - \vec{K}\cdot\vec{r})}\} \tag{109}$$

where

$$\Omega = \omega_2 - \omega_1 \tag{110}$$

$$\vec{K} = \vec{k}_2 - \vec{k}_1. \tag{111}$$

This interference pattern [(109)] induces a volume index grating via the Kerr effect. In general, the index grating will have a finite phase shift relative to the interference pattern because of the time-varying nature of the pattern. Thus, we can generalize (102) and write the index of refraction including the fundamental components of the Kerr-induced grating as

$$n = n_o + \Delta n_o + \tfrac{1}{2}\{n_2e^{i\phi}A_1^*A_2e^{i(\Omega t - \vec{K}\cdot\vec{r})} + \text{c.c.}\} \tag{112}$$

where both $\phi$ and $n_2$ are real and $\Delta n_o$ is a uniform change in index. Here again for the sake of simplicity we assume a scalar grating. The phase $\phi$ indicates the degree to which the index grating is temporally delayed (or spatially shifted) with respect to the interference pattern. Generally speaking, both $n_2$ and $\phi$ are functions of $\Omega$.

Here, $n_2\exp(i\phi)$ can be regarded as a complex Kerr coefficient. The finite phase shift is a result of the finite response of the material. A complex Kerr coefficient corresponds to a complex third-order nonlinear optical polarizability. It is known that the imaginary part of the third-order nonlinear optical polarizability is responsible for phenomena such as stimulated Brillouin scattering and stimulated Raman scattering [3]. Thus, we expect that the complex Kerr coefficient induced by moving gratings will also lead to energy coupling between the two waves.

To illustrate the physical origin of such a finite phase shift, we will now examine a classical model. In this

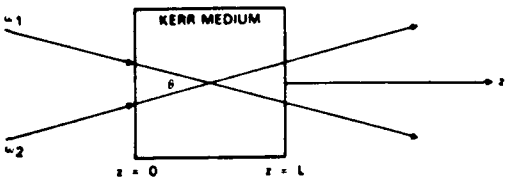


Fig. 9. Schematic drawing of two-wave mixing in Kerr media.

model, we assume that the formation of the holographic grating is instantaneous and the decay constant $\tau$ is finite. When the two waves are degenerate in frequency, a steady-state nonlinear response is described by (102) without phase shift. In the case of nondegenerate two-wave mixing, the intensity fringe, as described by (109), is moving in the nonlinear medium at a constant speed. The steady-state value of the self-induced index change must be derived from a treatment which considers the finite response time of the medium with respect to the displacement speed. Let the decay of index change be exponential, then the steady-state index change can be written

$$\Delta n = \frac{1}{\tau} n_{20} \int_{-\infty}^{t} \langle E^2(t') \rangle e^{(t'-t)/\tau}\, dt' \qquad (113)$$

where $n_{20}$ is the value of index change for the degenerate case.

Integration of (113) yields the following expression for $n_2 \exp(i\phi)$:

$$n_2 \exp(i\phi) = \frac{n_{20}}{1 + i\Omega\tau}. \qquad (114)$$

Note that the finite phase shift is related to the motion of the intensity pattern relative to the nonlinear medium. In addition to the finite phase shift, the motion of the fringe pattern relative to the medium also causes the index modulation to increase. According to (112) and (114), the index grating is spatially shifted relative to the intensity pattern by

$$\phi = -\tan^{-1}(\Omega\tau) \qquad (115)$$

where we recall that $\tau$ is the response time of the medium.

*1) Codirectional Two-Wave Mixing:* Now, by using (112) for $n$ and the scalar wave equation and by using the parabolic approximation (i.e., slowly-varying amplitudes), we can derive the following coupled equations:

$$\frac{d}{dz} A_1 = -i \frac{\omega^2 n_0 n_2}{2k_z c^2} e^{-i\phi} |A_2|^2 A_1$$

$$\frac{d}{dz} A_2 = -i \frac{\omega^2 n_0 n_2}{2k_z c^2} e^{i\phi} |A_1|^2 A_2 \qquad (116)$$

where we assume that $\omega_2 \simeq \omega_1 = \omega$, and $k_z$ is the $z$ component of the wave vectors (i.e., $k_z = k_1 \cos \frac{1}{2}\theta = k_2 \cos \frac{1}{2}\theta$). The parameter $\theta$ is the angle between the two beams. In (116), we have neglected the term $\Delta n_0$.

We now write

$$A_1 = \sqrt{I_1} e^{-i\psi_1}, \quad A_2 = \sqrt{I_2} e^{-i\psi_2} \qquad (117)$$

where $\psi_1$ and $\psi_2$ are the phases of the amplitudes $A_1$ and $A_2$, respectively. Using (116) and (117), the coupled equations (116) can be written as

$$\frac{d}{dz} I_1 = -gI_1 I_2 - \alpha I_1$$

$$\frac{d}{dz} I_2 = gI_1 I_2 - \alpha I_2 \qquad (118)$$

and

$$\frac{d}{dz} \psi_1 = \beta I_2$$

$$\frac{d}{dz} \psi_2 = \beta I_1 \qquad (119)$$

where

$$g = \frac{2\pi}{\lambda \cos(\theta/2)} n_2 \sin\phi, \quad 0 \le \theta < \pi/2 \qquad (120)$$

$$\beta = \frac{\pi}{\lambda \cos(\theta/2)} n_2 \cos\phi. \qquad (121)$$

In (118), we have added the attenuation term due to bulk absorption. The parameter $\alpha$ is the absorption coefficient. Note that beam 2 will be amplified, provided $gI_1 > \alpha$, according to (118). Also notice that the coupled equations (118) are exactly identical to those of the stimulated Brillouin scattering and stimulated Raman scattering. Solutions for the lossless case had been derived by previous workers [2]. We now derive the solution for the case of lossy nonlinear medium. Using the classical model mentioned above, beam 2 will gain energy from beam 1, provided that the phase shift $\phi$ is positive. Thus, according to (115), the low-frequency beam will always see gain.

The coupled equations (118) can be integrated exactly, and the solution is (see Appendix B)

$$I_1(z) = I_1(0) \cdot \frac{1 + m^{-1}}{1 + m^{-1} \exp\left[\frac{\gamma}{\alpha}(1 - e^{-\alpha z})\right]} \cdot e^{-\alpha z} \qquad (122)$$

$$I_2(z) = I_2(0) \cdot \frac{1 + m}{1 + m \exp\left[\frac{\gamma}{\alpha}(1 - e^{-\alpha z})\right]} \cdot e^{-\alpha z} \qquad (123)$$

where $m$ is the input beam ratio

$$m = \frac{I_1(0)}{I_2(0)} \qquad (124)$$

and $\gamma$ is given by

$$\gamma = g[I_1(0) + I_2(0)]. \qquad (125)$$

Substituting (122) and (123) for $I_1$ and $I_2$, respectively, into (119) and carrying out the integrations, we obtain

$$\psi_1(z) - \psi_1(0) = \frac{\beta}{g} \log \left\{ \frac{1 + m^{-1}}{1 + m^{-1} \exp\left[\frac{\gamma}{\alpha}(1 - e^{-\alpha z})\right]} \right\} \tag{126}$$

and

$$\psi_2(z) - \psi_2(0) = -\frac{\beta}{g} \log \left\{ \frac{1 + m}{1 + m \exp\left[\frac{\gamma}{\alpha}(1 - e^{-\alpha z})\right]} \right\}. \tag{127}$$

Note that according to (126) and (127), the phases of the two waves are not coupled. In other words, these two waves can exchange energy without any phase crosstalk. Such a phenomenon has been known in stimulated Raman scattering for some time, and can be employed to pump a clean signal beam with an aberrated beam. Here, the result can be applied to more cases, including forward stimulated Brillouin scattering.

If we neglect absorption (i.e., $\alpha = 0$), then $I_2(z)$ is an increasing function of $z$ and $I_1(z)$ is a decreasing function of $z$, according to (122) and (123), provided $\gamma$ is positive. Transmittance for both waves for the lossless case, according to (122) and (123), is

$$T_1 = \frac{I_1(L)}{I_1(0)} = \frac{1 + m^{-1}}{1 + m^{-1} \exp(\gamma L)}$$

$$T_2 = \frac{I_2(L)}{I_2(0)} = \frac{1 + m}{1 + m \exp(\gamma L)} \tag{128}$$

where $m$ is the incident intensity ratio $m = I_1(0)/I_2(0)$. Note that $T_2 > 1$ and $T_1 < 1$ for positive $\gamma$. The sign of $\gamma$ is determined by the sign of $n_2$ and the phase shift $\phi$. Interestingly, these expressions are formally identical to those of the photorefractive coupling. The major difference is that the $\gamma$ for Kerr media is proportional to the total power density of the waves, according to (125).

Fig. 10 illustrates the intensity variation with respect to $z$ for the case when $g = 10$ cm/MW, $\alpha = 0.1$ cm$^{-1}$, $I_1(0) = 100$ kW/cm$^2$, and $I_2(0) = 1$ kW/cm$^2$. Note that even with the presence of absorption, the intensity of beam 2 increases as a function of $z$ until $z = l_c$, where the gain equals the loss. Beyond $z = l_c$, the intensities of both beams are decreasing functions of $z$.

Similar results were obtained earlier by other workers in a study of stimulated scattering of light from free carriers in semiconductors [50].

According to (114), (115), and (120), the gain coefficient $g$ is a function of the frequency detuning and can be written

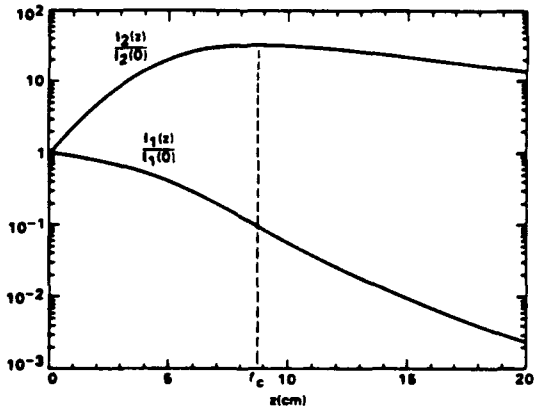


Fig. 10. Intensity variation with respect to $z$ in the Kerr medium.

$$g = \frac{2\pi n_{20}}{\lambda \cos(\theta/2)} \cdot \frac{-\Omega\tau}{1 + (\Omega\tau)^2} \tag{129}$$

where we recall that $\Omega = \omega_2 - \omega_1$ is the frequency detuning and $\tau$ is the grating decay time constant. We notice that the gain coefficient is positive for the beam with lower frequency provided that $n_{20}$ is positive. Such a gain coefficient is maximized at $\Omega\tau = \pm 1$. Such a dependence on frequency detuning can be used to measure the time constant $\tau$. Some experimental works will be discussed in Section IV-E.

*2) Contradirectional Two-Wave Mixing:* We now consider the case of contradirectional two-wave mixing in which beam 1 enters the medium at $z = 0$, and beam 2 enters the medium at $z = L$. The coupled-mode equations for the beam intensities can be obtained in a similar manner and are written

$$\frac{d}{dz} I_1 = -g I_1 I_2 - \alpha I_1$$

$$\frac{d}{dz} I_2 = -g I_1 I_2 + \alpha I_2 \tag{130}$$

where the intensity gain coefficient $g$ is given by

$$g = \frac{2\pi}{\lambda \sin(\theta/2)} n_2 \sin\phi, \quad \pi/2 < \theta \leq \pi. \tag{131}$$

We notice a slight difference between the two cases as compared with (120) for the codirectional coupling. Here, we recall that $\theta$ is the angle between the positive direction of the two wave vectors. Thus, for codirectional coupling, the angle $\theta$ is always less than 90°, whereas $\pi/2 < \theta < \pi$ for the contradirectional coupling. This is a result of the boundary condition in which we assume that the waves and the medium are all of infinite extent in a plane perpendicular to the $z$ axis.

Solutions of (130) for the case of lossless medium are given by

$$\frac{I_1(z)}{I_1(0)} = \frac{1-\rho}{1-\rho e^{-g\sigma z}}$$

$$\frac{I_2(z)}{I_2(0)} = \frac{1-\rho}{e^{g\sigma z}-\rho} \tag{132}$$

where $\sigma$ and $\rho$ are constants and are related to the intensities at $z = 0$,

$$\rho = \frac{I_2(0)}{I_1(0)}$$

$$\sigma = I_1(0) - I_2(0). \tag{133}$$

The constant $\sigma$ may be regarded as the net power flux through the medium.

The solutions of (132) are expressed in terms of $I_1(o)$ and $I_2(0)$, which are not input intensities. In the contradirectional coupling, we note that the incident intensities are $I_1(0)$ and $I_2(L)$.

For interaction $L$, such that $gaL >> 1$, the intensity growth for beam 2 is exponential and is given by, according to (124),

$$I_2(0) \simeq \frac{I_2(L)}{(1-\rho)} e^{g\sigma L}. \tag{134}$$

In SBS, $I_2(L)$ is virtually zero and represents intensity of noises or scattered light. The parameter $\rho = I_2(0)/I_1(0)$ is the phase-conjugate reflectivity of the SBS process. It is always less than unity for two reasons. First, in SBS there is no beam 2 incident at $z = L$; therefore, $\rho \leq 1$ is required by the conservation of energy. Second, the exponential gain per unit length $g\sigma$ is proportional to the power throughput. A reflectivity of $\rho = 100$ indicates a zero power flux and consequently zero gain.

### *B. Electrostrictive Kerr Effects*

The Kerr effect arises from several physical phenomena. These include molecular orientation, molecular redistribution, third-order nonlinear polarizability [3], electrostriction, and thermal changes. In liquids such as $CS_2$, contribution to the Kerr effect is dominated by the electrostriction.

The coupling of two electromagnetic waves via electrostriction has been known for some time and is responsible for SBS. Although this subject has been studied extensively [51], little attention has been paid to the "photorefractive" nature of such a process, which, we believe, can provide a great deal of insight into generalizing the SBS process. For example, there exists a similar spatial phase shift of 90° between the induced index grating and the light interference pattern in conventional SBS [52]. Such a spatial phase shift of 90° is responsible for the energy exchange between the incident wave and the phase-conjugated wave in SBS. In addition, self-pumped phase conjugation in $BaTiO_3$ crystals [53], [54] is very similar to the phase conjugation in SBS [55], [56]. The spatial phase shift of 90° can be utilized in other SBS configurations (e.g., injected SBS at $\theta \neq 180°$). In this section, we investigate the photoinduced index grating in nondegenerate two-wave mixing and focus our attention on the complex Kerr coefficient and the spatial phase shift.

Basic equations for the electrostrictive coupling between photons and phonons have been formulated and several theoretical papers on SBS have been published [51]. Most of the earlier work was concentrated on backward-wave coupling. Very little attention was paid to codirectional nondegenerate two-wave mixing. The mathematical formulation of such a coupling in Kerr media including material absorption has been recently solved and is described in Section IV-A. In this section, we focus our attention on the derivation of the photoinduced index grating as well as the relation between the photoelastic coefficient and the electrostrictive constant.

The electrostrictive pressure in liquids is given by

$$p = -\tfrac{1}{2}\gamma \langle E^2 \rangle \tag{135}$$

where $\langle E^2 \rangle$ is the time average of the varying electric field and is given by (109), and $\gamma$ is the electrostrictive coefficient which is defined as

$$\gamma = \rho\left(\frac{\partial \epsilon}{\partial \rho}\right) \tag{136}$$

where $\rho$ is the density and $\epsilon$ is the dielectric constant.

As a result of the electrostrictive pressure according to (135) and (109), a density wave in the medium is generated. By solving the isothermal Navier–Stokes equation [51] we obtain the complex amplitude of the induced density wave as

$$\Delta\rho = -\frac{1}{2}\frac{K^2\gamma}{\Omega^2 - \Omega_B^2 - i\Omega\Gamma_B} A_1^* A_2 e^{i(\Omega t - \vec{K}\cdot\vec{r})} \tag{137}$$

where $\Omega_B$ may be regarded as the resonance phonon frequency and is given by

$$\Omega_B = vK \tag{138}$$

with $v$ as the velocity of the acoustic wave, and $\Gamma_B$ is the inverse of the phonon lifetime and is given by

$$\Gamma_B = \eta K^2/\rho \tag{139}$$

with $\eta$ as the viscosity coefficient.

Using $\Delta\epsilon = 2n\epsilon_0\Delta n$ and the definition of the electrostrictive coefficient equation (135), we obtain the linear relation between the index grating and the density wave

$$\Delta n = \frac{\gamma}{2n\rho\epsilon_0}\Delta\rho. \tag{140}$$

Using the complex number representation, the induced index change can be written, according to (112),

$$\Delta n = n_2 e^{i\Phi} A_1^* A_2 e^{i(\Omega t - \vec{K}\cdot\vec{r})}. \tag{141}$$

Substituting (141) for $\Delta n$ and (137) for $\Delta\rho$ in (140), we obtain the following expression for the complex Kerr coefficient:

$$n_2 e^{i\Phi} = \frac{-K^2\gamma^2}{4n\rho\epsilon_0(\Omega^2 - \Omega_B^2 - i\Omega\Gamma_B)}. \tag{142}$$

Note that this complex Kerr coefficient is a function of the frequency difference between the two waves. At resonance $\Omega = \pm\Omega_B$, the Kerr coefficient is purely imaginary, indicating a 90° phase shift between the index grating and the intensity pattern.

The complex Kerr coefficient derived above is different from the traditional one used in self-focusing and self-phase modulation as described in [61]. The Kerr coefficient measured in those experiments may be regarded as the dc Kerr coefficient and is related to that of (142) by putting $\Omega = 0$. Such a dc Kerr coefficient is written

$$n_2(\Omega = 0) = \frac{\gamma^2}{4n\rho v'^2\epsilon_0} \quad \phi = 0 \tag{143}$$

where we recall that $v'$ is the acoustic velocity and $\rho$ is the density. At resonance ($\Omega = \pm\Omega_B$), the Kerr coefficient becomes, according to (142),

$$n_{2\text{Res}} = \frac{\gamma^2}{4n\rho v'^2\epsilon_0}\left(\frac{\Omega_B}{\Gamma_B}\right) \quad \phi = \pm\pi/2 \tag{144}$$

where the sign $\pm$ depends on the sign of $\Omega = \omega_2 - \omega_1$. According to (120) and (144), we note that gain coefficient $g$ is positive when $\omega_2 < \omega_1$. In other words, the beam with lower frequency always gains.

Notice that the magnitude of the Kerr coefficient at resonance is increased by a factor of

$$Q = \frac{\Omega_B}{\Gamma_B} \tag{145}$$

which may be regarded as the $Q$ parameter of the acoustic oscillation.

This parameter $Q$ depends on the phonon frequency and thus depends on the angle between the two beams at acoustic resonance. According to (138) and (139), we obtain

$$Q = \frac{\rho v'}{\eta K}. \tag{146}$$

The angular dependence is now obtained by using

$$K = 2k \sin \tfrac{1}{2}\theta \tag{147}$$

where $k = 2\pi n/\lambda$ and $\theta$ is the angle subtended by the wave vectors of the beams. This leads to

$$Q = \frac{\rho v'}{2\eta k} \cdot \frac{1}{\sin \frac{1}{2}\theta} \tag{148}$$

which can also be written

$$Q = Q_{\text{SBS}} \frac{1}{\sin \frac{1}{2}\theta} \tag{149}$$

where $Q_{\text{SBS}}$ is the $Q$ parameter for backward SBS with $\theta = \pi$. For liquids such as $CS_2$, $Q_{\text{SBS}}$ is of the order of 100. This parameter increases as $\theta$ becomes small and can reach as high as 10 000.

According to (144) and (149), the gain coefficients at resonance also depend on the angle $\theta$ between the beams. For contradirectional coupling, the angular dependence is, according to (149), (144), and (131),

$$g = g_{\text{SBS}} \frac{1}{(\sin \frac{1}{2}\theta)^2} \tag{150}$$

where we recall that $\pi/2 < \theta < \pi$, and $g_{\text{SBS}}$ is the gain coefficient at $\theta = \pi$, and is given by (for $\Omega = \omega_2 - \omega_1 = -\Omega_B$)

$$g_{\text{SBS}} = \frac{2\pi}{\lambda} \frac{\gamma^2}{4n\rho V^2\epsilon_0}\left(\frac{\Omega_B}{\Gamma_B}\right). \tag{151}$$

For codirectional coupling, the angular dependence is given by [according to (149), (144) and (120)]

$$g = g_{\text{SBS}} \frac{2}{\sin \theta} \tag{152}$$

where $g_{\text{SBS}}$ is given by (151) and $\theta$ is less than $\pi/2$ but greater than 0.

We note that the gain coefficient $g$ increases significantly for the codirectional case as $\theta$ decreases. This high gain may be difficult to observe because the phonons generated by two-wave mixing tend to walk out of the interaction region and thus reduce the resonance enhancement.

The electrostrictive Kerr effect and the photoelastic effect are very similar in nature. Both are related to the change of index of refraction as a result of the squeezing of the medium. Consequently, these two coefficients are related. Such a relationship has been derived [62] and is given by

$$n_2 = \frac{n^7\epsilon_0 p^2}{4B} \tag{153}$$

where $B$ is the bulk modulus, $p$ is the photoelastic coefficient [1], and $n$ is the index of refraction. Using the following relation:

$$B = \rho v'^2 \tag{154}$$

where $\rho$ is the mass density and $v'$ is the acoustic velocity, the Kerr coefficient can also be written

$$n_2 = \tfrac{1}{4} n_o \epsilon_0 v' M_2 \tag{155}$$

or

$$n_2 = \tfrac{1}{4}\epsilon_0 M_3 \tag{156}$$

where $M_2$ and $M_3$ are the acoustooptic figures-of-merit [1],

$$M_2 = \frac{n^6 p^2}{\rho v'^3} \quad M_3 = \frac{n^7 p^2}{\rho v'^2}. \tag{157}$$

### C. Nonlinear Optical Bragg Scattering

Acoustooptic Bragg scattering is a well-known phenomenon and has been widely used for beam steering, beam modulation, frequency shifting, and other applications. It is a physical process in which an incident laser beam is scattered from an acoustic field. The scattered

beam is shifted in frequency by an amount which is exactly the frequency of the acoustic field. In addition, the scattered beam propagates along a new direction which is determined by the Bragg condition [1].

If the Bragg cell is made of a nonlinear optical medium, the traveling interference pattern formed by the incident beam and the scattered beam may induce a volume index grating. Such a volume index grating will then affect the propagation of these two beams. If the optical nonlinearity of the medium is due to the electrostrictive Kerr effect, then an additional sound wave can be generated due to the two-beam coupling. This additional sound wave is added to the applied acoustic field, and thus enhances the diffraction efficiency under appropriate conditions.

From the quantum mechanical point of view, for each photon scattered, there is one phonon generated or annihilated depending on whether the frequency is downshifted or upshifted. In the case of frequency downshift, there is one phonon generated for each photon scattered. Thus the number of generated phonons is proportional to the scattered intensity. For low intensity light, these additional phonons are much smaller in number relative to the phonons of the applied acoustic field. However, for high-intensity laser beams, the number of generated phonons can be much larger than those of the applied acoustic field. The presence of these additional phonons effectively enhances the acoustic field and thus increases the diffraction efficiency.

Both acoustooptic Bragg scattering and nondegenerate two-wave mixing in Kerr media have been individually treated by previous scientists [1], [40]. In addition, the amplification of sound waves through the interaction of two laser beams with different frequencies has been observed experimentally [63]. The coupling between the Bragg scattered beam and the incident beam due to Kerr effect has recently been studied [64]. Such coupling leads to nonlinear optical Bragg scattering. In a Bragg cell with a low acoustic field, the diffraction efficiency may be low at low optical intensity. When the optical intensity is above some threshold, the phonon regenerative process leads to an avalanche in which all the photons are diffracted. Here, we describe a coupled-mode theory of the nonlinear optical Bragg scattering in Kerr media. An exact solution is obtained for the nonlinear diffraction efficiency.

Consider the nondegenerate two-wave mixing in the Bragg cell (see Fig. 11). If an acoustic field is applied such that the wave $A_2$ is generated by scattering of the incident wave $A_1$ from the sound wave, then the condition $\Omega = \pm vK$ is automatically satisfied provided that the wave $A_1$ is incident along a direction which satisfies the Bragg condition. Under these circumstances, the coupled-mode equations that govern the propagation of these two waves in the medium can be written

$$\frac{d}{dz}A_1 = -\tfrac{1}{2}g|A_2|^2A_1 - i\kappa A_2 \tag{158}$$

$$\frac{d}{dz}A_2 = \tfrac{1}{2}g|A_1|^2A_2 - i\kappa^*A_1 \tag{159}$$

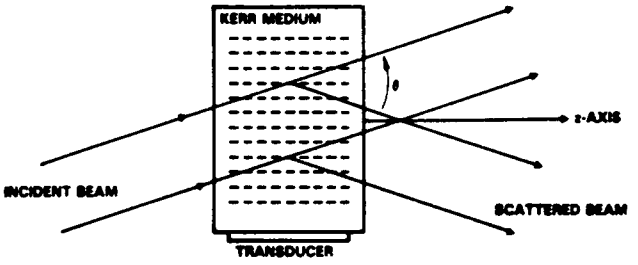


Fig. 11. Schematic drawing of nonlinear Bragg scattering in Kerr media.

where $\kappa$ is the Bragg coupling constant [1] and $g$ is the Kerr intensity coupling constant given by (120).

Note that the angle $\theta$ is twice the Bragg angle $\theta_B$ ($2k \sin \theta_B = K$). The phase $\phi$ is either $+90$ or $-90°$ depending on the sign of $\Omega = \omega_2 - \omega_1$. For the case when beam 2 is scattered with a frequency downshift (as shown in Fig. 11), the phase $\phi$ is $+90°$, indicating a gain for beam 2.

We again write

$$A_1 = \sqrt{I_1}e^{-i\psi_1} \quad A_2 = \sqrt{I_2}e^{-i\psi_2} \tag{160}$$

where $\psi_1$ and $\psi_2$ are the phases of the amplitudes $A_1$ and $A_2$, respectively. Using (160), the coupled equations can be written

$$I_1' - 2I_1i\psi_1' = -gI_1I_2 - 2i\kappa\sqrt{I_1I_2}e^{-i(\psi_2-\psi_1)}$$

$$I_2' - 2I_2i\psi_2' = gI_1I_2 - 2i\kappa^*\sqrt{I_1I_2}e^{-i(\psi_1-\psi_2)}, \tag{161}$$

respectively, where the prime indicates a differentiation with respect to $z$.

By rewriting $\kappa$ as $\kappa \exp(-i\sigma)$ so that $\kappa$ is now a positive number and splitting the real and imaginary parts, we obtain

$$I_1' = -gI_1I_2 - 2\kappa\sqrt{I_1I_2}\sin\Delta\psi \tag{162}$$

$$I_2' = gI_1I_2 - 2\kappa\sqrt{I_1I_2}\sin\Delta\psi \tag{163}$$

and

$$\psi_1' = \kappa(I_2/I_1)^{1/2}\cos\Delta\psi \tag{164}$$

$$\psi_{21}' = \kappa(I_1/I_2)^{1/2}\cos\Delta\psi \tag{165}$$

where

$$\Delta\psi = \psi_2 - \psi_1 + \sigma. \tag{166}$$

These equations are very similar to those that describe mode coupling in ring laser gyros [65], [66]. In fact, the relative phase between the waves can be written, according to (165), (166)

$$\Delta\psi' = \kappa\left[(I_1/I_2)^{1/2} - (I_2/I_1)^{1/2}\right]\cos\Delta\psi \tag{167}$$

which is similar to the well-known phase-coupling equations in ring laser gyros. In our case, since the wave $A_2$ is generated by Bragg scattering of the wave $A_1$ from the acoustic field, it is legitimate to assume that the phase of $A_2$ is connected to that of the incident wave $A_1$. Thus

$$\Delta\psi = \pi/2, \quad 3\pi/2 \tag{168}$$

are good solutions of (167).

For $g = 0$, exact solution of the coupled equations (158) and (159), subject to the boundary condition of $A_2(0) = 0$, yields a relative shift of $\Delta\psi = \pi/2$. We will take this as the proper solution to (167). Substitution of $\Delta\psi = \pi/2$ into (162) and (163) leads to

$$I_1' = -gI_1I_2 - 2\kappa\sqrt{I_1I_2}$$
$$I_2' = gI_1I_2 - 2\kappa\sqrt{I_1I_2}. \tag{169}$$

The coupled equation (169) can be integrated exactly, and the solution is

$$I_1(z) = I\cos^2 u$$
$$I_2(z) = I\sin^2 u \tag{170}$$

where $I$ is the incident intensity at $z = 0$ (i.e., $I_1(z) = I$ and $I_2(z) = 0$ at $z = 0$), and $u$ is given by [64]

$$\tan u = \frac{\tan(\kappa z\sqrt{1-b^2})}{\sqrt{1-b^2} - b\tan(\kappa z\sqrt{1-b^2})} \tag{171}$$

with

$$b = \frac{gI}{4\kappa} = \frac{\gamma L'}{4\kappa L} \tag{172}$$

where $\gamma = gI$ and $L$ is the length of interaction. We note that $b$ is a dimensionless parameter which is the ratio of Kerr coupling to Bragg coupling. Equation (171) is valid for all values of $b$. When the magnitude of $b$ becomes greater than 1 (i.e., $|b| > 1$), $\sqrt{1-b^2}$ becomes $i\sqrt{b^2-1}$ and $\tan \kappa z\sqrt{1-b^2}$ becomes $i\tanh \kappa z\sqrt{b^2-1}$. We also note that $\kappa$ is a positive number as defined earlier. The Kerr coupling constant $g$ can be either positive or negative depending on whether the frequency of beam 2 is downshifted or upshifted.

We now examine the intensity variation with respect to $z$ for various values of $b$. For $b > 1$, $I_2(z)$ reaches its maximum value $I$ (100 percent energy transfer) at distance $z$ such that $\tanh(\kappa z\sqrt{b^2-1}) = \sqrt{b^2-1}/b$. Beyond this point, the intensity $I_2(z)$ decreases and reaches its asymptotic value of $I/[2b(b-\sqrt{b^2-1})]$ which becomes $I$ when $b$ approaches infinity.

For $b = 1$, $I_2(z)$ reaches its maximum value $I$ at $z = 1/\kappa$. Beyond this point, the intensity $I_2(z)$ decreases and reaches its asymptotic value of $I/2$ at $z = \infty$.

For $0 \le b < 1$, $I_2(z)$ is a periodic function of $z$ with maximum value $I$ at points when $\tan(\kappa z\sqrt{1-b^2}) = \sqrt{1-b^2}/b$. The minimum value of $I_2(z)$ is zero, which occurs when $\tan(\kappa z\sqrt{1-b^2}) = 0$. Note that maximum or minimum occurs when $I_1I_2 = 0$.

For $-1 < b < 0$, $I_2(z)$ is also a periodic function of $z$ with maximum value $I$ at points when $\tan(\kappa z\sqrt{1-b^2}) = \sqrt{1-b^2}/b$. Compared with the case $0 \le b < 1$, we note that it takes a longer interaction length for $I_2$ to reach its maximum value because of the negative Kerr coupling. Minimum value of $I_2(z)$ is zero which also occurs when $\tan(\kappa z\sqrt{1-b^2}) = 0$.

For $b = -1$, $I_2(z)$ is a monotonically increasing function of $z$ with an asymptotic value of $I_2(z) = I/2$ at $z = \infty$. For $b < -1$, $I_2(z)$ is also a monotonically-increasing function of $z$ with an asymptotic value of $I_2(z) = I/(2b^2 - 2b\sqrt{b^2-1})$ at $z = \infty$. Fig. 12 plots the intensity of $I_2(z)$ as a function $z$ at various values of $b$.

We now examine the diffraction efficiency which is defined as

$$\eta = \frac{I_2(L)}{I} = \sin^2 u \tag{173}$$

as a function of intensity $I$ (or $b$) for a given Bragg coupling constant $\kappa$ and a length of interaction $L$. Fig. 13 plots the diffraction efficiency $\eta$ as a function of the parameter $b$ for various values of $\kappa L$. We note that for $b > 0$ (or $g > 0$) the diffraction efficiency $\eta$ is an increasing function of intensity and can reach nearly 100 percent at high optical intensities. The enhancement in the diffraction efficiency due to strong Kerr coupling can be employed for the steering of high-power lasers.

When $b \gg 1$ and $b\kappa L \gg 1$, the asymptotic expression for the diffraction efficiency is, according to (171) and (173)

$$\eta = 1 - 4b^2\exp(-4\kappa Lb). \tag{174}$$

We note that the diffraction efficiency approaches 100 percent exponentially at large $b$ (high intensity). When $b$ approaches $-\infty$, the asymptotic form of the diffraction efficiency is, according to (171) and (173)

$$\eta = \frac{1}{4b^2}\left[1 - 2\exp(-2\kappa L|b|)\right]. \tag{175}$$

According to (172) and (174), for small $\kappa L$, high diffraction efficiency occurs when $\gamma L \gg 1$ (or $gIL \gg 1$), which corresponds to the Kerr regime. However, the diffraction efficiency is zero when $\kappa L = 0$, according to (171) and (173).

At $b = 0$, (173) reduces to $\eta = \sin^2 \kappa L$, which is the familiar expression of the Bragg cell diffraction efficiency.

For such nonlinear Bragg scattering to be seen, the Kerr coupling constant must be comparable with the Bragg coupling constant. Thus the parameter $b$ must be of the order of 1. If $b = 1$ is used as an example, the Kerr intensity-coupling constant must be

$$gI = 4\kappa.$$

We now take a Bragg coupling constant of $\kappa = 1\ \text{cm}^{-1}$ as an example and use a nonlinear medium such as $CS_2$. From the data available in [51], the Kerr coupling constant $g$ for a Bragg angle of 5° ($\theta = 10°$) is $g = 1.5$ cm/MW, and the radio frequency required is 640 MHz. Thus, the optical intensity needed for observation of a significant nonlinearity in Bragg scattering, according to the above condition, is approximately 2.7 MW/cm$^2$.

The results show that diffraction efficiency is a nonlinear function of the optical intensity and can be greatly enhanced by increasing the intensity of the optical wave.

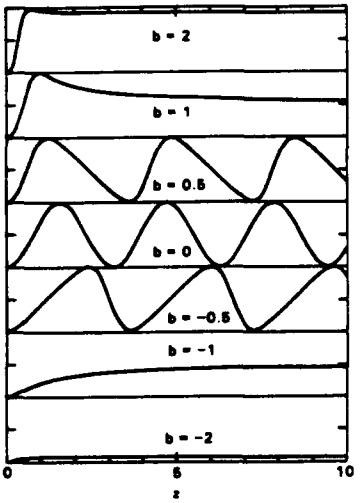


Fig. 12. Intensity variation of the scattered beam $I_2(z)$ as a function of $z$ for various values of $b$.

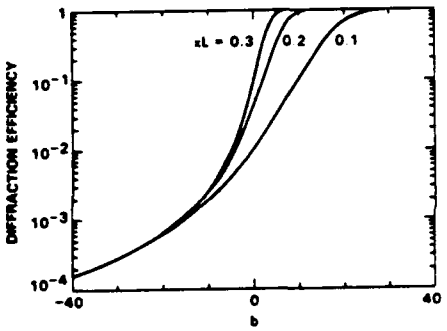


Fig. 13. Diffraction efficiency $\eta$ as a function of the parameter $b$ for various values of $\kappa L$.

It can be used as a nonlinear device in which high-efficiency diffraction only occurs when the optical intensity is above a threshold.

### *D. SBS, SRS, and Photorefractive Two-Wave Mixing*

Thus far we have discussed two-wave mixing in photorefractive crystals and Kerr media. In photorefractive two-wave mixing the frequency difference between the two beams is zero or small (a few Hertz). For two-wave mixing in Kerr media or stimulated Brillouin scattering (SBS), the frequency difference can be as large as a few gigahertz. Energy exchange between two beams also occurs in stimulated Raman scattering (SRS) [2]. The frequency difference between the beams in Raman scattering is in the range of terahertz.

There are several common features among the three types of two-wave mixing. All three types of wave mixing show nonreciprocal energy exchange without phase crosstalk. In fact, if we examine their coupled-mode equations (15) and (116), we note that the mathematical formulations are very similar. A fundamental difference exists between these types of two-wave mixing. In SBS and SRS, the gain coefficient (125) is proportional to the total intensity, whereas the photorefractive gain coefficient is independent of the intensity. Thus, for high-power applications, SBS and SRS can be efficient means for beam coupling. In addition, the frequencies of the idler wave are very different. In SRS, the idler wave is optical phonon. In SBS, the idler wave is acoustic phonon. Also, in photorefractive two-wave mixing, the idler wave is a holographic grating. As a result of the finite frequency of the idler wave, the coupled waves in these three processes are different in frequencies. For SBS and nondegenerate two-wave mixing in photorefractive media, the frequency difference is small so that the two waves propagate at virtually the same speed. In SRS, the large Stokes shift may lead to a significant difference in the phase velocity of the two waves due to dispersion. This may result in a phase mismatch in the wave coupling.

The coupled equations for stimulated Raman scattering are identical to those of the stimulated Brillouin scattering, except for the possibility of dispersion. In fact, it is known that, like SBS, SRS also exhibits phase conjugation [67]. The energy coupling in both SBS and SRS is due to the imaginary part of the third-order dielectric susceptibility [2]. If we examine (10) and (13), we notice that the energy coupling in photorefractive crystal is due to the out-of-phase term of the index grating. This spatial phase shift is 90° in crystals such as $BaTiO_3$, which operates by diffusion only. If we interpret the idler wave in SBS and SRS as a traveling index grating, then the spatial phase shift is also exactly 90° in resonant scattering [see (142)].

In view of the above discussion, we may generalize the meaning of photorefractive effect to include other phenomena such as the Kerr effect. In other words, the generalized photorefractive effect is a phenomenon in which a change of the index of refraction is induced by the presence of optical beams. Thus, we may view SBS and SRS as nondegenerate photorefractive two-wave mixing in nonlinear media.

### *E. Experimental Work*

It was shown earlier that energy transfer in two-wave mixing requires a finite spatial phase shift between the intensity pattern and the induced index grating. In Kerr media where the response is local, such a spatial phase shift can be induced by the use of moving gratings in the medium. Thus, energy transfer is possible in nondegenerate two-wave mixing in Kerr media.

Although the concept of using moving gratings in local media for the energy coupling between two beams had been suggested in the 1970's [41]–[49], no experimental results were reported until recently. In 1986, a steady transfer of energy was observed in a two-wave mixing experiment in atomic sodium vapor [68]. In that experiment, a flash-pumped dye laser was used to pump a cell of sodium vapor that was inserted into a ring resonator. The laser frequency was detuned slightly from the sodium $D$ line. The parametric gain due to the two-wave mixing leads to a unidirectional oscillation in a ring resonator.

The frequency of the oscillating beam in the ring resonator was measured and was found to be lower than that of the pump beam. In a later experiment using a CW dye laser, a frequency shift of several MHz's was measured [69]. The frequency shift agrees with our theoretical result [see (120) and (115)], which indicates that the low-frequency beam gets amplified when the Kerr coefficient is positive. By tuning the frequency of the dye laser to the other side of the $D$ line, an opposite sign of the frequency shift was observed. This indicates the reverse of sign of the Kerr coefficient at this new frequency. In addition, the frequency of oscillation and the intensity of oscillation are functions of the cavity length. Oscillation ceases at cavity lengths when the frequency shifts are less than 8 or more than 50 MHz. Similar observations on the dependence on cavity length were found in photorefractive unidirectional ring resonators [70], [71].

In a two-wave mixing experiment, a fluorescent-doped boric acid glass is used as the nonlinear material [72]. In this experiment, a frequency shift of 0.1 Hz was induced by reflecting one of the beams off a mirror that was translated at a constant velocity by a piezoelectric transducer (PZT). By varying the frequency difference between the beams and monitoring the change in intensity of the probe beam, a time constant of 100 ms was measured. In a similar experiment, a ruby crystal is used as the nonlinear medium [73]. Energy coupling at a frequency shift of up to 500 Hz was observed. A time constant of 3.4 ms was determined by measuring the probe intensity at various frequency shifts. In addition, a net gain (exceeding the absorption and reflection loss) of more than 50 percent was observed.

Recently, energy transfer between two coherent beams in liquid crystals has been observed by several workers [74]. The energy exchange is due to the thin holograms in the medium. In these configurations, the scattering of light by the induced grating is in the Raman–Nath regime due to the small interaction length. The presence of higher order scattering terms results in a multiwave mixing that leads to the energy transfer from the strong beam to the weak beam. If the interaction length is increased, the energy transfer will decrease because the interaction will be in the Bragg regime.

## V. Applications

The photorefractive coupling of two waves in electrooptic crystals has a wide range of applications. These include real-time holography, self-pumped phase conjugation [53], ring resonators [54], [70], [71], [75], laser gyros [72], nonreciprocal transmission [76], image amplification [20], vibrational analysis [77], and image processing [78], [79], etc. Some of these applications will be discussed in this section.

### A. Photorefractive Resonators

The coherent signal beam amplification in two-wave mixing can be used to provide parametric gain for unidirectional oscillation in ring resonators. Such oscillation has been observed by using a $BaTiO_3$ crystal pumped with an argon ion or a HeNe laser [54]. Unlike the conventional gain medium (e.g., He–Ne), the gain bandwidth of photorefractive two-wave mixing is very narrow (a few hertz's for $BaTiO_3$; see also Fig. 4). Despite this fact, the ring resonator can still oscillate over a large range of cavity detuning. This phenomenon was not well understood until a theory of photorefractive phase shift was developed [70]. The theory shows that oscillation can occur at almost any cavity length despite the narrow-band nature of two-wave mixing gain, provided the coupling is strong enough. Such a theory is later verified experimentally by studying the frequency of unidirectional ring oscillation at various cavity detunings [71].

Referring to Fig. 14, we now investigate the oscillation of a ring resonator in which a photorefractive crystal is inserted. Let us focus our attention on the region occupied by the photorefractive crystal and examine the gain due to two-wave mixing. The results of nondegenerate two-wave mixing derived in Section II-C can be used to explain the ring oscillation.

In a conventional ring resonator, the oscillation occurs at those frequencies

$$f = f_o + N\frac{c}{S} \tag{176}$$

which lie within the gain curve of the laser medium (e.g., He–Ne). Here, $S$ is the effective length of a complete loop, $f_o$ is a constant, and $N$ is an integer. For $S \leq 30$ cm, these frequencies (176) are separated by the mode spacing $c/S \geq 1$ GHz. Since the width of the gain curve for the conventional gain medium is typically several GHz due principally to Doppler broadening, oscillation can occur at almost any cavity length $S$. On the contrary, if the bandwidth of the gain curve is narrower than the mode spacing $c/S$, then oscillation can sustain, provided the cavity loop is kept at the appropriate length.

Unlike the conventional gain medium, the bandwidth of photorefractive two-wave mixing is very narrow. Using photorefractive crystals that operate by diffusion only, e.g., $BaTiO_3$, the coupling constant can be written, according to (48)

$$\gamma = \frac{\gamma_o}{1 + (\Omega\tau)^2} \tag{177}$$

where $\gamma_o$ is the coupling constant for the case of degenerate two-wave mixing (i.e., $\Omega = \omega_2 - \omega_1 = 0$) and is given by

$$\gamma_o = \frac{4\pi\Delta n_s}{\lambda\cos(\theta/2)}. \tag{178}$$

The parametric two-wave mixing gain is given by, according to (50)

$$g = \frac{I_2(L)}{I_2(0)} = \frac{1+m}{1+me^{-\gamma L}}e^{-\alpha L} \tag{179}$$

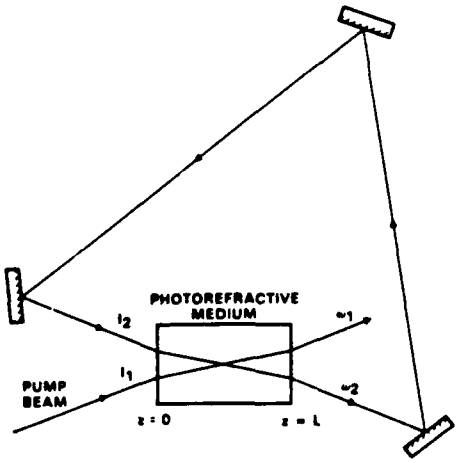


Fig. 14. Schematic drawing of a unidirectional photorefractive ring resonator.

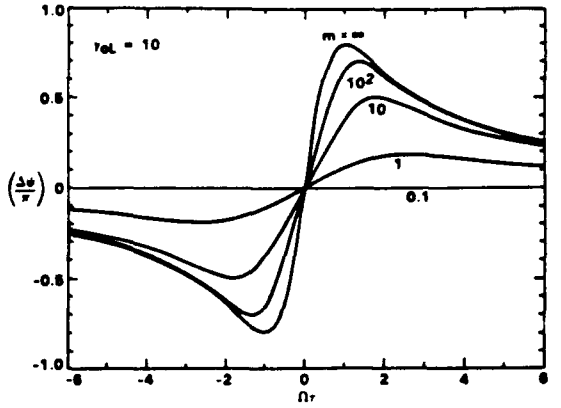


Fig. 15. Photorefractive phase shift $\Delta\psi$ as a function of $\Omega\tau$ for various values of $m$.

where we recall that $m$ is the input beam ratio $m = I_1(0)/I_2(0)$ and $L$ is the length of interaction. Note that amplification ($g > 1$) is possible only when $\gamma > \alpha$ and $m > (1 - e^{-\alpha L})/(e^{-\alpha L} - e^{-\gamma L})$. Also note that $g$ is an increasing function of $m$ (i.e., $\partial g/\partial m > 0$) and $g$ is an increasing function of $L$, provided $\gamma > \alpha$ and

$$L \leq \frac{1}{\gamma} \ln\left[\frac{m(\gamma - \alpha)}{\alpha}\right]. \tag{180}$$

The gain as a function of frequency $\omega_2$ (or equivalently as a function of $\Omega = \omega_2 - \omega_1$), has been plotted in Fig. 4 for various values of $m$. Note that gain is significant only when $|\omega_2 - \omega_1|\tau < 1$. For materials such as $BaTiO_3$ and SBN, $\tau$ is between 1 and 0.1 s. Thus, the gain bandwidth is only a few hertz. In spite of such an extremely narrow bandwidth, unidirectional oscillation can still be observed easily at "any" cavity length in ring resonators using $BaTiO_3$ crystals as the photorefractive medium. Such a phenomenon can be explained in terms of the additional phase shift [(24) and (25)] introduced by the photorefractive coupling. This phase shift is a function of the oscillation frequency and is plotted in Fig. 15 as a function of $\Omega\tau$. For $BaTiO_3$ crystals with $\gamma_o L > 4\pi$, this phase shift can vary from $-\pi$ to $+\pi$ for a frequency drift of $\Delta\Omega\tau = \pm 1$. Such a phase shift is responsible for the oscillation of the ring resonator which requires a round-trip phase shift of an integer times $2\pi$.

*1) Oscillation Conditions:* We now examine the boundary conditions appropriate to a unidirectional ring oscillator. At steady-state oscillation, the electric field must reproduce itself, both in phase and intensity, after each round-trip. In other words, the oscillation conditions can be written

$$\Delta\psi + \int k\, ds = 2N\pi \tag{181}$$

and

$$gR = 1 \tag{182}$$

where $\Delta\psi$ is the additional phase shift due to photorefractive coupling, the integration is over a round-trip beam path, the parameter $R$ is the product of the mirror reflectivities, and $g$ is the parametric gain of (179).

If we define a cavity detuning parameter $\Delta\Gamma$ as

$$\Delta\Gamma = 2N'\pi - \int k\, ds \tag{183}$$

where $N'$ is an integer chosen in such a way that $\Delta\Gamma$ lies between $-\pi$ and $+\pi$, then the oscillation condition (181) can be written

$$\Delta\psi = \Delta\Gamma + 2M\pi \tag{184}$$

where $M$ is an integer. In other words, oscillation can be achieved only when the cavity detuning can be compensated by the photorefractive phase shift.

Equations (181) and (182) may be used to solve for the two unknown quantities $m = I_1(0)/I_2(0)$ and $\Omega = \omega_2 - \omega_1$. If we fix the pump intensity $I_1(0)$ and the pump frequency $\omega_1$, then (181) and (182) can be solved for the oscillation frequency $\omega_2$ and the oscillation intensity $I_2(0)$. Substituting (179) for $g$ in (182) and using (25), we obtain

$$\Delta\psi = -\frac{\beta}{\gamma} \ln\left(\mathrm{Re}^{-\alpha L}\right). \tag{185}$$

This equation can now be used to solve for the oscillation frequency $\Omega\tau$. For the case of pure diffusion, using (46) for $\phi_o = \pi/2$ and (19) and (20), we obtain from (185)

$$\Omega\tau = \frac{2\Delta\psi}{\alpha L - \ln R} = \frac{2(\Delta\Gamma + 2M\pi)}{\alpha L - \ln R} \tag{186}$$

where $\Delta\Gamma$ is the cavity detuning and is given by (183). Substituting (179) for $g$ in (182), we can solve for $m$ and obtain

$$m = \frac{I_1(0)}{I_2(0)} = \frac{1 - \mathrm{Re}^{-\alpha L}}{\mathrm{Re}^{-\alpha L} - e^{-\gamma L}}. \tag{187}$$

Since $m$ must be positive, we obtain from (187) the threshold condition for oscillation

$$\gamma L > \gamma_t L \equiv \alpha L - \ln R \qquad (188)$$

where $\gamma_t$ is the threshold parametric gain constant. Since $\gamma$ is a function of frequency $\Omega$, (188) dictates that the parametric gain is above threshold only in a finite spectral regime. Using (177) for $\gamma$, (188) becomes

$$|\Omega\tau| < \left[\frac{\gamma_o L}{\alpha L - \ln R} - 1\right]^{1/2} \qquad (189)$$

where we recall that $\gamma_o$ is the parametric gain at $\Omega = \omega_2 - \omega_1 = 0$. Equation (189) defines the spectral regime where the parametric gain $\gamma$ is above threshold (i.e., $\gamma > \gamma_t$).

We have thus far obtained expressions for the oscillation frequency [(186)] and the spectral regime where the gain is above threshold. The ring resonator will oscillate only when the oscillation frequency falls within this spectral region. The oscillation frequency $\omega_2 = \omega_1 + \Omega$ is determined by (186), with $\Delta\Gamma$ being the cavity detuning (183).

The same oscillation frequency must also satisfy (189). Thus, we obtain the following oscillation condition:

$$\frac{2|\Delta\psi|}{\alpha L - \ln R} < \left[\frac{\gamma_o L}{\alpha L - \ln R} - 1\right]^{1/2}, \qquad (190)$$

which can also be written

$$\gamma_o L > \gamma_t L + \frac{1}{\gamma_t L}(2\Delta\psi)^2 \equiv G_t L \qquad (191)$$

where $\gamma_t$ is the threshold parametric gain of (188) for the case when $\Delta\psi = 0$, and $G_t$ may be considered as the threshold gain for the case when $\Delta\psi \neq 0$. According to (191), the threshold gain increases as a function of the cavity detuning $\Delta\Gamma$. The cavity detuning $\Delta\Gamma$ not only determines the oscillation frequency [(186)], but also the threshold gain $G_t$.

The $\Delta\Gamma$ in (183) is the cavity detuning and is defined between $-\pi$ and $\pi$. However, the photorefractive phase shift (25) can be greater than $\pi$. When this happens, the unidirectional ring resonator may oscillate at more than one frequency. These frequencies are given by (186), with $M = 0, \pm 1, \pm 2, \cdots$, etc., and with their corresponding threshold gain given by

$$G_t L = \gamma_t L + \frac{1}{\gamma_t L}[2(\Delta\psi + 2M\pi)]^2. \qquad (192)$$

In other words, for each cavity detuning $\Delta\Gamma$, the ring resonator can support multimode oscillation, provided the coupling constant $\gamma_o$ is large enough. Fig. 16 shows the oscillation intensity, as well as the oscillation frequency as functions of cavity detuning $\Delta\Gamma$. Note that for larger $\gamma_o L$, the resonator can oscillate at almost any cavity detuning $\Delta\Gamma$, whereas for small $\gamma_o L$, oscillation occurs only when the cavity detuning is limited to some small region around $\Delta\Gamma = 0$.

In summary, ring oscillation occurs when the two-wave mixing gain dominates cavity losses and the round-trip optical phase reproduces itself (to within an integer multiple of $2\pi$). The condition on phase is unique because of a significant contribution to the optical phase shift due to nondegenerate photorefractive two-wave mixing. This condition is satisfied at any cavity length if the oscillation frequency is slightly detuned from the pump frequency, since the photorefractive phase shift [(185)] depends on the detuning. The frequency difference $\Omega$ ($= \omega_2 - \omega_1$) between the pumping and oscillating beams can be written

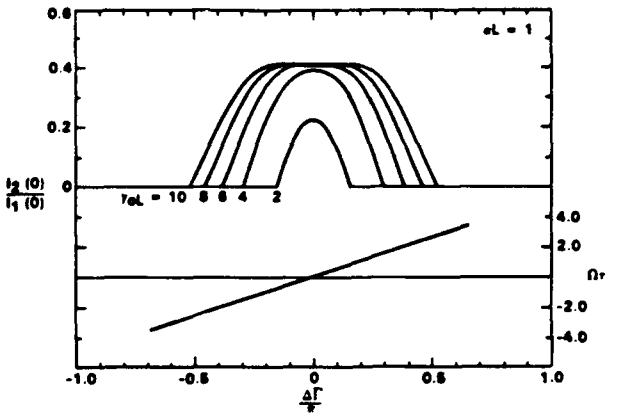


Fig. 16. Oscillation intensity as a function of cavity detuning $\Omega\tau$ for various values of $\gamma_o L$.

$$\Omega = [2(\Delta\Gamma + 2M\pi)/\tau A] \qquad (193)$$

where $\Delta\Gamma$ is the cavity-length detuning with respect to an integer multiple of optical pump waves in the cavity, $M$ is an integer, $\tau$ is the photorefractive time response, and $A$ represents the total cavity loss. There are threshold conditions for oscillation involving cavity loss and gain (taking $M$ to be zero):

$$|\Omega| \leq (1/\tau)(\gamma L/A - 1)^{1/2} \qquad (194)$$

$$|\Delta\Gamma| \leq (A/2)(\gamma L/A - 1)^{1/2} \qquad (195)$$

where $\gamma$ is the degenerate two-wave mixing coupling coefficient, $L$ is the interaction length, and $A = -\ln(RT_sT_p)$ (with $R$ being the product of the reflectivities of the cavity mirrors and output coupler; $T_s$ is the transmission through the photorefractive crystal accounting for the absorption, Fresnel reflections, and scattering (or beam fanning); and $T_p$ is the effective transmission through the pinhole aperture).

This theory predicts that the unidirectional ring resonator will oscillate at a frequency different from the pump frequency by an amount directly proportional to the cavity-length detuning. Furthermore, in a photorefractive material with moderately low $\tau$, the theory postulates a threshold where oscillation will cease if the cavity detuning (frequency difference) becomes too large. Such a theory has been validated experimentally in a $BaTiO_3$ photorefractive ring resonator [71].

The experiments performed to examine the above theory will now be discussed in detail. Fig. 17 shows the experimental setup. A single-mode argon-ion laser (514.5

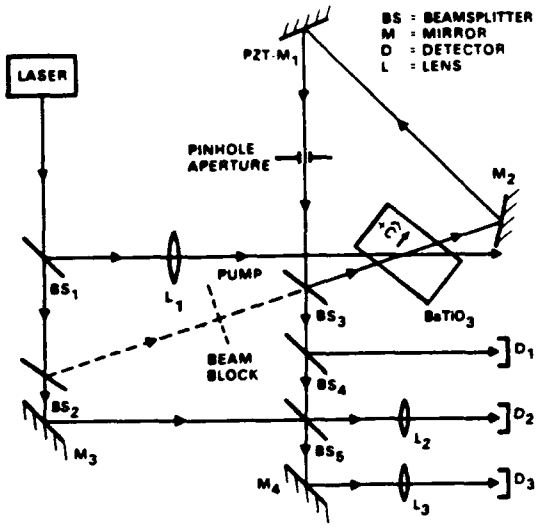


Fig. 17. Optical setup for the photorefractive unidirectional ring resonator with variable cavity length. The beat frequency between the self-oscillation and pump beams is derived from the motion of the interferograms at $D_2$ or $D_3$ [71].

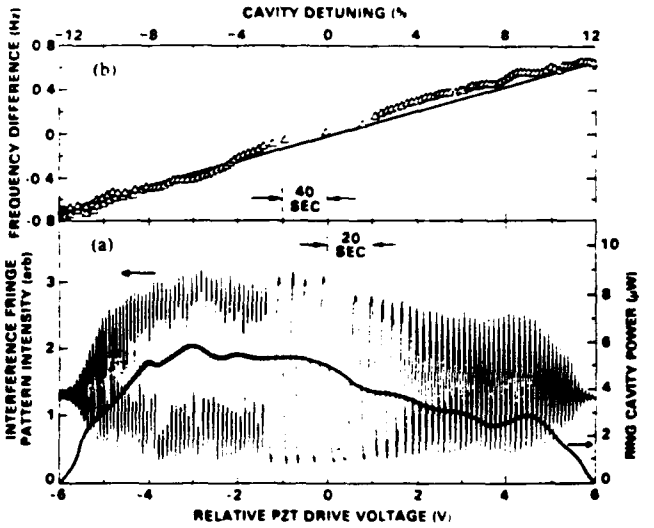


Fig. 18. Characteristics of the unidirectional self-oscillation as a function of ring-cavity length (i.e., PZT voltage or cavity detuning, where 100 percent implies a detuning of one full optical wave): (a) ring-cavity intensity (right) and beat-frequency signature (left); (b) frequency difference between the self-oscillation and the pumping beam [71].

nm) is used to pump a $BaTiO_3$ crystal which is inserted into a ring resonator. Two-wave mixing in $BaTiO_3$ provides the parametric gain needed for the oscillation in the *unidirectional ring cavity, formed by two planar mirrors* ($M_1$ and $M_2$) and a planar beam splitter ($BS_3$). The oscillation beam in the ring-cavity is sampled through the output coupler $BS_3$, its intensity being detected at $D_1$ while the beat frequency between it and the pumping beam is determined using complementary fringe patterns formed at detectors $D_2$ and $D_3$. Without a ring-cavity pinhole aperture, unidirectional oscillation can be observed at any cavity length. However, dynamically unstable multiple spatial modes are evident [80], [81] in the fringe patterns at $D_2$ and $D_3$. To obtain a single mode (and clean fringe patterns), a 200 $\mu$m pinhole is placed in the ring cavity. The basic premises of the theory [70] are verified by slowly ramping the PZT voltage and observing the beat frequency, along with the ring-cavity oscillation intensity. Typical results are shown in Fig. 18(a) for an 80 mW pump beam incident at 40° from the $c$ axis of $BaTiO_3$ and at 20° from the oscillating beam (both angles are external in air).

The intensity of the unidirectional oscillation versus cavity length [Fig. 18(a)] indicates threshold gain conditions [(194) and (195)]. The beat frequency between oscillating and pumping beams, as observed in the time variation of the fringe-pattern intensity [Fig. 18(a)], clearly corresponds to the position of the PZT $- M_1$. When $M_1$ is exactly at the correct position (chosen as the origin), the fringe pattern is stationary, i.e., there is no frequency shift. As $M_1$ moves away from this origin, the fringe motion becomes faster and the frequency difference increases. Fig. 18(b) shows the linear dependence of the frequency difference on cavity detuning with the ramping period equal to 20 000 s for improved resolution.

The frequency difference changes sign as $M_1$ slowly moves through the origin. The observed sign is consistent with the sign of the phase shift between the light intensity pattern and index modulation that determines the direction of energy exchange in two-wave mixing. The beat-frequency signature [Fig. 18(a)] is also a periodic function of PZT mirror position. The observed beat-frequency signature reproduces itself with a $M_1$ displacement of every $\sim\lambda/2$, as expected (i.e., a cavity length detuning periodicity of $\lambda$). Experimentally, the frequency threshold for oscillation is approximately a linear function of the pumping-beam intensity, as shown in Fig. 19(a). According to Fig. 18(a), this frequency threshold is inversely proportional to $\tau$, but $\tau$ can be approximately proportional to the inverse of the pump intensity (assuming that the cavity intensity is negligible by comparison) when the photoconductivities dominate [82]. Therefore, the observed dependence [Fig. 19(a)] agrees with theory.

The oscillation conditions for the unidirectional ring resonator are dependent on the two-wave mixing gain ($\gamma L$) in the photorefractive medium. $\gamma L$ is varied by rotating the $BaTiO_3$ crystal with respect to the pumping and oscillating beams [83]. When the gain is too small, no unidirectional oscillation is observed, regardless of ring-cavity length. For $\gamma L$ just above threshold, two pronounced differences are evident, contrasting with $\gamma L$ large. First, the amount of cavity detuning that is accommodated before oscillation ceases is greatly reduced. Second, the maximum frequency difference between the pumping and oscillating beams is much less. The quantitative trends of these two effects are given in Fig. 19(b) for a pump power of 80 mW.

The threshold oscillation conditions given in expressions (194) and (195) agree with the data [Fig. 19(b)].

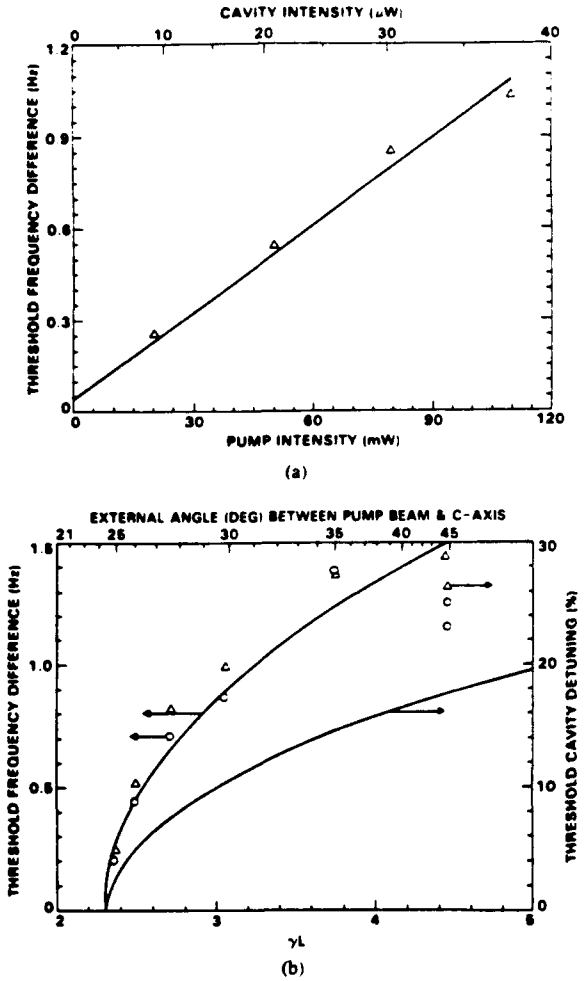


Fig. 19. Oscillation threshold behavior for the unidirectional ring resonator: (a) maximum beat frequency as a function of pumping-beam or ring-cavity power along with a linear fit (solid-line); (b) maximum beat frequency (left) and cavity detuning (right) as a function of two-wave mixing gain $\gamma L$, where $\gamma L$ is related to the external angle that the pumping beam makes the crystal's c axis as shown (top scale). Note: the two solid curves in (b) correspond to the evaluation of (194) and (195) as described in text [71].

The solid curve associated with the left-hand scale of Fig. 19(b) is generated from (194) for $A = 5.1$ and $\tau = 0.53$ s. This cavity-loss factor $A$ is estimated independently from $R \times 0.99 \times 0.91 \times 0.81$ (for $M_1$, $M_2$, and $BS_3$, respectively), $T_s = 0.52$, and $T_p = 0.016$ (for a cavity length of 50 cm). Accumulating these contributions gives $A = 5.2$, in excellent agreement with the observed 5.1. The right-hand scale of Fig. 19(b) shows the dependence of threshold cavity detuning (i.e., the maximum detuning that will still support self-oscillation) on $\gamma L$, along with the prediction from (195), where $\Delta\Gamma$ is normalized by $2\pi$. Remarkable agreement is obtained using $A = 5.1$ from Fig. 19(a) and no adjustable parameters.

The interdependence of the optical cavity length and the beat frequency between the oscillating and pumping beams is a general property of photorefractive resonators. These results are not unique to the optical setup shown in Fig. 17. Similar behavior is observed with other configurations. First, the orientation of the $BaTiO_3$ crystal in Fig. 17 can be altered so that the pumping and oscillating beams enter the $a$ face but in such a way that no self-pumping occurs [53]. Second, the $BaTiO_3$ can be replaced by crystals of strontium barium niobate [84], [85] (nominally undoped and cerium doped). Third, a linear resonator (Fig. 20) can act as a self-pumped phase conjugator [54]. The observed frequency shift of the phase-conjugate beam is exactly twice that of the self-oscillation, which is necessary to satisfy energy conservation for slightly-nondegenerate four-wave mixing [86]. In all three variations, the measured frequency differences correlate with cavity length detuning; results equivalent to those shown in Fig. 18 are obtained.

In summary, the experimental results indicate that the frequency difference between the oscillating and pumping beams in the unidirectional ring resonator depends on the optical cavity length. This dependence supports the theory [70] that uses a photorefractive phase shift associated with slightly-nondegenerate two-wave mixing to satisfy the round-trip phase-oscillation condition for the resonating beam. Similarly, the observed frequency shifts in other photorefractive resonators, including self-pumped phase conjugators, may also be explained by the same mechanism. This is the subject of the next section.

### *B. Resonator Model of Self-Pumped Phase Conjugators*

The theory of unidirectional photorefractive ring resonators described in the previous section can be extended to explain the phenomenon of self-pumped phase conjugation using $BaTiO_3$ crystals (sometimes referred to as the cat mirror [53]). It is known that optical four-wave mixing can be used to generate phase conjugated waves. In self-pumped phase conjugation, no counterpropagating beams are supplied externally to provide the pumps needed in the four-wave mixing process. In addition, self-pumped phase conjugators using photorefractive crystals such as $BaTiO_3$ have received considerable attention because of the relatively high reflectivities (e.g., 30–50 percent) that can be easily achieved even with low-power lasers [53], [54], [87]. There have been several models developed for the self-pumped phase conjugation inside $BaTiO_3$ crystals. These include backscattering via 2-$k$ gratings [55], [56], two coupled interaction regions [57], enhanced coupling via frequency-shifted waves [58], time-dependent four-wave mixing [59], and photovoltaic contributions [60]. In what follows, we present a resonator model of self-pumped phase conjugation. Such a model explains the origin of phase conjugation inside a $BaTiO_3$ crystal and also explains the frequency shift of the order of $\pm 1$ Hz [56], [80], [89].

Referring to Fig. 21, we consider the incidence of a laser beam into a cube of photorefractive cyrstal. The crystal cube can be viewed as a dielectric optical cavity which supports a multitude of modes. These modes are trapped inside the crystal due to total internal reflection at the surfaces. When a laser beam is incident into the crys-

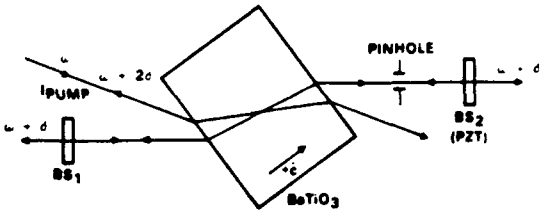


Fig. 20. Self-pumped phase conjugator using external reflectors to generate the self-oscillation with frequency shift $\delta$ and the phase-conjugate reflection with a frequency shift $2\delta$, where $\delta$ is proportional to the linear cavity length [71].

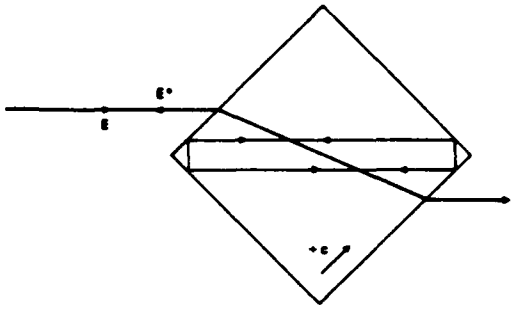

Fig. 21. Resonator model of self-pumped phase conjugators.

tal, some of the modes may be excited, as a result of the strong parametric gain due to two-wave mixing. In particular, ring oscillations such as those shown in Fig. 21 can be generated according to the theory developed earlier. When the configuration of the resonance cavity relative to the incident laser beam support bidirectional oscillation, a phase-conjugate beam is generated via the four-wave mixing process.

According to this theory, the frequency of oscillation inside the crystal can be slightly detuned from that of the pump beam. Let $\omega$ be the frequency of the incident laser beam; the frequency of the internal oscillation can be written

$$\omega' = \omega + \delta \tag{196}$$

where $\delta$ is the frequency detuning and is on the order of $\pm 1$ Hz for $BaTiO_3$. Note that this frequency detuning depends on the path length of the ring oscillation inside the crystal. The bidirectional oscillation provides the counter propagating beams needed for the pump. As a result of the conservation of energy, the phase conjugated beam has a frequency of $\omega + 2\delta$.

The resonator model presents a simple explanation of the frequency shift observed in $BaTiO_3$ self-pumped phase conjugators [56], [88], [89]. In addition, experimental evidence indicates that internal oscillations inside the crystal play a key role in the generation of phase conjugated waves [90].

### C. Optical Nonreciprocity

We mentioned earlier that the energy transfer in two-wave mixing may have application in optical nonreciprocity. We now discuss in some detail the nonreciprocal intensity transmission and nonreciprocal phase shifts due to two-wave mixing in photorefractive media. It is known in linear optics that the transmittance as well as the phase shift experienced by a light beam transmitting through a dielectric layered medium is independent of the side of incidence. This is known as the left- and right-incidence theorem and is a result of the principle of reversibility [91]. This theorem is no longer true when the photorefractive coupling is present. Such nonreciprocal transmittance was first predicted by considering the coupling between the incident beam and the reflected beam inside a slab of photorefractive medium [92]. The reflected beam is due to the dielectric discontinuity at the slab boundaries. As a result of the photorefractive contradirectional two-wave mixing, energy exchange occurs between the incident and reflected beams. Such an energy exchange leads to an asymmetry in the transmittance. Fig. 22 shows the two transmittances as a function of the coupling constant. Notice that a significant nonreciprocal transmittance is present due to the photorefractive coupling. In the extreme case of strong coupling ( $\gamma L >> 1$ ), the slab almost acts as a "one-way" window. Such nonreciprocal transmission has been observed in $BaTiO_3$ and $KNbO_3$:Mn crystals in the visible spectral regimes [93], [94].

In addition to the nonreciprocal intensity transmission, there exists a nonreciprocal phase shift in contradirectional two-wave mixing according to (37), provided $\beta \neq 0$. Such nonreciprocal phase shifts may be useful in some applications, including the biasing of ring laser gyros [66], [75] [94]. In what follows, we consider the photorefractive coupling of the counterpropagating beams inside a ring resonator.

Referring to Fig. 23, we consider the insertion of a thin slab of photorefractive crystal into a ring resonator. The photorefractive crystal is oriented such that nonreciprocal transmission occurs. In the absence of the photorefractive medium, the two oppositely-directed ring oscillators are degenerate in frequency in an inertial frame. As a result of the nonreciprocal transmission, the symmetry is broken and the degeneracy is removed. Since this may lead to a split in the frequency of oscillations, it provides a bias for the ring laser gyro operation.

Using the result derived in Sections II-B and II-C, we obtain the following expression for the transmittance of the two waves:

$$T_1 = \frac{I_1(L)}{I_1(0)} = \frac{1 + m^{-1}}{1 + m^{-1}\exp(\gamma L)}$$

$$T_2 = \frac{I_2(0)}{I_2(L)} = \frac{1 + m}{1 + m\exp(-\gamma L)} \tag{197}$$

where $m$ is the incident intensity ratio $m = I_1(0)/I_2(L)$. Note that $T_1 < 1$ and $T_2 > 1$ for positive $\gamma$. The sign of $\gamma$ depends on the direction of the $c$ axis.

With $I_1(z)$ and $I_2(z)$ given by (33), the phases $\psi_1$ and $\psi_2$ can be integrated directly from (31). The phase shifts

Rockwell International
Science Center
IEEE JOURNAL OF QUANTUM ELECTRONICS, VOL 25, NO 3, MARCH 1989

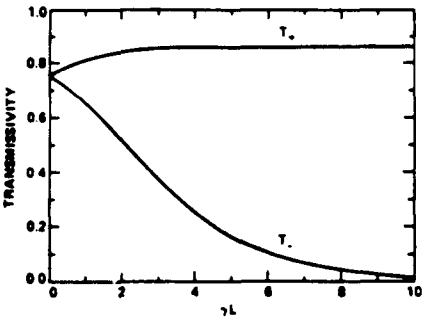


Fig. 22. Transmissivities from the right-hand side and the left-hand side as functions of photorefractive coupling $\gamma L$

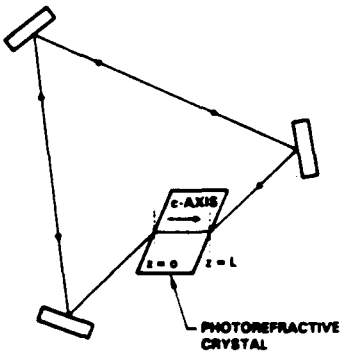


Fig. 23. Schematic drawing of a ring laser resonator filled with a photorefractive crystal plate

in traversing through the medium are $kL + \psi_1(L) - \psi_1(0)$ and $kL + \psi_2(0) - \psi_2(L)$ for waves $E_1$ and $E_2$, respectively. These two phase shifts are different by an amount $\Delta = \psi_2(0) - \psi_2(L) - [\psi_1(L) - \psi_1(0)]$, which, according to (31) is given by

$$\Delta = -\int_0^L d(\psi_1 + \psi_2) = -\int_0^L \beta \frac{I_2 - I_1}{I_2 + I_1}\, dz. \quad (198)$$

Note that this difference in phase shifts is zero when $I_2(z) = I_1(z)$ between $z = 0$ and $z = L$, which corresponds to $C = 0$ in (33) (recall that $I_1(z) - I_1(z) = 2C$]. Using (33) and carrying out the integration in (198), we obtain the following expression for this phase shift difference:

$$\Delta = \frac{2\beta}{\gamma} \ln T_2 - \beta L \quad (199)$$

where $T_2$ is the beam intensity transmittance given by (197). Note that $\Delta$ can also be written as $\Delta = (2\beta/\gamma) \log T_1 + \beta L$. For small couplings, i.e., $\gamma L << 1$, this difference in phase shifts can be written approximately as

$$\Delta = \beta L \frac{m - 1}{m + 1} + \beta \gamma L^2 \frac{m^2}{(1 + m)^3} \quad (200)$$

where we recall that $m = I_1(0)/I_2(L)$.

In a conventional ring laser gyro, the oscillation frequency as well as the intensity are the same for two beams in an inertial frame. The oscillation occurs at thos frequencies

$$f = N\frac{c}{S} \qquad N = \text{integer} \quad (201)$$

which lie within the gain curve of the laser medium (e.g., He–Ne). Here $S$ is the effective length of a complete loop and $N$ is a larger integer. For $S \leq 30$ cm, these frequencies (201) are separated by the mode spacing $c/S \geq 1$ GHz. Since the width of the gain curve is typically 1.5 GHz due to principally Doppler broadening, the gyro usually oscillates at a single longitudinal mode.

The oscillation intensity inside the laser cavity is determined by the gain as well as the loss and is given by [88]

$$I_o = \kappa(g_o - g_t) \quad (202)$$

where $\kappa$ is the constant which depends on the laser medium, $g_o$ is the unsaturated gain factor per pass, and $g_t$ is the threshold gain factor. Note that both $g_o$ and $g_t$ are dimensionless. In a conventional ring resonator, the threshold gain for both traveling waves is given by

$$g_t = \alpha L - \ln R \quad (203)$$

where $\alpha$ is the loss constant (including bulk absorption and scattering) and $R$ is the product of the three-mirror reflectivities.

In the presence of the photorefractive coupling, the unequal transmissivities make the threshold gain different for the two waves which now become

$$g_{t1} = \alpha L - \ln T_1 R \qquad g_{t2} = \alpha L - \ln T_2 R \quad (204)$$

where $T_1$ and $T_2$ are the beam transmittances given by (197). The difference in the threshold gain leads to a split in the oscillation intensity. The fractional difference in the oscillation intensity is given approximately by

$$\frac{I_2 - I_1}{I_2 + I_1} = \frac{\ln_2 - \ln T_1}{(g_o - g_t)} = \frac{\gamma L}{2(g_o - g_t)}. \quad (205)$$

If we now assume that the beam intensities are nearly uniform in the photorefractive material (i.e., $\gamma L << 1$), the difference in phase shift $\Delta$ can be written, according to (198) and (205)

$$\Delta = -\frac{\beta \gamma L^2}{2(g_o - g_t)}. \quad (206)$$

This expression agrees with (200) provided $(g_o - g_t) << 2$, which is legitimate because $(g_o - g_t)$ is typically on the order of $10^{-2}$.

The unequal phase shift for the oppositely-directed traveling waves corresponds to different effective optical path lengths for the waves. This results in a difference $\Omega$ between the angular frequencies of the laser oscillation of the two beams. The difference is $\Omega \equiv \omega_2 - \omega_1 = -c\Delta/S$, which can be written, according to (206), (19), and (20)

$$\Omega = \frac{c}{S} \cdot \frac{-L^2}{2(g_o - g_t)} \cdot \frac{2\pi^2}{\lambda^2} n_1^2 \sin\phi \cos\phi \quad (207)$$

where we recall that $\phi$ is the relative phase shift between the index grating and the interference pattern. We note that $\Omega$ is not zero provided $\sin\phi\cos\phi \neq 0$.

We now examine the angular frequency split $\Omega$ for various cases. For the pure diffusion case (i.e., no external electric field) in photorefractive material, the phase shift $\phi$ is given by $\phi = \pi/2 - \tan^{-1}\Omega\tau$, according to (46). Thus (207) becomes

$$\Omega = \frac{4\pi^2(\Delta n_s)^2 L^2 c\Omega\tau}{\lambda^2 S(g_o - g_t)(1+\Omega^2\tau^2)^2} \tag{208}$$

which has three solutions. The trivial one is $\Omega = 0$, which corresponds to an unsplit oscillation. The other roots are given by

$$\Omega_o = \pm\frac{1}{\tau}\frac{2\pi\Delta n_s}{\lambda} L\left[\frac{c\tau}{S(g_o - g_t)} - 1\right]^{1/2}. \tag{209}$$

Taking $\tau = 100$ ms, $S = 30$ cm, $g_o - g_t = 0.01$, $L = 1$ mm, $\Delta n_s = 10^{-5}$, $\lambda = 0.6328$ $\mu$m, (209) yields $\Omega_o = 10^3$ $s^{-1}$, which corresponds to a frequency split of 160 Hz. Whether the ring gyro will oscillate at the same frequency ($\Omega = 0$) or with a split $\Omega_o$, or both, is a subject of mode stability.

It is shown that there are three modes of oscillations. The stability of these modes will determine the actual mode of oscillation at steady state. To investigate this issue, we need to examine the effect of small perturbation on the oscillation frequencies. Using (207) and $\phi = \pi/2 - \tan^{-1}\Omega\tau$, we consider that the frequency difference $\Omega$ is slightly deviated from the solution by $\delta\Omega$. This $\delta\Omega$ will change the holographic grating phase shift by $\delta\phi$. Equation (207) will then yield the resulting frequency difference $\Omega + d\Omega$ after substituting $\phi + \delta\phi$ for $\phi$ on the right-hand side. The criterion for stable oscillation is

$$\left(\frac{d\Omega}{\delta\Omega}\right) < 0. \tag{210}$$

Using (46) and (207), we can plot the right-hand side of (207) as a function of $\Omega\tau$. The solution of (207) can then be obtained by drawing a straight line through the origin with a slope of $1/\tau$. The intersections of the straight line with the curve give the solutions of (207). The ratio $(d\Omega/\delta\Omega)$ is proportional to the slope at the intersections. We note that the solution at $\Omega = 0$ has a positive slope which indicates that this mode of oscillation is unstable according to the criterion equation (210). The other two solutions of (209) are stable because they have a negative slope. Negative slope indicates that any deviation $\phi\Omega$ caused by perturbation will eventually damp out.

In summary, we found that if the crystal is acentric, the nonlocal response of the crystal leads to unequal transmittance and phase shifts of the two waves. These, in turn, lead to a split in the oscillation intensity as well as oscillation frequency. The frequency split may be utilized to bias a laser gyro away from its lock-in region. In the above derivation, the bulk absorption in the photorefractive material is neglected. This is legitimate provided $\alpha \ll \gamma$, which is generally true in most photorefractive crystals. The attenuation in the crystal may affect the difference in phase shift according to (198) because $I_2 - I_1$ is no longer a constant. Numerical analysis is required to include the attenuation and obtain a more accurate result.

### *D. Real-Time Holography and Beam Processing*

We mentioned the holographic implications of two-wave mixing in photorefractive media earlier. Let us now elaborate on this idea in some detail. The formation of an index grating due to the presence of two coherent laser beams inside a photorefractive crystal is formally analogous to the recording process in conventional holography. Consider the procedure shown in Fig. 24(a), in which two laser beams intersect and form an induced index grating. The index grating, as given by (10), contains the product of the amplitudes $A_1$ and $A_2$. This index grating is a hologram formed by a "reference" beam $A_1$, and an "object" beam $A_2$. The transmission function of such a hologram can be written

$$t \sim \Delta n \sim A_1^* A_2 \exp(-i\vec{K}\cdot\vec{r}) + A_1 A_2^* \exp(i\vec{K}\cdot\vec{r}) \tag{211}$$

where $A_1$ and $A_2$ denote the complex amplitudes of the reference and object fields, respectively.

In the reconstruction step [see Fig. 24(b)], the hologram is illuminated by the reference beam $A_1 \exp(-i\vec{k}_1\cdot\vec{r})$. The diffracted beam can be written

$$\eta A_1 A_1^* A_2 \exp(-i\vec{k}_2\cdot\vec{r}) \tag{212}$$

where $\eta$ is the diffraction efficiency. We notice that the phase of $A_1$ cancels out and the diffracted beam is a reconstruction of the object beam $A_2 \exp(-i\vec{k}_2\cdot\vec{r})$. Similarly the "reference" beam $A_1$ can be reconstructed by illuminating the hologram with "object" beam $A_2$ [see Fig. 24(c)], provided beam $A_2$ is a phase object (i.e., $A_2$ has phase variation with $|A_2| =$ constant).

In addition to the holographic analog, two-wave mixing exhibits amplification which is a unique feature not available in conventional holography. Using these two properties, two-wave mixing can be used for beam processing. As a result of the real-time holographic nature, photorefractive two-wave mixing exhibits nonreciprocal energy transfer without any phase crosstalk [96]. This characteristic can be seen directly by examining the coupled equations (17) and (18).

The lack of phase crosstalk can be understood also in terms of the diffraction from the self-induced index grating in the photorefractive crystal. Normally, if a beam that contains phase information $\psi(r, t)$ is diffracted from a fixed grating, the same phase information also appears in the diffracted beam. In self-induced index grating, the phase information $\psi(r, t)$ is impressed onto the grating in such a way that diffraction from such a grating will be accompanied by a phase shift $-\psi(r, t)$. Such a dynamic hologram makes self-cancellation of phase information

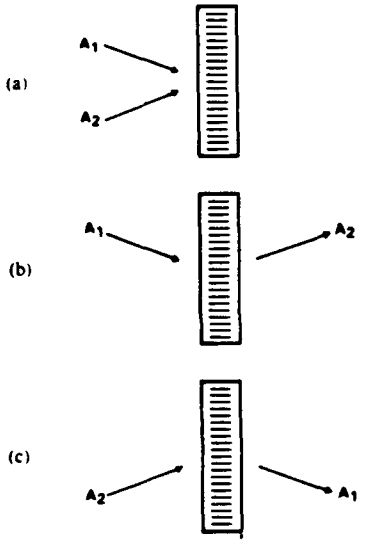


Fig. 24 Real-time holography

possible when the incident beam is diffracted from the grating produced by the incident and the reference beams. Such a self-cancellation of phase information is actually equivalent to the reconstruction of the reference beam when the hologram is read out by the object beam.

Energy transfer without phase crosstalk can be employed to compress both the spatial and the temporal spectra of a light beam [97]. In other words, the energy transfer without phase crosstalk can be utilized to clean up both the spatial-wavefront and temporal wavefront aberrations. In what follows, we will describe separately the cleanup of these two types of aberration.

In the cleanup of spatial aberration, a spatial mode filter (e.g., a pinhole mirror) is used to select a clean part of the aberrated beam. The rest of the beam consists of several spatial-frequency components. After the separation, these two portions of the beam are brought together at a photorefractive crystal. Because of the energy transfer without phase crosstalk, the signal beam can be amplified without bearing any phase information from the aberrated part of the beam.

The experimental configuration is shown schematically in Fig. 25. An argon-ion laser beam with output power of a few hundred milliwatts at 514.5 nm is used as the coherent light source. The polarization of the laser output is rotated 90° into the plane of incidence so that the largest effective electrooptic coefficient of the SBN crystal, essentially $r_{33}$, can be used. The beam splitter BS is used to split the incoming beam into the pump and the signal beams, which are mutually coherent. The beams are then loosely focused onto the sample $S$ by the focusing lenses $FL_1$ and $FL_2$, respectively. The average spot size of each beam inside the sample is approximately 3 mm in diameter. The sample used for the experiment was a crystal of single ferroelectric domain of SBN with a 5 × 6 mm cross section and a thickness of 6 mm. The external angle $\theta$ subtended by the two beams was approximately 10°.

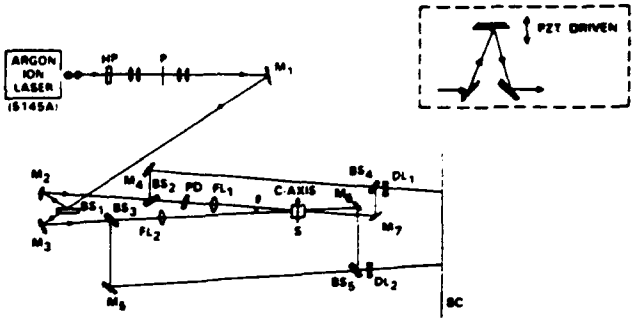


Fig. 25. Schematic diagram of the experimental setup for spatial wavefront correction. For temporal wavefront correction, the phase distorter (PD) is replaced by the set of mirrors shown in the inset. BS, beam splitter; DL, diverging lens; FL, focusing lens; HP, half-wave plate (5145 nm); $M$, plane mirror; $P$, polarizer; PD, phase distorter; $S$, sample; SC, screen [96].

The beam splitters $BS_2$ and $BS_4$ together with the mirrors $M_4$ and $M_7$ constitute a Mach–Zehnder interferometer whose output fringe pattern represents the spatial phase of the pump output. Similarly, the beam splitters $BS_3$ and $BS_5$ and the mirrors $M_5$ and $M_6$ constitute another interferometer for displaying the spatial phase of the signal output. The diverging lenses $DL_1$ and $DL_2$ are used to magnify the fringe pattern projected onto the screen SC.

Without the spatial phase distorter PD in the paths of the beams, the fringes of each are concentric circles, representing the spherical wavefront introduced by the converging lenses $FL_1$ and $FL_2$. Pictures of such fringes are shown in Fig. 26(a). With the phase distorter PD (a microscope slide etched with hydrofluoric acid) in the path of the pump beam (see Fig. 25), the spatial wavefront of the pump becomes strongly aberrated, as shown on the left-hand side of Fig. 26(b). The wavefront of the amplified beam, however, remains essentially undistorted [the right-hand side of Fig. 26(b)].

With the pump intensity on the order of 400 mW/cm$^2$ (total power of the order of 30 mW) and a signal-beam intensity on the order of 8 mW/cm$^2$, a signal gain (defined as the ratio of signal output power with and without the pump beam) of about 10 has been achieved with our SBN sample, for the experimental configuration described above, with no special care or optimization. For the case corresponding to the pictures shown in Fig. 26, the signal gain decreases from 10 to 7 as the phase aberrator is introduced. Our experimental results clearly demonstrate that energy transfer without phase crosstalk can be realized by two-wave mixing in photorefractive media.

The cleanup of temporal aberration can be understood in terms of nondegenerate two-wave mixing in photorefractive media. Let the frequencies of the two beams be $f_1$ and $f_2$, respectively. In the photorefractive medium, these two beams generate a traveling interference pattern. This interference pattern induces an index grating. The index grating has a frequency of $(f_2 - f_1)$. As a result of the nonlocal response of the crystal, energy transfer occurs that allows one beam to accept and the other beam to donate energy. Note that when beam 2 is diffracted from

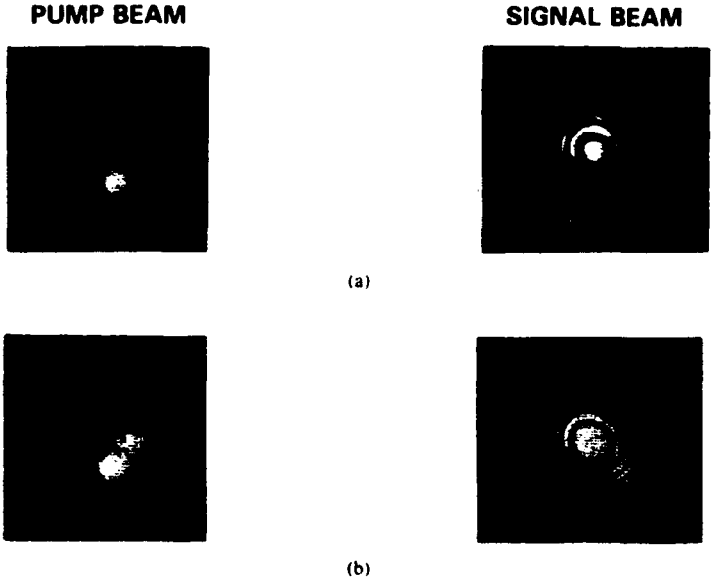


Fig. 26. Interference fringes representing the spatial phase of the pump output and the amplified signal output. (a) With no phase distorter in both arms. (b) With phase distorter in the pump beam prior to entering the photorefractive material [96].

the holographic grating, its frequency is shifted to $f_1$ because the index grating is traveling with a frequency of $(f_2 - f_1)$. Thus photons of frequency $f_2$ can be converted to photons of frequency $f_1$. A temporally-aberrated beam may be considered as a superposition of several frequency components. Thus, by using a frequency filter to select a single-frequency component and then to recombine it with the rest of the beam at a photorefractive crystal, it is possible to clean up the temporal aberration of light beams. In our experimental work, we use a piezoelectrically driven mirror to introduce the temporal wavefront aberration. The experimental setup is almost identical to that used in the previous experiment except that the spatial distorter PD (see Fig. 25) is now replaced by a temporal phase modulator. As the mirror moves at a constant velocity $v$, the frequency $f$ of the pump beam is Doppler shifted by an amount $\Delta f$ given by

$$\Delta f = 2fv/c$$

where $f$ is the original pump frequency, $v$ is the linear velocity of the moving mirror, and $c$ is the velocity of light in air. This frequency shift, or, equivalently, the temporal phase modulation, is picked up by a detector at the output port of the Mach-Zehnder interferometer. The temporal phase variation of the pump outside with a frequency modulation of 2 Hz is shown in the lower trace of the oscillogram (Fig. 27). The corresponding temporal phase variation of the amplified signal, as picked up by a similar detector, is represented by the upper trace of the oscillogram. Notice that the temporal phase of the amplified signal is essentially unperturbed. The signal gain, however, drops rapidly as the pump-modulation frequency is increased. Experimental results for the signal

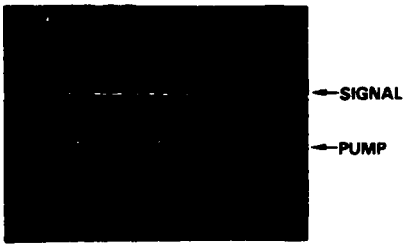


Fig. 27. Temporal phase variation of the pump output and amplified signal output [96].

gain versus pump-modulation frequency at various pump and signal power levels are given in Fig. 28.

The experiment described above can be viewed as a nearly-degenerate two-wave mixing experiment with a very small frequency offset ($\Delta f$) of a few hertz. The solid lines in Fig. 28 represent the theoretical fits based on (48) and (50) using the time constant $\tau$ as the adjustable parameter. The dependence of the material time constant on the input-beam intensity ratio and the total input intensity can thus be deduced. A typical result is illustrated in Fig. 29. Note that the time constant is relatively insensitive to input-beam intensity ratio.

In conclusion, we have demonstrated nonreciprocal energy transfer without phase crosstalk and have succeeded in beam cleanup by using photorefractive two-wave mixing in SBN crystals. Both spatial and temporal phase aberration of laser beams can be cleaned up, provided that the phase aberration does not change significantly over a period that is the time constant of the material. The hologram recording time $\tau$ of SBN crystals is also obtained

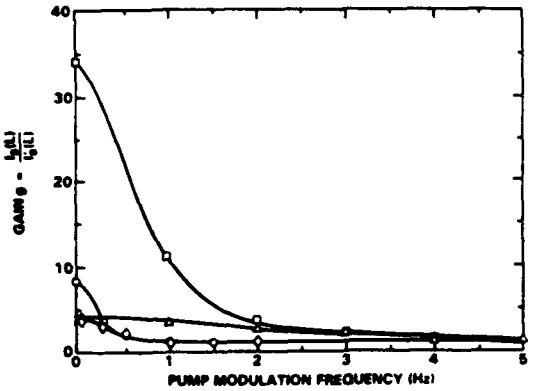


Fig. 28. Signal gain versus pump modulation frequency at various pump and signal power levels. $I_s(0)$, signal input power; $I_p(0)$, pump input power; $I_s(L)$, signal output power with pump beam on; $I_s'(L)$, signal output power with pump beam off. ○: $I_p(0) = 10$ mW, $I_s(0) = 0.26$ mW; ◇: $I_p(0) = 10$ mW, $I_s(0) = 2.5$ mW; □: $I_p(0) = 200$ mW, $I_s(0) = 0.4$ mW; △: $I_p(0) = 200$ mW, $I_s(0) = 48$ mW. The solid lines are the theoretical fits with the time constant $\tau$ as the adjustable parameter [96].

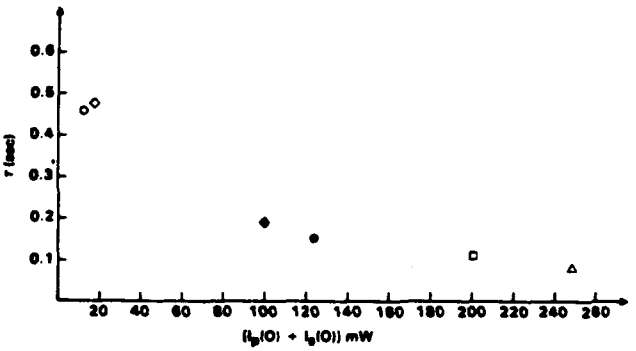


Fig. 29. Dependence of the time constant (hologram recording time) of the SBN sample on total input power and the beam power ratio. $I_s(0)$, signal input power; $I_p(0)$, pump input power, $m = I_p(0)/I_s(0)$. ○: $I_p(0) = 10$ mW, $I_s(0) = 0.26$ mW, $m = 40$. ◇: $I_p(0) = 10$ mW, $I_s(0) = 2.5$ mW, $m = 4$; ◆: $I_p(0) = 100$ mW, $I_s(0) = 0.2$ mW, $m = 500$; ●: $I_p(0) = 100$ mW, $I_s(0) = 24$ mW, $m = 4$; □: $I_p(0) = 200$ mW, $I_s(0) = 0.4$ mW, $m = 500$; △: $I_p(0) = 200$ mW, $I_s(0) = 48$ mW, $m = 4$ [96].

experimentally. Although the physical mechanism is different from the Raman coupling, the phenomenon of energy exchange without phase crosstalk is similar to the Raman beam cleanup [98]-[100].

The laser beam cleanup technique can also be used in conjunction with a phase conjugation to correct for the distortion due to crystal imperfection. Such a scheme has been used to clean up laser beams using a SBN crystal for two-wave mixing and a $BaTiO_3$ crystal as the conjugator [101].

Two-wave mixing in nonlinear media can be used for applications in optical information processing. The formation of holograms (volume index grating) can be used for the storage of three-dimensional information [12]. The nonreciprocal energy transfer can be used for the amplification of spatial images [77]. In the area of optical computing, digital logic operation using two-beam coupling in photorefractive materials has been proposed and demonstrated [102]. Such logic operations use the nonlinear phenomena of signal beam saturation and pump beam depletion in two-wave mixing. In addition, the erasure of hologram by a third beam can be used to control the efficiency of two-beam coupling. Recently, the transient response of the photorefractive effect was used for the time differentiation of coherent optical images.

## VI. Conclusions and Discussions

In conclusions, we have considered the coupling of two electromagnetic waves in various nonlinear media, including photorefractive crystals, Kerr media, and cubic semiconductors. The energy transfer as well as the phase shift due to coupling were derived and discussed. The results were then used to understand the oscillation of photorefractive ring resonators as well as the physical origin of self-pumped conjugators. We also presented a coupled-mode analysis of the coupling of two polarized beams in cubic photorefractive crystals. Cross-polarization two-beam coupling was discussed in some detail. In the last part of the paper, we discussed several applications using two-beam coupling in photorefractive crystals. These include ring laser gyros, real-time holography, beam processing, and information processing.

## Appendix A
## Kerr Coefficients

### A. Conversion Between Units and Definitions

The Kerr effect is traditionally described by a dependence of the index of refraction on the electric field by

$$n = n_o + n_2\langle E^2\rangle \qquad \text{(A1)}$$

where $n_o$ is the index of refraction at $E = 0$, $n_2$ is the Kerr coefficient, and the brackets $\langle\ \rangle$ stand for time-average. Some workers adopted the following definition:

$$n = n_o + n_2 I \qquad \text{(A2)}$$

where $I$ is the intensity of electromagnetic radiation measured in units of $W/m^2$ in the MKS system of units. The conversion from both definitions and between MKS and ESU units is given in Table III. We note that

$$I = c\epsilon_0\langle E^2\rangle \qquad \text{(A3)}$$

and

$$\text{for } E \quad 1 \text{ ESU} = 3 \times 10^4 \text{ V/m}$$

$$\text{for } I \quad 1 \text{ ESU} = 10^{-3} \text{ W/m}^2$$

### B. Relationship Between $n_2$ and $\chi^{(3)}$

The Kerr coefficient $n_2$ is also related to the third-order dielectric susceptibility $\chi^{(3)}$. Here we derive the relationship between them for isotropic media such as liquids or gases. In addition to the CGS and MKS units, there are several conventions used in the definition of $\chi^{(3)}$ [1], [2]. In this paper, we adopt the following definition of $\chi^{(3)}$:

$$P = \epsilon_o\chi^{(1)}E + \chi^{(3)}E^3 \qquad \text{(A4)}$$

TABLE III
CONVERSION TABLE FOR KERR COEFICIENTS

| $n = n_0 + n_2 \langle E^2 \rangle$ | | $n = n_0 + n_2 I$ | |
|---|---|---|---|
| ESU | MKS $(v/V)^2$ | ESU | MKS $(m^2/W)$ |
| 1 | $1/9 \times 10^{-8}$ | $4.2 \times 10^{-10}$ | $4.2 \times 10^{-7}$ |
| $10^{-11}$ | $1/9 \times 10^{-19}$ | $4.2 \times 10^{-21}$ | $4.2 \times 10^{-18}$ (for $CS_2$) |

where $P$ is the polarization and $E$ is the electric field. Using the complex number representation [1] for sinusoidal varying field such as the one given in (6), the complex amplitude of the polarization at frequency $\omega$ is

$$P(\omega) = \epsilon_0 \chi^{(1)} E + 3/4\, \chi^{(3)} E^* E E. \quad \text{(A5)}$$

If we rewrite (A5) as

$$P(\omega) = [\epsilon_0 \chi^{(1)} + 3/4\, \chi^{(3)} E^* E] E \quad \text{(A6)}$$

then the index of refraction can be written

$$\epsilon_0 (n^2 - 1) = \epsilon_0 \chi^{(1)} + 3/4\, \chi^{(3)} E^* E] E. \quad \text{(A7)}$$

We now compare (A7) with

$$\Delta n = n_2 \langle E^2 \rangle = 1/2\, n_2 E^* E \quad \text{(A8)}$$

and we obtain

$$n_2 = \frac{3}{4\epsilon_0 n} \chi^{(3)}. \quad \text{(A9)}$$

## APPENDIX B

The solution of the nonlinear coupled differential equations (118) and (119) is derived in this appendix.

By adding the two equations in (118) and carrying out the integration, we obtain

$$I_1 + I_2 = C \exp(-\alpha z) \quad \text{(B1)}$$

where $C$ is a constant equal to $I_1(o) + I_2(o)$. Using (B1) and (118), we can eliminate $I_2$ and obtain

$$\frac{d}{dz} I_1 + (\alpha + gCe^{-\alpha z}) I_1 = g I_1^2 \quad \text{(B2)}$$

which is a Bernoulli equation and can be integrated directly. The solution is

$$I_1(z)^{-1} = e^{\int P(z) dz} \left\{ -g \int e^{-\int P(z) dz} + C' \right\} \quad \text{(B3)}$$

where $C'$ is a constant of integration and $P(z)$ is given by

$$P(z) = \alpha + gCe^{-\alpha z}. \quad \text{(B4)}$$

To simplify (B3), we need to use the following integral formula:

$$\int e^{-ax + be^{-ax}} dx = \frac{1}{ab} e^{be^{-ax}}. \quad \text{(B5)}$$

Using (B4) and (B5), (B3) can be written

$$I_1(z) = \frac{Ce^{-\alpha z}}{1 + CC' \exp\left[ -\frac{1}{\alpha} gC \exp(-\alpha z) \right]}. \quad \text{(B6)}$$

Putting $z = o$ in (B6) and solving for $C'$, we obtain

$$C' = \frac{1}{C} \frac{I_2(0)}{I_1(0)} \exp\left[ \frac{1}{\alpha} gC \right] \quad \text{(B7)}$$

where we recall that $C = I_1(0) + I_2(0)$. Using the definitions for $m$ and $\gamma$ from (124) and (125), respectively, and (B7), $I_1(z)$ can be rewritten in the form of (122). The solution for $I_2(z)$ can be obtained from (122) and (B1). This completes the solution for $I_1(z)$ and $I_2(z)$.

Solutions for the phases $\psi_1$ and $\psi_2$ can be obtained by substituting (122) and (123) for $I_1(z)$ and $I_2(z)$, respectively, into (119) and carrying out the integration. The process requires the following integral formula:

$$\int \frac{e^{-\alpha x}}{1 + B \exp\left[ \frac{1}{\alpha} A \exp(-\alpha x) \right]} dx = \frac{1}{A} \log \left\{ 1 + \frac{1}{B} \exp\left[ -\frac{1}{\alpha} A \exp(-\alpha x) \right] \right\}. \quad \text{(B8)}$$

Using the expressions for $I_1(z)$ and $I_2(z)$ and the above formula, we arrive at (126) and (127). This completes the derivation of $I_1(z)$ and $I_2(z)$.

## ACKNOWLEDGMENT

The author wishes to acknowledge helpful discussions and collaborations with his colleagues M. Khoshnevisan, M. D. Ewbank, A. E. T. Chiou, I. McMichael, and T. Chang. The author also acknowledges the referees for their careful and critical review of the manuscript and their comments.

## REFERENCES

[1] See, for example, A. Yariv and P. Yeh, *Optical Waves in Crystals*. New York: Wiley, 1984.
[2] E. N. Leith and J. Upatneiks, "Wavefront reconstruction with different illumination and three-dimensional objects," *J. Opt. Soc. Amer.*, vol. 54, p. 1295, 1964.
[3] See, for example, Y. R. Shen, *Principles of Nonlinear Optics*. New York: Wiley, 1985.
[4] See, for example, *Laser Handbook*, vol. 4, M. L. Stitch and M. Bass, Eds. New York: Elsevier, 1985, pp. 333-485.
[5] See, for example, D. Pepper, "Applications of optical phase conjugation," *Sci. Amer.*, vol. 254, p. 74, 1986.
[6] A. Yariv, "Phase conjugate optics and real-time holography," *IEEE J. Quantum Electron.*, vol. QE-14, pp. 650-660, 1978.
[7] A. Ashkin, G. D. Boyd, J. M. Dziedzic, R. G. Smith, A. A. Ballman, J. J. Levinstein, and K. Nassau, "Optically induced refractive index inhomogeneities in $LiNbO_3$ and $LiTaO_3$," *Appl. Phys. Lett.*, vol. 9, pp. 72-74, 1966.
[8] V. L. Vinetskii, N. V. Kukhtarev, S. G. Odulov, and M. S. Soskin, "Dynamic self-diffraction of coherent light beams," *Sov. Phys.—Usp.*, vol. 22, pp. 742-756, 1979.
[9] N. V. Kukhtarev, V. B. Markov, S. G. Odulov, M. S. Soskin and V. L. Vinetskii, "Holographic storage in electro-optic crystals. Beam coupling and light amplification," *Ferroelectrics*, vol. 22, pp. 961-964, 1979.
[10] J. Feinberg, D. Heiman, A. R. Tanguay, Jr., and R. Hellwarth, "Photorefractive effects and light-induced charge migration in barium titanate," *J. Appl. Phys.*, vol. 51, p. 1297, 1980; —*J. Appl. Phys.*, vol. 52, p. 537, 1981; S. Ducharme and J. Feinberg, "Speed of the photorefractive effect in a $BaTiO_3$ crystal," *J. Appl. Phys.*, vol. 56, p. 839, 1984.
[11] R. A. Mullen and R. W. Hellwarth, "Optical measurements of the photorefractive parameters of BSO," *J. Appl. Phys.*, vol. 58, 1985.

[12] D. L. Staebler and J. J. Amodei, "Coupled wave analysis of holographic storage in $LiNbO_3$," *J. Appl. Phys.*, vol. 43, p. 1042, 1972.
[13] V. Markov, S. Odulov, and M. Soskin, "Dynamic holography and optical image processing," *Opt. Laser Technol.*, vol. 11, p. 95, 1979.
[14] A. Marrakchi, J. P. Huignard, and P. Gunter, "Diffraction efficiency and energy transfer in two-wave mixing experiments with $Bi_{12}SiO_{20}$ crystals," *Appl. Phys.*, vol. 24, p. 131, 1981.
[15] J. Feinberg and R. W. Hellwarth, "Phase conjugating mirror with continuous wave gain," *Opt. Lett.*, vol. 5, pp. 519-521, 1980.
[16] D. W. Vahey, "A nonlinear coupled-wave theory of holographic storage in ferroelectric materials," *J. Appl. Phys.*, vol. 46, p. 3510, 1975.
[17] J. Feinberg, "Asymmetric self-defocusing of an optical beam from the photorefractive effect," *J. Opt. Soc. Amer.*, vol. 72, p. 46, 1982.
[18] P. Yeh, "Contradirectional two-wave mixing in photorefractive media," *Opt. Commun.*, vol. 45, pp. 323-326, 1983.
[19] Y. H. Ja, "Energy transfer between two beams in writing a reflection volume hologram in a dynamic medium," *Opt. Quantum, Electron.*, vol. 14, p. 547, 1982.
[20] J. P. Huignard and A. Marrakchi, "Coherent signal beam amplification in two-wave mixing experiments with photorefractive BSO crystals," *Opt. Commun.*, vol. 38, p. 249, 1981.
[21] L. K. Lam, T. Y. Chang, J. Feinberg, and Hellwarth, "Photorefractive-index gratings formed by nanosecond optical pulses in $BaTiO_3$," *Opt. Lett.*, vol. 10, p. 475, 1981.
[22] P. Yeh, "Fundamental limit of the speed of photorefractive effect and its impact on device applications and material research," *Appl. Opt.*, vol. 26, p. 602, 1987; *Appl. Opt.*, vol. 26, p. 3190, 1987.
[23] E. Voit, M. Z. Zha, P. Amrhein, and P. Gunter, "Reduced $KNbO_3$ crystals for fast photorefractive nonlinear optics," in *Tech. Dig. Top. Meet. Photorefractive Materials, Effects, Devices*, Los Angeles, CA, Aug. 12-14, 1987 vol. 17, paper WA1-2, p. 2.
[24] A. M. Glass, M. B. Klein, and G. C. Valley, "Fundamental limit of the speed of photorefractive effect and impact on device applications and materials research: Comment," *Appl. Opt.*, vol. 26, p. 3189, 1987.
[25] M. B. Klein, "Beam coupling in undoped GaAs at 1.06 $\mu$m using the photorefractive effect," *Opt. Lett.*, vol. 9, p. 350, 1984.
[26] G. Albanses, J. Kumar, and W. H. Steier, "Investigation of the photorefractive behavior of chrome-doped GaAs using two-beam coupling," *Opt. Lett.*, vol. 10, p. 650, 1986. ——, *Opt. Lett.*, vol. 12, p. 120, 1986.
[27] D. Rak, I. Ledoux, and J. P. Huignard, "Two-wave mixing and energy transfer in $BaTiO_3$, application to laser beam steering," *Opt. Commun.*, vol. 49, p. 302, 1984.
[28] Ph. Refregier, L. Solymer, H. Rajbenbach, and J. P. Huignard, "Two-beam coupling in photorefractive $Bi_{12}SiO_{20}$ crystals with moving gratings: Theory and experiments," *J. Appl. Phys.*, vol. 58, p. 45, 1985.
[29] M. D. Ewbank, private communication.
[30] P. Yeh, "Photorefractive two-beam coupling in cubic crystals," *J. Opt. Soc. Amer. B*, vol. 4, p. 1382, 1987.
[31] T. Y. Chang, A. E. T. Chiou, and P. Yeh, "Photorefractive two-beam coupling with polarization flip in gallium arsenide," in *Tech. Dig. Top. Meet. Photorefractive Materials, Effects, Devices*, vol. 17. Washington, DC: Opt. Soc. Amer., 1987, pp. 55-58.
[32] P. Yeh and L.-J. Cheng, "Cross-polarization two-beam coupling in photorefractive GaAs crystals," in *Tech. Dig. Top. Meet. Photorefractive Materials Effects, Devices*, vol. 17. Washington, DC: Opt. Soc. Amer., 1987, pp. 59-61.
[33] L.-J. Cheng and P. Yeh, "Cross-polarization two-beam coupling in photorefractive GaAs crystals," *Opt. Lett.*, vol. 13, p. 50, 1988.
[34] B. Fischer, J. O. White, M. Cronin-Golomb, and A. Yariv, "Nonlinear vectorial two-beam coupling and focused four-wave mixing in photorefractive materials," *Opt. Lett.*, vol. 11, p. 239, 1986.
[35] M. Cronin-Golomb, J. O. White, B. Fischer, and A. Yariv, "Exact solution of a nonlinear model of four-wave mixing and phase conjugation," *Opt. Lett.*, vol. 7, pp. 313-315, 1982.
[36] I. McMichael and P. Yeh, "Phase shifts of photorefractive gratings and phase-conjugate waves," *Opt. Lett.*, vol. 12, p. 48, 1987.
[37] P. Yeh, "Contradirectional two-wave mixing in photorefractive media," *Opt. Commun.*, vol 45, pp. 323-326, 1983.
[38] L. J. Cheng and G. Gheen, "Photorefractive GaAs as an optical processing medium," presented at CLEO'88, Anaheim, CA, Apr. 25-29, 1988, paper ThQ1.
[39] B. Imbert, H. Rajbenbach, S. Mallick, J. P. Herrian, and J. P. Huignard, "High photorefractive gain in two-beam coupling with moving fringes in GaAs:Cr crystals," *Opt. Lett.*, vol. 13, pp. 327-329, 1988.
[40] P. Yeh, "Exact solution of a nonlinear model of two-wave mixing in Kerr media," *J. Opt. Soc. Amer. B*, vol. 3, pp. 747-757, 1986.
[41] Y. Anan'ev, "Possibility of dynamic correction of wave fronts," *Sov. J. Quantum Electron.*, vol. 4, pp. 929-931, 1975.
[42] D. I. Stasel'ko and V. G. Sidorovich, "Efficiency of light-beam conversion by dynamic three-dimensional phase holograms," *Sov. Phys.—Tech. Phys.*, vol. 19, pp. 361-365, 1974.
[43] V. G. Sidorovich and D. I. Stasel'ko, "Transformation of light beams by dynamic corrections using three-dimensional displacement phase holograms," *Sov. Phys.—Tech. Phys.*, vol. 19, pp. 1593-1597, 1975.
[44] D. I. Stasel'ko and V. G. Sidorovich, "Efficiency of light-beam transformation by dynamic phase holograms. I," *Sov. Phys—Tech. Phys.*, vol. 21, pp. 205-208, 1976.
[45] V. Vinetskii, N. Kukhtarev, S. Odulov, and M. Soskin, "Dynamic conversion of light beams by phase-shifted free-carrier holograms," *Sov. Phys.—Tech. Phys.*, vol. 22, pp. 729-732, 1977.
[46] V. L. Vinetskii, N. V. Kukhtarev, and M. S. Soskin, "Transformation of intensities and phases of light beams by a transient 'undisplaced' holographic grating," *Sov. J. Quantum Electron.*, vol. 7, pp. 230-233, 1977.
[47] V. L. Vinetskii, N. V. Kukhtarev, S. G. Odulov, and M. S. Soskin, "Dynamic self-diffraction of coherent light beams," *Sov. Phys. — Usp.*, vol. 22, pp. 742-756, 1969.
[48] V. L. Vinetskii, N. V. Kukhtarev, and T. I. Semenets, "Kinetics of dynamic self-diffraction of light beams in bulk media with local response," *Sov. J. Quantum Electron.*, vol. 11, pp. 130-132, 1981.
[49] N. V. Kukhtarev, P. D. Pavlik, and T. I. Semenets, "Optical hysteresis in wavefront reversal by traveling holographic gratings," *Sov. J. Quantum Electron.*, vol. 14, pp. 282-284, 1984.
[50] P. A. Apanasevich and A. A. Afanasev, "Stimulated scattering of light from free carriers created in a semiconductor by absorption of light," *Sov. Phys.—Solid State*, vol. 20, no. 1, pp. 53-56, 1978.
[51] See, for example, W. Kaiser and M. Maier, "Stimulated Rayleigh, Brillouin and Raman spectroscopy," in *Laser Handbook*, F. T. Arecchi and E. O. Schulz-Dubois, Eds. Amsterdam, The Netherlands: North-Holland, 1972, ch. E2.
[52] D. Poul and W. Kaiser, "Time-resolved investigation of SBS in transparent and absorbing media: Determination of phonon lifetimes," *Phys. Rev. B.*, vol. 1, pp. 31-43, 1970.
[53] J. Feinberg, "Self-pumped continuous-wave phase conjugator using internal reflection," *Opt. Lett.*, vol. 7, pp. 486-490, 1982; ——, "Continuous-wave self-pumped phase conjugator with a wide field of view," *Opt. Lett.*, vol. 8, pp 480, 1983.
[54] J. O. White, M. Cronin-Golomb, B. Fischer, and A. Yariv, "Coherent oscillation by self-induced gratings in photorefractive crystals," *Appl. Phys. Lett.*, vol. 40, pp. 450-452, 1982.
[55] T. Y. Chang and R. W. Hellwarth, "Optical phase conjugation by backscattering in the photorefractive crystal barium titanate," *Opt. Lett.*, vol. 10, pp. 408-410, 1985.
[56] J. F. Lam, "Origins of phase conjugate waves in self-pumped photorefractive mirrors," *Appl. Phys. Lett.*, vol. 46, pp. 909-911, 1985.
[57] K. R. MacDonald and J. Feinberg, "Theory of a self-pumped phase conjugator with two coupled interaction regions," *J. Opt. Soc. Amer.*, vol. 73, pp. 548-553, 1983.
[58] K. R. MacDonald and J. Feinberg, "Enhanced four-wave mixing by use of frequency-shifted optical waves in photorefractive $BaTiO_3$," *Phys Rev. Lett.*, vol. 55, pp. 821-822, 1985.
[59] D. J. Ganthica, P. Narum, and R. W. Boyd, "Observation of deterministic chaos in a phase-conjugate mirror," *Phys. Rev. Lett.*, vol. 58, pp. 1644-1647, 1987.
[60] M. C. Gower, "Photoinduced voltages and frequency shifts in a self-pumped phase-conjugating $BaTiO_3$ crystal," *Opt. Lett.*, vol. 11, pp. 458-460, 1986.
[61] See, for example, T. Y. Chang, "Fast self-induced refractive index changes in optical media: A survey," *Opt. Eng.*, vol. 20, pp. 220-232, 1981.
[62] M. Khoshnevisan and P. Yeh, "Relationship between nonlinear electrostrictive Kerr effects and acousto-optics," *Proc. SPIE*, vol. 739, pp. 82-86, 1987.
[63] A. Korpel, R. Adler, and B. Alpiner, "Direct observation of optically induced generation and amplification of sound," *Appl. Phys. Lett.*, vol. 5, pp. 86-89, 1964

[64] P. Yeh and M. Khoshnevisan, "Nonlinear optical Bragg scattering in Kerr media," *J. Opt. Soc. Amer. B*, vol. 4, pp. 1954-1960, 1988.
[65] P. Yeh, "Photofractive coupling in ring resonators," *Appl. Opt.*, vol. 23, pp. 2974-2978, 1984.
[66] P. Yeh and M. Khoshnevisan, "Phase conjugate ring gyros and photorefractive-biased ring gyros," *SPIE*, vol. 487, pp. 102-109, 1984.
[67] B. Ya. Zel'dovich and V. V. Shkunov, "Wavefront reproduction in stimulated Raman scattering," *Sov. J. Quantum Electron.*, vol. 7, pp. 610-615, 1977.
[68] G. Grynberg, E. LeBihan, and M. Pinard, "Two-wave mixing in sodium vapour," *J. Physique*, vol. 47, pp. 1321-1325, 1986.
[69] D. Grandclement, G. Grynberg, and M. Pinard, "Observation of cw self-oscillation due to pressure-induced two-wave mixing in sodium," *Phys. Rev. Lett.*, vol. 59, pp. 40-43, 1987.
[70] P. Yeh, "Theory of unidirectional photorefractive resonators," *J. Opt. Soc. Amer. B*, vol. 2, pp. 1924-1928, 1985.
[71] M. D. Ewbank and P. Yeh, "Frequency shifted cavity length in photorefractive resonators," *Opt. Lett.*, vol. 10, pp. 496-498, 1985.
[72] M. Kramer, W. Tompkin, and R. Boyd, "Nonlinear-optical interactions in fluorescein-doped boric acid glass," *Phys. Rev. A*, vol. 34, pp. 2026-2031, 1986.
[73] I. McMichael and P. Yeh, "Nondegenerate two-wave mixing in ruby," in *Dig. Int. Conf. Quantum Electron.* Washington, DC: Opt. Soc. Amer., 1987, paper MDD3, pp. 10-13.
[74] See, for example, I. C. Khoo and T. H. Liu, "Probe beam amplification via two- and four-wave mixing in a nematic liquid crystal film," *IEEE J. Quantum Electron.*, vol. QE-23, pp. 171-173, 1987, and references therein.
[75] P. Yeh, "Photorefractive coupling in ring resonators," *Appl. Opt.*, vol. 23, pp. 2974-2978, 1984.
[76] ——, Electromagnetic propagation in photorefractive layered media," *J. Opt. Soc. Amer.*, vol. 73, pp. 1268-1275, 1983.
[77] J. P. Huignard and A. Marrackchi, "Two-wave mixing and energy transfer in $B_{12}SiO_{30}$ crystals: Application to image amplification and vibration analysis," *Opt. Lett.*, vol. 6, pp. 622-624, 1981.
[78] V. Markov, S. Odulov, and M. Soskin, "Real-time contrast reversal using two-wave mixing in $LiNbO_3$," *Opt. Laser Tech.*, vol. 11, pp. 95-99, 1979.
[79] P. Yeh and A. E. T. Chiou, "Real-time contrast reversal via four-wave mixing in nonlinear media," *Opt. Commun.*, vol. 64, pp. 160-166, 1987.
[80] J. Feinberg and G. D. Bacher, "Self-scanning of a continuous-wave dye laser having a phase-conjugate resonator cavity," *Opt. Lett.*, vol. 9, pp. 420-422, 1984.
[81] G. Valley and G. Dunning, "Observation of optical chaos in a phase-conjugate resonator," *Opt. Lett.*, vol. 9, pp. 513-515, 1984.
[82] P. Gunter, "Holography, coherent light amplification and optical phase conjugation with photorefractive materials," *Phys. Rep.*, vol. 93, pp. 201-299, 1982.
[83] As the orientation of the two-wave mixing fringe pattern with respect to the crystal axes changes, the effective electrooptic coefficient (and coupling efficiency of the index grating) is modified. $\gamma L$ is independently measured by removing ring-cavity mirror $M_2$ and using an attenuated probe beam from $BS_2$ with an external angle of 20° between probe and pump beams.
[84] Provided by R. Neurgaonkar, Rockwell International, Thousand Oaks, CA.
[85] B. Fischer, M. Cronin-Goulomb, J. O. White, A. Yariv, and R. Neurgaonkar, *Appl. Phys. Lett.*, vol. 40, p. 863, 1982.
[86] P. Yeh, M. D. Ewbank, M. Khoshnevisan, and J. M. Tracy, "Doppler-free phase-conjugate reflection," *Opt. Lett.*, vol. 9, pp. 41-43, 1984.
[87] R. A. McFarlane and D. G. Steel, "Laser oscillator using resonator with self-pumped phase-conjugate mirror," *Opt. Lett.*, vol. 8, pp. 208-210, 1983.
[88] W. B. Whitten and J. M. Ramsey, "Self-scanning of a dye laser due to feedback from a $BaTiO_3$ phase-conjugate reflector," *Opt. Lett.*, vol. 9, pp. 44-46, 1984.
[89] K. R. MacDonald and J. Feinberg, "Anomalous frequency and phase shifts in self-pumped phase conjugators," *J. Opt. Soc. Amer. A*, vol. 1, p. 1213, 1984.
[90] M. D. Ewbank and P. Yeh, "Frequency shifts of self-pumped phase conjugators," *Proc. SPIE*, vol. 613, pp. 59-69, 1986.
[91] See, for example, Z. Knittl, *Optics of Thin Films*. New York: Wiley, 1976, p. 240.
[92] P. Yeh, "Electromagnetic propagation in a photorefractive layered media," *J. Opt. Soc. Amer.*, vol. 73, pp. 1268-1271, 1983.
[93] M. Z. Zha and P. Gunter, "Nonreciprocal optical transmission through photorefractive $KNbO_3$:Mn," *Opt. Lett.*, vol. 10, pp. 184-186, 1985.
[94] K. R. MacDonald, J. Feinberg, M. Z. Zha, and P. Gunter, "Asymmetric transmission through a photorefractive crystal of $BaTiO_3$," *Opt. Commun.*, vol. 50, pp. 146-150, 1984.
[95] See, for example, A. Yariv, *Quantum Electronics*. New York: Wiley, 1975, p. 187, eqs. (9.3)-(15).
[96] A. E. T. Chiou and P. Yeh, "Beam cleanup using photorefractive two-wave mixing," *Opt. Lett.*, vol. 10, pp. 621-623, 1985.
[97] P. Yeh, "Spectral compression using holographic two-wave mixing," in *Dig. Conf. Lasers, Electro-Optics*. Washington, DC: Opt. Soc. Amer., 1985, p. 274.
[98] V. I. Bespalov, A. A. Betin, and G. A. Pasmanik, "Reproduction of the pump wave in stimulated scattering radiation," *Izv. Vyssh. Ucheb. Zaved. Radiofiz.*, vol. 21, p. 961, 1978.
[99] J. Goldhar and J. R. Murray, "Intensity averaging and four-wave mixing in Raman amplifiers," *IEEE J. Quantum Electron.*, vol. QE-18, p. 399, 1982.
[100] R. S. F. Chang and N. Djeu, "Amplification of a diffraction-limited Stokes beam by a severely distorted pump," *Opt. Lett.*, vol. 8, pp. 139-141, 1983.
[101] A. E. T. Chiou and P. Yeh, "Laser beam cleanup using photorefractive two-wave mixing and optical phase conjugation," *Opt. Lett.*, vol. 11, pp. 461-463, 1986.
[102] Y. Fainmain, C. C. Guest, and S. H. Lee, "Optical digital logic operations by two-beam coupling in photorefractive material," *Appl. Opt.*, vol. 25, pp. 1598-1603, 1986.

**Pochi Yeh** (M'78-SM'87), photograph and biography not available at the time of publication.